Metrology of the dopants in ZnO nanostructures by atom probe tomography

Nooshin Amirifar

THESE

Pour obtenir le grade de Docteur

opéré par l'Université de Rouen

Spécialité : Science des matériaux

Métrologie des dopants dans les nanostructures ZnO par sonde atomique tomographique

Présentée et soutenue publiquement par

Nooshin AMIRIFAR

Thèse soutenue publiquement le 25 septembre 2015 devant le jury composé de		
M. Bruno MASENELLI	Professeur - INL Lyon	Rapporteur
M. Xavier PORTIER	Professeur - CIMAP Caen	Rapporteur
M. Hervé RINNERT	Professeur - IJL Nancy	Examinateur
M. Vincent SALLET	Chergé de recherche - GEMaC Versailles	Examinateur
M. Etienne TALBOT	Maître de conférences – GPM Rouen	Co-encadrant
M. Rodrigue LARDE	Maître de conférences – GPM Rouen	Co-encadrant
M. Philippe PAREIGE	Professeur – GPM Rouen	Directeur de thèse

Thèse dirigée par Pr. Philippe PAREIGE
Groupe de Physique des Matériaux UMR 6634 CNRS
Université et INSA de Rouen

Acknowledgment

Foremost, I would like to express my sincere gratitude to my advisors Prof. Philippe Pareige, Dr. Etienne Talbot and Dr. Rodrigue Lardé for their continuous support during my Ph.D. study and related research, for their patience, motivation, and immense knowledge. Their guidance helped me in all the time of research and writing of this thesis.

Besides, I would like to thank my thesis committee for their encouragement, insightful comments, and hard questions which incented me to widen my research from various perspectives.

Also, I thank ANR MAD-FIZ project for funding my Ph.D. thesis and I'm grateful to all my collaborators in GEMAC, INL, NEEL, CEA-LETI, CIMAP and IPCMS laboratories for providing samples, information, frequent meetings and discussions.

My sincere thank also goes to GPM laboratory staff for all administrative, instrumental guidance and measurements and also for creating such a great working atmosphere. I would like to especially thank Dr. Lorenzo Rigutti, Prof. François Vurpillot, Dr. Angela Vella and Dr. Alain Lusson for all the fruitful discussions.

I am grateful to then Prof. Didier Blavette, director of doctoral school, for all his care and attentions for Ph.D. students.

My appreciation also extends to my laboratory colleagues, Constance, Nicolas, Mykola, Mohit, Safa, Jonathan, Alfia, Yana, Constantin, Adeline, Antoine and Claire for stimulating discussions, for hard days we were working together before deadlines, and for all the fun we have had during past years.

My very very especial thank goes to Aurélien, Isabelle, Manon and Martin who made my days in Rouen delighted, with whom I share unforgettable memories. They took such an especial place in my heart and I can never imagine my stay in Rouen without their presence.

Last but not least, I thank my family for supporting me spiritually throughout my life and giving me the confidence I needed to accomplish challenges. I would like to especially thank my fiancé, Michał, who has been the biggest inspiration of my life, I don't know how I could make it through hard days without his enormous positive vibes.

List of figures:

Introduction

The invention of the first semiconductor-based transistor in the first half of the last century has paved the way for the fabrication of more advanced semiconductor based electrical and optical devices. Si and GaAs have become the most popular semiconductors used in these devices. However, the rapid advance in electronics and optoelectronics has increased the demand for faster, smaller and more powerful devices, usually beyond the physical properties of these semiconductors.

In the past years, much attention has been drawn to ZnO, as its large and direct band gap of 3.37 eV offers many promising properties for short wave-length optoelectronics, transparent electronics, spintronic devices and sensor applications. The exciton binding energy of 60 meV can provide roughly twice higher luminescent efficiency than its rival semiconductor, GaN. Moreover, ZnO is non-toxic and it can be obtained in wide range of nanostructures using many different synthesis methods which makes it a flexible material for more complex and advanced devices. However, many difficulties are encountered when it comes to the introduction of the impurities to ZnO matrix. The presence of many defects and natural n-type conductivity of ZnO has made it difficult to produce a high, stable and reliable p-type ZnO. In the last decade, significant efforts and improvements in crystal growth and characterization techniques has made it possible to have a better understanding of the p-type doping process of ZnO.

Yet, additional material and process development issues are necessary aiming the control on doping process and the improvement of crystal quality. Size reduction from bulk and thin films to nanowires has shown a considerable enhancement for achieving p-type ZnO. For nanowires, higher quality of ZnO can be achieved as the impact of substrate nature on nanowires is decreased. Nanowires also exhibit excellent optical properties due to the smaller presence of deep levels, usually associated to intrinsic point defects.

For optical devices such as LEDs, the incorporation of rare earth elements in ZnO matrix has been of a great interest to produce different color of emissions. Nevertheless, the optical properties of these materials are found to be strongly dependent on the quality of the doped ZnO. Hence, a well-established method is necessary to control the distribution and concentration of the dopants for a reliable emission. Many elaboration methods have been developed for an optimum emission from rare earth elements embedded in ZnO. However, many observations have

remained under debates basically due to the lack of proper characterizing technique. In this thesis, we introduce atom probe tomography as a powerful technique for a quantitative picture of the dopant spatial distribution in ZnO nanowires and thin films. Different nanostructures elaborated by different growth techniques have been studied by atom probe tomography. These studies allow us to assess and develop atom probe tomography for characterizing ZnO nanomaterials.

This thesis comprises five parts:

- First chapter contains the information about the properties of ZnO and its applications for optoelectronic and electronic devices. The main objective and interest of this thesis are also discussed in this chapter.

- In the second chapter, the synthesis methods and the conventional characterization techniques used in this work are explained.

- The third chapter is dedicated to the fundamentals of atom probe tomography (APT) technique. Different methods of specimen preparation for APT of nanowires have been suggested. Since this technique is recently developed for semiconductor materials and in particular barely discussed for ZnO, in this chapter we mainly focus on development of APT for ZnO nanomaterials. The influence of certain APT analysis parameters on the quality and accuracy of measurements is examined. These fundamental studies are to perform more precise APT analyses of the doped and undoped ZnO materials. These studies are then applied in characterizing different doped ZnO material discussed in chapter four and five.

- In chapter four, p-type doping of ZnO nanowires has been discussed. The main interest of achievement of a p-type ZnO is to provide the near UV emission p/n ZnO homo-junction. Two different doping processes have been used and the success or the failure of these techniques is studied by APT. These results obtained by APT, were used to explain the results observed by different conventional techniques such as XRD, Raman and photoluminescence.

- In chapter five, we focus on the enhancement of ZnO emission by doping with rare earth elements. The influence of the growth parameters on optical properties of doped ZnO thin films are examined by photoluminescence. APT is used to relate the significant change in optical properties of these samples to distribution and quantity of the incorporated dopants.

Finally, the major results of this thesis will be summarized in the conclusion. Some prospective are also proposed following this work.

CHAPTER I Zinc oxide properties and applications

In last decades, zinc oxide (ZnO) has received a considerable attention due to its potential applications in optoelectronic, photonic and electric devices such as short-wavelength LEDs and photodiodes. In order to discuss the application of ZnO-based devices, first we should have a good knowledge of ZnO material, structure and its general properties. Hence, the objective of this chapter is to provide general information about ZnO material and the recent reports on its application in short-wavelength ZnO LEDs.

I.1 Wide band gap light emitting diodes

In the past decade, the rapid increase in demand for new electronic and optoelectronic devices, has brought a considerable attention on light emitting diodes (LED) based on wide band gap semiconductors. LEDs have fast response, low pollution, excellent durability and long lifetime (more than 100,000 h). Unlike other light sources, LED produces light directly instead of generating a byproduct of heated filaments or ionizing gas; making it a true “cold” light. Red and green light-emitting diodes have been used for almost fifty years. White LED particularly, has shown to be a significant potential solution for brand new applications in room lightening, mobiles and displays. White-light LED can be obtained using few main techniques: uniting a short wavelength LED such as UV or blue LED coated with yellow phosphors which appears white to human eye [Park 2014] or triad of red, green, blue colors (RGB system) [Huang.S 2014] giving rise to a white light. Each technique has its own advantages and drawbacks. RGB system involves more complex procedures and it needs a stronger control on color rendering. Hence, this method becomes more costly and less straight forward than phosphorous conversion method. However, RGB system has more color flexibility which can help to reach a real ‘’day light’’ color LEDs [U.S. Department of energy].

Nevertheless, despite the high demand and great efforts undertaken in the research community as well as in industry, blue light remained a long sought after of lighting technology for three decades.

First blue LEDs were made following the achievement in fabrication of high quality GaN by Isamu Akasaki, Hiroshi Amano and Shuji Nakamura in the early 1990s [Amano1989 -

Nakamura 1991]. On October 2014, this achievement has received the Nobel Prize in physics for the invention of efficient blue LED as a step forward for bright and energy saving white light source.

Basically, a light emitting diode is a semiconductor based electric device which creates light under an electric current. The emission from LED is directly related to the semiconductor that is used. Components of a light emitting diode are illustrated in *Figure I.1*.

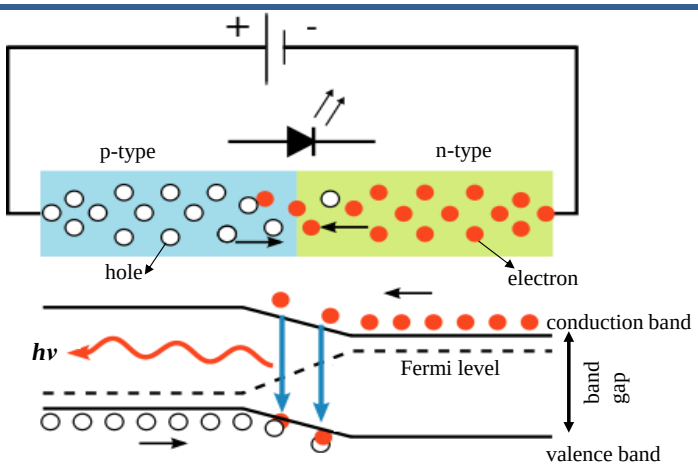

Figure I.1: Principle and components of Light Emitting Diode (LED). In order to emit light, a current is applied by connecting p-type semiconductor to positive voltage and n-type semiconductor to negative voltage via metallic contacts. In a p-n junction biased with a forward voltage, electrons are injected from the n- to the p-side, and holes are injected in the opposite direction. Light is emitted due to the electron-hole recombinations.

A simple LED is composed of a junction of a positive and a negative direct band-gap semiconductor (p-n junction). The light is released when an electron from higher energy level falls into a hole at lower energy level. The color of the light depends on the difference in the energy of these two levels corresponding to the band gap of the semiconductor. Many additional electrical transitions become possible when dopants or defects are introduced into the semiconductor lattice. For example, substituting lattice ions with impurity atoms having a nuclear charge greater than that of the lattice, creates discrete electron levels at the energies above the valence band. These dopants are called donor creating an n-type semiconductor. If the dopants carry a nuclear charge less than that of the lattice ion (acceptors), unoccupied electron acceptor levels are introduced at energies below the conduction band (p-type semiconductor).

The density of dopants in an n-type or a p-type semiconductor is generally in the range of 10^{12} to 10^{20} cm^{-3} [Özgür 2005].

LED development began with infrared and red devices made with gallium arsenide (GaAs). Advances in materials science have made it possible to produce devices with light in a variety of colors and shorter wavelengths.

Considering the band gap energy of most common semiconductors, developing an affordable high energy emissions in the range of blue and UV is narrowed down to only few semiconductors.

Among all semiconductors, ZnO has received much attention due to its large and direct band gap (~3.4 eV), allowing for the application in short wavelength LEDs. Its direct band gap provides the same momentum of electrons and holes in the conduction and the valence. Thus, an electron-hole recombination can directly emit a photon. Among all large band gap semiconductors, gallium nitride (GaN) is the main rival of ZnO as they have many similar properties. Nevertheless, ZnO has many more advantages over GaN that makes ZnO a more suitable semiconductor for LED devices:

- Large exciton binding energy of 60 meV (at room temperature) of ZnO as compared to GaN (24 meV). This large exciton binding energy indicates that the excitonic emission in ZnO can persist at room temperature and higher which allows ZnO based devices operate at room temperature and above. The prototype ZnO based LEDs have been shown to operate at nearly 400°C [Wei 2007].
- ZnO offers a higher band gap (3.4 eV) and by band gap engineering (doping with Cd or Mg) this value can be raised to the range of 3-4.5 eV [Makino 2001].
- ZnO can be synthesized in different ZnO nanostructures using low cost methods, whereas GaN film is prepared on some limited substrate (SiC, Sapphire, and Si). Furthermore a good quality ZnO film can be achieved at much lower growth temperature (about 500 °C) comparing to the one of GaN (>1000°C).
- ZnO is cheap, abundant and non-toxic and resistant to high radiation.

However, some difficulties are encountered in synthesis and doping process of ZnO material that prevents the large-scale application of this material in short-wavelength LED devices. The properties of ZnO and the origin of these difficulties are discussed in the following sections.

I.2 Zinc oxide: Material properties and applications

I.2.1 General properties

ZnO is a II-VI semiconductor, which attracted many attention due to its possible applications in optoelectronic, photonic and electronic devices. ZnO has a wide and direct band gap of 3.437 eV at 2K and a large exciton binding energy of 60 meV [Look 2001].

ZnO can exhibit a hexagonal wurtzite structure, a cubic rock salt structure or a cubic zinc blend structure. In normal conditions of temperature and pressure, the wurtzite structure is the most stable one. The lattice parameters for wurtzite structure at room temperature are a=b=3.249 Å and c=5.2042 Å [Klingshirn 2010 - Özgür 2005]. In ZnO wurtzite structure, each oxygen anion is surrounded by four zinc cations and together they form a tetrahedral structure (*Figure I.2.a*).

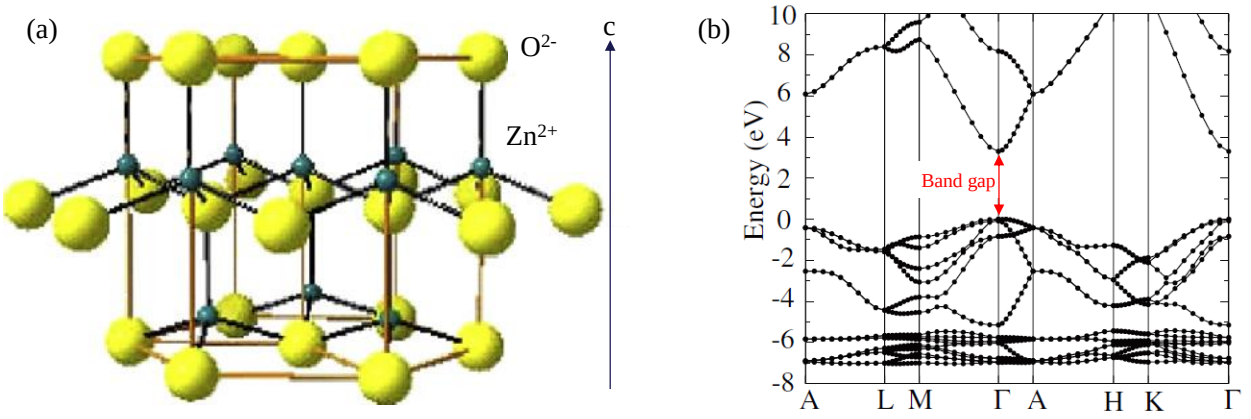

Figure I.2: (a) The wurtzite structure model of ZnO. The unit cell contains two zinc cations and two oxygen anions, forming a sequence of O–Zn double layers stacked along the c-axis [Yang 2008]. (b) Electronic band structure of ZnO where the energy of the valence band maximum is set to zero [Janotti 2009].

Figure I.2.b shows the electronic band structure of ZnO. The ten narrow bands below -4 eV mainly consist of the Zn 3d-orbitals, and the six moderately dispersive bands from -4 to 0 eV consist of the O 2p bonding states. The first two conduction band states are strongly Zn localized and correspond to empty Zn 4s-orbitals. Both the valence band maximum and the lowest conduction band minimum occur at Γ indicating that ZnO has a direct band gap [Janotti 2009].

The highest growth rate in ZnO is along the c-axis [Özgür 2005]. Along c-axis, the crystal can be considered to have a stacking sequence of zinc cations and oxygen anions which give rise to the piezoelectric properties in ZnO. Hence, depending on whether ZnO material is O-terminated or Zn-terminated, the polarity along c-axis changes that can influence the structure and properties of ZnO. Therefore, the growth direction together with the polar surfaces allows ZnO to present a wide range of novel structures that can be grown by adjusting the growth conditions.

Pure, p-type and n-type ZnO thin films have been produced using several deposition methods: pulse laser deposition (PLD), molecular beam epitaxy (MBE), diffusion, magnetron sputtering and chemical vapor deposition using different dopants. Pure and doped ZnO nanowires can be grown via vapor transport process, hydrothermal methods and CVD mechanisms using metal-organic precursor.

Each method provides different kinetic parameters for different crystal planes that are governed by the growth technique and the experimental conditions. Various ZnO nanostructures can be carried out by different synthesis techniques. The flexibility in morphology makes ZnO a great potential for novel or more complex device design. Only by means of the controllable synthesis parameters, such as deposition temperature and pressure as well as the carrier flux, different morphology of ZnO with different properties can be carried out. *Figure I.3.a* to *d* shows examples of ZnO nanostructures such as ZnO nanowires [Fang 2008], nanobelts [Pan 2001], hierarchical nanowires [Wang 2004] and comb-like [Wang 2003].

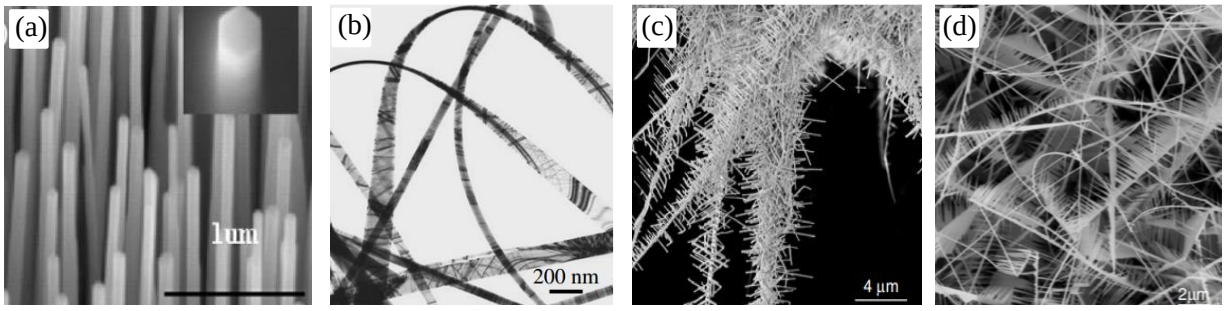

Figure I.3: (a) ZnO nanowires grown by physical vapor deposition [Fang 2008], (b) ZnO nanobelts grown by sublimation of Zn powder [Pan 2001], (c) ZnO hierarchical nanowires grown by vapour liquid solid and SnO_2 as catalyst [Wang 2004], (d) ZnO comb-like result of surface polarization induced growth due to the chemically active (0001) Zn plane [Wang 2003].

Hence, the growth condition is an important issue influencing the morphology and the properties of ZnO. Fang *et al.* studied the influence of the growth temperature on ZnO nanowires using a simple physical vapor deposition method. By controlling growth temperature, well-aligned ZnO nanowire arrays along the normal direction of the substrate were obtained [Fang 2008]. As the growth temperature increased the distribution of nanowires become denser with a smaller length and larger diameter. XRD results of the ZnO nanowires grown at different temperatures are compared with the XRD pattern obtained for ZnO thin film shown in *Figure I.4*. It can be seen that nanowires exhibit a stronger intensity of the peak at (002) and this intensity increases as the growth temperature is increasing. The shift in the peak shows the c-parameter for the lattice is increasing for higher growth temperature. Fang *et al.* conclude that the growth temperature is a critical experimental parameter for the formation of different morphologies of ZnO nanostructures: it determines the amount of reactive vapor generated and the surface diffusion length of the adsorbed vapor species [Fang 2008]. The influence of the parameters is further discussed in chapter II.

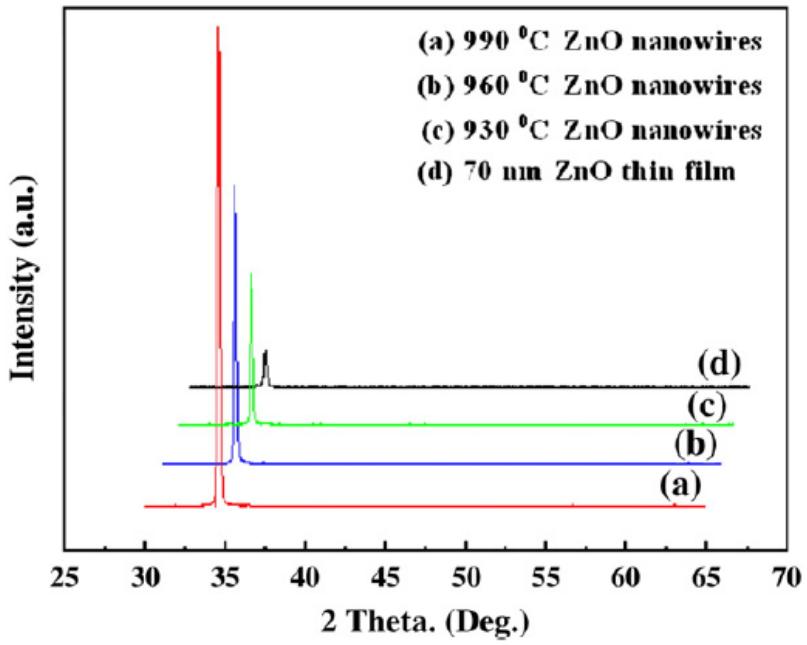

Figure I.4: XRD pattern of synthesized ZnO nanowire arrays at different growth temperatures (a) 990°C, (b) 960°C (c) 930°C and (d) 70 nm ZnO thin film [Fang 2008].

For electrical and optical applications, a reproducible and reliable method to grow high quality ZnO is an inevitable step. A high quality ZnO can also be a good host material for introducing the dopants. ZnO can be doped with different elements regarding the desired application. However, ZnO suffers from many native defects that strongly affect its properties. Since the presence of these defects is highly dependent on the growth technique and conditions, finding a reliable method for ZnO growth and doping is very important task.

I.2.2 Defects in ZnO

ZnO has a number of intrinsic defects that can directly influence its wide range of properties by affecting the doping and growth related diffusion mechanism and concentration of the carriers. Therefore, in order to use ZnO materials in devices, it is important to know and control these defects. Native defects associated with ZnO are Zn vacancy (V_{Zn}), O vacancy (V_O), Zn interstitial (Zn_i), O interstitial (O_i), Zn antisite (Zn_O) and O antisite (O_{Zn}). Among all, Zn interstitials and O vacancies are known to be the predominant defect types in ZnO [Özgür 2005]. Most of the defects commonly mentioned and discussed for ZnO are quite small and qualified as point defects. The concentration of a point defect (c) depends on its formation energy (E^f) given by the equation (I.1),

$$c = N_{sites} \exp\left(-\frac{E^f}{k_B T}\right), \qquad \text{(I.1)}$$

where N_{sites} is the concentration of the sites in the crystal that the defect can be incorporated on, k_B is the Boltzmann constant and T is the temperature [Kittel 2004].

The formation energy of the defects in ZnO was calculated by Kohan and Van de Walle [Kohan 2000 - Van de Walle 2001]. The formation energy of a point defect is not constant and it depends on the growth or annealing conditions. In O-rich conditions, zinc vacancies are dominant, whereas oxygen vacancies are more likely in Zn-rich conditions [Kohan 2000].

For example, forming an oxygen vacancy requires the removal of one oxygen atom. This is determined by the relative abundance of Zn and O atoms, expressed by the chemical potentials of Zn and O, respectively (μ_{Zn} and μ_O). However, for a charged vacancy, the formation energy

further depends on the Fermi level E_F, which is the energy of the electron reservoir such as electron chemical potential.

The formation energy of a point defect in a charge state of q is given by,

$$E^f(q) = E^{total}(q) - n_{Zn}\mu_{Zn} - n_O\mu_O - qE_F, \quad \text{(I.2)}$$

and $E^{total}(q)$ is the total energy of the system containing n_{Zn} and n_O zinc and oxygen atoms, and μ_{Zn} and μ_O are the chemical potential for Zn and O, and E_F is the Fermi energy [Janotti 2009 - Morkoç 2009]. Since the chemical potentials depend on the growth conditions, the change in the condition can influence the defect concentration in ZnO. Some typical defects in ZnO at their different charge state are shown in *Figure I.5* [Janotti 2009].

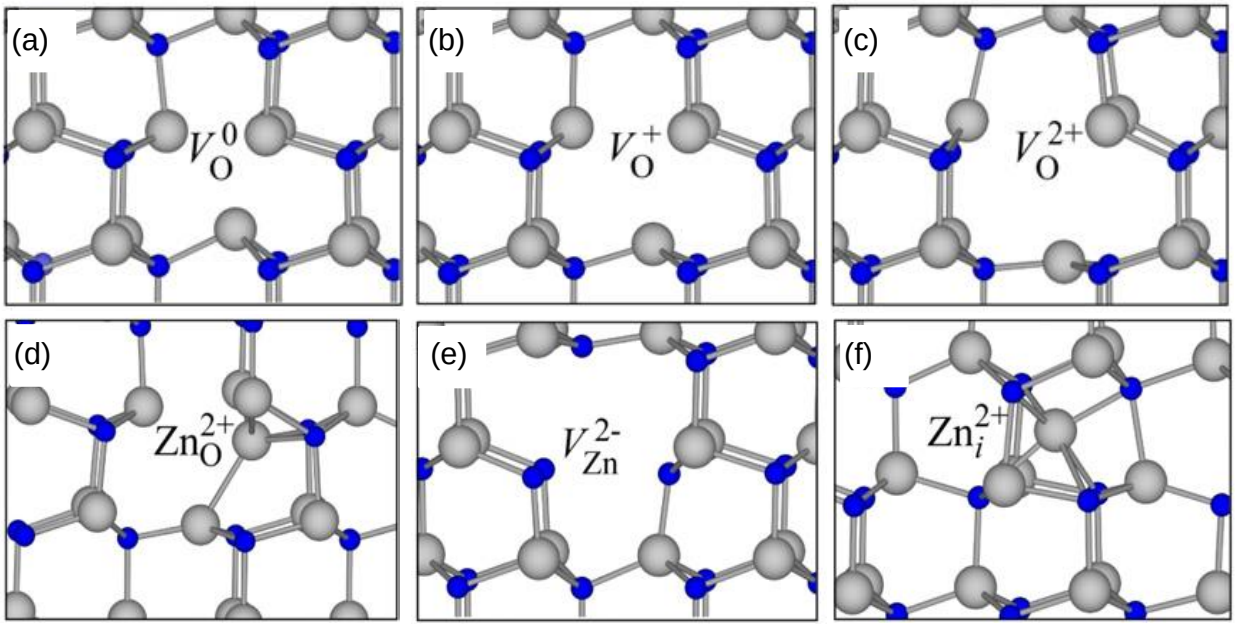

Figure I.5: Ball and stick model of local relaxed atomic position of Zn and O atoms around oxygen vacancy at (a) neutral,(b)+1 charge, (c) +2 charge states, (d) Zn antisite in 2+ charge state, (e) Zn vacancy at -2 charge state, (f) Zn interstitial in 2+ charge state. The Zn atoms are shown in grey and oxygen atoms are in blue [Janotti 2009].

I.2.3 Electrical properties of ZnO

The electrical properties of ZnO are strongly influenced by the point defects concentrations and dislocation number density. However, the electrical conductivity of ZnO can be tuned from

insulating to very high conductive behavior by introducing different dopants [Özgür 2005]. *Figure I.6* shows the dopants substituting Zn or O sites in ZnO creating p-type or n-type conductivity. Once the elements of group VA replace oxygen sites in ZnO, they are considered as acceptors, while group VIIA are donors. If the elements of group IA replace zinc sites, they are acceptors, while group IIIA replacing zinc atoms behave as donor.

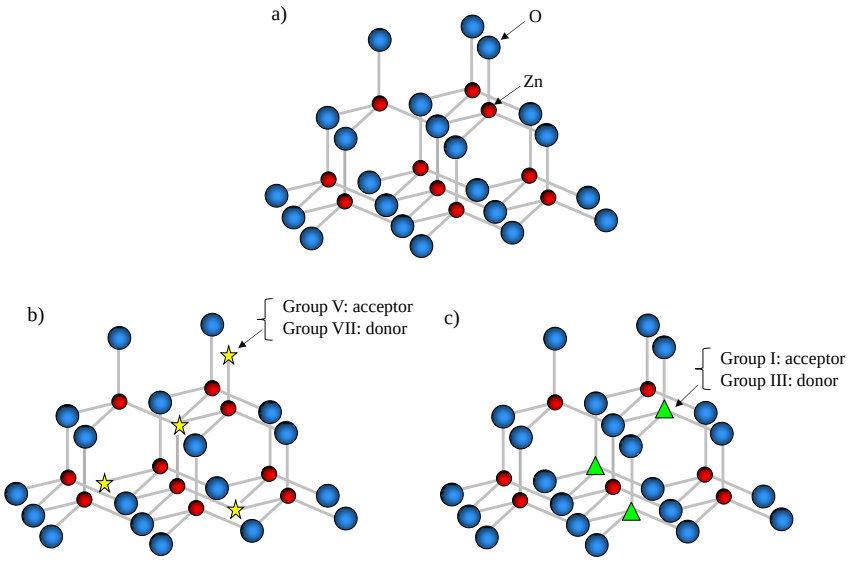

Figure I.6: (a) Undoped ZnO, Zn atoms are shown in red and oxygen atoms in blue representing a defect-free wurtzite structure, (b) dopants replacing oxygen atoms, (c) dopants replacing zinc sites.

Figure I.7.a presents schematic view of the band gap energy levels in ZnO. The valence band in ZnO splits into three states named A, B and C which is caused by crystal field and spin orbit interaction [Meyer 2004]. The ZnO band gap of 3.437 eV refers to the difference in energy level between the subband-A and conduction band. Introducing donor and acceptors creates energy levels close to the conduction and valence band respectively (*Figure I.7.b).* More transitions can occur due to the presence of donor and acceptor levels, such as, transfer of electrons from donor states to the conduction band or from the valence band to the acceptor states.

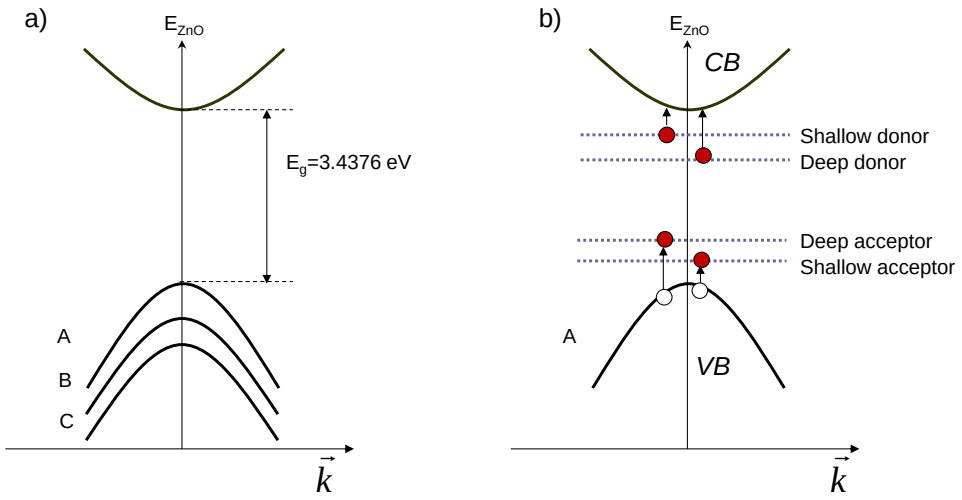

Figure I.7: (a) Three valence bands (A, B, C) in ZnO [Meyer 2004], (b) formation of donor-acceptor levels, electrons (red circle) can leave to higher energy level and leave behind a hole (white circle).

Nevertheless, achieving a high quality p-type ZnO remains a major challenge because ZnO exhibits unintentional n-type conductivity. The origin of this behavior is still under debate, but it has been mainly addressed to the deviation from stoichiometry due to the presence of intrinsic defects such as zinc interstitial (Zn_i) and oxygen vacancy (V_O) or/ and presence of hydrogen impurities [Janotti 2009].

Difficulties in both n-type and p-type doping have not been a surprising issue in wide band gap semiconductors. For example, GaN, ZnS and ZnSe are easily doped to n-type while p-type doping is the major obstacle. This situation is opposite for the case of ZnTe [Özgür 2005].

Hence, in order to take advantage of potential offered by zinc oxide in devices working at UV or visible range, it is important to find a reliable synthesis method for high quality n-type and p-type ZnO materials. The high quality ZnO p-n junction is the revolutionary step leading towards a whole new technology.

- n-type ZnO

As-grown ZnO often presents unintentional n-type conductivity with a very high electron density of more than 10^{17} cm^{-3} [Yang 2008]. Prior to year 2000, it was assumed that Vo and Zn_i are responsible for n-type behavior of ZnO since most samples are grown under zinc rich condition. In 2000, this assignment was challenged by Kohan *et al.* and Van de Walle [Kohan

2000 - Van de Walle 2000]. Kohan *et al*. theoretically proved that both V_O and Zn_i have high formation energy and they are deep donor rather than shallow. They also showed that neither Vo nor Zn_i are present at the measurable amount and even if they are present, their ionization energy is too high to produce free electrons. Later Zhang *et al.* showed that Zn_i is rather a shallow donor than deep one [Zhang 2001]. On the other hand, positron annihilation spectroscopy was used to study the introduction and recovery of point defects in electron-irradiated n-type ZnO, and the results suggest that a shallow V_O related state may also exist [Tuomisto 2005]. Van de Walle theoretically showed that the unintentional incorporation of hydrogen impurities in ZnO crystal structure acts as a shallow donor and causes the n-type behavior in ZnO. Hydrogen that is always present in all ZnO growth techniques can form a strong bond with oxygen in ZnO. The incorporation of hydrogen later was experimentally proved by different authors [Hofmann 2002 - Nickel 2003].

The theoretical calculations coupled with experimental results can lead to the conclusion that native defects do not play a significant role in n-type conductivity of undoped ZnO. However it was found that native defects, especially Zn_i, contribute significantly to n-type conductivity in ZnO, as complexes rather than isolated elements [Look 2005]. Look *et al.* showed both theoretically and experimentally, under N ambient, the Zn_i-N_O complex is a stronger candidate than H or any other known impurity [Look 2005].

Zhang *et al.* calculated the defect formation energies together with the defect transition energies [Zhang 2001]. They explained that native defects that act as donor (V_O, Zn_i and Zn_O) can lead to n-type doping of ZnO. For that, these dopants should have low formation enthalpy to be formed readily. This can occur for V_O and Zn_i in Zn-rich condition. Besides, the electron compensating centers such as O_i and V_{Zn} must have high formation enthalpy even if E^f is high in the gap, in order to avoid their formation. It is approximately true for zinc-rich but not for oxygen-rich conditions. Eventually, the defects that act as donors must have shallow levels in order to produce electrons. Only Zn_i and Zn_O can meet this condition. Hence, the intrinsic n-type behavior of ZnO is due to Zn_i in Zn-rich ambient.

So far, there is no definite explanation for the natural n-type conductivity of ZnO. Therefore, in order to have a controlled n-type doping of ZnO, it is important to investigate the possible impurities that act as shallow donor and can be used to make n-type ZnO in a stable manner [Zhang 2001].

n-type doping of ZnO is possible by column VIIA elements such as F, Cl, I substituting for O sites giving rise to the carrier concentration up to 10^{20} cm^{-3} [Cao 2011 - Chikoidze 2008 - Zheng 2011]. High quality n-type ZnO can also be achieved by intentional doping with the column IIIA elements such as Al, Ga, In. These elements can substitute for zinc sites and act as donors and can produce carrier concentration more than 10^{20} cm^{-3}. These donors can produce n-type ZnO transparent materials with highest conductivity available today and hence, they are preferred as donor dopants [Behrends 2012 - Hafdallah 2011 - Kim 2010 - Su 2012].

- p-type ZnO

As it was explained previously, unintentional n-type behavior of ZnO is the main problem in achieving a p-type ZnO and the reason behind this behavior has remained controversial. The difficulties involved in the p-type doping of ZnO, can rise from several reasons:

- The native defects play a role as compensating centers in p-type conductivity. When the impurity atom is introduced, spontaneously, opposite-charged native defects are generated which compensate for the effect of the dopants [Desnica 1998].
- Hydrogen impurities can incorporate in ZnO structure and act as acceptor-killer center [Theys 2002].
- Park *et al.* have shown that if the dopant cannot be introduced to the appropriate host crystal site due to the low solubility or insolubility, the dopant can behave as a donor. They have shown that when the column-I elements occupy the interstitial site they behave as donors and not acceptors [Park 2002].
- Even if the dopants are soluble and they occupy the appropriate site they can stay un-ionized because they form a deep level rather than a shallow acceptor level at normal temperature [Zhang 1999].

Native defects such as O_i and V_{Zn} can also behave as acceptors in ZnO in certain conditions [Look 2006]:

i. O_i and V_{Zn} that behave as acceptors must have shallow levels, so that they produce holes easily which is only the case in V_{Zn}.

ii. In order to increase the concentration of acceptors, they must have low formation enthalpy, even if the formation energy of the acceptor defect is low. This is the case only for O-rich conditions.

iii. V_O, Zn_i and Zn_O can compensate for the hole centers, therefore they must have high formation enthalpy so that they do not form. This condition cannot be met for neither Zn-rich nor O-rich conditions.

Therefore, it was concluded that ZnO could not be doped under thermal equilibrium because the formation energies of V_O, Zn_i and Zn_O (which act as donors) are low and they form readily. Also, it is hard to produce acceptors in Zn-rich conditions and as it was mentioned before most samples are grown under zinc rich condition.

Hence, to create shallow acceptor levels, the growth condition must be controlled carefully to produce ZnO with low compensating defects. Prior to 1999, there was only one report of p-type ZnO, where both the method reliability and material quality were poor [Minegishi 1997]. Since then, a vast experimental literature has been done in order to find the origin of difficulties in growth of p-type ZnO that is yet, controversial.

So far many groups have reported the achievement of p-type ZnO using different techniques and different dopants [Kao 2014 - Myers 2012 - Xiao 2008]. Theoretically, the intentional doping of ZnO materials is possible by elements of group IA and VA.

Using ab-initio calculations, Vidya *et al.* showed that acceptors occupying the cation site make shallow acceptor level rather than dopants at the anion site. It was found that the acceptors occupying cation sites make less perturbation in valence band maximum than dopants at anion sites [Vidya 2012].

Previously, it was observed that, once the acceptors are introduced, the E_F moves towards the valence band maximum. Simultaneously, the formation energy of the charge donor defects decreases as they donate the electrons to Fermi level reservoir. Therefore, theoretically elements of column IA such as Li, Na, K were considered to be able to create p-type conduction in ZnO as they sit on cation sites. Zinc oxide thin films doped with Li, Na, K have been prepared by pulse laser deposition and radio frequency magnetron sputtering where doping enhanced the electrical, optical and also magnetic properties [Huang.Y 2014 - Lü 2010 - Yi 2010].

Among all, lithium has attracted more attention since it is the most common unintentional dopant in hydrothermally grown ZnO [Monakhov 2009]. Theoretically, Li atom replacing cation sites

should act as acceptor. However, it was found that the type of charge carrier Li forms depends on the site it occupies. For example, Li at the interstitial site Li_i behaves as a donor and it is stable in Zn-rich and equilibrium conditions. On the other hand, Li substituting Zn sites (Li_{Zn}) behaves as acceptor. However, Li_{Zn} is stable only in O-rich conditions, where the formation energy of Li_i is lower than Li_{Zn} in p-type ZnO and hence can be formed more readily [Vidya 2012]. It was realized, having small atomic radii, group I elements prefer to occupy the interstitial sites rather than substitutional sites and hence they act as donors. In case of Na and K, the longer bond length than Zn-O bond length, increases the formation of the native defects that are acceptor killers [Look 2004].

For Li complex with defects, it was shown that L_i-V_O appears as donor and it is stable under Zn-rich condition. On the other hand, Li_{Zn}-V_{Zn} is stable under O-rich condition and behaves as acceptor. Therefore it was concluded that, obtaining Li doped p-type ZnO is more likely under O-rich condition. The same behavior can be considered for the other elements of the same group as well [Vidya 2012].

Previously, it was discussed that the H impurities incorporate as a donor in ZnO. This contrasts with the conventional behavior of hydrogen in semiconductors, whereby it counteracts the prevailing conductivity. In other words, it is expected that H should incorporate as an acceptor in n-type ZnO. This paradox was theoretically explained by Van de Walle by the fact that H^- (act as acceptor) has never lower formation energy than H^0 or H^+ (donors). Hence, the donor site is always preferred state in thermodynamic equilibrium [Van de Walle 2000].

Elements of column VA such as N, P, As and Sb are also possible dopants for p-type ZnO where they replace anion sites [Chu 2008 - Fan 2007 - Fang 2009 - Zheng 2009]. Among all, nitrogen is considered as the most suitable acceptor for a successful p-type ZnO. Having similar atomic radius, it was naturally accepted that nitrogen atoms replace oxygen sites. Larger ionic radius of P and As than oxygen, casts the doubt about the success in doping with P and As. The ionic radius of P and As seem to be too large to occupy the oxygen site within the host lattice. However, there are several reports of achieving p-type ZnO doped with As or P with a hole concentration of above 10^{18} cm^{-3}. In ZnO doping with As, Vaithianathan *et al.* reported the preparation of arsenic doped p-type ZnO films using a Zn_3As_2/ZnO target by pulsed laser deposition. Room temperature Hall measurements revealed that the As-doped ZnO films exhibited p-type conductivity after being annealed at 200 °C in N_2 ambient for 2 min with the

hole concentrations varied between 2.48×10^{17} and $1.18\times10^{18}\,cm^{-3}$ [Vaithianathan 2005]. However, this discussion has become more complex considering what would happen if As substitutes for Zn site rather than O site. It was shown theoretically that As_{zn}-$2V_{Zn}$, acts as a shallow acceptor. These observations on both As and Sb showed that they both have low acceptor-ionization energies and obtaining *p*-type ZnO, requires O-rich growth or annealing conditions [Limpijumnong 2004]. Vaithianathan *et al*. also reported p-type ZnO thin films doped with phosphorus by pulsed laser deposition. The ZnO:P films were thermally annealed at temperatures between 600 and 800 °C and revealed p-type behavior with a hole concentration of 5.1×10^{14} and $1.5\times10^{17}\,cm^{-3}$ [Vaithianathan 2005].

Generally accepted, nitrogen was found to be the best candidate for p-type doping of ZnO as it has the smallest ionization energy and it does not create antisites. Numerous experimental efforts by many different groups have reported a successful p-type conductivity of N-doped ZnO. The concentration of about 10^{17} cm^{-3} was achieved by Look *et al*. [Look 2002]. However, they have not resulted in stable and reproducible p-type material, bringing doubt on the efficiency of nitrogen as a shallow acceptor and whether nitrogen is actually a deep acceptor [Lyons 2009].

Up to this day, among all possible dopants, nitrogen is still considered to be the most promising dopant. Despite facing many limits such as low solubility, poor stability and thermal instability of ZnO:N, the hole concentration up to 2.29×10^{18} cm^{-3} was reported [Alves 2009 - Chao 2013 - Dhara 2012 - Kerr. 2007 - Zeng 2007]. Most of the attempts for p-type doping of ZnO have been dedicated to doping with nitrogen acceptors. Nitrogen doped ZnO thin films were carried out using plasma-assisted molecular beam epitaxy on c-plane sapphire. The samples exhibit a hole concentration of $4.45x10^{17}$ cm^{-3} with a hole mobility of $0.18cm^2/Vs$ and a resistivity of 78 Ω.cm [Sun 2006]. Different ZnO nanostructures were chosen for p-doping. Marzuki *et al.* elaborated nitrogen doped ZnO nanowires deposited on c-plane sapphire substrate using metal organic chemical vapor deposition technique and diallylamine ($C_6H_{11}N$) as nitrogen source. The presence of nitrogen atoms were examined by Raman spectroscopy and photoluminescence shown in *Figure I.8*. Local micro-Raman measurements (*Figure I.8.a)* show a decrease in nitrogen concentration from the bottom to top of the nanowire. PL spectra *(Figure I.8.b)* confirmed that the DAP (donor-acceptor-pair) is more important on the bottom of the nanowires [Marzouki 2010].

It was found that untreated nitrogen doped ZnO sample generally exhibited poor electrical properties and crystalline quality. Thermal annealing were usually employed to treat ZnO:N sample since it is an effective technique to improve crystalline quality and to activate acceptor impurities in ZnO. However, thermal annealing in air resulted in decomposition of nitrogen and oxygen from the sample causing ZnO:N with poor properties.

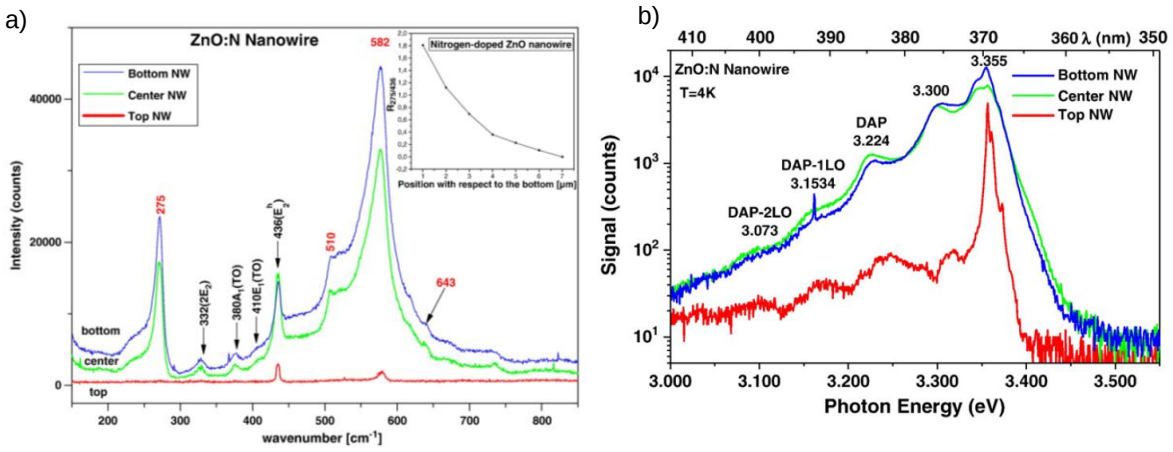

Figure I.8: (a) Micro-Raman spectra of one nitrogen-doped ZnO nanowire. The inset shows variation of R275/436 along a single nitrogen-doped ZnO nanowire. (b) Micro-photoluminescence (µ-PL) spectra at 4 K of a nitrogen-doped ZnO nanowire recorded at different positions [Marzouki 2010].

To solve this problem, Sun *et al.* suggested the annealing in N_2O plasma protective ambient, that can provide both nitrogen ion and oxygen ion. In this case, the decomposition of nitrogen and oxygen from ZnO:N sample during thermal annealing process under high temperature was restrained [Sun 2008].

Despite all the attempts, the choice of dopant and growth technique remains controversial and the reliability of p-type ZnO is still under debate [Look 2004].

I.2.4 Optical properties of ZnO

Both the presence of the defects and the incorporation of the dopants can affect the optical properties of ZnO. Defects and impurities create discrete electronic states in the band gap and hence they influence the optical emission and absorption in ZnO.

In semiconductors, apart from defects and impurities, intrinsic optical transitions take place between electrons in the conduction band and holes in the valence band. The emission of photons in semiconductors occurs when an electron from higher energy level recombines with the hole from a lower energy. The energy of the emitted photon depends on the difference in the energy of these two levels. There are five main radiative recombination processes commonly observed in semiconductors, shown in *Figure I.9*.

- Band to band recombination, is an intrinsic transition and it involves the recombination of an electron from the conduction band with a hole on the valence band. This process is dominant at room temperature but rarely seen for low temperatures (*Figure I.9.a*).
- Excitonic recombination of free excitons: when electron and hole remain bound to each other due to the Coulomb force, they create excited states slightly less than band gap energy. These electron-hole pairs are known as exciton and they are referred as "free excitons" (FE). An exciton can move in the crystal but since electron and hole are bound, they move together causing neither photo-conductivity nor current (*Figure I.9.b*).
- Donor-acceptor recombination: as it was seen previously, introducing acceptors and donors to the semiconductor creates energy levels in the band gap. The recombination can occur between the electron on the neutral donor and the hole on the neutral acceptor (*Figure I.9.c*).
- Excitonic recombinations of bound excitons are extrinsic transitions and related to dopants or defects that create discrete electronic energy levels in the band gap. A free hole can recombine with the electron on the neutral donor forming a positively charged excitonic ion which is known as "bound exciton" (*Figure I.9.d*). Similarly a free electron can recombine with the hole on the neutral acceptor (*Figure I.9.e*).

Undoped ZnO materials exhibit two main band emissions: an intense UV band and a visible broad band. UV band is referred to the excitonic recombination across the band gap. However, the origin of the visible luminescence in ZnO remains controversial and it is mainly addressed to the presence of the intrinsic point defects. Chen *et al.* used *in-situ* laser-induced luminescence to study the visible luminescent characteristics of ZnO in nitrogen and oxygen ambients. In N_2 atmosphere, green, yellow and orange luminescence was observed. Once the samples were treated in oxygen atmosphere, the green luminescence turned into yellow and the yellow luminescence to orange. The results indicate that the visible luminescence in ZnO is associated

with the oxygen vacancies in ZnO and the green, yellow and orange luminescence appear in high, moderate and low concentration of oxygen vacancy, respectively [Chen.J 2004].

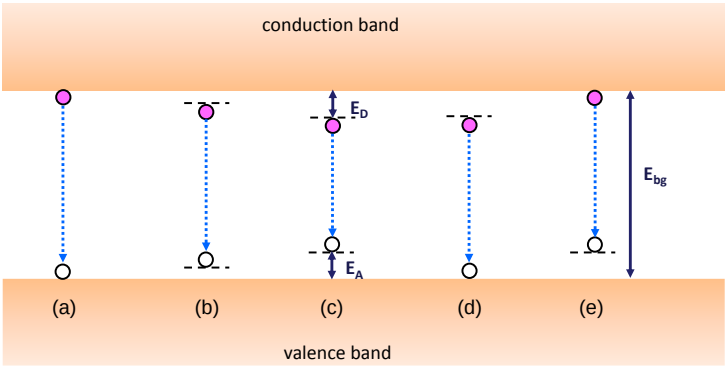

Figure I.9: Radiative recombination process in semiconductors, (a) band to band, (b) free exciton, (c) donor-acceptor, (d) and (e) bound exciton. E_D and E_A, corresponds to the donor and acceptor energy levels and E_{bg} corresponds to the energy of the band gap.

In general, the emission of green light is mainly assigned to the two main mechanisms, deep copper acceptors [Dingle 1969] and intrinsic point defects such as oxygen vacancies (V_O) [Kang 2003 - Rakhesh 2007], excess of Zn in the form of zinc interstitial (Zn_i) [Liu 1992] , or oxygen antisite defects (O_{Zn}) [Lin 2001].

Thermal annealing was usually employed to treat doped ZnO samples since it is an effective technique to improve the crystalline quality as well as optically activation of the impurities. *Figure I.10* shows the influence of thermal annealing of ZnO thin films grown by magnetron sputtering annealed in a thermal furnace with air and nitrogen ambient at 800 °C for 30-120 min. The photoluminescence results show that the UV peaks of the annealed ZnO films were shifted approximately 1-3 nm toward shorter wavelength while its intensity increased after thermal annealing. There was no deep-level emission peaks related to point defects after thermal annealing. It means that optical properties are improved by high temperature annealing. Especially in air ambient, the oxygen vacancies are resolved by the supply of oxygen from air ambient [Lee 2009].

Nevertheless, the doping of ZnO is an important bottleneck for many applications because the quality of ZnO and dopant incorporation is strongly dependent on the synthesis conditions.

Even a very small amount of native defects and impurities (down to 0.01 ppm) can significantly change the electrical and optical properties of ZnO [Stavola 1998].

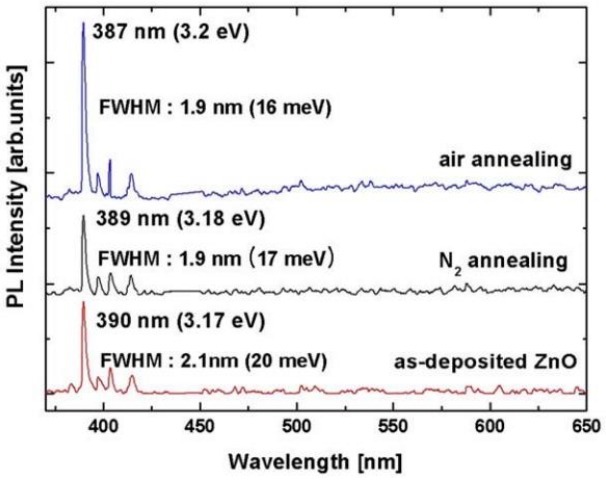

Figure I.10: Photoluminescence spectra of the as-deposited ZnO film and ZnO films annealed at 800°C for 30-120 min in N_2 and air ambient [Lee 2009].

Although the undoped ZnO exhibits visible light emission due to the defects, this emission is not adequate for lightening applications as it is governed by random luminescence. Making use of excellent luminescence properties of ZnO in UV and light regions through a controlled process, ZnO can be doped with rare earth elements (REE). Doping with rare earth elements has attracted much attention. Their partially filled *d* and *f* orbitals give rise to the additional optical transitions providing great luminescent centers. These transitions result in unique optical properties that are used extensively in new generation of optical devices [Bünzli 2005].

In general, rare earth ions exist in trivalent state e.g. Eu^{+3}, Tb^{+3}, etc. Once a rare earth atom is substituted in a host crystal, the energy levels in the atom are disturbed by host crystal field causing a redistribution of the electrons at 4f sub-shell in rare earth ion. *Figure I.11* shows the discrete energy levels for different RE ions [Bünzli 2005].

The emission from RE dopants begins with absorption process which means the transition of an electron from the ground state to higher excited states.

Then the electron at higher excited energy level loses its energy and drops to the available states just below the previous state. When the energy corresponding to this transition is small, the electron loses its energy to the lattice. Otherwise, this energy is given out in the form of

emission. Therefore in RE elements incorporated in a crystal, the emission corresponds to the transition from the intermediate states to the ground state (*Figure I.11* blue lines).

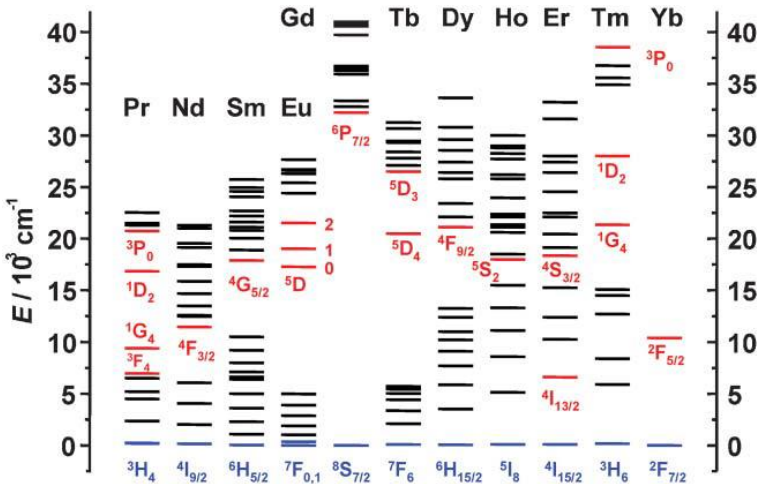

Figure I.11: Discrete 4f energy levels for RE ions. Red lines correspond to the main luminescent levels and blue lines to fundamental level [Bünzli 2005].

What brings a special attention in doping with RE elements is resulting from the emission energy they can provide. This emission can vary from near IR and visible to UV region depending on the RE element that is used for doping. *Figure I.11*, shows the different discrete 4f energy levels for RE ions. In REE, *5s* and *5p* shells are filled with electrons which shield the inner shell *4f* electrons from the environment. Transition between shielded *4f* electrons leads to a rich spectrum of absorption lines that exhibit many extraordinary optical properties giving rise to the great interest in doping with REE. Doping with REEs can also optically activate ZnO and result in emission in visible spectral region. Tb doped ZnO can emit green light where, Eu doped ZnO leads to the emission of red light [Cetin 2009 - Kumar 2014] . It is important to note that most of RE ions are optically active only when they are in their trivalent state.

Due to the large difference in radius size between rare earth ions (RE^{3+}) and Zn^{2+}, it is still quite difficult to incorporate RE ions into the lattice position of the Zn ions in ZnO. Moreover, the optical properties of the RE ion are mainly dependent on the local environment or symmetry of the host material. Therefore, manipulating the concentration of the dopants and controlling the aspect ratio of the nanostructures are still remaining challenges.

I.2.5 Hetero-junction ZnO LED

Difficulties in p-type doping of ZnO has led the ZnO based device technology to an alternative approach. Some attempts have been made to develop the growth of n-type ZnO on p-type materials (ZnTe, Cu_2O, $SrCu_2O_2$) to form LEDs [Hosono 2002].

In particular, n-ZnO/p-GaN hetero-junction has attracted much attention. The small lattice mismatch of 1.8% between p-type GaN and ZnO, has been practically demonstrated to be useful for commercial devices [Kim 2007 - Lee 2009].

Shen *et al.* have deposited highly crystalline ZnO epitaxial films on commercial p-type GaN substrates via radio frequency (RF) magnetron sputtering [Shen 2014]. The schematic diagram of n-ZnO/p-GaN heterojunction is shown in *Figure I.12.a*. Electroluminescence spectra of the fabricated junction were obtained under different forward bias voltage (*Figure I.12.b*).

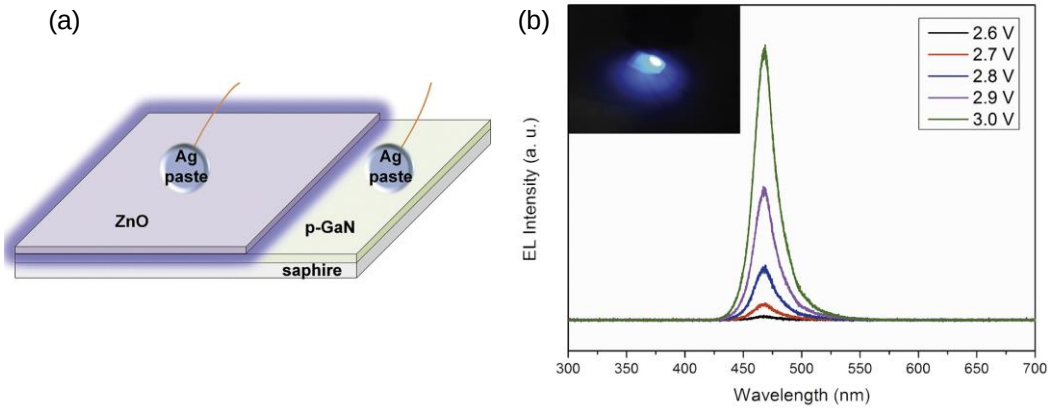

Figure I.12: (a) Schematic diagram of n-ZnO/p-GaN heterojunction. (b) Electroluminescence spectra of the fabricated n-ZnO/p-GaN LED under different forward bias voltages. The blue light emission observed under a dc bias of 3 V is shown in the inset [Shen 2014].

A dominant emission peak was observed in all spectra, centered at 460 nm. A blue light was observed for the voltage of more than 2.7 V. The emission remained stable under different applied voltage bias.

Lee *et al.* have shown the effects of thermal annealing in air and N_2 ambient on the structural, optical, and electrical properties of zinc oxide (ZnO) films deposited on a p-GaN substrate by magnetron sputtering. In the case of N_2 ambient, room-temperature electroluminescence (EL) in the violet region with peak wavelength at 400 nm was observed

under forward bias. In air ambient, EL spectrum consisted of a broad band from 400 nm to 700 nm and a yellow emission was observed [Lee 2009].

I.2.6 Homo-junction ZnO LED

For practical device applications, durable and reproducible p-type ZnO is essential. Nevertheless, the fabrication of ZnO homo-junction LEDs has been restricted by the bottlenecks in synthesis of high quality p-type ZnO. In the last decade, following the enhancement in p-type doping of ZnO, the fabrication of homo-junction ZnO LED has made a great progress and a number of reports have shown achievement of UV and near UV band emission [Chu 2008 - Kong 2008 - Sun 2008 - Tsukazaki 2005].

Tsukazaki *et al*. claimed a reliable and a reproducible way to fabricate p-type ZnO and consequently, a homo-structural p–i–n junction (*Figure I.13*). n-type and p-type ZnO thin films were prepared by molecular beam epitaxy (MBE). Undoped ZnO was sandwiched between p-type and n-type ZnO that were highly doped with N and Ga, respectively. High quality p-type ZnO was obtained using a repeated temperature modulation and layer-by-layer growth technique as shown in *Figure I.13.a* [Tsukazaki 2005].

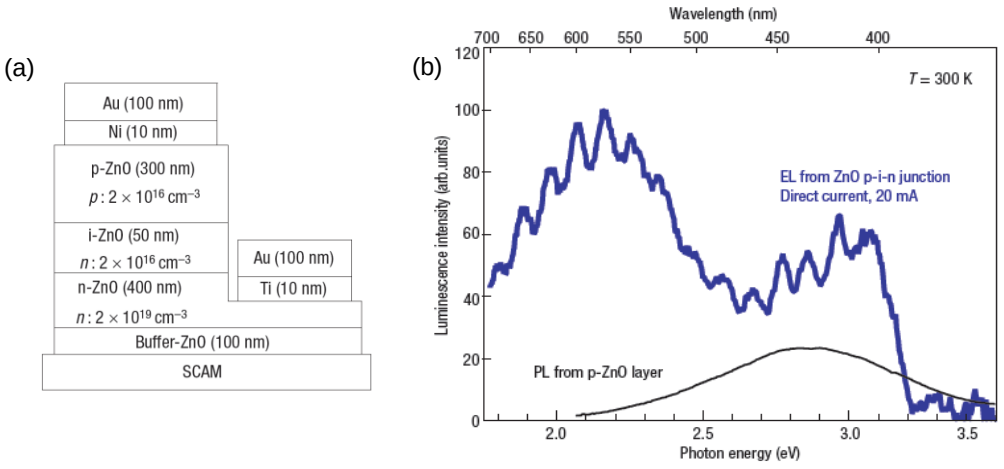

Figure I.13: (a) The structure of p-i-n homo-junction ZnO LED, (b) Electroluminescence spectrum from the p–i–n junction (blue) and photoluminescence (PL) spectrum of a p-type ZnO film measured at 300 K [Tsukazaki 2005].

The electroluminescence (EL) spectrum from the p–i–n junction exhibits a luminescence from violet to green region (*Figure I.13.b_blue*). Room temperature PL spectrum of the p-type ZnO film (*Figure I.13_black*) shows a peak at 430 nm that is consistence with EL observations. Tsukazaki *et al.* could prove that ZnO is a potential material for making short-wavelength optoelectronic devices, bringing more appreciation and attention to ZnO materials.

In recent years, one-dimensional (1D) ZnO nanostructures such as nanorods, nanowires and nanotubes have been studied extensively. Compared to bulk and thin films, ZnO 1D-nanostructures have more advantages: they have large surface-to-volume ratio, high quality single crystals and high optical properties.

p-type ZnO nanowires have been obtained by direct growth method on doped or undoped n-type ZnO nanostructures. Electroluminescence from ZnO nanowire p-n homo-junction was observed by several groups as listed in *Table I.1*.

Table I.1: Comparison of 1D homo-junction ZnO LED developed by different growth techniques

Reference	***Growth technique***	***Structure***	***Emission range(nm)***
[Tao 2012]	*CVD*	*p-ZnO:P/n-ZnO*	*390, 519*
[Yang 2008]	*Ion implantation*	*p-ZnO:As/n-ZnO*	*380, 630*
[Sun 2009]	*Ion implantation*	*p-ZnO:P/n-ZnO*	*UV, 510, 800*
[Fang 2009]	*Hydrothermal*	*p-ZnO:P/n-ZnO*	*415, 450-650*
[Zhang 2008]	*CVD*	*p-ZnO:As/n-ZnO*	*382, 510*

Chen *et al.* have reported a successful fabrication of 1D ZnO homo-junction LED. The p-type phosphorous doped ZnO nanowires were deposited on top of n-type Zn doped ZnO nanowires by catalyst free thermal vapor deposition method [Chen.M.T. 2010]. Nanowires were grown on Si substrate covered with a very thin ZnO layer. The morphology and structure of the nanowires are shown in *Figure I.14*. The electroluminescence spectra of the nanowires under different applied voltages are shown in *Figure I.14.c*. The spectra exhibit the short-wavelength emission at 342 nm and the blue shift from 342 to 325 nm as the operating voltage further increases.

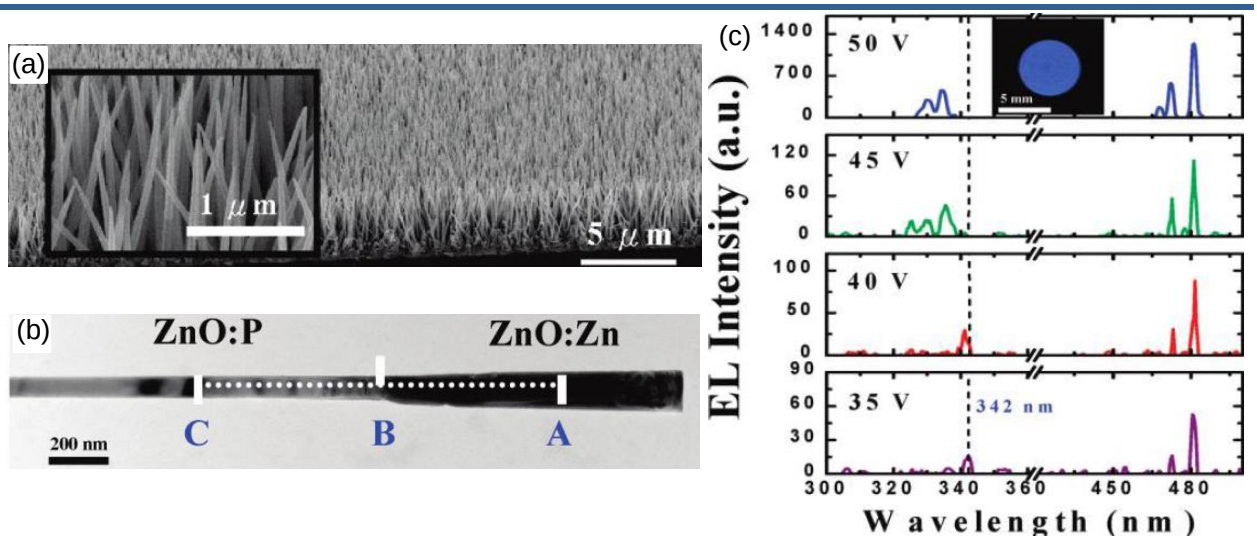

Figure I.14: (a) SEM image of vertically aligned p-n ZnO nanowires. (b) TEM image of a single nanowire, A, and C are referring to n-type and p-type sections respectively, and B refers to the interface of these two segments. (c) Electroluminescence spectra from the p–n junction under different applied voltage at 300 K. [Chen.M.T 2010].

Tao *et al.* reported the fabrication of 1-dimension ZnO homo-junction LED. The phosphorous doped p-type ZnO nanowires were grown on n type ZnO using chemical vapor deposition method and Si as the substrate. The presence of phosphorous dopants in ZnO nanowires was confirmed using XRD and PL. Emission from homo-junction LED nanowires showed two main peaks at 390 and 519 nm. These peaks were assigned to exciton related emission and defect related recombination [Tao 2012].

Same homo-junction structure was used to fabricate 1-dimension ZnO LED by Fang *et al.* using hydrothermal method. The electroluminescence of the LED, showed the peaks at 415 nm and in the visible range of 450 to 650 nm [Fang 2009].

Despite many great efforts and achievements in p-type doping and fabrication of homo-junction ZnO based LEDs, for large scale productions, reliability of the methods yet needs more investigations.

I.3 Conclusion and scope

In this chapter, the great potential and interest in application of zinc oxide materials for electronic and optoelectronic devices are highlighted. Doped ZnO nanostructures have been extensively studied for their applications in Light Emitting Diodes (LEDs). ZnO is able to provide a wide range of emissions, from visible to ultra violet, by introducing proper dopant impurities.

Nevertheless, the main obstacle on the way to a large-scale production of ZnO based devices is to find a reliable and reproducible method for the synthesis of high quality doped and undoped ZnO nanomaterials. Particularly, for short wavelength ZnO based LEDs, the synthesis of high quality n-type and p-type ZnO is crucial. So far, a p-type ZnO has been hard to achieve due to the intrinsically n-type behavior of ZnO.

There are already reports showing the feasibility of achieving homo-junction ZnO LEDs. However, the absence of large scale production of ZnO based homo-junction LEDs, challenges the reliability and efficiency of these techniques. Until this date, the choice of dopant and growth technique remains controversial and finding a reproducible p-type ZnO is still under debate.

For ZnO based devices, the control of dopant incorporation in ZnO matrix is the necessary step to control the properties of doped ZnO. Hence, a thorough understanding of the dopant incorporation in ZnO is the first step to confront the limits in doping of ZnO.

In the present work, we study the influence of different elaboration methods and synthesis conditions used for doping of ZnO thin film and nanowires. The recent most popular dopants were used to tune the optical and electrical properties of ZnO. The success and efficiency of each doping synthesis method is investigated by using different techniques such as: Raman spectroscopy, photoluminescence and TEM. As far as the dopant characterization is considered, the dopant metrology in individual ZnO nanowire or thin film is performed by atom probe tomography.

Hence, this work integrates two main objectives: 1) providing a more precise insight into the application of atom probe tomography and enhancing the quality and reliability of the measurements for ZnO materials. 2) applying this technique to study the influence of the elaboration methods on dopant incorporation and distribution in single ZnO nanowire and thin film.

CHAPTER II Elaboration and characterization techniques

One of the advantages of ZnO over other semiconductors is that it can be prepared by different synthesis techniques in various nanostructures. However, for electrical and optoelectronic applications, the synthesis technique strongly influences the properties of ZnO. As it was explained in the first chapter, the main challenge in industrializing ZnO based devices is to find an efficient and reproducible elaboration technique. In the present work, pure and doped ZnO in the form of thin film and nanowire were prepared using different synthesis techniques. The failure or success of the doping process then is studied using different characterization techniques. Hence, this chapter consists of two sections: first, description of the elaboration techniques used in this work and influence of different elaboration parameters, second, the description of the methods used for characterization of the elaborated samples. Basics and principle atom probe tomography technique will be discussed separately in details in chapter III.

II.1 Elaboration techniques

In this work, two elaboration methods are used for the preparation of doped and undoped ZnO nanostructures. ZnO thin films were prepared using magnetron sputtering and ZnO nanowires were grown by metal-organic chemical vapor deposition (MOCVD).

II.1.1 Thin film preparation: Magnetron sputtering

Magnetron sputtering is a physical vapor deposition (PVD) process, widely used for deposition of conductive oxide thin films at low temperatures with good optical and electrical properties [Balestrieri 2013 - Kim 2006 - Ziani 2014]. It is one of the most popular growth techniques for early ZnO investigations because of its low cost, simplicity and low operating temperature.

Figure II.1.a shows the schematic view of magnetron sputtering system. A source of the material desired to be deposited (target) is bombarded with inert gas ions, typically argon (Ar^+).

By application of high voltage that can be either RF (radio frequency) or DC, the Ar plasma is created between cathode and anode. The RF power source then sends radio waves through the plasma to ionize the gas atoms. The collision of these ions onto the target ejects target atoms from its surface towards the substrate. The target atoms travel to the substrate and begin to form a coating layer. As more and more atoms reach the substrate, they begin to bind to each other, forming a tightly bound atomic layer. Depending on the sputtering time one or more layers of atoms can be deposited, allowing for the production of precise layered thin film structures.

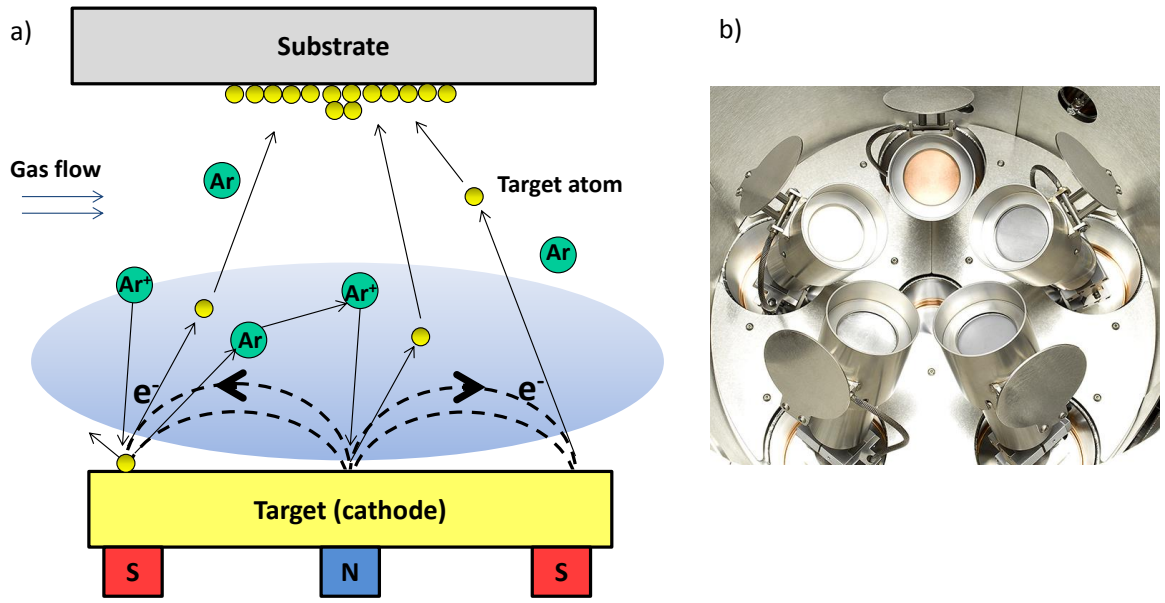

Figure II.1: (a) The basic component of a magnetron sputtering system. Ionized argon bombards a target ejecting atoms which are being then deposited on the substrate. Electron and argon ions form plasma near the target due to the magnetic field resulting in a higher efficiency, (b) Inside sputter deposition tool with five magnetron sources with shutters, chimneys, and tilt.

In RF magnetron sputtering, the influence of parameters must be taken into account prior to the elaboration set-up as they rule the structure, properties and quality of the synthesized materials.

- Influence of parameters in magnetron sputtering

Sputtering pressure, sputtering time, the distance between the substrate and the target, RF power and substrate temperature are the main parameters. These parameters can directly affect the properties of the deposited materials by changing factors such as mean free pass of sputtering

species, surface mobility and defect concentration of doped and undoped ZnO thin films resulting in different morphology, electrical and optical properties.

- *Sputtering pressure and flow rate:* Ar sputtering pressure can influence the crystal quality and properties of the grown ZnO thin film. The influence of Ar sputtering pressure on the growth of zirconium doped ZnO thin film was examined in the range of 0.5 to 3Pa. It was observed that the crystallinity increases and the electrical resistivity decreases when the sputtering pressure increases from 0.5 to 2.5 Pa. However, for more than 2.5 Pa it was observed that, as the pressure increased the crystallinity decreased and resistivity increased [Hanfa 2009]. Besides the Ar pressure, the increase in the flow rate of argon showed an increase in the band gap of Al-doped ZnO thin film [Huang.D 2013].

- *Target-to-substrate distance:* the distance between target and substrate is a very important factor as it influences the growth rate. Increasing this distance results in a slower growth rate and thus an enhancement of the crystal quality as well as the electrical resistivity. In case of Al doped ZnO thin films, raising the distance from 45 to 70 mm led to a more stoichiometric value of O/Zn ratio and it could vary the optical band gap of Al doped ZnO from 3.18 to 3.36 eV [Jeong 2004].

- *RF power:* Varying the RF power can directly change the morphology of the samples as it changes the growth rate. In the synthesis of Zr doped ZnO thin films, the increase in RF power has improved the crystallinity, conductivity of the samples. However, applying very high powers led to deterioration of crystallinity and reduction of the conductivity [Mao-Shui 2007].

- *Substrate temperature:* the substrate temperature, is one of the most important factors as it has a strong effect on improving the surface morphology and thus, it affects the crystallinity and optical properties [Bhavanasi 2013].

- *Post-deposition annealing temperature:* annealing the grown samples can heal the undesirable defects in the crystal structure and change the properties of the grown

sample. In doped samples, depending on the annealing temperature, redistribution of the dopants can occur upon annealing, which can strongly change the optical and electrical properties of the sample.

In the present work, we are only focused on the influence of two latter growth parameters (growth and annealing temperatures) on the morphology and optical properties of the doped samples. The other parameters were kept fixed. The samples studied in this work are elaborated under the condition explained in the following.

- **Preparation of the terbium and ytterbium doped ZnO thin films**

Two different series of ZnO thin films were studied in this work. First series of thin films were doped by Terbium (Tb) grown by radio frequency (RF) magnetron sputtering using a pure ZnO target and silicon as the substrate at CIMAP laboratory. Doping was obtained by arranging 10 calibrated terbium oxide (Tb_4O_7) pellets on the surface of the ZnO target. Deposition was performed on a (100) silicon substrate heated at 100°C. The total pressure and RF power to target were fixed at 1.5 Pa and 1.91 $W.cm^{-2}$, respectively. The substrate was placed at the distance of 70 mm from the target. Post-annealing treatments were carried out for 1h under continuous nitrogen flow at different temperatures in order to track its influence on ZnO:Tb films properties [Ziani 2014]. The investigated Tb doped ZnO samples are summarized in *Table II.1*.

Table II.1: List of studied Tb doped ZnO thin film samples prepared at CIMAP Caen.

samples	*T1*	*T2*	*T3*	*T4*
doped	*No*	*Yes*	*Yes*	*Yes*
annealing temperature (°C) for 1hr	*600*	*As grown*	*600*	*800*

Second series of investigated ZnO thin films were doped by ytterbium (Yb) .Yb-doped ZnO thin films were deposited on silicon substrate by RF magnetron sputtering using an Orion 3 device from AJA International Co at IPCMS[1] laboratory. Doping was carried out by placing pure Yb discs on the surface of a pure zinc target (sputtering with substrate-on-top configuration). Oxygen was added in the sputtering chamber to form the final $Zn_{1-x}Yb_xO$ oxide. The Ar/O_2 gas flow ratio was optimized and kept to a value of 4. The substrate was placed at the distance of 120 mm from the target. The silicon substrates were taken from 500 μm thick 4″ CZ-100 wafers with resistivity varying from 0.07 to 5Ω.cm. Substrates were cleaned from the organic contaminations by piranha procedure and further dipped in HF in order to remove the oxide at the substrate surface. Two halogen lamps in the deposition chamber provide the temperature in the range of 15 °C to 400 °C. The RF power and deposition pressure were optimized to 50 W and 3.4 mTorr (0.45 Pa), respectively. Post-deposition annealing was done in a quartz tube under both Ar and O_2 gas flows and at temperature of 700°C [Balestrieri 2013]. Hence, the samples listed in *Table II.2* are chosen for further investigation in this work.

Table II.2 : List of studied Yb doped ZnO thin film samples prepared at IPCMS Strasbourg.

Sample	*Y1*	*Y2*	*Y3*
growth temperature(°C)	*15*	*400*	*15*
annealing temperature (°C)	_	_	*700(°C) for 10 min*
thickness (nm)	*100*	*100*	*100*

II.1.2 Nanowire preparation: metal-organic chemical vapor deposition

Metal-organic chemical vapor deposition (MOCVD) is a technique widely used in manufacturing light-emitting diodes (LEDs), lasers, transistors, solar cells and other electronic and optoelectronic devices.

[1] Institut de Physique et de Chimie de Strasbourg

Figure II.2.a shows the schematic principle of MOCVD technique. The mechanism by MOCVD is mainly a self-nucleation process and layer-by-layer growth method using metal organics as the precursor. Since metalorganics have only one dangling bond, they can be easily converted to chemical vapors and hence, they allow for low temperature growth relevant to the pressure that precursor vapor offers. In a typical MOCVD, a carrier gas delivers the vapor-phase precursors. The precursors are decomposed due to the applied temperature and ZnO deposition occurs as a result of chemical reactions on the substrate. Hence, one of the main issues in MOCVD is to find precursor combination so that the chemical reaction is only taking place at the substrate surface, but not in the gas phase. As Zn precursors metal-organic compounds such as dimethyl-metals and diethyl metals have been used successfully [Kanjolia 2011 - Marzouki 2010 - Souissi 2013].

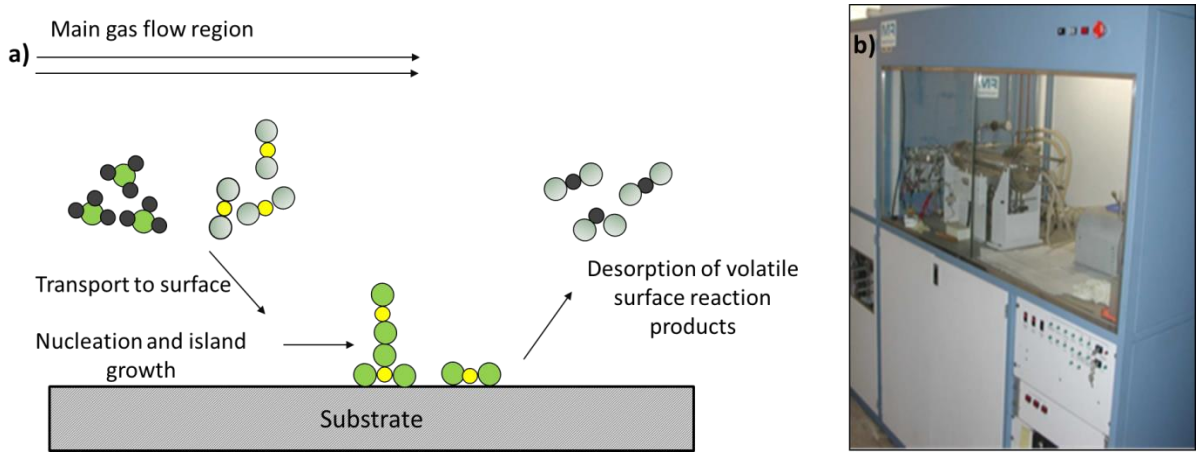

Figure II.2: (a) principle of MOCVD, to produce compound semiconductors, the chemicals are vaporized and transported into the reactor together with other gases, there the chemical reaction takes place that turns the chemicals into desired crystals and (b) horizontal MOCVD reactor used for the growth of nanowires at GEMaC laboratory, Versailles.

Oxygen molecule and nitrous oxide (N_2O) are commonly used as oxygen precursor. For high temperature MOCVD growth (600-1000°C), N_2O is widely used as oxygen precursor whereas for the growth process at lower temperatures the use of O_2 is more often. The reactions take place in a reactor where a necessary temperature profile is created in the gas flow direction *(Figure II.2.b).*

MOCVD was first used for the deposition of thin films. Nevertheless, MOCVD has later become a pioneer method to reproduce large area, catalytic free, long, vertically aligned ZnO nanowires with excellent morphological, structural and optical properties. In this work, the MOCVD growth concerns only the spontaneous growth of nanowires. The catalyst free and spontaneous growth of nanowires and the transition from thin film to nanowires occur only by changing the growth parameters.

The MOCVD growth mechanism of the nanowires involves two steps: nucleation and growth. First, nuclei that can have different crystallographic orientations are formed on the substrate. Then the growth of nanowires takes place along specific direction. The preferred growth axis is then ruled by the growth condition and choice of substrate. For ZnO, generally c-axis offers the fastest growth rate and considered as the preferred growth direction.

- Influence of parameters in MOCVD

  The MOCVD parameters play a very important role not only on the properties of the grown materials, but also on their morphology. One dominant factor governing morphology of the nanowires is O/Zn partial pressure usually referred as $R_{VI/II}$ parameter. It was observed that low $R_{VI/II}$ typically favors the growth of nanostructures whereas high $R_{VI/II}$ is used to grow 2D layers [Behrends 2009 - Chen.Y.J 2009 - Choi 2011 - Montenegro 2012] .

  Montenegro *et al.* have proposed three growth mechanisms under different VI/II ratios using N_2O and DMZn-TEN (dimethylzinc-triethylamine) as oxygen and Zn precursors, respectively. *Figure II.*3 shows the three suggested growth mechanisms of nanowires, nanotubes and thin films. At low $R_{VI/II}$, high mobility of Zn and sufficient diffusion can allow for a growth governed by surface energy. Since the growth surface energy of the c-plane is higher, the growth of the c-oriented nanowires tends to minimize this energy resulting in the formation of well-defined hexagonal ZnO nanorods. At higher $R_{VI/II}$, the higher adsorption of oxygen atoms makes the migration of Zn atoms difficult resulting in a lateral growth and formation of 2D layer. At an intermediate $R_{VI/II}$, the mobility of Zn and diffusion length is reduced and if the mobility becomes too low, it can favor the formation of the nanotubes [Montenegro 2012].

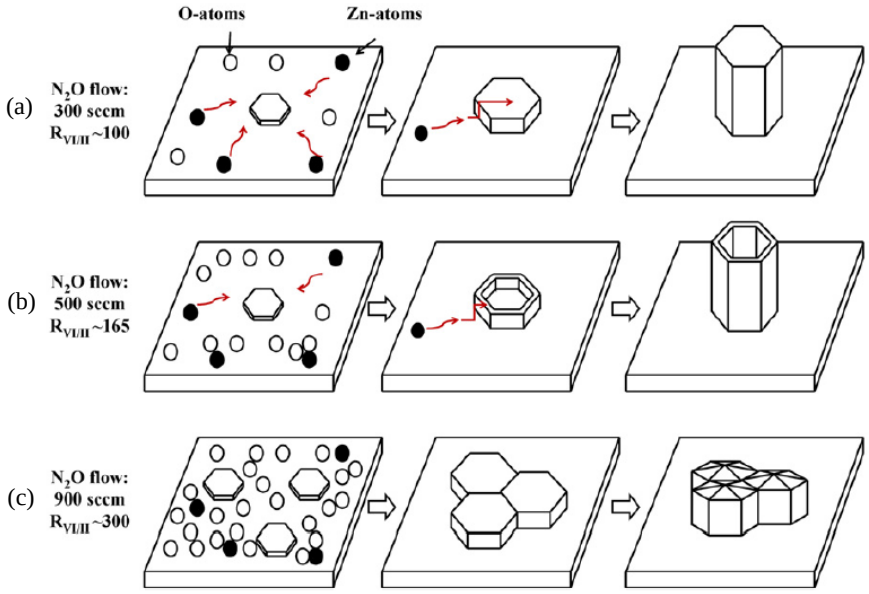

Figure II.3: Proposed growth mechanisms under various $R_{VI/II}$: (a) well-defined hexagonal ZnO nanowires, (b) ZnO nanotubes, (c) formation of ZnO 2D film [Montenegro 2012].

Behrands *et al.* have investigated the effect of different growth parameters such as deposition time, substrate temperature and reactor pressure [Behrends 2009]. The parameters show a strong effect on controlling the density, length and the diameter of the grown nanopillars.

It was observed that a low deposition temperature decreases the mobility of the molecules reaching the substrate and thus favors the growth of 2D thin films. However, increasing the reactor pressure have shown to increase the diameter of the nanowires [Behrends 2009 - Nath 2012]

In the growth of ZnO nanowires, the choice of substrate is very important as it affects the final morphology of the nanowires. *Figure II.*4 shows the effect of different sapphire substrates on the morphology of the grown ZnO under the same condition. Beside the difference in the morphology of the samples, it was observed that the nanowires grown on the c-plane sapphire exhibit better optical properties [Kar 2010].

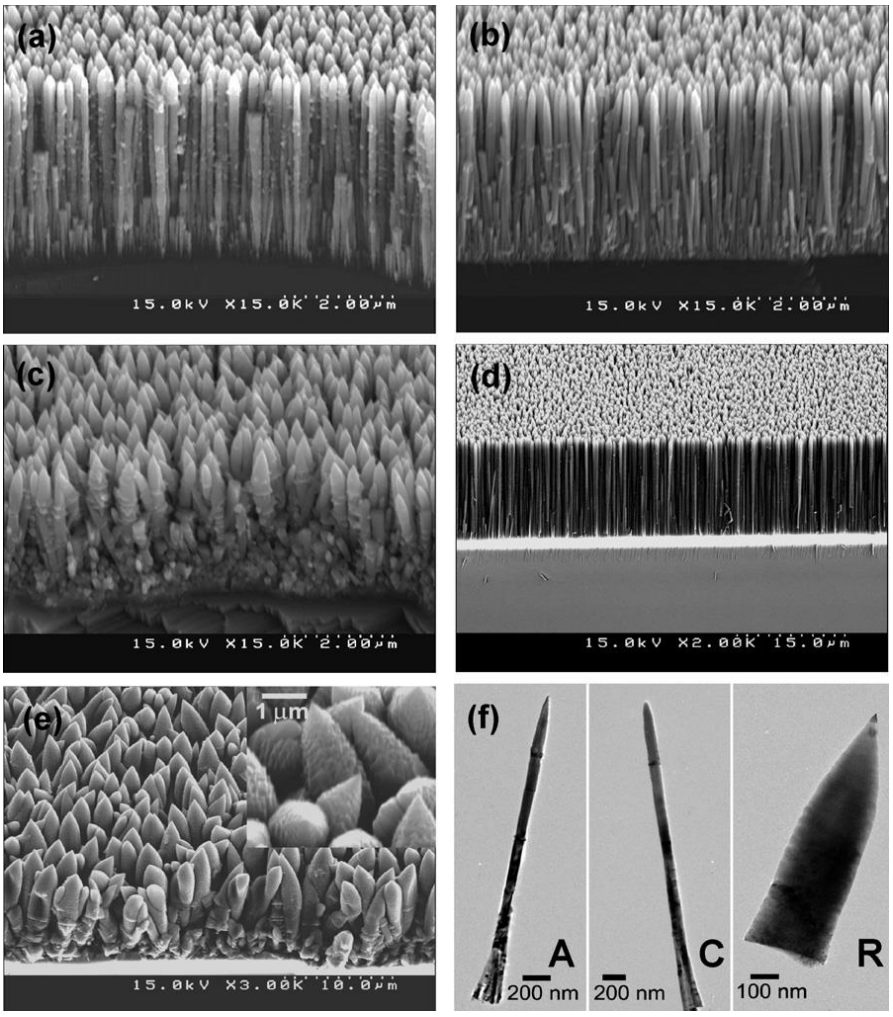

Figure II.4: Micrographs of ZnO nanostructures on (a) A (11-20) , (b) C (0001), (c) R (-1-012)-plane sapphires for 15 min growth, (d) C-, (e) R-plane sapphires for 90 min growth, and (f) bright-field TEM image images [Kar 2010].

In this work, the MOCVD growth parameters were chosen so that the spontaneous growth of ZnO pure or doped nanowires would occur. Taking advantage of large length to surface ratio of nanowires, different *ex-situ* and *in-situ* techniques were used in order to achieve p-type ZnO nanowires. A successful incorporation of the dopants in ZnO nanowires and their conductivity are the main interests in growth and investigation of these nanowires. The growth conditions used in the present work are described as follows.

- **Nitrogen doped ZnO nanowires**

Nitrogen-doped ZnO nanowires have been grown in a horizontal MOCVD reactor working at low pressure on (0001) sapphire substrate with diethylzinc (DEZn), NO_2, NH_3 as zinc, oxygen and nitrogen sources. Growth of nanowires was carried out at 800°C and the pressure of 50 Torr (6666.1 Pa) for 30 minutes in the presence of Helium as a carrier gas. At the $R_{VI/II}$ of 540 (ratio of NO_2 to DEZn), different concentrations of NH_3 were used for doping. The concentration of 0, 10, 15 and 20 ml, have been chosen to study the effect of dopant concentration on the properties of ZnO nanowires.

The undoped and doped nanowires grown by MOCVD were prepared at GEMaC laboratory,

II.1.3 Ex-situ doping process

In this work, the *ex-situ* p-type doping process of ZnO nanowires was carried out using spin-on-dopant method (SOD). The *ex-situ* doping was performed at CEA-Leti laboratory. Since, this technique is generally known for doping of thin films, the main challenge in here is to investigate if this technique can result in successful incorporation of acceptors in ZnO nanowires. The growth parameters and doping conditions are discussed in chapter IV.

- <u>Principle of the technique</u>

Doping of semiconductors can be carried out through an *ex-situ* diffusion process called spin-on-dopants. This method provides an impurity source for doping of semiconductors. The dopants are introduced by application of a homogenous solution (containing the intended impurities) on a planar semiconductor surface followed by annealing treatment. Schematic principle of SOD method is shown in *Figure II.*5.

The advantage of SOD technique is uniform doping with high yields, convenient application of dopant with non-hygroscopic solutions, simultaneous diffusion of “p” and “n” types and simultaneous diffusion of different concentrations of the same dopant, a lower cost technique compared to ion implant technique and the possibility of semiconductor junction fabrication.

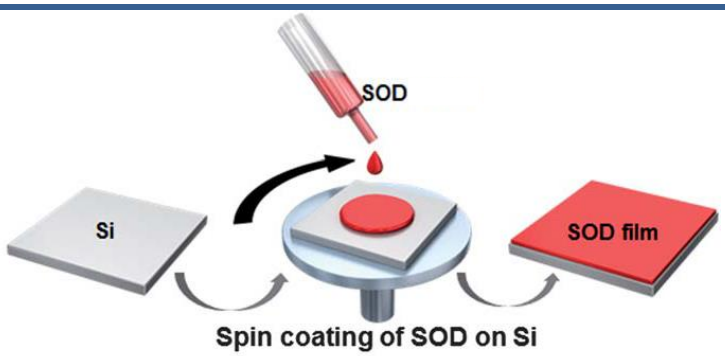

Figure II.5: schematic of SOD process, spin on dopant solution is deposited on a substrate followed by spinning. Diffusion takes place by applying high temperature [Sohn 2014].

SOD used for doping of thin films involves 4 basic steps as follow:

1. Cleaning of the substrate,
2. Application of dopants to the substrate followed by spinning,
3. Inducing an elevated temperature for the diffusion of dopants,
4. Etching and post diffusion clean-up.

- Influence of parameters

At each step, the selection of the parameters can directly influence the quality of the doped material, hence they must be chosen carefully. Dopants and solvent must be chosen with respect to the substrate properties. Some solutions require a pre-diffusion bake to remove excess of solvent. The typical spinning speed used is between 2000 to 6000 rpm[2] and as the spinning speed increases, the thin film becomes thinner. An average time of spinning is about 5 second which should be selected with respect to the expected thickness and spinning speed. The diffusion temperature plays an important role as well as other parameters to yield desired substrate resistivity and junction depth. Since the dopant diffusion occurs at very high temperatures, aside from desirable dopants, sometimes due to the poor experimental condition, the distribution of already existing impurities in the lattice can be severe at these temperatures. Once the diffusion is performed at elevated temperatures, it is important to avoid a rapid withdrawal of the sample from the furnace and to allow the samples having time to come to thermal equilibrium. A rapid

[2] revolutions per minute, number of turns of the object around an axis divided by time

withdrawal can cause the high-temperature disorder-dispersed impurity phase and vacancy interstitial concentrations frozen into the crystal influencing the properties of the doped material.

II.1 Characterization techniques

In this section we will discuss the basic principle of different characterization techniques used to investigate the elaborated samples. The characterization techniques described in this section are the conventional techniques providing a wide range of information about the crystal structure, morphology and optical properties of the elaborated thin films and nanowires.

II.1.1 Transmission Electron Microscopy

Transmission electron microscope (TEM) is a technique offering the investigation of detailed nano and micro structures at high resolution (<1 nm). It also enables to investigate the crystal structures, specimen orientations and chemical compositions of phases, precipitates and contaminants through diffraction pattern, X-ray and electron-energy analysis. This microscope is based on transmitting electrons accelerated up to high energy levels (few hundreds keV) and focused on an ultrathin specimen. As these electrons reach the specimen, they can scatter or backscatter elastically or inelastically, or produce many interactions, source of different signals such as X-rays, Auger electrons or light (*Figure II.6.a*).

The elastically scattered electrons are the ones used to make the TEM image. The image projected by the electrons transmitted directly through the specimen is referred as a bright field image. In the bright field mode of the TEM, an aperture allows only the direct beam to pass. In this case, the image results from a weakening of the direct beam by its interaction with the sample. If the direct beam is blocked by the aperture and only one or more diffracted beams are allowed to pass the objective aperture, a dark field (DF) image can be obtained. Since diffracted beams have strongly interacted with the specimen, very useful information is present in dark field images such as planar defects, stacking faults or particle size.

Figure II.6.b shows an example of TEM image obtained for ZnO:Yb thin film.

The signals provided by inelastic interactions between electrons and matter are used to characterize the specimen chemical composition. X-rays energy dispersive spectroscopy (EDS) is commonly used as a quick method for identifying and quantifying the elements with a resolution up to 0.2 nm. However for identification of the light elements ($Z < Z_{Al}$) electron energy loss spectrometry (EELS) is particularly used providing a better spatial resolution.

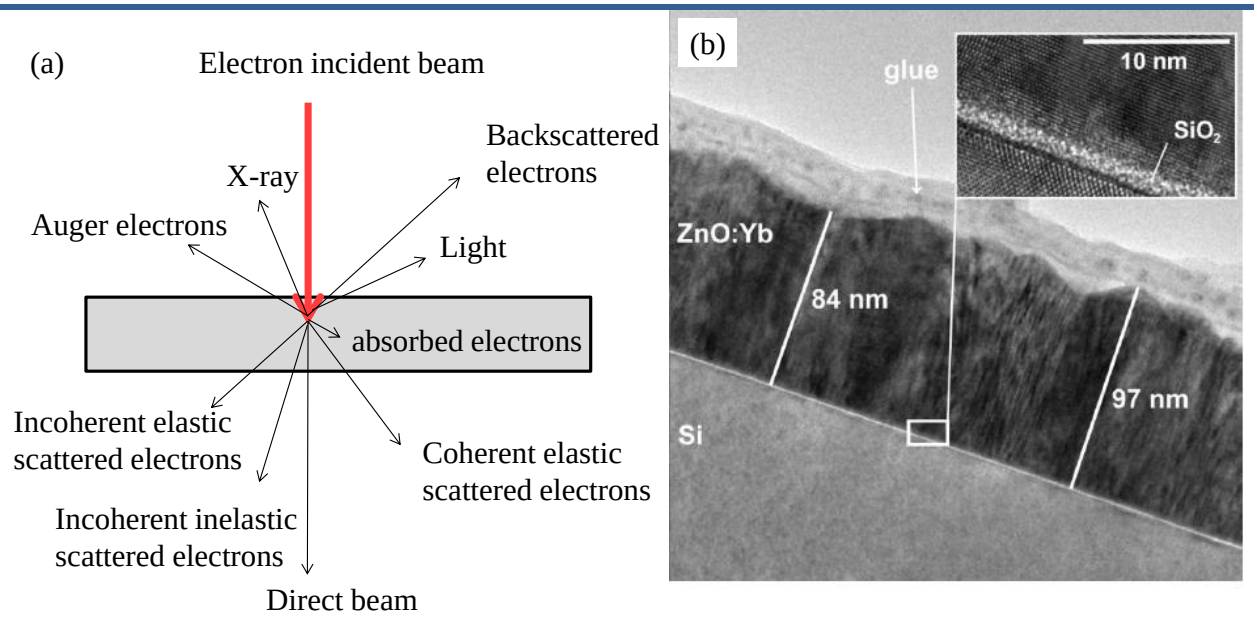

Figure II.6: (a) interactions between electrons and the material creating different sorts of scattering. The scattering can be elastic or inelastic used for different means of characterizations in TEM.(b) TEM image of the interface of Yb doped ZnO thin film and Si substrate. The inset shows a high resolution TEM image of the interface revealing a thin layer of SiO_2 [Balestrieri 2014].

Lattice can be imaged by the interference of the diffracted beams with the direct beam. If the point resolution of the microscope is sufficiently high and a suitable crystalline sample oriented along a zone axis, then HRTEM images are obtained. The inset in *Figure II.6.b* presents the high resolution TEM image of the ZnO:Yb and Si substrate interface. The atomic planes of the thin film and Si substrate can be observed clearly in the HRTEM image.

Very often, imaging of materials in bright field can be unsuitable due to non monotonic contrast, such as that generated by diffraction or Fresnel fringes. Hence a z-contrast imaging mechanism is usually used generated by high angle annular dark field (HAADF) scanning transmission

electron microscopy (STEM). By using a STEM detector with a large inner radius, a HAADF detector, electrons are collected which are not Bragg scattered. Such HAADF images show little or no diffraction effects, and their intensity is approximately proportional to Z^2.

The transmission electron microscope used in this work is a JEOL ARM 200F equipped with HAADF detector and EDS operating at electron beam energy of 200 keV. For atomic resolution imaging two modes are used: The high-resolution transmission electron microscopy (HRTEM) and the scanning transmission electron microscopy (STEM) [Williams 2009].
For TEM observations of nanowires, nanowires were removed from the substrate by scratching, and then spread on a copper grid covered with a thin carbon film.

II.1.2 Photoluminescence

Photoluminescence (PL) has long been used to investigate the optical properties of the material. Besides, it is also a powerful technique to probe discrete energy levels and to extract valuable information of the semiconductor sample by identifying extremely low concentrations of intentional and unintentional impurities that can strongly affect material quality and device performance.

PL measurements involve the excitation of an electron into a higher energy state that eventually falls back to a lower unoccupied state with an emission of a photon. Since the initial excitation is by incident light this process is called photoluminescence. The efficiency of photoluminescence signal is determined by the nature of optical excitation (radiative and non-radiative recombinations) and properties of material such as defects or impurities. Performing PL at very low temperatures (few Kelvin) often reveals spectral peaks associated with impurities contained within the host material.

ZnO shows a great variety of richly structured luminescent lines covering almost all the visible and near UV spectral range. *Figure II.7* demonstrates the typical PL spectrum of bulk ZnO obtained at 4.2 K [Meyer 2004].

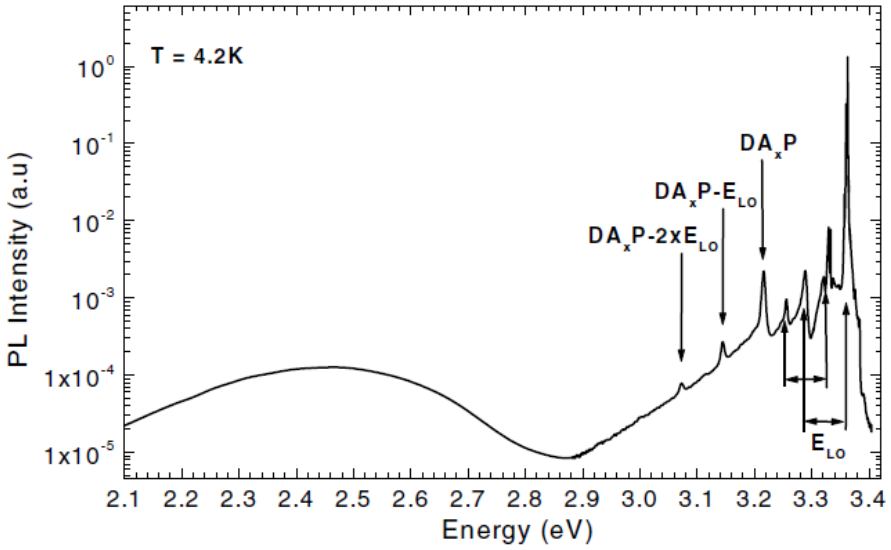

Figure II.7: Photoluminescence spectra of bulk ZnO substrate provided by at 4.2 K. The spectrum presents excitonic (~2.45eV), donor-acceptor-pair (DAP) (3.3-3.5 eV) and its replica with longitudinal optical phonons (2.9-3.3 eV) [Meyer 2004].

Generally, PL spectrum of ZnO contains a broad band centered around 2.45 eV extending from blue to the green range. Main peaks originate from bound excitons (BE) recombinations followed by phonon replicas with an energy separation of about 72 meV. The photoluminescence of ZnO has been well discussed for more than 50 years; however, despite the large number of publications, there are some aspects which remain unclear. For example, for many optoelectronic purposes, ZnO has been doped with different impurities, which generates particular exciton emission lines to donor or acceptor impurities.

The photoluminescence system used in this work includes an excitation source consists of an argon laser Spectra-Physics 2085 beam lock that can provide different lines in the range of visible and ultraviolet between 530 nm and 275-300 nm. The samples are placed in a bath of helium cryostat operating between 2 and 300 K. In this work PL measurements of nanowires were performed at 2 K in order to minimize thermally activated non-radiative recombination processes and thermal line broadening and to obtain the most complete spectroscopic information. The basic PL experimental set-up is shown in *Figure II.8.*

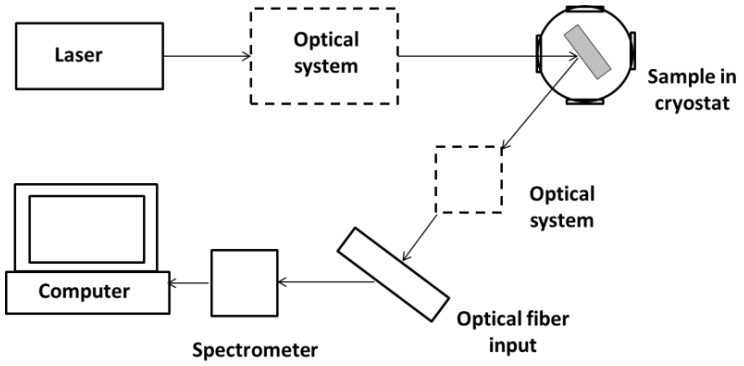

Figure II.8: Basic photo-luminescent experiment set-up including an excitation laser source and spectrometer and detecting system. Optical systems are to guide and adjust the initial and resulted beams. For low temperature PL measurements, the sample is held in cryostat.

The spectral analysis can be carried out by two Horiba-Jobin-Yvon monochromators: Low resolution with a Triax 550 monochromator equipped with a multi-channel analysis (1024x256 pixels) with a CCD camera or high resolution with a U1000 double monochromator equipped with a photomultiplier. The covered wave length range is from 300 nm to about 1 micron. All PL analyses of nanowires were carried out at GEMaC laboratory by Dr. Alain Lusson and Emir Zehani.

II.1.3 Raman spectroscopy

Raman scattering is an optical and non-destructive characterization method commonly used to provide information about the chemical composition, crystal quality and the influence of dopants on lattice vibration properties. Raman spectroscopy is based on the inelastic scattering of monochromatic light within the studied samples. Once the laser light interacts with molecular vibrations, phonons or other excitations in the sample, the energy of the laser photons can be shifted up or down and therefore providing information about the vibrational modes in the system. A Raman spectrum is usually presented as intensity versus Raman shift which is the frequency difference between the scattered light and the monochromatic excitation source.

Raman spectroscopy has been successfully used to study different semiconducting materials. Wurtzite-structured ZnO belongs to the space group of C_6V^4 with two formula units per primitive cell, giving rise to phonon modes $\Gamma=2A_1 +2B_1 +2E_1+2E_2$. Among these modes, the optical modes are $\Gamma= A_1 +2B_1 +E_1+2E_2$ where only A_1, E_1, E_2 modes are Raman active and B_1 modes are Raman silent modes. E_2 mode is a nonpolar mode with two frequencies: E_2(high) which involves with the vibration of oxygen sublattice and E_2(low) which is mainly associated with the vibration of Zn sublattice. For long range electrostatic forces, A_1 and E_1 modes are polar and they split into transverse and longitudinal optical phonons ascribed TO and LO, respectively [Cuscó 2007]. *Table II.3* presents the classical Raman active modes and phonon combinations of wurtzite ZnO at the corresponding Raman shift values.

Table II.3: Raman active phonons in wurtzite-structured ZnO and their corresponding wavenumber value [Cuscó 2007].

Vibrational mode	*E_2(low)*	*E_2(high)- E_2(low)*	*A_1(TO)*	*E_1(TO)*	*E_2(high)*	*A_1(LO)*	*E_1(LO)*
Raman shift (cm^{-1})	*99*	*333*	*378*	*410*	*438*	*574*	*590*

Figure II.9 shows an example of Raman spectra of undoped ZnO and nitrogen doped ZnO nanowires grown by MOCVD. Typical vibrational modes of ZnO can be observed for both undoped and N-doped ZnO nanowires. Additional vibrational modes are observed for nitrogen doped ZnO nanowires which can be related to the presence of nitrogen.

In this work, Raman spectra of the samples are provided by Horiba Jobin Yvon Labram HR 8500 (confocal) and using green irradiation. Raman spectroscopy of the ZnO:N nanowires were carried out at GEMaC laboratory by Dr. Alain Lusson. ZnO:P nanowires and ZnO:Tb thin films were analyzed in GPM laboratory using the same Raman spectrometer and measurement condition.

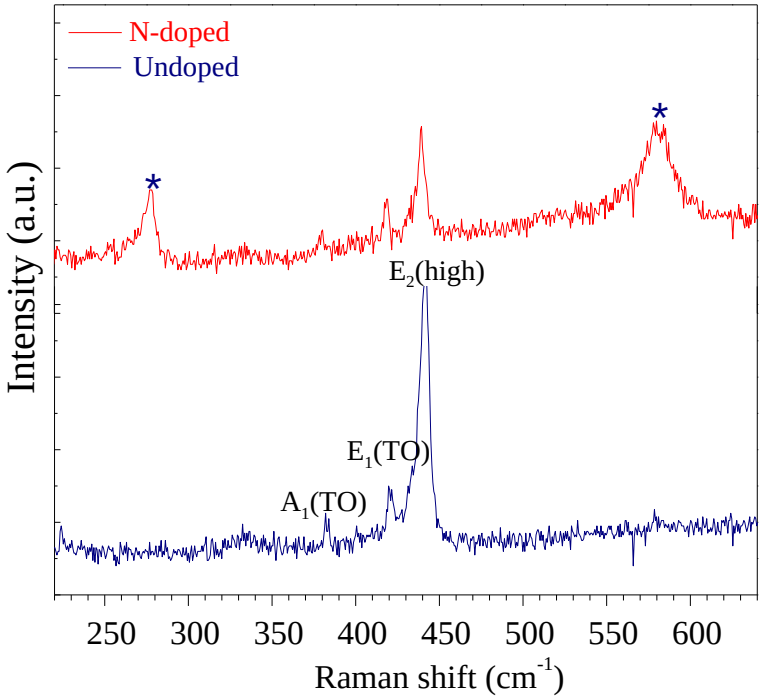

Figure II.9: Raman spectra of ZnO doped and undoped nanowires are shown in blue and red respectively.

II.2 Conclusion

In this chapter, first the elaboration methods used for the growth of different doped and undoped ZnO nanostructures is discussed. In the second section, the most common characterization techniques used for studying ZnO materials are introduced. The techniques that are explained in this section are used to investigate the incorporation of dopants in the elaborated samples by MOCVD, Magnetron sputtering and SOD *ex-situ* doping. Each characterization technique discussed in this chapter can provide information about the failure or success of the synthesis method which is discussed further in the following chapters. Nevertheless, complementary information is provided by atom probe tomography technique. As it was mentioned previously, this technique is new for characterization of semiconducting materials and in particular never discussed in details for ZnO materials. Hence, the following chapter is devoted to the principle of this technique and its application in investigation of nanomaterials.

CHAPTER III Atom probe tomography of ZnO materials: fundamental studies

One of the challenges for the investigation of nanomaterials is the development and use of characterizing tools dedicated to the metrology of dopants in semiconductors. For this mean, the use of techniques with atomic resolution is demanded. Secondary ion mass spectrometry (SIMS), which has long been the reference technique, is nowadays limited. Indeed, three-dimensional (3D) atomic imaging and spectroscopy capabilities are now required to image structures whose complexity tends to be inversely proportional to their sizes. Among all the nanoscale-sensitive analytic techniques, Atom Probe Tomography (APT) appeared to be one of the most promising tools thanks to its unique capability of combining the atomic scale resolution with quantitative chemical analysis. Over the past few years, very innovative improvements have been brought to this technique. Introducing ultrafast femtosecond laser pulsing to primitive atom probes has given rise to the development of the Laser Assisted Tomographic Atom Probe (LA-TAP) extending the field of applications to materials used in nano-electronics such as semiconductors or insulators [Gault 2006].

Atom Probe Tomography is a three-dimensional high-resolution analytical microscope that is built on the concept of field evaporation of atoms from the surface of a needle-shaped specimen. The emergence of APT started with the studies on ionization of atoms in free space under electric field in 1928 by Oppenheimer [Oppenheimer 1928]. In 1956, E.W.Müller invented the Field Ion Microscope (FIM) which made it possible to see the atoms of the surface for the first time [Müller 1956]. Müller continued the development on FIM and by combining FIM, a detector with a single atom sensitivity and time of flight mass spectrometry, he was able to develop the first atom probe in 1968 [Müller 1968]. This atom probe was able to identify the chemical nature of the detected atoms and since it was able to demonstrate one dimensional composition profile, it was called 1D-AP [Müller 1968]. In the last decades, APT has evolved notably and today it is considered as a unique instrumental technique providing ultimate chemical information together with 3-dimensional distribution map of specimen at atomic level.

Nevertheless, despite the great interest in application of APT for ZnO and in general semiconducting materials, there is a lack of fundamental studies on acquisition of reliable APT measurements. Hence, prior to apply this technique to ZnO materials, we need to be able to perform a reliable APT analysis and for that, having a good knowledge of the APT principle is crucial.

Therefore, this chapter includes four main parts. In the first section, a general overview on the basic principle of atom probe tomography and the physical phenomena behind this technique is discussed. In the second part, we will be mainly focused on the application of APT for semiconducting materials. Due to the recent application of APT for semiconductors, the advances, difficulties and problems concerning the application of this technique in such materials are discussed in detail. In the last two sections, we address two main problems often encountered in APT of semiconductors: 1) APT specimen preparation of nanowires, 2) adapting APT to ZnO nanostructures for reliable and reproducible measurements. Once these problems are resolved, we are able to apply this technique for further investigation of doped ZnO nanostructures discussed in chapters IV and V.

III.1 Basic principle of Atom Probe Tomography

The basic operating principle of APT involves a specimen in the shape of a very sharp tip with a radius less than 50 nm at the apex that is cooled down to a temperature less than 80K in ultra-high vacuum. A high direct current voltage (V_{dc}) of about few kilovolts is applied to the specimen that creates a high electric field at the apex of the tip. By applying additional high voltage or laser pulses, the atoms from the surface are field evaporated and fly towards the detector which is perpendicularly placed in front of the tip. *Figure III.*1 shows the principle of APT.

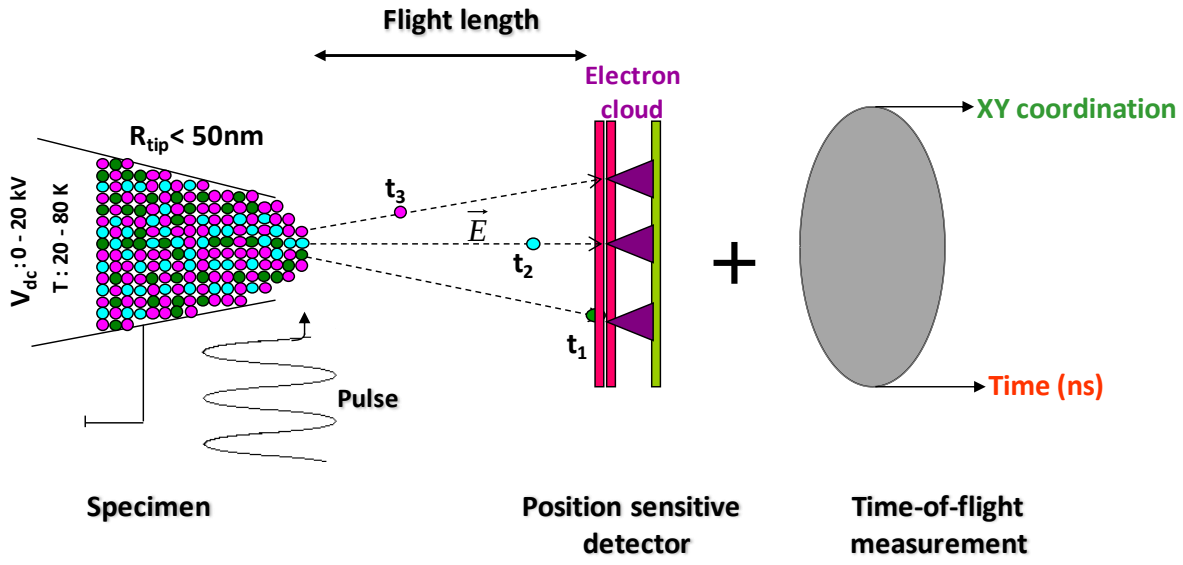

Figure III.1: Principle of atom probe tomography. Specimen in the shape of a sharp needle is cooled down to cryogenic temperatures. A high positive V_{dc} is applied to the tip. Evaporation of the atoms from the surface of the tip occurs by applying an additional high voltage or laser pulse. The atoms follow the electric line and reach the detector.

By applying a positive standing voltage at the tip with a small radius, a strong electric field is created at the apex which keeps the specimen positively charged. The electric field (E) created at the apex of the tip is given by:

$$E = \frac{V_{dc}}{\beta.R}, \qquad \text{(III.1)}$$

where V_{dc} is the voltage applied on the tip, β is a numerical factor in the range of 2-8 accounting for the fact that the end of the tip is not spherical but hemispherical and R is curvature radius of the tip.

When the electric field is sufficiently high to ionize the surface atoms, the positive ions created at the surface of the specimen are repelled by the specimen and accelerated along the electric field lines established between the specimen and the detector. This process is called '*field evaporation'*. Since the electric field is higher at the protuberant points of the tip (e.g. edge of atomic terraces), the evaporation of ions from these points happens first.

Once the evaporated ion is collected by the detector, its chemical identification is possible via mass spectroscopy where the ion mass to charge ratio is determined from its time of flight [Gault 2012 - Miller 1996].

APT analysis basically involves the field evaporation, time of flight mass spectroscopy, mass spectrum and data analysis and volume reconstruction, which are discussed in following sections.

III.1.1 Theory of field evaporation

The main process involved during APT analysis is field evaporation. It involves a combination of ionisation and desorption of an atom from a surface that is subjected to a very intense electric field. Under a sufficiently high electric field, the atom can be pulled away from the specimen surface as an ion, leaving behind one electron. To remove an atom from the surface of the specimen, the atom needs to overcome an energy barrier that bonds it to the surface, as shown in *Figure III.*2. This energy barrier is reduced by the application of the electric field and by thermal activation.

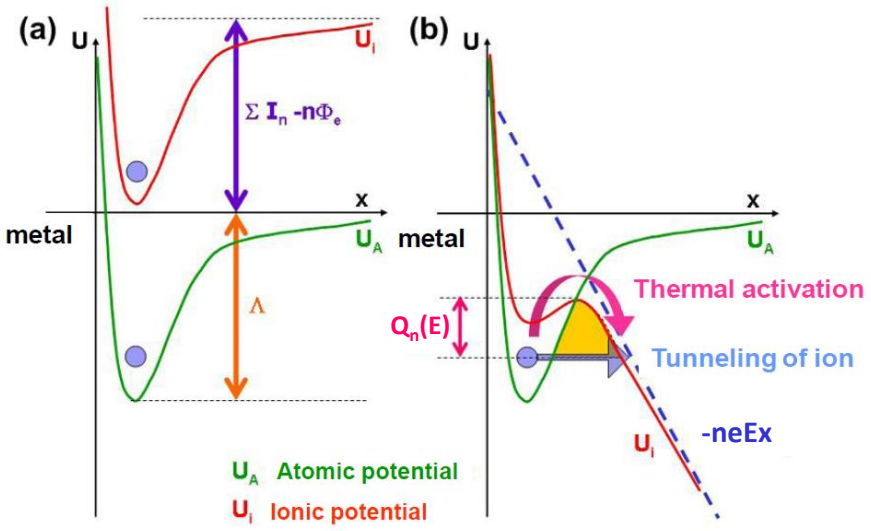

Figure III.2: Diagram of atomic and ionic potential as a function of distance (a) in absence of electric field and (b) in presence of the electric field. Λ is the sublimation energy, I_n is the n^{th} ionization potential, φ_e is the work function, Q(E) is energy barrier in the presence of an electric field [Miller 1996].

To explain the mechanism of evaporation, two models are proposed: image hump model [Müller 1956] and charge exchange model [Gomer 1959]. In first model, it is considered that the atom is fully ionised at a critical distance from the surface before leaving the specimen whereas in the later model the charge is progressively pulled away from the atom as it is escaping the surface. In image hump model, for the particle to be ionised and repelled from the surface, it must cross the so-called Schottky hump, which is a field dependent barrier *Q(E)* that represents the activation energy for field evaporation.

For triggering the evaporation, a potential lower than the one required for evaporation is applied to the specimen. A high voltage pulse with a nanosecond rise time (V_{pulse}~ $0.2V_{dc}$) is usually used for the controlled field evaporation of surface atoms. In laser pulsed atom probe, a pulse of laser with a duration time in the order of femtoseconds replaces the voltage pulse. The laser pulse, gives rise to a local increase of the temperature that induces evaporation. *Figure III.*3 shows how variation in voltage or temperature can influence the field evaporation [Marquis 2010].

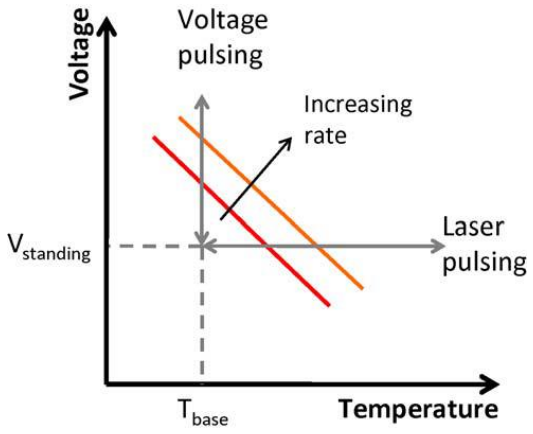

Figure III.3: Evaporation rate as a function of tip temperature and applied voltage [Marquis 2010].

The choice of applying a laser or voltage pulse mode is directly related to the nature of the material that we are analysing. Voltage pulse is commonly used for metallic materials whereas, for poor conductive materials the use of laser pulse mode is more appropriate. This will be further discussed in section III.2.

The number of atoms that evaporate per second is called evaporation rate, which is usually assumed to be through a thermally activated field evaporation process. The thermal agitation of

the atoms results in their vibration on the surface with a frequency (v_0) which is estimated to be in the range of 10^{12} to 10^{13} Hz depending on the applied temperature and field. On each of this vibration, the atoms attempt to overcome the energy barrier that holds it on the surface, and escape to the free space. The evaporation rate ($\Phi_{evaporation}$) for an ion is given as

$$\Phi_{evaporation} = v_0 \exp(-\frac{Q(E)}{k_B T}), \quad \text{(III.2)}$$

where $Q(E)$ is the field-dependent height of the barrier, k_B is the Boltzmann constant and T is the absolute temperature. The exponential term reflects the probability of field evaporation and hence the evaporation rate. The expression of the energy barrier $Q(E)$ depends on the model considered which experimentally is expressed as a linear function of the field

$$Q(E) \approx Q_0[1-\frac{E}{E_{evap}}], \quad \text{(III.3)}$$

where Q_0 is activation energy in the absence of the field, E_{evap} is the field allowing for the evaporation of the material when the energy barrier at 0 K is reduced to zero. The evaporation field (E_{evap}) can be calculated for different elements. For example, for pure zinc, E_{evap} is 29V/nm. However, in atom probe experiments, the evaporation rate is not measured directly, instead, it is the detection rate which is measured. The detection rate ($\Phi_{detection}$) associated with a single pulse is measured in atom per pulse and it is given by

$$\Phi_{detection} = \tau.\eta.N_{atm}.v_0.\exp(-\frac{Q(E)}{k_B T}), \quad \text{(III.4)}$$

where the τ is the evaporation pulse duration which is about 1 ns for voltage pulsed atom probe and about 350 fs for the laser pulsed one. η is the efficiency of the detection system (~0.5 to 0.6) which will be discussed further in III.1.3. N_{atm} is the number of atoms across the entire surface of

the specimen that can be evaporated. Hence, the detection rate is therefore directly linked to the amplitude of the electric field. Using equation (III.3), equation (III.4) can be modified to

$$\frac{E}{E_{evap}} = 1 + \frac{k_B}{Q_0} \ln\left(\frac{\Phi_{detection}}{\tau.\eta.N_{atm}.\nu_0} \right) T \,, \qquad \text{(III.5)}$$

reflecting that the evaporation field ratio decreases linearly with the temperature of the tip.

Most atom probe experiments are carried out under constant detection rate which is usually set in the range of 0.2% to 5% of ion per pulse. As the atoms from the surface evaporate layer by layer, the specimen radius becomes larger resulting in higher N_{atm} and lower electrical field. Hence, in order to keep the $\Phi_{detection}$ constant during the experiment, the voltage should be increased. Atom probe experiments are thus performed under a slowly changing electric field to compensate the increase in the radius and N_{atm}.

Field evaporation can also be considered as a two-step process suggested by Kingham: initial evaporation and subsequent post-ionization. It is shown by Kingham that theoretically post-ionization of field evaporated ions may occur, whereby a positive ion being accelerated away from a metal surface in a strong electric field loses one or more electrons by tunneling into the substrate.

There are thus two different possible processes of field evaporation:

(a) the ion being initially evaporated in its final observed charge state conducting the information directly related to the local electronic structure of the surface,

(b) the ion being initially evaporated in some lower charge state and then being post-ionized to its final observed charge state which carries the information about the characteristic of the initial charge state of the ion and the modification caused by post-ionization.

In given cases, the probability of post-ionization may be very low so that the initial and final evaporated charge states are the same.

Based on a physically realistic potential model, Kingham predicted the probability of post-ionization as a function of field strength for all elements of interest in field evaporation. *Figure III.*4 shows the Kingham curve calculated for Zn presenting the evolution of Zn different ionization states as a function of the field [Kingham 1982].

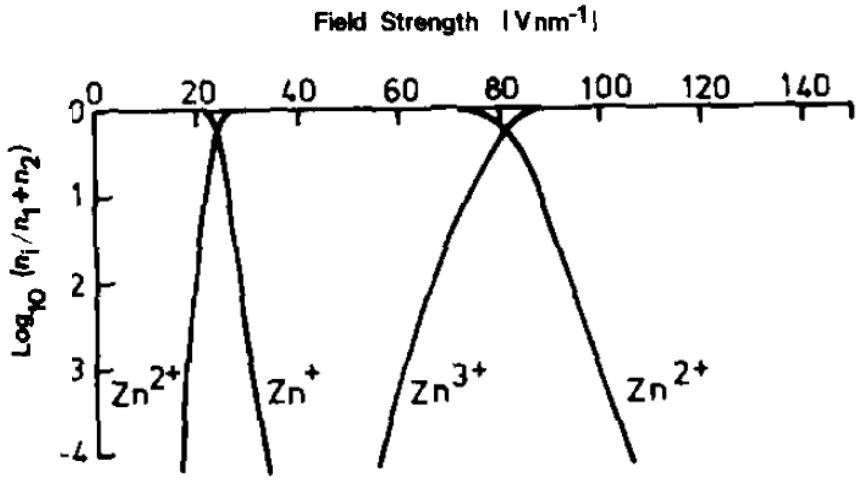

Figure III.4: The relative abundance of singly and doubly charged zinc ions plotted logarithmically against field strength [Kingham 1982].

Therefore, knowing the charge state ratio of an element can allow us to deduce the relative value of the field and vice-versa. However, Kingham curves can predict the charge states of the elements as a function of field for pure materials only and not for semiconductors such as ZnO.

III.1.2 Time of flight mass spectroscopy

The first step in identification of each atom is to measure its time-of-flight (ToF) corresponding to the time needed for an ion to travel from the surface of the specimen to the detector. In voltage and laser pulsed atom probe, the departure time is measured when the pulse is applied. A position sensitive detector is placed in front of the tip, providing the arrival time and the position of the atoms.

The mass-to-charge ratio *(m/n)* of arriving ions is then deduced from the energy conservation between the potential energy of the atom at the voltage of $V_{total} = V_{dc} + V_{Pulse}$ and its kinetic energy upon evaporation given by:

$$neV_{total} = \frac{1}{2} m \frac{L^2}{t^2}, \qquad \text{(III.6)}$$

leading to:

$$\frac{m}{n} = 2eV_{total}\frac{t^2}{L^2}, \qquad \text{(III.7)}$$

where t is the time of flight (assuming the acceleration time is negligible), L is the flight distance, m is the ion mass, n is the ion charge state and e is the electron elementary charge. Note that for laser pulse atom probe tomography, $V_{pulse} = 0$.

By field evaporating the specimen, atomic layer-by-atomic layer, a mass spectrum of atoms is obtained. The mass spectrum gives the number of detected single or molecular ions corresponding to the calculated mass (a.m.u.). A typical mass spectrum of ZnO materials is shown in *Figure III.*5. Each peak is assigned to a specific m/n ratio corresponding to different chemical species.

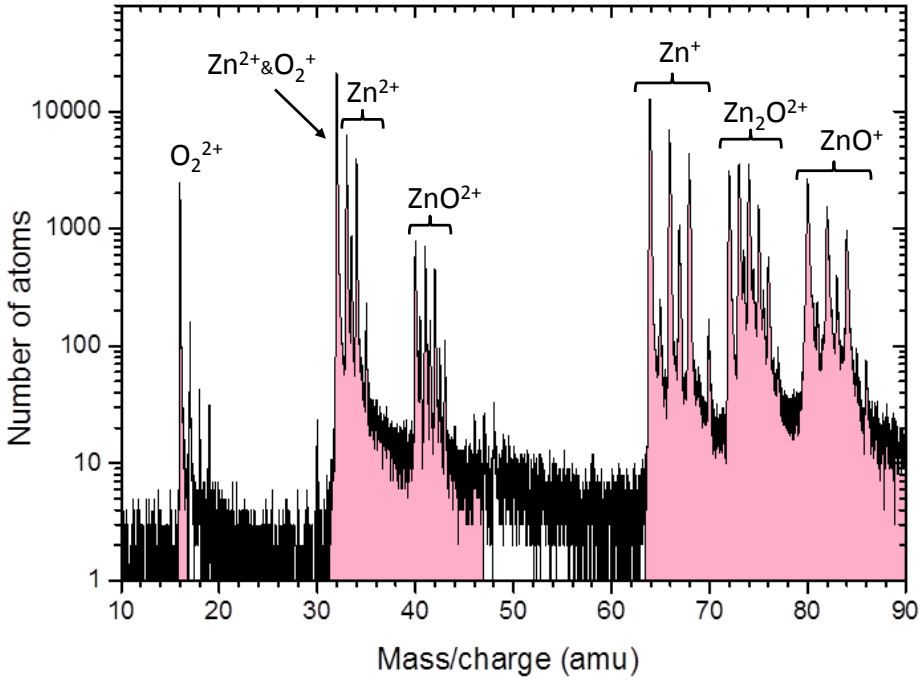

Figure III.5: Mass spectrum of ZnO obtained at laser energy of 0.5nJ using UV source. The peak at 32 belongs to both oxygen and zinc atoms.

Besides, APT is also able to distinguish different isotopes of each single chemical element. *Table III.1* presents the common species detected in mass spectra of ZnO materials at their corresponding *m/n* ratios and charge states given for different Zn isotopes.

Table III.1: Peaks corresponding to the presence of Zn and O or combination of both observed in mass spectrum obtained by APT.

Ion	O_2	*Zn*	*ZnO*	Zn_2O	Zn_3O_2
+1 charged (a.m.u.)	*32*	*64/ 66/67 /68/70*	*80/82/83/ 84/86*	_	_
+2 charged (a.m.u.)	*16*	*32/ 33 /33.5/34/35*	*40/40.5/ 41/41.5/42/43*	*72/73/73.5/ 74/75/76*	*112/115/ 116.5/118*

Once the different peaks of the mass spectrum are clearly identified, the atomic concentration of the elements in the studied system can be obtained simply by counting the number of atoms of each species collected by the detector which is given as the number of atoms in each peak of the mass spectrum.

Hence, the atomic concentration (C) of element 'A' corresponds to the number of A atoms divided by the total number of atoms.
The statistical uncertainty of the measurement (ΔC) is given by

$$\Delta C = 2\sqrt{\frac{C(1-C)}{n}}, \qquad \text{(III.8)}$$

where C is the atomic concentration of the measured species and n is the total number of atoms in the volume.

In some cases like in ZnO, the mass-over-charge ratio of two peaks overlaps and it can significantly affect the determination of the elements composition. In ZnO, the peak at 32 a.m.u. corresponds to both Zn^{2+} and also O_2^+ (*Figure III.*5). The peaks are hence decomposed based on the expected number of counts signified by the isotopic abundance of the elements. In order to

count the number of impacts corresponding to the Zn^{2+} or O_2^+ at the peak 32 a.m.u., we first should find the number of Zn^{2+} at this peak (n_{Zn32}). For that, we need to know the number of Zn^{2+} impacts excluding the ones at the peak 32 a.m.u. ($n_{Zn"}$) which can be obtained directly from mass spectrum. Considering the abundancy of the Zn^{2+} isotope at 32 a.m.u. is 48.3 %, we can conclude that $n_{Zn"}$ corresponds to the 51.7 % of the total Zn^{2+} atoms. Hence, the number of Zn^{2+} at 32 a.m.u. can be calculated as n_{Zn32}= 48.3x $n_{Zn"}$/51.7. Once the number of counts for Zn^{2+} at 32 a.m.u. is found, the O_2^+ counts can be deduced from the total number of counts at this peak.

There is also an uncertainty on ascribing the peak at 16 a.m.u. that can be attributed to $^{16}O^+$, $^{16}O_2^{2+}$ or a mixture of both. The real nature of this peak is still under debate and has been identified as $^{16}O_2^{2+}$ by several authors [Duguay 2010 - Ngamo 2010 - Talbot 2013] or $^{16}O^+$ [Kinno 2014]. This problem can be solved by considering which assignment can provide an expected stoichiometry [Bachhav 2011].

Very often in atom probe tomography, there are some ions which are evaporated from the surface of the specimen between pulses or in a multiple ion evaporation events that influences the composition of the elements. These events can create noise on the mass spectrum or cause an inaccuracy in the composition via three main phenomena.

a) Evaporation between pulses: During field evaporation of atoms, there are some atoms which evaporate at some time after the pulse and their time of departure ($t_0+\Delta t$) remains unknown, and hence what detector detects as a time of flight is inaccurate. This means that when they hit the detector, the recorded time of flight is random, degrading the mass resolution or increasing the back ground noise (*Figure III*.6.*a*).
b) Evaporation in a multiple ion evaporation events: It corresponds to the event where two ions are evaporated at the same time but at some time after the pulse (*Figure III*.6.*b*).
c) Ion dissociation during flight: When a molecular ion composed of few ions is evaporated, it can dissociate during the flight, and generate few ions which are flying at different speeds; therefore they are reaching the detector at different times (*Figure III*.6.*c*).

In the mass spectra of ZnO, it is common to see that the peaks are followed by a tail. Basically, in pulsed laser atom probe, the temperature of the tip increased from less than 100K to almost room temperature. The main peaks seen on the mass spectra are obtained at the maximum

temperature. However, even after the pulse, there are still some ions flying towards the detector with a slightly different and longer ToF which degrades the mass resolution of the spectrum.

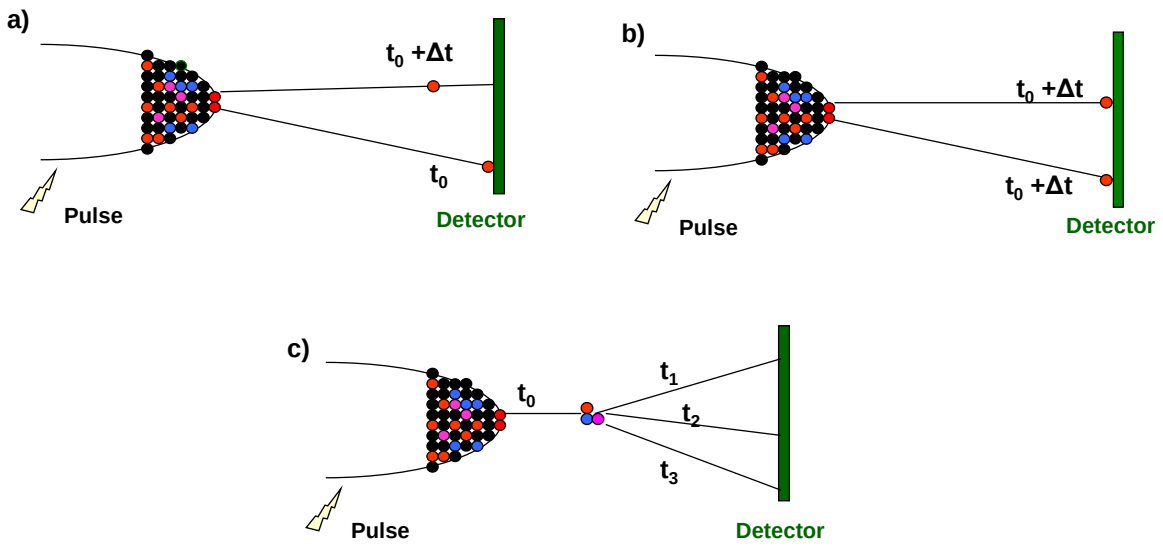

Figure III.6: Three different possible inaccuracies caused by multiple event evaporation, (a) evaporation between pulses, (b) evaporation in a multiple ion evaporation events, (c) ion dissociation during flight.

The longer the heat retained at the specimen apex, the higher the probability of delayed evaporation is. This occurs often for poor thermal conductive materials.

III.1.3 Three dimensional reconstruction of analysed volume

The most recent generation of atom probes are equipped with an advanced delayline based position sensitive detectors (aDLD). Once the ion reaches aDLD system, it passes through micro channel plates (MCP) creating an electron cloud [Da Costa 2005]. The electron cloud is then focused onto two polarized conductive lines placed behind MCP. The passage of the electron cloud in the vicinity of the conductor induces two signals that are then propagated towards each end of the conductive lines. Detecting these signals provides information about the lateral coordination of the impact.

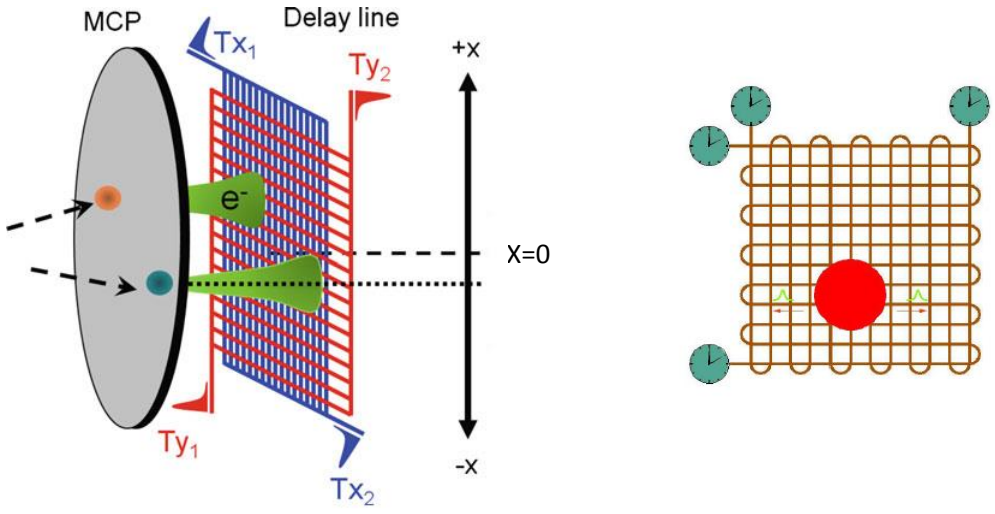

Figure III.7: Schematic of an advanced delay line detectors composed of a microchannel plate (MCP) and polarized conductive lines. The passage of the electron through the MCP creates an electron cloud that reaches the conductive lines, creating signals. These signals are used for identification and position detection of the impacts [Gault 2012].

The success in detecting the signal ion received on the detector surface is defined as the detection efficiency. This detection efficiency (η) is theoretically limited by the open area of the MCP. The fraction of the surface area of the detector that is not intercepted by micro-channels is about 62%. The X_d and Y_d coordinates of the impact therefore can be determined for each impact (*Figure III.*7).

The 3D reconstruction of the analyzed volume considers APT as a projection microscope [Bas 1995]. It assumes that ions fly along straight lines from the specimen surface to the detector (*Figure III.*8). These straight lines originate from the projection point (*P*) along the specimen axis at the distance of (m+1)R from the specimen apex surface where *m* is the dimensionless geometric factor and *R* is the radius of the specimen as it is shown in *Figure III.*8.

The *x* and *y* coordinates of the atoms for the reconstruction are calculated by back-projection from the position of impact on the detector (X_d,Y_d) using the following relations

$$x = \frac{X_d}{M}, \qquad y = \frac{Y_d}{M}, \tag{III.9}$$

where *M* is the magnification and is given as,

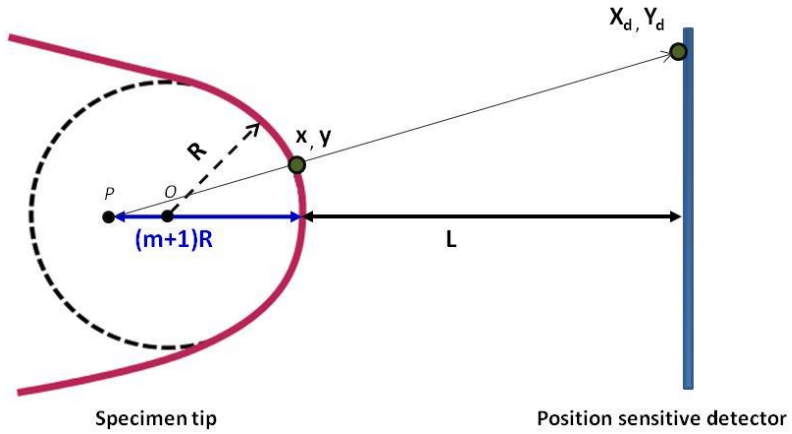

Figure III.8: Schematic illustration of specimen projection and analysed volume in APT. The specimen tip (shown in red) is perpendicular to the position sensitive detector placed at the distance of L.

$$M = \frac{L}{(m+1)R}. \tag{III.10}$$

Since the radius of the tip is increasing during the field evaporation of the specimen, in 3D reconstruction of the volume, the increase of the radius is taken into account as it is given in equation (III.1).

To calculate the third dimension (z) corresponding to the depth of the atoms in the analysed volume, evaporation of an ion is assimilated to the evaporation of a tranche of a material with a volume of V_{at}. The increment of the depth Δz is thus calculated for each event written as:

$$\Delta z = \frac{V_{at}}{\eta S}, \tag{III.11}$$

where S is the surface of the tranche of the evaporated material which can be obtained by magnification ($S=S_{detector}/M^2$). At each impact, z is incremented with a volume of Δz.

For each atom hitting the detector, different information is provided: the chemical nature of the detected ion and its coordinates x, y, and z. This information leads to the 3D reconstruction of the analysed volume.

III.2 Development of the laser assisted APT for semiconductor materials

Earlier than 2006, APT was limited only to metallic materials. In conductive materials, a voltage pulse is used to increase the field at the tip of the specimen to above the threshold required for ion evaporation. However, for poor conducting materials such as semiconductors and oxides, the high voltage pulses cannot be transmitted at the apex of the specimen efficiently due to the high electrical resistance. Moreover, applying cyclic electrical pulses, generates high stress on these materials, and thus increases the risk of rupture of the specimen. Since 2006, using laser pulse made it possible to perform APT on semiconductors and even insulated materials [Gault 2006].

First applications of pulsed laser field evaporation for poor conducting materials were performed on silicon [Grovenor 1982 - Kellogg 1982 - Tsong 1982 - Tsong 1984]. It was observed that APT analysis of silicon using a pulsed laser APT results in the evaporation of Si in the form of monoatomic Si^{+} and Si^{2+} and an improvement in the mass spectrum [Grovenor 1982], whereas, using electrical APT have shown the evaporation of Si atoms in the form of clusters resulting in a poor mass resolution [Sakurai 1978]. Grovenor *et al.* compared the atom probe measurements of silicon using both voltage pulse and laser pulse. As it is shown in *Figure III*.9, the mass spectrum obtained by laser pulsing (*Figure III*.9.*a*) shows higher resolution compared to the mass spectrum obtained by voltage pulsing (*Figure III*.9.*b*). A closer look at these mass spectra clearly shows that different isotopes of Si^{2+} can be obtained only by laser pulsing method (*Figure III*.9.*c* and *d*). On early attempts, in order to use the electrical pulsed atom probe for semiconductors, due to the poor conductivity of the semiconductors, the pulsed voltage atom probe measurements were carried out on highly doped semiconductors using a high voltage pulse.

It was observed that the propagation of the high pulse voltage in the specimen generates a mechanical shock and increased the fracture in brittle materials causing problem even for doped materials. Therefore, to enhance the field evaporation, analyses have been carried out at higher temperatures than usual [Tsong 1978].

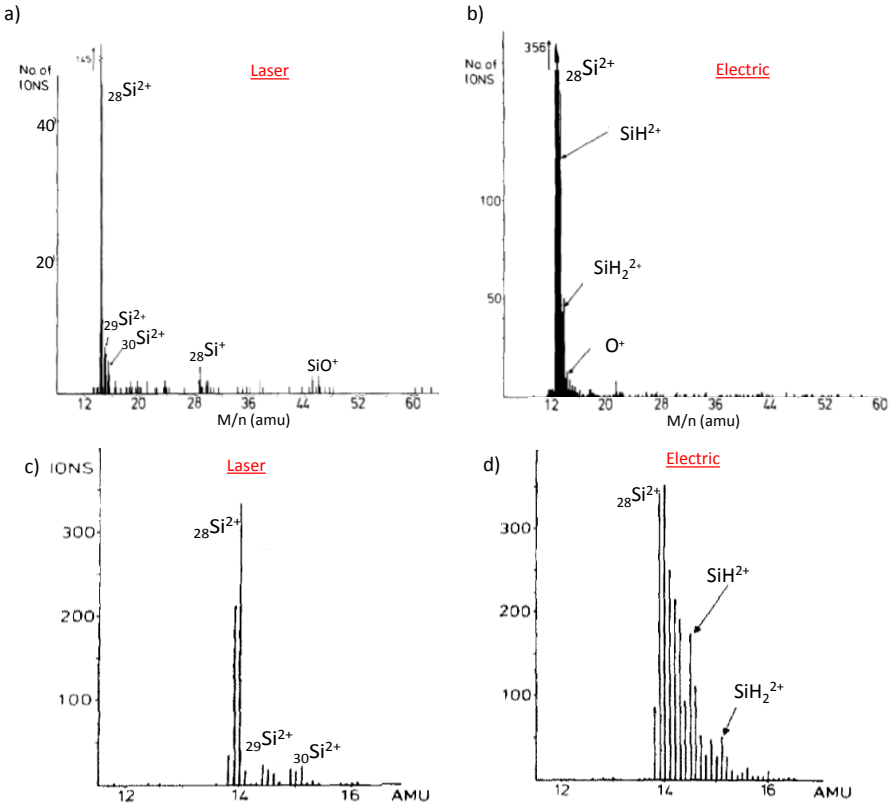

Figure III.9: Mass spectra obtained by APT on silicon samples at different conditions: (a) laser pulsing at base temperature of 77K and voltage of 17kV, (b) using voltage pulsing at base temperature of 300K and 17 kV where the tip was maintained at room temperature. Short range spectra (12-16 a.m.u.) obtained by (c) laser and (d) voltage pulsing presenting the difference in the resolution of Si^{2+} isotopes obtained for each mode [Grovenor 1982].

In 1985, Cerezo *et al.* performed pulsed laser atom probe analysis on GaAs and InAs [Cerezo 1985]. Previously, using electric mode atom probe of GaAs and InAs always resulted in Ga/As and In/As compositional ratio values, very far from their stoichiometric ones. Cerezo *et al.* have observed that using pulsed laser atom probe could provide the Ga/As and In/As compositional ratios very close to the stoichiometric values (0.99 and 0.97, respectively). Hence, pulsed laser atom probe was found to be the most successful method for the study of poor conductive materials as it provided a better mass resolution and a quantitative analysis.

However, in the early works, the stability of the lasers available in 1980s and the difficulties in performing a controllable evaporation limited the application of this technique. Moreover, the physical phenomena behind laser-semiconductor interaction, field ionization and field

evaporation in LA-APT were the main issues remained unclear for many poor conductive materials.

Tsong *et al.* have suggested the mechanism of photo-ionization of the surface atoms gives rise to the generation of ions. Three different photo-ionization paths have been proposed that are demonstrated in *Figure III.10* [Tsong 1976 - Tsong 1984].

(a) A direct electric transition from the atomic state to vacant state by absorption of a photon followed by a tunnelling of electrons from the vacant state to the conduction band of the semiconductor (*Figure III.10.a*).

(b) Absorption of the photon results in the direct transition of the electron to the conduction band in semiconductor (*Figure III.10.b*).

(c) Absorption of the photon occurs in valence band or below Fermi level of semiconductor creating many holes, allowing for the tunnelling of adatom electrons to these vacant electronic states (*Figure III.10.c*).

The third path (c) is referred more often in the literature.

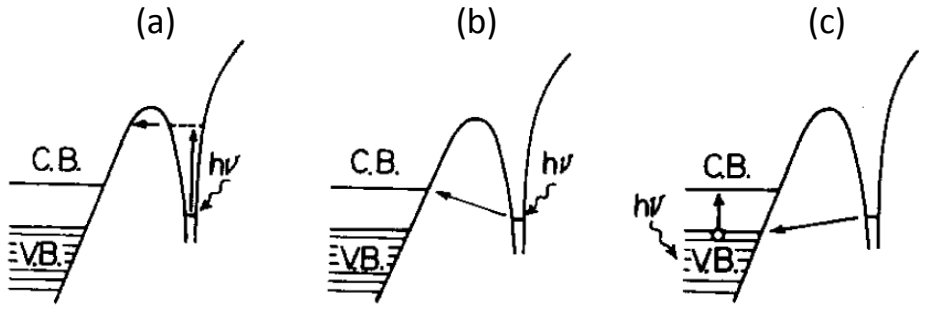

Figure III.10: Photon-assisted field evaporation from a surface of a semiconductor through three different paths (a, b and c)[Tsong 1976].

Nevertheless, the theory of field evaporation through photo-ionization is applicable for materials with large band gap where the lifetime of the ions is long enough for the evaporation. For metals, the re-neutralization of the ions from a conduction band electron is rapid and hence the experimental detection is more difficult [Tsong 1976].

Another theory of field evaporation beside photon-ionization is through thermal mechanism. Once the laser interacts with the specimen, a localized heat occurs on the tip which assists the field evaporation by transferring energy to the surface atoms, and assisting them to overcome the potential barrier for ionization. The surface is quenched, as the heat propagates away from the specimen apex. Hence, the evaporation occurs at each successive increase and decrease of temperature at the surface of the specimen which is referred as thermal pulsing. This thermal pulsing temperature is higher than the base temperature at which the specimen is maintained [Kellogg 1980].

In the past decades, the introduction of advanced lasers to the atom probes together with the improvements in 2D detectors, time-of-flight mass spectroscopy and analytical software, has given rise to a renaissance of APT particularly for semiconducting materials. Variety of laser-assisted atom probes are introduced such as Local Electrode Atom Probe (LEAP), Laser Assisted Wide Angle Tomographic Atom Probe (LAWATAP) equipped with a femtosecond pulsed laser.

In 2009, Cadel *et al.* have reported the high depth resolution of silicon substrate and doped silicon semiconductors bringing the application of APT to a more advanced level. Cadel *et al.* were able to provide the 3D mapping of silicon by LA-APT revealing the atomic planes in the <111> direction (shown in *Figure III.11*).

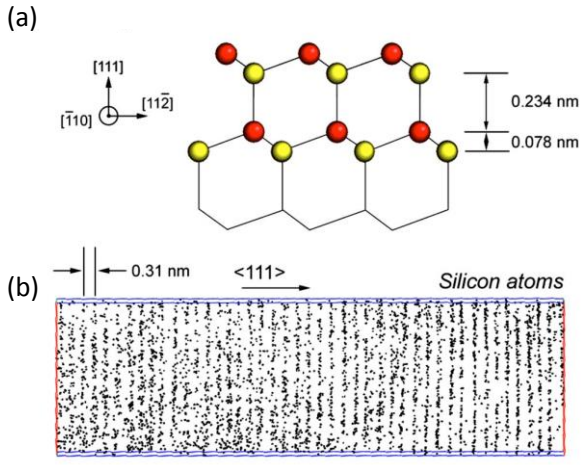

Figure III.11: (a) Schematic of diamond structure projected on {110} plane providing a stacking of {111} layers, (b) 3D map of silicon atoms ordered in sequenced planes along [111] direction obtained by LA-APT [Cadel 2009].

Analyses were also carried out on an epitaxial growth multilayer stack consisting of ultrathin boron doped silicon films separated by undoped silicon films [Cadel 2009]. *Figure III.12.a* shows the 3D map of four boron doped layers separated by 18.3 nm ultrathin silicon layers. The concentration profile shown in *Figure III.12.b* was derived from the reconstructed volume and superimposed on the concentration profile obtained by SIMS.

Such results evidenced the great improvement of laser assisted atom probe tomography of semiconducting materials.

The application of LA-APT technique was then significantly increased in order to investigate metallic, semiconductor and oxide nanomaterials such as magnetic multilayers [Lardé 2009], transistors [Inoue 2009], Si nanowires [Roussel 2011], silicon-rich silica/silica multilayers [Talbot 2009] and doped thin film semiconductors [Lardé 2011]. *Figure III.*13 shows the recent examples of application of APT for semiconducting materials. The 3D reconstruction of pure silicon nanoclusters embedded in SiO_2 is shown in *Figure III.13.a*.

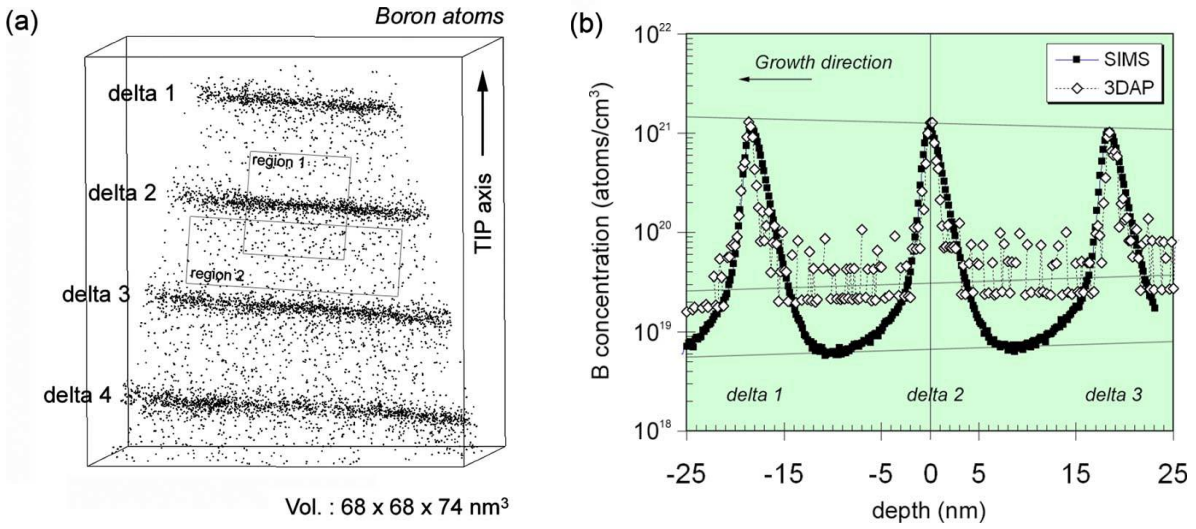

Figure III.12: (a) 3D map of multilayer boron doped Si, (b) concentration profile of boron derived from the 3D map of (a) superimposed the corresponding SIMS profile for comparison [Cadel 2009].

Using LA-APT could reveal the successful sequence of embedded nanoclusters in the matrix together with the concentration profile acquired along the reconstructed volume and across a single nanocluster [Talbot 2009]. *Figure III.*13.*b* presents the 3D reconstructed volume of

heavily Mn doped Ge thin films revealing the formation of self-organized Mn nanocolumns in Ge matrix [Mouton 2012].

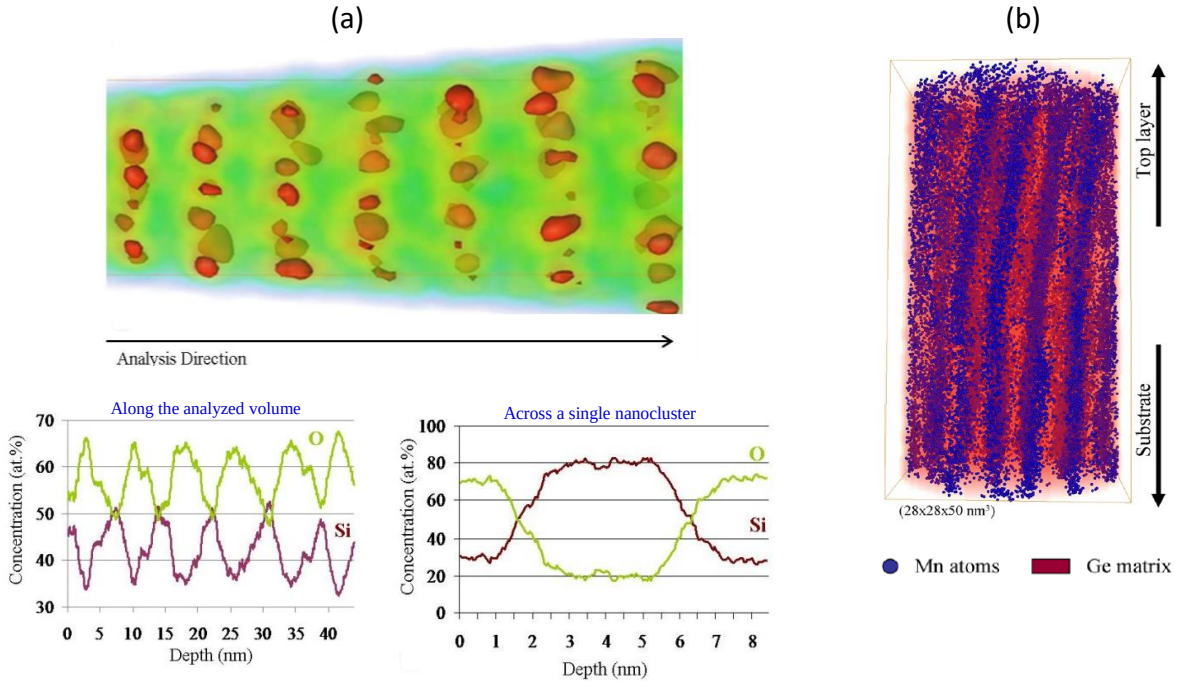

Figure III.13: Two examples of recent application of LA-APT for semiconducting materials, (a)3D reconstruction of silicon nanoclusters (in red) embedded in silica matrix (in green),with the corresponding concentration profile along the analyzed volume [Talbot 2009],(b)3D reconstructed volume of Mn-rich self-organized nanocolumns embedded in Ge matrix [Mouton 2012].

Despite many successful reports on application of LA-APT for certain semiconducting and insulating materials, the application of this technique for many other poor conducting materials encountered unreliability in APT measurements. This unreliability is mainly due to the fact that, the physical phenomena behind laser-semiconductor interaction in LA-APT are not fully understood.

Moreover, recently it was shown that in laser assisted atom probe tomography of semiconducting materials and metal oxides, the laser parameters were found to be very important factors governing the field evaporation. Number of reports has been devoted to the influence of laser energy on different system and semiconducting materials.

Gilbert *et al*. have studied the influence of laser energy on boron doped silicon using a femtosecond pulsed laser atom probe [Gilbert 2007]. They have observed that a better mass resolution can be obtained at very low laser pulsed energy <1μJ/pulse. At lower laser energy

(*Figure III.14.a*), silicon appeared to be evaporated mainly as Si^{2+} with low background noise whereas at higher laser energy a broad peak evolved in addition to the first peak, both corresponding to Si^{2+} ions (*Figure III.14.b*).

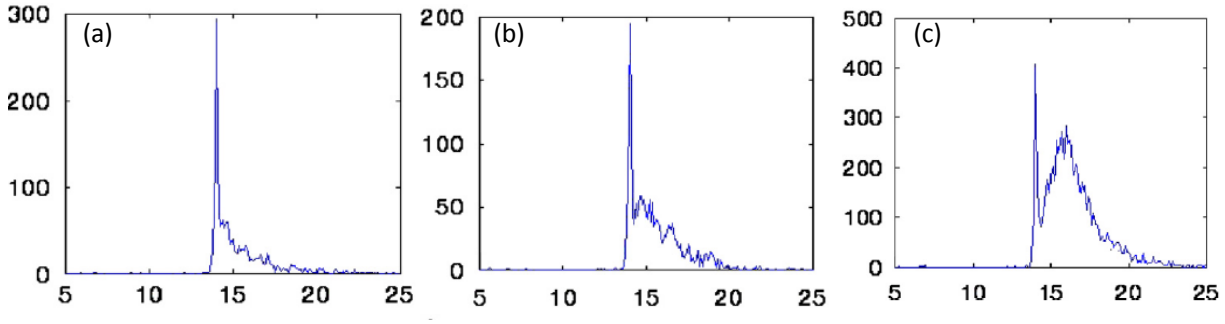

Figure III.14: Mass spectra of B doped silicon obtained for different laser intensities, (a) 750nJ/pulse, (b) 3µJ/pulse, (c) 7µJ/pulse [Gilbert 2007].

As the laser intensity was increased, the broad peak was found overriding the first peak shown in *Figure III.*14.*c*. This phenomenon was considered to be where the evaporation time of the ions (~several nanoseconds) is much longer than the laser pulse duration. Besides, proper quantitative measurements in APT of semiconductors were found to be strongly affected by the laser parameters. The deviation from stoichiometric measurements have been reported for different semiconductor and metal oxide materials such as MgO [Devaraj 2013], GaN [Diercks 2013] and ceria [Kirchhofer 2013]. In LA-APT of MgO, Devaraj *et al.* have observed oxygen deficiency at high laser pulse energies.

Therefore, a proper selection of laser parameters is very important in atom probe tomography of semiconductors which should be adapted according to the material that is studied. In laser assisted APT, the selection of a proper laser wavelength is one of the most important parameters. To unbind the electrons from the atoms and create free negative carriers in the conduction band and positive holes in the valence band, a laser wavelength providing a higher energy than the band gap energy should be used. Thus, in case of ZnO, UV light (λ=343 nm, E_λ=3.62 eV) theoretically offers a better absorption.

In case of APT analysis of ZnO materials, only few reports can be found in the literature [Chen.Y.M 2011 - Dawahre 2012]. Among all, only one report has briefly discussed the influence of the laser concerning only the quality of APT analyses for ZnO materials [Chen.Y.M 2011].

Chen *et al.* performed laser assisted APT analysis of ZnO using different laser wavelength (green and UV) and laser pulse energies. *Figure III.15* shows APT mass spectra of ZnO obtained by UV and green laser. The mass spectra of ZnO were only obtained for UV mode whereas, no spectrum related to ZnO was observed for green mode indicating the importance of laser wavelength selection in APT of ZnO [Chen.Y.M 2011].

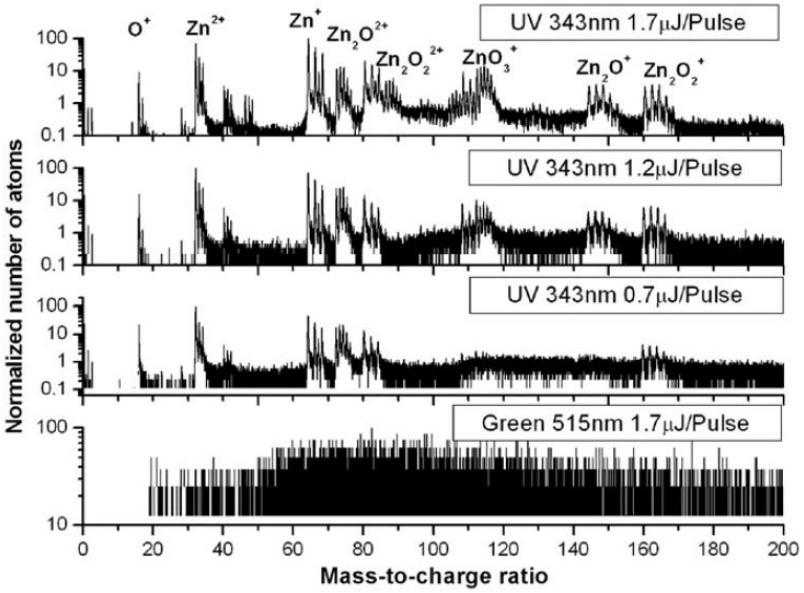

Figure III.15: Mass spectra of ZnO single crystal obtained by atom probe tomography using green and UV laser modes. For UV mode, the APT was performed at different laser pulse energies [Chen.Y.M 2011].

Therefore, due to the quantitative and qualitative deviation in APT analyses as a function of laser parameter in semiconductors and metal oxides, prior to apply this technique to ZnO doped materials, it is crucial to perform a comprehensive fundamental study in order to obtain a reliable APT analysis of ZnO materials.

The first step in APT analysis is the specimen preparation which is a very delicate task and will be discussed in the following section.

III.3 APT specimen preparation for ZnO nanostructures

One of the main challenges in atom probe tomography of semiconductors is the APT specimen preparation. The sample preparation for semiconducting thin films has already an established process. However, coming to nanowires, many limits are encountered for APT sample preparation due to the nanowires morphology. Hence, in this section first, the procedure of APT sample preparation for thin films is discussed. Then, different approaches, for specimen preparation of nanowires with different lengths are suggested in this work.

III.3.1 APT sample preparation of ZnO thin film

For metallic materials, a needle shape specimen is directly made by electrochemical polishing, where analysed material is immersed in an appropriate electrolyte under a positive potential of several tens of volt.

For semiconductors like ZnO, electrochemical polishing is not a possible technique. In this case, the sample preparation is carried out with a dual beam system consisting of Focused Ion Beam (FIB) and Scanning Electron Microscope (SEM).

FIB system uses a finely focused beam of ions (usually gallium). When the gallium beam strikes the sample surface, it generates many species including sputtered atoms and molecules, secondary electrons and secondary ions offering different abilities to FIB. Focused ion beam instrument has the ability to mill, image or deposit material depending on the nature of the ion beam-solid interactions. Low beam currents are used for imaging and high beam currents are applied for specific sputtering or milling [Orloff 2003]. The deposition is performed by decomposing gaseous molecules with chemical reaction using ion beam. Most commonly Pt, W, C, and SiO_2 are used as deposition materials. This process is called ion beam induced deposition (IBID).

The instrument used in this work is a SEM-FIB N-Vision, made by Zeiss. This instrument combines high resolution imaging with a focused ion beam, allowing for the identification and a controlled etching of the area of interest on the sample.

The APT specimen preparation of the thin films is possible using an established method called lift-out process in FIB. *Figure III.16* shows different steps of sample preparation from a thin film. In this process, a blade with the thickness of few micrometers in the sample is made by

sputtering the sample (*Figure III.16.a)*. During imaging and milling in FIB, Ga ions can be implanted into the specimen and induce damages. Hence, a thin protecting layer of tungsten or platinum is deposited on the area of interest, before FIB imaging and milling.

The blade is then extracted by a micromanipulator (*Figure III.16.b*) and placed on top of a support tip (W-tip) previously prepared by electrochemical polishing (*Figure III.16.c*). The contact between the thin film and the support tip is reinforced using IBID. In order to shape the specimen and reach the specimen radius of <50 nm, the tip is resized using different milling currents using annular milling (*Figure III.16.e*). Annular milling gradually reduces the radius of the tip by decreasing the milling current of 1.5 nA to 150 pA at the voltage of 30 keV. Once the radius of the tip is less than few hundred nanometers, lower currents (up to 10 pA) are used (*Figure III.16.f*). The final step is to remove the protecting layer using a low voltage of 2 keV allowing a slow removal of surface layers from the tip *Figure III.16.e.*

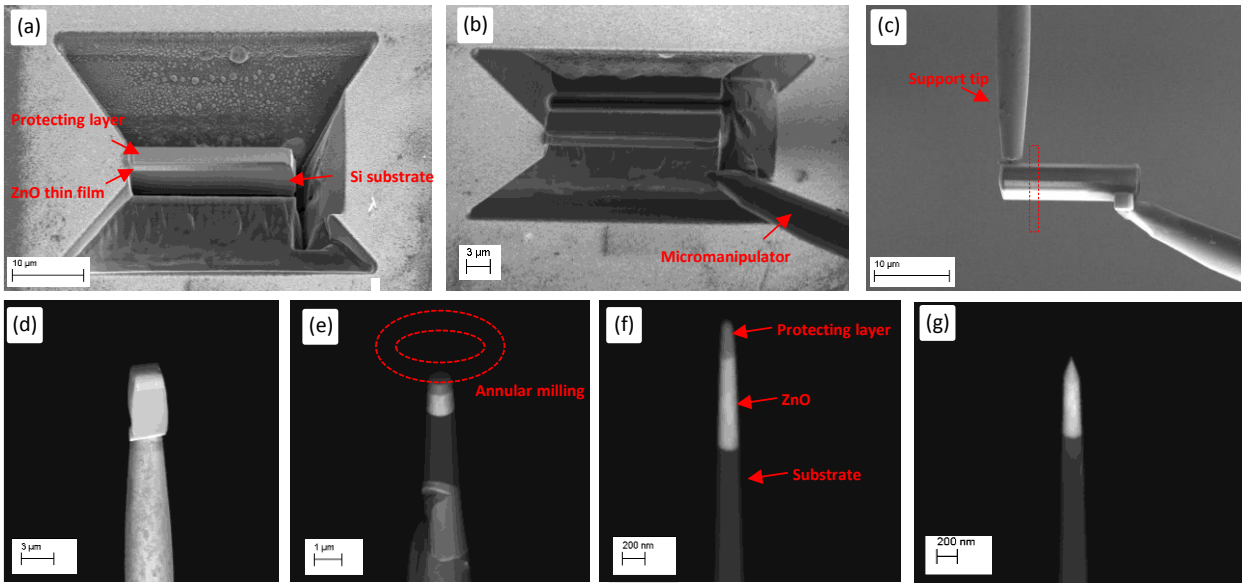

Figure III.16: APT specimen preparation using lift-out method.(a) forming a blade in the thin film, (b) extracting the blade by a micromanipulator, (c) welding the specimen on the previously polished support tip, (d) thin film mounted on the support tip,(e, f) gradual size reduction by annular milling using different current masks, (g) low voltage cleaning of the tip.

III.3.2 Developing APT sample preparation techniques for ZnO nanowires

The main difficulty in atom probe analysis of ZnO single nanowires is the specimen preparation process. Different techniques have been suggested in order to mount a single nanowire on top of a support tip [Blumtritt 2014 - Chen.W 2011].

In this work, we have developed several techniques in order to increase the efficiency of sample preparation of ZnO nanowires of different lengths. Since these techniques are strongly dependent on the length and size of the nanowires, we have categorized the techniques with respect to their length. It is very important to mention that using FIB for sample preparation of ZnO nanowires can create extreme damages to the nanowire. Since, the deposition of the protecting layer on nanowires is not practical, the milling of ZnO nanowires should be performed without this protecting layer and at very low voltage or current.

- Nanowire length >5 µm (*Figure III.17*): In this case nanowires are long enough to be easily visible under the optical microscope. Nanowires are dispersed on a clean glass lamella by simply robing the nanowires over the glass surface very gently. Under the optical microscope, the deposited nanowires can be picked up with a sharp tungsten tip previously prepared by electrochemical polishing (*Figure III.17.b*).

Top of the W-tip is dipped slightly in epoxy glue in order to overcome the electrostatic forces between the lamella's surface and the nanowire and also to reinforce the attachment between ZnO nanowire and W tip.

Eventually the attachment between the nanowire and the support tip is reinforced again using Pt deposition. It should be noted that we have observed the welding using IBID brings sever sputtering damages during deposition. Therefore, instead of ion beam, electron beam induced deposition mode (EBID) is used for Pt welding which causes much smaller sputtering effect.

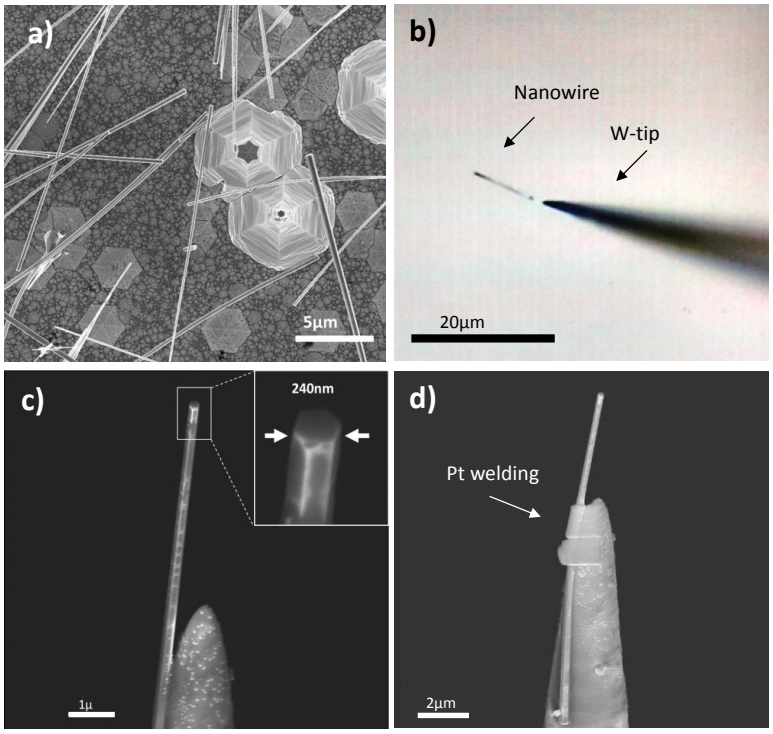

Figure III.17: APT specimen preparation for a single ZnO nanowire. (a) overall view of the ZnO nanowires grown on sapphire substrate, (b) ZnO nanowire mount on a support tip under optical microscope, (c) SEM image of mounted nanowire, (d) the reinforcement of the attachment between ZnO nanowire and the support tip using Pt deposition.

In case of having a nanowire with a large diameter, annular milling is performed carefully using the minimum current (1 pA) allowed by the device at 30 keV as it is presented in *Figure III.18.*

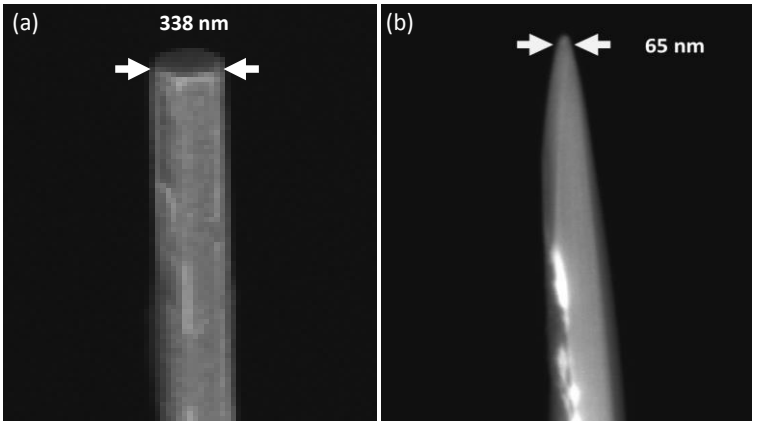

Figure III.18: APT specimen preparation of a single ZnO nanowire (a) before annular milling, (b) after annular milling in FIB using a Ga beam with 1 pA and 30 keV.

- Nanowire length <5 µm: in this case the nanowires are invisible or hardly visible under the optical microscope. *Figure III.19* shows the images of nanowires of about 2 µm length using SEM (*Figure III.19.a* and *b*) and optical microscope (*Figure III.19.c*).

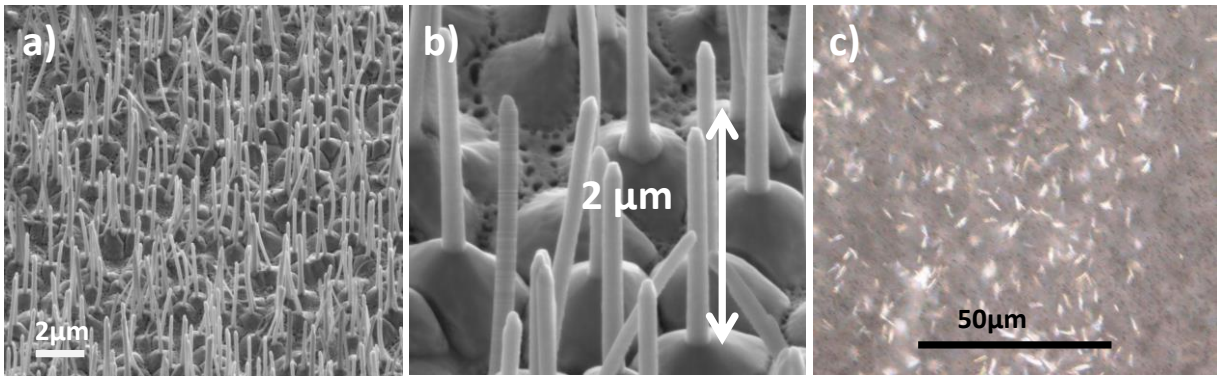

Figure III.19: ZnO nanowire with a length <5µm, (a) overall view using SEM, (b) magnified view of (a), (c) overall view of the same sample under the optical microscope.

As it is clear in *Figure III.19.c* these nanowires are hard to be distinguished under the optical microscope. In this case, we have established different methods in order to prepare APT samples of short nanowires.

- Lift-out process: A blade of nanowires is created using FIB. Annular milling is then performed so that only one nanowire remains on the support tip. *Figure III.20* shows different steps of this method. However, for a highly dense distribution of nanowires, selecting only one nanowire is not always an easy task. Moreover, since it is not possible to deposit a protecting layer, the annular milling process can easily damage the specimen which decreases the efficiency of this method.

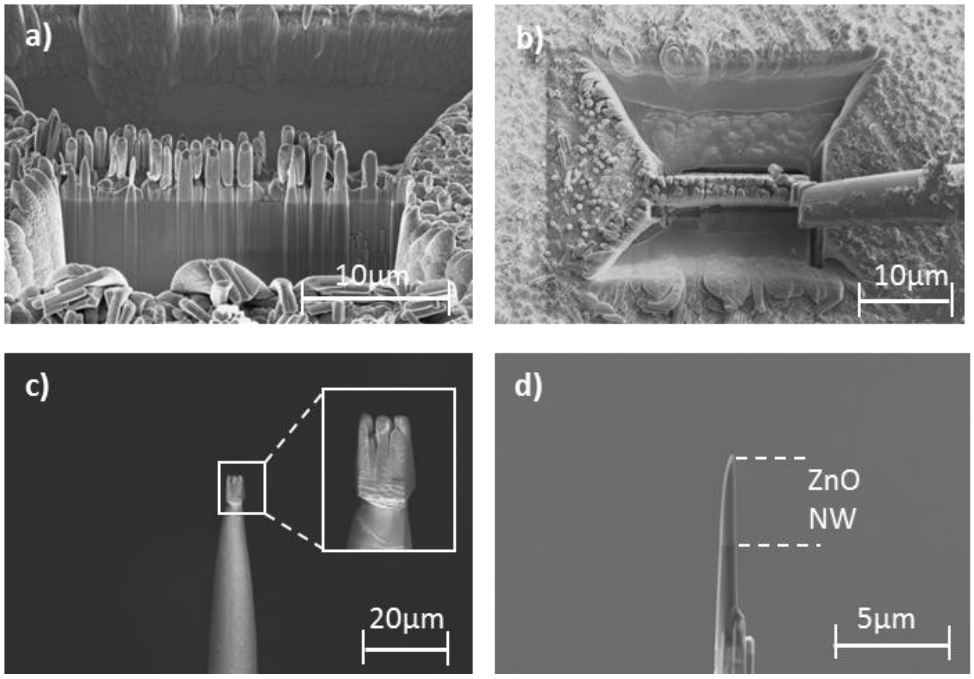

Figure III.20: APT specimen preparation of a single nanowire by lift-out method, (a) a blade is created using FIB, (b) the blade was lifted out using a micromanipulator to be placed on a support tip, (c) nanowires mounted on top of a support tip, (d) using annular milling to form an APT specimen of only one nanowire.

Selecting nanowires using micromanipulator in SEM: The same process for mounting a nanowire under the optical microscope is used for smaller nanowires using SEM (shown in *Figure III.21*. The nanowires are dispersed on a clean surface such as silicon. Taking advantage of electrostatic forces, when the micromanipulator reaches the nanowire, it attracts the nanowire (*Figure III.21.b*). Then the nanowire is mounted on top of a support tip previously inserted into the SEM chamber. The contact between nanowire and support tip is reinforced using EBID mode. Annular milling can be performed if the diameter of the nanowire is large.

However, this method encounters many limits since it is based on electrostatic forces. As it is shown in *Figure III.21.c*, while lifting up a nanowire, neighbouring nanowires are also attracted to the micromanipulator by electrostatic forces and mounted on the support tip.

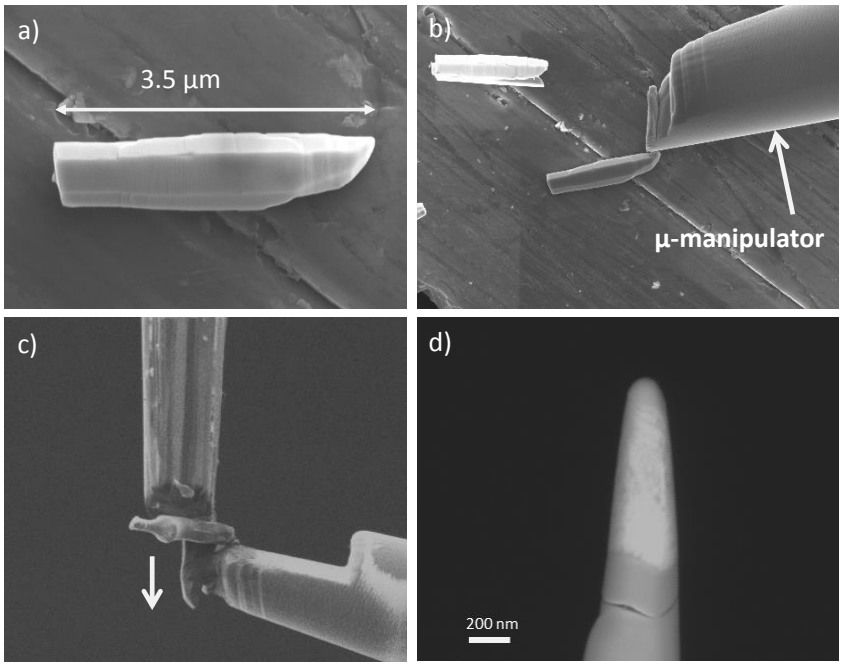

Figure III.21: APT specimen preparation single nanowire in SEM mode, (a) selected nanowire dispersed on the substrate, (b) picking up a nanowire by micromanipulator, (c) mounting the nanowire on top of a support tip (where the neighbouring nanowire is also attached horizontally), (d) ZnO nanowire after annular milling.

A precise annular milling sometimes could be helpful to avoid the presence of unwanted nanowires (*Figure III.21.d*). Nevertheless, mounting the nanowire perpendicularly to the support tip can also be very interesting as it allows for a radial APT analysis of the nanowire.

- Mounting nanowires under the optical microscope: even if the nanowires of about 2 µm length are not very well observable under the optical microscope, it is still possible to use the optical microscope for sample preparation. We have realized that nanowires placed perpendicularly to the sharp edges of a substrate are easier for mounting. In this way, smaller surface of the nanowire is in touch with the substrate causing smaller nanowire-substrate electrostatic forces making it possible to mount the nanowire on the support tip (*Figure III.*22). Using clean lamella substrates with sharp edges allows the deposition of

nanowires on the edges, simply by robbing the nanowire samples on the edges and surfaces of the clean lamella such as Si.

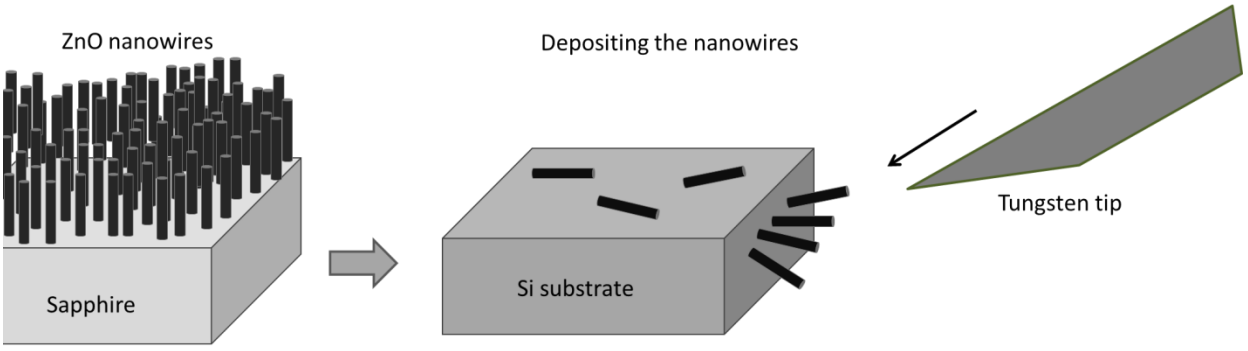

Figure III.22: APT specimen preparation for nanowires, a w-tip is used to pick up the nanowires deposited at the edge of the substrate.

Depending on the density distribution, diameter and length of the nanowires, one of the techniques above can be used. Nevertheless, nanowires with the length of ~8 µm or more are easier to manipulate under optical microscope and hence, they are more practical for APT sample preparation. In this work, sample preparation using optical microscopy was mostly used.

The APT specimen of ZnO thin films and nanowires are then moved to atom probe instrument for analyses.

III.4 Quantitative ZnO analysis using Laser-Assisted Atom Probe Tomography

In this part, we will discuss the influence of different laser parameters (such as laser wavelength and laser pulse energy) for pure and doped ZnO nanowires and thin films. The instrument used in this work is a Laser Assisted Wide Angle Tomographic Atom Probe (LAWATAP). The laser system is an Ytterbium-doped laser with the impulsion duration of 400 fs. The total laser power is 1 W and the laser frequency is 100 kHz. LAWATAP can provide three different wavelengths, infrared (λ~1030 nm), green (λ~515 nm) and ultraviolet (λ~343 nm). In this work, all the atom probe analyses were carried out at 80 K and at a fixed detection rate of $\Phi=2x10^{-3}$ atom/pulse.

III.4.1 Mass spectra

APT experiments were performed on undoped ZnO thin films and nanowires at different laser pulse energies (LPE) in green and UV modes. The effect of the LPE and laser wavelength on the mass spectra obtained for ZnO nanowire and thin film is shown in *Figure III.*23. All the mass-over-charge ratio peaks can be identified to Zn, O or molecular ions of both as it is indicated in *Figure III.23.a.*

For both nanowires and thin films specimens, when lower laser pulse energies are used (*Figure III.*23.*b* and *c*), the intensity of certain peaks such as Zn^+ at ~ 64 a.m.u. decreases. This loss in Zn^+ intensity is simultaneous with the increase of the Zn^{2+} amount. This indicates a presence of a stronger electric field at the surface of the tip causing the post-ionization of the Zn atoms [Kingham 1982]. No significant difference has been observed between nanowires (*Figure III.*23.*b*) and thin films (*Figure III.*23.*c*). Moreover, at higher LPE, peaks corresponding to $Zn_3O_2^{2+}$ are revealed at around 112 a.m.u. (*Figure III.*23.*a* and *d*). These molecular ions commonly appear at higher LPE, because the electric field is not strong enough to avoid molecular evaporation. Furthermore, at lower LPE (*Figure III.*23.*b*), the peak at 16 a.m.u. corresponding to oxygen becomes more important. *Figure III.23.e* and f show the mass spectra obtained in green mode at low and higher LPE with the values of 10 nJ/pulse and 50 nJ/pulse, respectively.

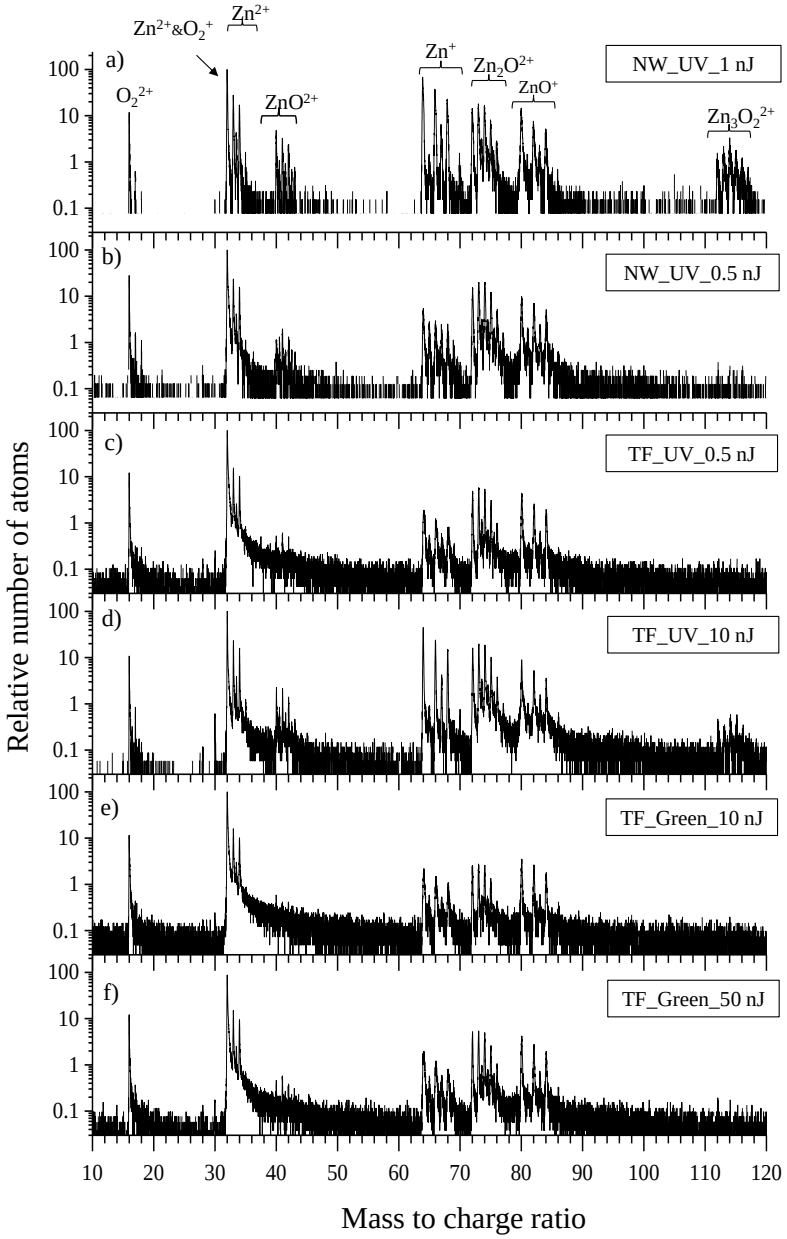

Figure III.23: Mass spectra for the relative number of atoms obtained by atom probe analysis of pure ZnO thin film (TF) and nanowire (NW) at different LPE using green and UV modes. The figure presents the mass spectra of ZnO nanowire using UV laser at (a) 1nJ, (b) 0.5nJ, ZnO thin film at (c) 0.5nJ and (d) 10 nJ using UV laser, and ZnO thin film at (e) 10 nJ and (f) 50 nJ using green laser acquired at 80 K. The peak at 32 consists of both oxygen and zinc atoms, and the peak at 16 a.m.u. consists of pure O_2^{2+} or pure O^+ or a mixture of both.

Previously, Chen *et al.* have shown that ZnO spectra cannot be confirmed using green mode since it provides energy smaller than the energy of ZnO band gap energy (*Figure III.15*)

[Chen.Y.M 2011]. However, Silaeva *et al.* have shown that the absorption can be also possible using laser mode with laser energy lower than that of the band gap by increasing the standing voltage [Silaeva 2014]. Therefore, as green laser offers lower energy (λ=515 nm, E_λ=2.41 eV) than that of ZnO band gap, in our APT analyses in green mode, the V_{dc} was increased so that the detection rate remained constant. For the mass spectra obtained in green mode, the same behavior, previously seen for UV mode, can be observed. For instance, increasing the LPE gives rise to an increase in the intensity of the peak at 64 a.m.u. However, in green mode, this increase of the intensity appears less important as compared to the one of UV one.

Comparing the mass spectra obtained in green and UV modes shows that the intensity of the peaks at LPE for the green mode exhibits the same behavior as the one obtained for smaller LPE using UV mode. However the mass resolution (m/Δm) at full-width-half-maximum (FWHM) of the peaks does not vary significantly for different conditions. *Table III.2* shows the mass resolution of the peak at 32 a.m.u. corresponding to the mass spectra shown in *Figure III.*23.

*Table III.2: The FWHM mass resolution of the peak at 32 a.m.u. corresponding to the mass spectra shown in Figure III.*23.

	(a)	*(b)*	*(c)*	*(d)*	*(e)*	*(f)*
Sample	*NW*	*NW*	*TF*	*TF*	*TF*	*TF*
Mode	*UV*	*UV*	*UV*	*UV*	*Green*	*Green*
LPE (nJ/pulse)	*1*	*0.5*	*0.5*	*10*	*10*	*50*
m/Δm (FWHM)	*400*	*533*	*457*	*640*	*457*	*400*

As it is presented in *Table III.2***,** no significant influence of the condition on mass resolution is observed, although higher resolution is obtained in UV mode and at higher LPE. Lower resolution in green mode as compared to the UV one for the same sample can be expected as the interaction of green laser with materials involves a deeper interaction and a slower quenching. However, in our experiments, APT of ZnO thin films with green laser at any LPE shows a sufficiently high resolution of mass spectra which was not the case previously shown by Chen *et al. (Figure III.15)* [Chen.Y.M 2011].

As mentioned before, a higher electric field leads to post-ionization of ions creating more doubly charged ions [Kingham 1982]. Since the Kingham curve concerns only pure Zn metal, for the Zn ions in ZnO semiconductor, the determination of Zn charge state ions cannot provide the direct value of the field strength for ZnO sample. Therefore, the Zn^{2+}/Zn^{+} ratio has been chosen as a reliable parameter to indirectly quantify the electric field strength and allowing us to compare APT experiments. Such a ratio is extracted from mass spectra (*Figure III.23*) by comparing intensities of Zn^{2+} and Zn^{+} ions respectively in the 32-35 a.m.u. and 64-70 a.m.u. mass ranges values. One should keep in mind that in all Zn^{2+}/Zn^{+} ratios, the amount of O_2^{+} at the peak 32 a.m.u. is excluded. *Figure III.*24 shows the evolution of the Zn^{2+}/Zn^{+} ratio using UV and green modes at different LPE. For UV laser pulses, the Zn^{2+}/Zn^{+} ratio ranges from ~2.5 to ~4.5 and decreases monotonously with the increase in the LPE. This clearly indicates that the increase in LPE leads to a decrease of the surface electric field at a constant detection rate. In this case, the decrease of the electric field is consistent with the observed decrease of the DC voltage.

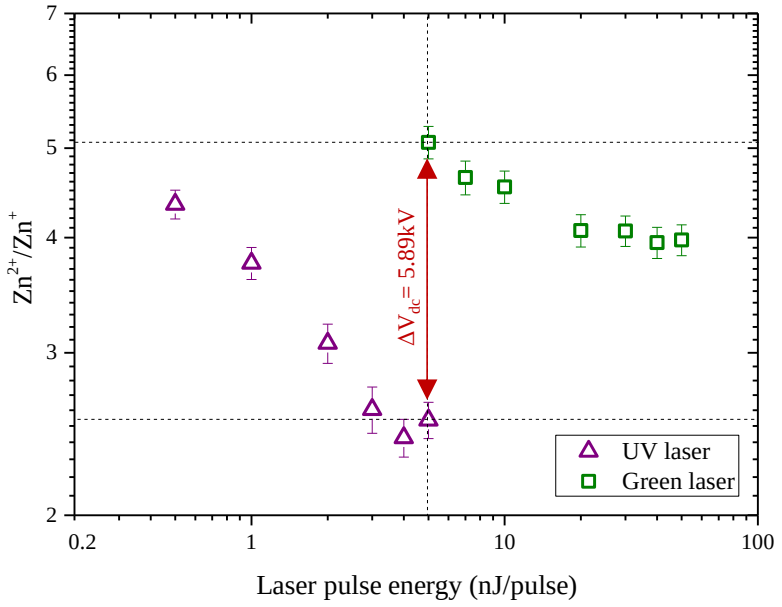

Figure III.24: Influence of LPE on Zn^{2+}/Zn^{+} ratio using UV and green modes. For the same LPE of 5 nJ, green mode provides higher ratio.

In green mode, the Zn^{2+}/Zn^{+} ratio decreases slightly in the range of ~4 to ~5. Green LPE provides a higher Zn^{2+}/Zn^{+} ratio than UV mode at the same LPE value. This indicates the

presence of a higher electric field at the surface of the tip. Considering a lower absorption of ZnO in green mode, a higher DC voltage is necessary in order to achieve the same detection rate as under UV illumination. This translates into a higher DC field and to an increase in Zn^{2+}/Zn^{+} ratio. In the present case, the difference in voltage is measured to ΔV_{dc}=5.89 kV. It can be noted that the further increase or decrease of LPE is not possible in UV and Green modes due to the instrumental limits.

Indeed, for both modes, if the LPE is too low, the continuous voltage induces an electric field higher than the atom field evaporation threshold resulting in an ungoverned field evaporation of atoms and a loss of chemical identification of the ions. If the LPE is too high, some laser ablation phenomena can be observed. From these results we can conclude that, APT analysis at low electric field using green mode cannot be performed whereas the UV mode appears to be more versatile.

III.4.2 Chemical composition measurements

The atomic concentration of the elements can also be obtained simply by assigning each peak of the mass spectra to the corresponding ion and counting the number of atoms of each element associated to the peak.

Figure III.25 shows the evolution of Zn and O concentrations as a function of Z^{2+}/Zn^{+} ratio. The oxygen peak at 16 a.m.u. has been considered as O_2^{2+}.

These measurements have been obtained for three cases: a) ZnO thin film in UV mode, b) ZnO thin film in green mode and c) ZnO nanowires in UV mode. The Zn^{2+}/Zn^{+} ratio has been tuned by changing the laser pulse energy (*Figure III.*24). We evidenced a continuous increase (decrease) of oxygen concentration (zinc concentration) with the increase of Zn^{2+}/Zn^{+} ratio from X_O=33% (X_{Zn}=67%) to X_O=56% (X_{Zn}=44%). The expected stoichiometric measurement (50/50) is achieved at Zn^{2+}/Zn^{+}~3.8.

This condition can only be obtained in UV mode. As mentioned previously, we cannot achieve this condition in green mode due to the continuous evaporation of atoms at very low green laser pulse energies. Moreover, in the same condition of UV LPE and mass to charge ratio, we observe the same behaviour on thin films and nanowires, indicating that sample morphology does not play a role in evaporation. Using the green mode provides the same trend as UV mode

at first, followed by a stabilized value for zinc and oxygen atomic concentrations that is due to the stabilization of electric field mentioned previously (*Figure III.24*).

As it is clear in *Figure III.25*, using UV mode and keeping a Zn^{2+}/Zn^{+} ratio in the range of ~0.2 to ~3.8, results in an oxygen concentration lower than the zinc concentration. This result indicates a loss in detection of oxygen atoms in the APT experiments.

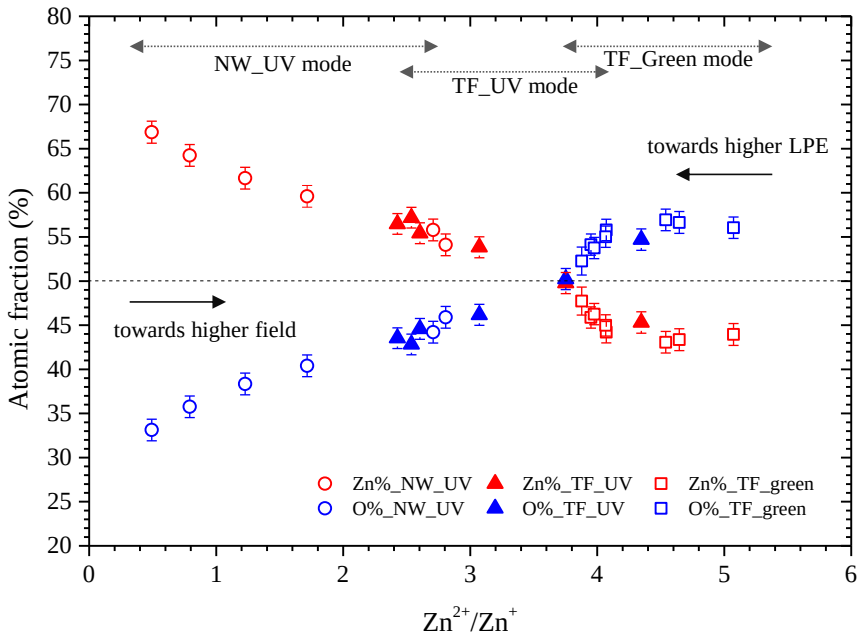

Figure III.25: The comparison of Zn (in red) and O (in blue) composition obtained by atom probe analysis for ZnO pure thin film (TF) using UV mode (solid triangle) and green mode (open square) and ZnO pure nanowires (open circle) at different LPE, as a function of charge state ratio representing the strength of the field on the tip.

For Zn^{2+}/Zn^{+} ratio ranges from ~4 to ~5, for both green and UV modes, we observe the opposite behaviour suggesting a loss of zinc atoms. Our results clearly indicates that APT experiments of ZnO, must be carried out with much care as the measured concentration is strongly dependent on the analysis parameters (laser wavelength, laser pulse energy, and continuous voltage).

Atomic concentrations of zinc and oxygen have been also calculated considering the peak at 16 a.m.u. contains dominantly O^{+} ions. *Figure III.26* shows the atomic fraction of Zn and O for both cases using UV (a) and green mode (b). In this case, the corresponding Zn^{2+}/Zn^{+} value at

which the expected stoichiometry is measured, reduces only to 1-5% lower than the one obtained previously.

These results suggest that in this range of the field strength (in the case we study here), assigning the peak at 16 a.m.u. to either O^+ or O_2^{2+} a.m.u. does not modify the overall behavior of the measured fractions, and yields only minor changes in measured composition. Therefore, in this work, the compositional information is carried out considering the peak at 16 a.m.u. contains only O_2^{2+} ions.

The loss of oxygen by the increase of LPE has been also evidenced in the literature. Santhanagopalan *et al.* have shown this effect on $LiFePO_4$ samples [Santhanagopalan 2015]. They mentioned that an accurate measurement of oxygen content in green mode is possible but such a condition does not provide reliable measurement of Li composition. The chemical compositions appeared to be more accurate in UV mode despite of some oxygen deficiency.

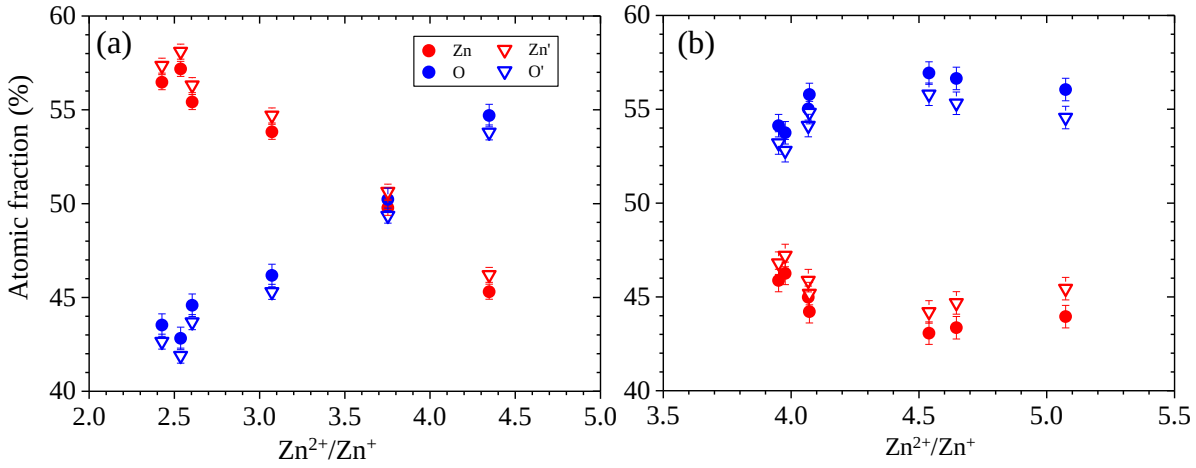

Figure III.26: The composition comparison of Zn (in red) and O (in blue) of ZnO pure thin film (TF) using UV mode (a) and green mode (b) as a function of Zn charge state ratio. Zn' and O' correspond to the compositions considering peak at 16 a.m.u. is dominantly O^+ (open triangle). Solid circle refers to the composition considering 16 a.m.u. is dominantly O_2^{2+} a.m.u.

The dependence of chemical composition on LPE has also been previously observed for MgO [Devaraj 2013], CeO_2 [Kirchhofer 2013], GaN [Riley 2012]. In all cases, the concentrations of the metallic element decreased while the concentration of non-metallic element

increased by increasing the surface electric field (decreasing the LPE). In the case of MgO, this behavior was addressed to the formation of holes localized on the oxygen corners of MgO lattice due to the laser irradiation [Devaraj 2013]. These holes were found to be responsible for the formation of oxygen and magnesium neutrals. The neutral species that are not field ionized would go undetected and therefore result in a loss of these elements. Comparing to O, Mg has a relatively smaller field ionization potential. Hence, it is less likely for desorbed neutral oxygen atoms to be field ionized at lower field. For GaN, the field evaporation of c-axis GaN nanowire is found to be influenced by the formation of N_2 dimers. At high laser energies, sublimation of N_2 leads to the highly Ga-rich measurements [Riley 2012].

In case of zinc oxide, one possible reason can be the difference in field ionization potentials of zinc (~9.39 eV [Gault 2012]) and oxygen (~13.61 eV [Devaraj 2013]). At high laser pulse energies, the surface electric field is strong enough to ionize only zinc atoms and not oxygen atoms leading to the oxygen deficiency. At lower laser pulse energies, the surface electric field is strong enough to ionize oxygen atoms (and/ or oxygen molecules) that can lead to the increase in field evaporation efficiency of oxygen. Moreover very high field can cause continuous ionization and evaporation of zinc atoms between and after pulses that could not be detected.

III.4.3 APT analysis of doped ZnO materials

The results obtained previously for undoped ZnO have evidenced how variation of laser pulse energy and wavelength can significantly deviate the composition of elements from the stoichiometric value. Therefore, APT experiments on doped ZnO with an improper LPE can result in a bias on the concentration of the zinc, oxygen and consequently the dopant. Therefore, we found it crucial to investigate the influence of LPE on dopant concentration of doped ZnO materials. Two different ZnO doped nanostructures were chosen: europium doped ZnO thin films and nitrogen doped ZnO nanowires.

Figure III.27 presents Eu and N dopant concentrations as a function of Zn^{2+}/Zn^{+} ratio where all measurements were carried out at constant evaporation rate using UV mode.

We can observe that Eu concentration decreases with increase of surface electric field (decrease in LPE) as it was previously observed for Zn. On the other hand, the N concentration increases by increasing the field (decreasing the LPE) as seen previously for oxygen.

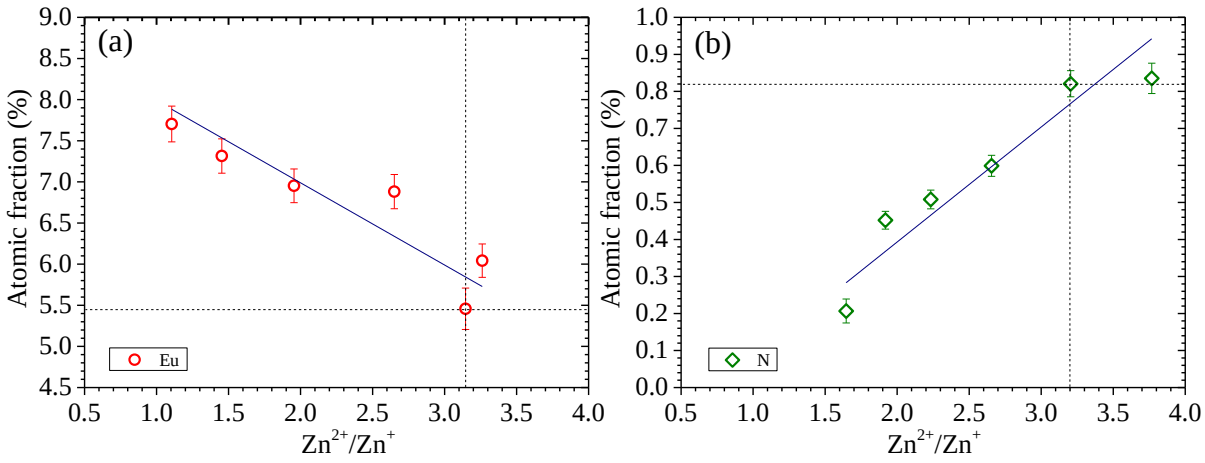

Figure III.27: Atomic composition of two doped samples: (a) Eu doped ZnO thin film and (b) Nitrogen doped ZnO nanowire.

The N-rich measurement at high electric field has also been reported previously [Diercks 2013]. However, in most of the systems such as GaN, MgO, ZnO and CeO, the lower field yields a cation-rich measurement and higher field results in anion-rich measurements. We have realized that the similar behavior of these elements can be associated with their similarity in their electronegativity value and their ability of losing electrons. For most of lanthanides, the electronegativity is of the order ~1.2 which is close to the electronegativity of Zn (1.65) while the electronegativity of O and N are 3.44 and 3.04, respectively [Allred 1961]. The same conclusion can be made for the systems discussed previously. Ga, Mg and Ce exhibiting similar electronegativity values of 1.81, 1.31, 1.12 respectively [Allred 1961] show the same concentration trend as a function of surface electric field. It is worth mentioning that regardless of the morphology of the tip and the APT condition for these two samples, the stoichiometric value for Zn/O was obtained at almost the same value of Zn^{2+}/Zn^{+} which indicates the great importance of laser pulse energy and the resulting surface electric field.

These results can bring confusion about the accurate concentration of the ZnO elements and dopants due to the strong dependence of concentration on the APT parameters. Nevertheless, we have observed that strong deviation of concentration occurs only at high laser energies where the surface electric field is not uniform, as it will be shown in the following. Hence, we suggest that the condition that provides the stoichiometric ratio of Zn/O can be assigned to the correct

measurements and dopant concentration referring to this condition could be considered as the appropriate value. For Eu and N doped ZnO the stoichiometric ratio of Zn/O value is achieved at the Zn^{2+}/Zn^{+} ratio of 3.26 and 3.12 resulting in the Eu and N atomic concentration of about 6% and 0.8 % respectively.

Nevertheless, once APT condition for good quantitative measurements for a particular system is found, we suggest comparing the dopant concentration obtained by APT with other techniques. However, this is not always possible, as for most popular dopants such as the ones studied in this work (REE and nitrogen), common techniques of concentration measurements such as EDX and secondary ion mass spectrometry (SIMS) encounter many limits and hence they cannot provide precise values.

Therefore, for a comparison, we have measured the dopant concentration of an aluminum doped ZnO thin film by both APT and SIMS. Aluminum is chosen as the dopant because its concentration is measurable with other techniques as well as APT. Aluminum doped ZnO films are grown by MOCVD on sapphire substrate (at GEMaC) using Al precursor of trimethylaluminium. ZnO:Al film exhibits a thickness of about 600 nm. The concentration of Al measured by SIMS and APT is shown in *Figure III.28.*

Figure III.28.a shows the SIMS measurement of the sample down to a depth of about 1.5µm carried out at GEMaC laboratory. At a depth lower than 500 nm, the concentration of Al is measured to be about $1x10^{20}$ atm.cm^{-3}. APT was also performed on the same sample. The depth from the surface of the thin film of the APT analyzed volume was about 200 nm. The average Al concentration in the analyzed volume was measured $1.2x10^{20} \pm 0.1x10^{20}$ atm.cm^{-3} which is consistent with the results obtained by SIMS.

Figure III.28.b shows the distribution of aluminum atoms in the analyzed volume. For most Al doped thin films grown on sapphire substrate some variation of Al concentration is also expected due to the diffusion of Al atoms from the sapphire (Al_2O_3) substrate towards the ZnO thin film.

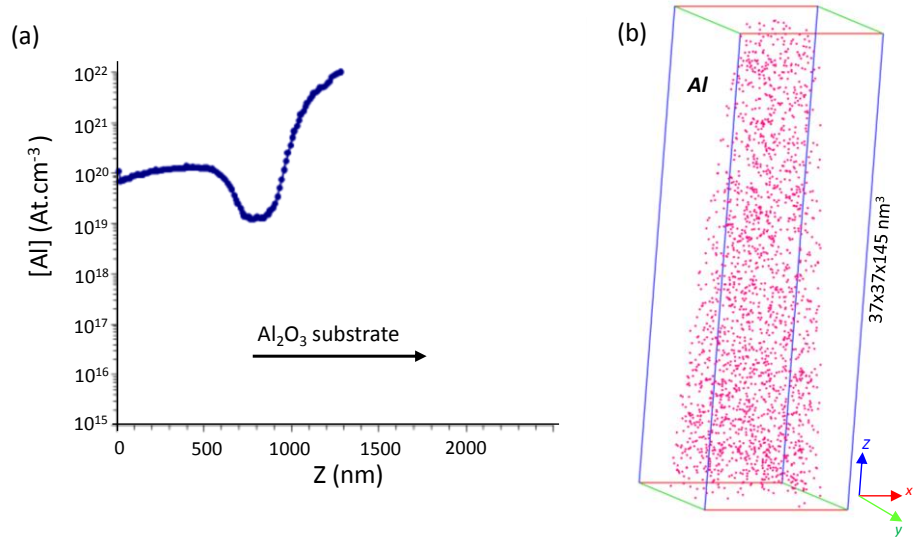

Figure III.28: (a) Aluminum concentration as a function of analysis depth for a ZnO:Al thin film obtained by SIMS (b) Al distribution obtained by APT 3D reconstruction on the same sample.

III.4.4 Surface field distribution

The strong variation in compositions under different laser pulse energies is further studied by tracking the changes in the electric field at the surface of the specimen. Since the surface electric field directly influences the surface atoms, its distribution on the surface becomes very important. Hence, systematic series of laser pulse energies were used for APT analyses on the same specimen. The concentration and the distribution of the surface electric field at each LPE were carried out.

The relative LPE and V_{dc} used are presented in *Table III.3.* The analyses were performed on nitrogen doped ZnO nanowires.

Table III.3: Laser pulse energy values for APT of nitrogen doped ZnO single nanowire using UV laser with the relative V_{dc} at the corresponding LPE values.

	(a)	*(b)*	*(c)*	*(d)*	*(e)*	*(f)*
LPE (nJ/pulse)	*0.5*	*1*	*2*	*3*	*4*	*5*
V_{dc} (kV)	*7.36*	*6.75*	*6.18*	*5.8*	*5.49*	*5.27*

The presence of a uniform or non-uniform distribution of the surface electric field is investigated by plotting the charge state hitmap of Zn charge states at different LPE. Such hitmaps corresponds to the impact of the ions on the detection system.

Hence, it can be used as an indicator of the electric field distribution at the surface of the tip. Thus, it can help us to have a better understanding of evaporation event of the ions and the variation in concentrations.

Figure III.29 presents the hitmaps of Zn charge states and their ratio. Since the peak at 32 a.m.u. contains both oxygen and zinc ions, for a more precise comparison, the peaks related to the maximum zinc isotope at 32 and 64 a.m.u. are excluded and not shown in the hitmaps. These Zn charge state ratio hitmaps are only to provide the information about the surface electric field distribution and thus, they should not be confused with the exact precise values of Zn charge state ratio deduced by peak deconvolution shown previously.

The charge state ratio hitmap also depicts a uniform distribution indicating the surface electric field is uniform. However, as the LPE increases, the uniform distribution of Zn^+ is disturbed strongly. For LPE >2 nJ, the Zn^+ distribution becomes more and more inhomogeneous with a lower detection of Zn^+ in certain zone forming a clear hexagonal shape. The origin of this particular shape is discussed later. The change in the charge-state-ratio reflects the inhomogeneous surface electric field distribution at higher LPE: higher field inside the hexagonal region and lower field out of this region.

However, the distribution of Zn^{2+} does not seem to be affected by the variation in LPE except for the LPE =5 nJ (*Figure III.29.f*).

Quantitative information was carried out by calculating the O and Zn composition and the Zn charge-state-ratio at each LPE (0.5, 1, 2, 3, 4 and 5nJ). The results are presented in *Figure III.30.*

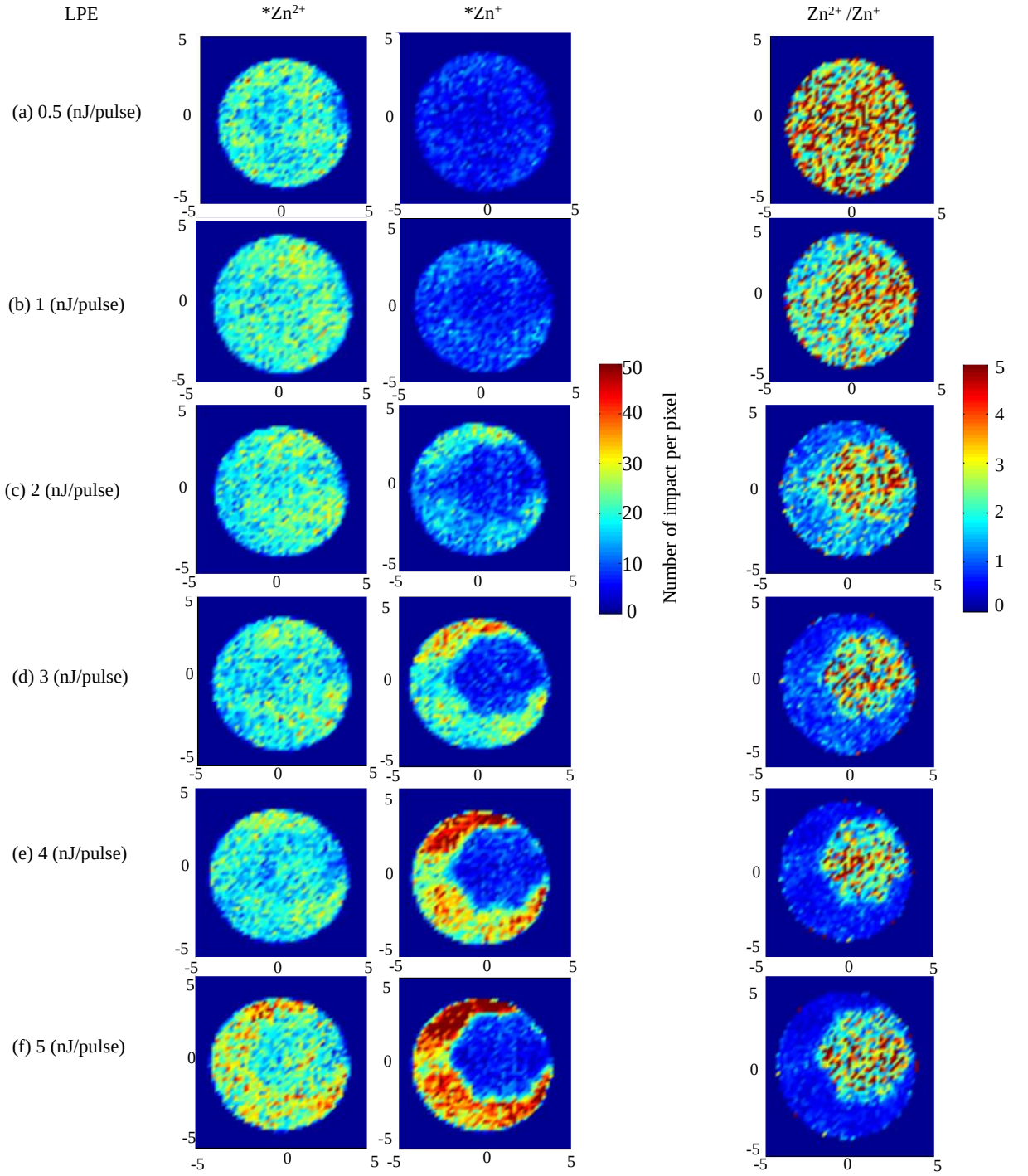

*Figure III.29: APT of nitrogen doped ZnO single nanowire using UV laser. Hitmap of the detected *Zn^{+}, *Zn^{2+} and their ratio (the star indicates that the Zn atoms corresponding to the major isotopic peak is excluded) at the corresponding laser pulse energies and V_{dc} voltage (more details in Table III.3). Increasing the laser pulse energy results in a non-uniform detection of the elements.*

The same evolution of Zn and O concentration as a function of charge state ratio can be observed as it was seen previously for ZnO. The stoichiometric value is obtained for a Zn^{2+}/Zn^{+} ratio of 3.2 (LPE =1 nJ) where both Zn^{+} and Zn^{2+} ions are homogeneously distributed.

Considering the hitmaps and composition evolution by LPE, we can conclude that APT analysis at higher LPE give rise to the non-uniform distribution of the surface electric field and lower detection of Zn^{+} ions in particular zone. The non-uniform field results in the deviation Zn and O compositions from the stoichiometric value. However, in order to investigate the origin of this particular field distribution at high LPE, we only focused on APT analysis performed at 5nJ where this behavior appeared more severely.

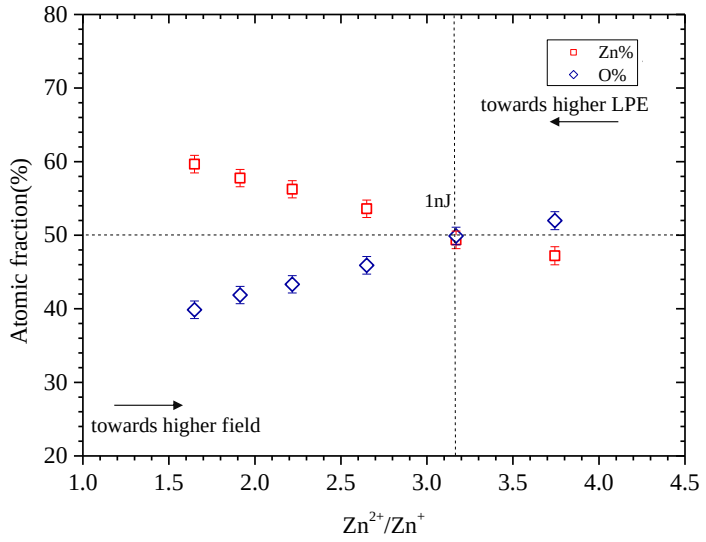

Figure III.30: Atomic fraction of zinc and oxygen obtained at each LPE as a function of charge state ratio. The stoichiometric ratio of Zn/O was obtained at the LPE of 1 nJ referring to the charge state ratio of about 3.2.

Figure III.31.a shows 2D view of the APT reconstructed volume presenting the distribution of Zn^{+} ions collected at LPE of 5 nJ. Each red point represents one detected Zn^{+} ion exhibiting a lower detection of Zn^{+} ions in a clear hexagonal region.

In order to investigate the influence of the crystallographic orientation on this specimen field ion microscopy (FIM) was performed.

FIM imaging was performed using a mixture of Ne and He gas as the imaging gas at the pressure of 10^{-6} bar (0.1 Pa) and the temperature of 80K. Imaging was carried out using UV at

low LPE of 0.1 nJ and a V_{dc} of 8kV. Interestingly, FIM image (*Figure III.31.b)* clearly exhibits a crystallographic pole at the place where a hexagon is observed in APT reconstructed volume. Hence, it brings the interest to investigate the local concentration of the elements in and out of the hexagonal region.

Figure III.31.c presents composition profile of Zn and O measured in the box indicated in the *Figure III.31.a.* It was observed that the field is strongly increased in the hexagonal zone and out of this zone; the field appeared at a very low value of Zn^{2+}/Zn^{+}. Hence, this strong difference in surface electric field results in the Zn/O ratio of about 70/30 at the low surface electric field region, evolving to almost 50/50 in the core region.

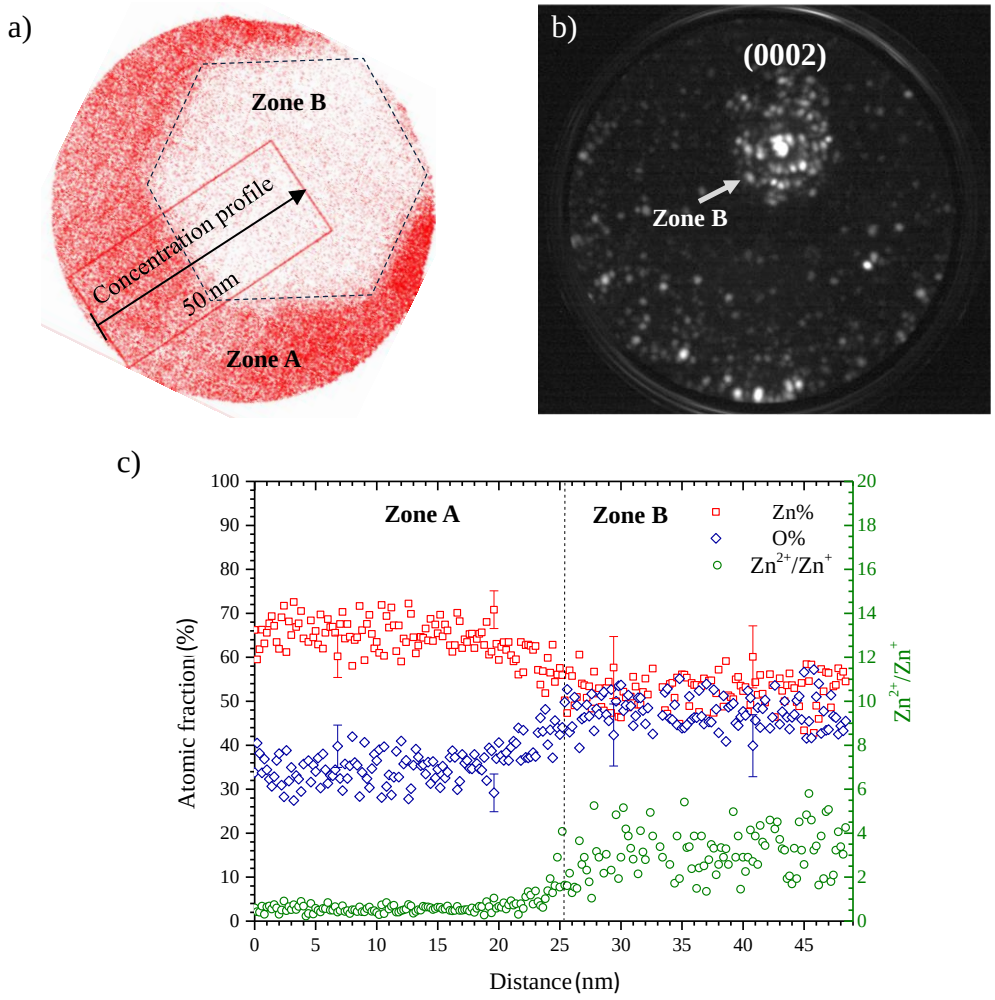

Figure III.31: (a) Distribution of Zn^{+} ions at LPE=5 nJ, (b) Field ion microscopy image of the same nanowire presenting the existence of a crystallographic pole at the place where the highest field is seen (c) concentration profile for a 3D selected zone shown in (a). For clarity reason, only few error bars are shown. Zone A and B refer to the rich and poor Zn^{+} impact areas.

Inside the hexagon region, the electric field is the highest and the measured Zn^{2+}/Zn^{+} is close to the one observed for LPE=1 nJ. Inhomogeneity in the electric field at the surface leads then to a bias in the global composition measurements. However, this inhomogeneity of the surface electric field was not clearly observed on the ZnO thin films.

In order to well understand these phenomena on ZnO nanowires, further investigations in HRTEM and SAED diffraction were performed on a single nanowire of the same sample (shown in *Figure III.32*).

Figure III.32.b shows that the nanowire is well single crystallized in the wurtzite structure with a (0002) growth axis. The FIM image (*Figure III.31.b*) confirms the orientation of the nanowires during the APT analysis.

It can be noted that the observed pole corresponds to the highest electric field region of the entire FIM image. We can then conclude that the hexagonal area (the highest electric field region observed in APT) is correlated to the (0002) crystallographic direction of ZnO.

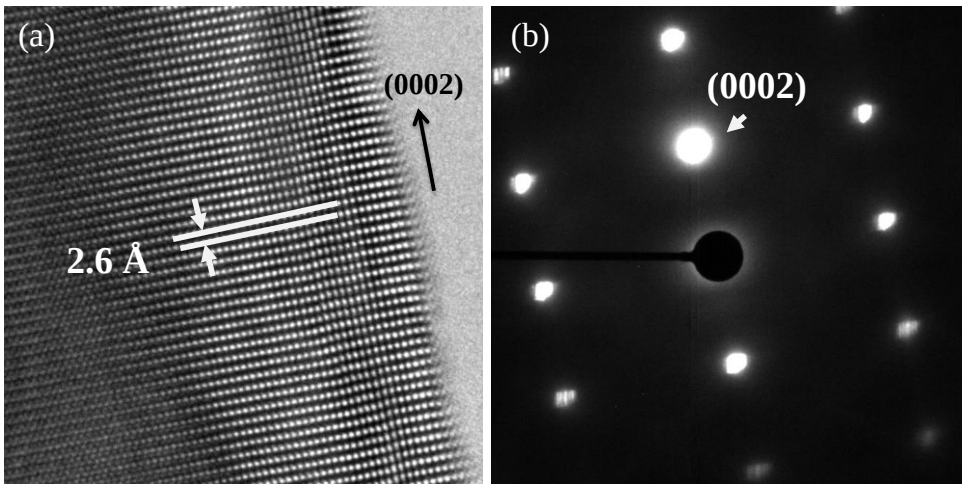

Figure III.32: (a) HTREM and (b) diffraction pattern in zone axis [01-10] of nitrogen doped ZnO nanowire, indicating the preferential growth along c-axis.

These results can suggest that the distribution of the electric field at the tip surface is dependent on the crystallographic direction. Moreover, this dependence becomes accentuated at higher LPE.

In order to understand the crystallographic poles in ZnO, the ball-and-stick model of ZnO stacking layers (zinc and oxygen) is provided (shown in *Figure III.33.a* and *b*).

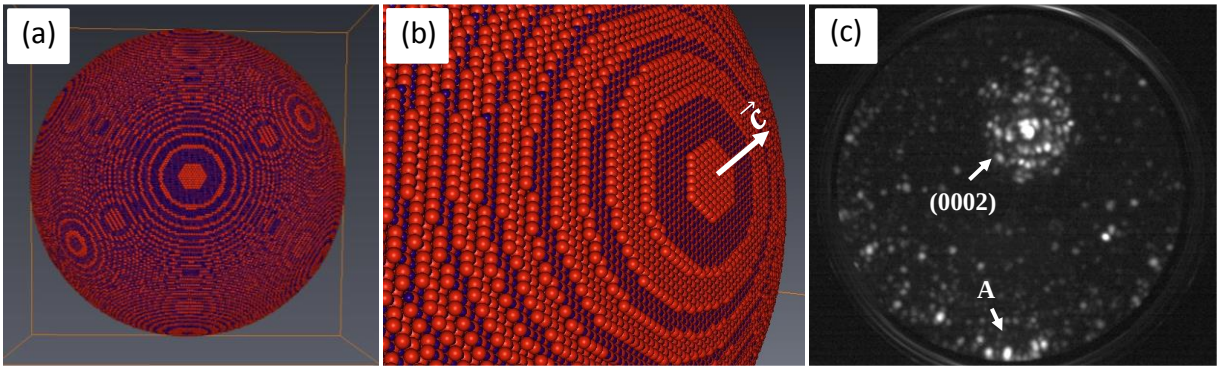

Figure III.33: (a) ball-and-stick model of ZnO stacking sequences of zinc and O along c-axis showing different crystallographic poles (circles with traces), (b) the pole corresponding to (0002) growth direction observed previously by FIM analysis (c).

In this model, ZnO is considered in its hexagonal crystal structure with preferential growth direction along c-axis. The bonds (sticks) are shown in smaller ratio as compared to the balls for clarity. The volume is made by the stacking of Zn and oxygen layers.

The model clearly depicts the presence of several hexagonal crystallographic poles in ZnO (*Figure III.33*.c).

Therefore, the crystallographic poles can clearly influence the surface electric field and cause unreliability in compositional measurements. Nevertheless, this effect is shown to be much more pronounced at higher laser pulse energies. This effect was better observed in APT of nanowires due to their higher crystal quality and mono crystal structure.

III.5 Conclusion

In this chapter the basic principle of atom probe tomography has been explained. Different challenges and approaches to APT specimen preparation have been demonstrated for ZnO thin films and nanowires. In APT of ZnO materials we have observed that, the measured concentrations of oxygen and zinc are strongly dependent on the analysis parameters (laser wavelength, laser pulse energy and continuous voltage). The influence of these parameters has been studied on undoped ZnO nanomaterials as well as on doped one. For both green and UV laser modes (λ=515 nm and λ =343 nm), at fixed evaporation flux, the variation of the laser pulse energy leads to the variation of the surface electric field expressed by the Zn^{2+}/Zn^{+} ratio. This parameter which is accurately measurable in APT experiment was chosen as the pertinent parameter to correlate the variation of the LPE and V_{dc} to the variation of the surface

electric field. We have shown that APT analyses are quantitative for a precise range of surface electric field (Zn^{2+}/Zn^{+} ratio around 3.5) in both UV and green mode. In green mode, the field evaporation of ZnO materials is possible. Nevertheless, the V_{dc} has to be strongly increased (as compared to the UV mode) leading to a high surface electric field. It was observed that decreasing the laser pulse energy creates higher field on the tip and leads to zinc-rich measurements whereas higher laser pulse energies results in oxygen rich-measurements.

The reason behind this behavior is yet ambiguous. However, it can be addressed to the formation of neutral oxygen at lower field which cannot be detected resulting in the oxygen deficiency. By increasing the field, more oxygen atoms are ionized leading to a higher concentration of oxygen. Moreover, at higher field the zinc atoms can evaporate between or after pulses causing lower detection of zinc atoms.

The same variations in concentration have been also observed for Eu and nitrogen doped ZnO nanomaterials. Concentration of Eu dopants was decreased by the increase in the field as it was seen previously for Zn. Nitrogen dopants on the other hand showed the same behavior as oxygen where, by increasing the field, the concentration of the nitrogen increased. However, we have observed the accurate value can be achieved at low LPE, where the surface electric field is more uniform and the stoichiometric ratio of Zn/O can be obtained regardless of the specimen radius size.

We have also observed, in nitrogen doped ZnO nanowires, the crystallographic orientation plays an important role on field evaporation of Zn^{+} ion at high LPE resulting in the deviation from stoichiometric condition. This dependence appeared less important for ZnO thin films.

The experimental results reported here show that, although there are challenges on APT of ZnO materials proper stoichiometric field evaporation can be carried out by adjusting the operating parameters in order to obtain an optimum surface electric field, which can be accessed via the Zn^{2+}/Zn^{+} ratio.

For all systems studied, we have observed a strong influence of the different factors resulted from either ZnO crystal or APT analysis parameters on the quantitative measurements. However, the explanation of the compositional bias needs further experimental investigation for a larger series of ZnO doped materials specifically aimed for quantitative investigation. A good choice of material can allow us to perform quantitative measurements using other techniques (e.g. SIMS) for a comparison.

We suggest that such fundamental studies can be also applied for other semiconducting materials where the electronegativity of the cations and anions are close to the one of Zn and

O respectively. This fundamental study can help the atom probe and materials science community to perform more reliable analyses and to harvest all the advantages that atom probe tomography technique can offer.

CHAPTER IV Towards p-type ZnO nanowires

As it was mentioned in the first chapter, the main obstacle in commercializing ZnO for optical and electrical means is providing a high quality p-type ZnO. Despite many reports on the successful p-type doping of ZnO, the choice of dopant and growth technique remains controversial and the reliability of p-type ZnO is still under debate. Even if long-lasting and robust ZnO-based devices are ever to be produced, the quality of layers has to be yet improved. Thus, in this chapter we report an investigation of ZnO nanowires doped with different popular acceptors: nitrogen and phosphorous, using MOCVD growth technique and *ex-situ* doping of pure ZnO NWs, respectively. Once we are able to achieve p-type ZnO nanowires, a ZnO homo-junction can be built by deposition of p-type ZnO on top of the n-type ZnO. *Figure IV.*1 shows the different steps for fabrication of 1D ZnO p-n homo-junction.

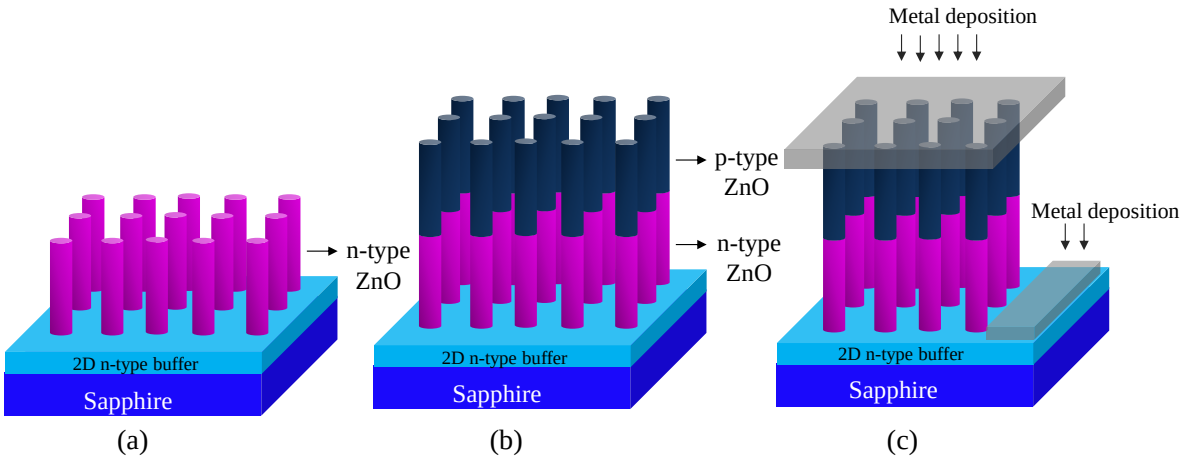

Figure IV.1: Schematic view of preparation process of 1D ZnO p-n homo-junction,(a) vertically aligned n-type ZnO nanowires are grown on sapphire substrate covered with a ZnO buffer layer, (b) p-type nanowires are deposited on top of n-type nanowires, (c) metallic contacts are then grown on n-type zone and p-type zone as bottom and top electrodes.

Therefore, the goal of this chapter is to investigate the success of the two growth methods used for the synthesis of p-type ZnO nanowires by PL, TEM, Raman and APT. The application of the PL and Raman spectroscopy has been dated long back and been widely used. However, such techniques suffer from many instrumental limits or they are limited to certain nanostructures and thus, they are not always able to explain all the observed properties in the fabricated ZnO. For device application, information about the concentration and

distribution of dopants are very important issues that affect the device operation and thus, should not be neglected. Using atom probe tomography technique allows us to investigate the incorporation of the dopants in ZnO nanowires beyond the limits of conventional techniques. Hence in this work, we combine the information obtained by atom probe tomography with the results obtained by conventional techniques in order to provide comprehensive information about the incorporation of dopants in ZnO. Such studies can directly reflect the failure or success of each doping process used in this work.

IV.1 Phosphorous *ex-situ* doped ZnO nanowires

In the framework of the ANR MADFIZ project[1], undoped ZnO nanowires prepared by MOCVD at GEMaC laboratory were doped at CEA-LETI laboratory using spin on doping (SOD) method. Nevertheless, as it was discussed in II.1.3, this technique is mainly known for thin films. Previously, Jang *et al* have attempted to prepare p-type bulk ZnO using phosphorous diffusion from a zinc phosphide source (Zn_3P_2) in a closed ampoule system [Jang 2005]. In our work, we apply this diffusion method for *ex-situ* doping of the pure ZnO nanowires. As this doping process involves diffusion of dopants, the use of nanowires can offer a great advantage due to their large surface to volume ratio. The incorporation of dopants was further explored by atom probe tomography. *Figure IV.2* shows different steps of the doping process.

The pure ZnO nanowires grown by MOCVD (*Figure IV.2.a*) are doped by spin-on-doping method where a commercially available phosphorous doped glass (Accuspin P-8545 from Honeywell[2]) was deposited by spin coating on ZnO NWs (*Figure IV.2.b).*

A volume of 100 µl of dopant source was used for a 2 in. wafer. The rotating speed during the deposition was fixed at 200 rpm initially and then increased to 2000 rpm to increase the thickness of deposited layer. In order to allow phosphorous atoms diffuse in ZnO NWs, the samples were annealed at two different temperatures, 750°C and 850°C for 4 hours under nitrogen ambient (*Figure IV.2.c).*

[1] French National Agency project Nos. MADFIZ ANR-11-NANO-0013.
[2] Phosphorus doped silicon oxide polymers designed for SOD doping

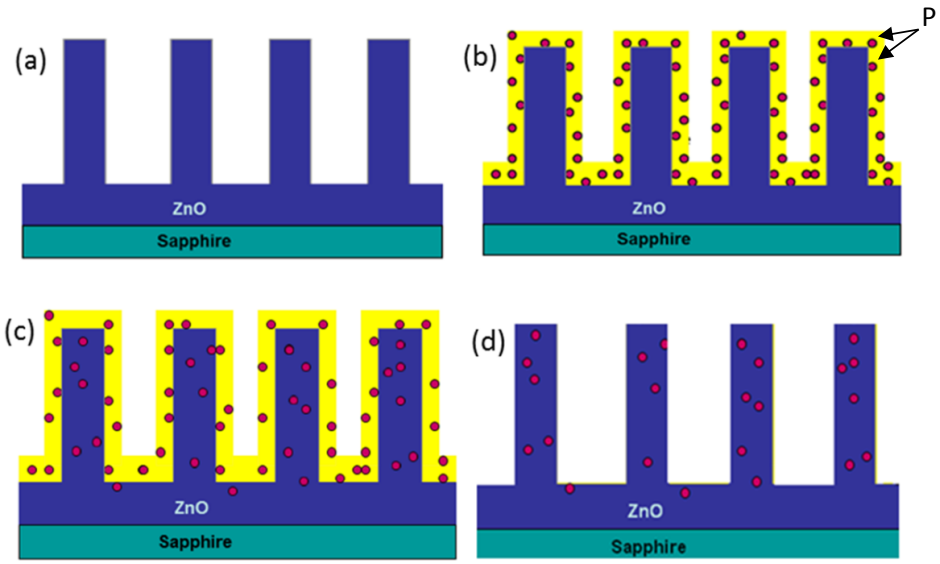

Figure IV.2: schematic of ex-situ phosphorous doping process of ZnO nanowire by spin-on doping. (a) pure ZnO NWs grown by MOCVD, (b) doping NWs by spin on coating, (c) annealing at 750 and 850°C and diffusion of the P atoms, (d) removing the coating layer by reactive ion etching.

Considering the phosphorous diffusion in ZnO at 550 °C is $D_p=5.6x10^{-13}$ cm^2/s [Jang 2005], we are able to roughly calculate the diffusion length (L_d) for phosphorous atoms in ZnO using a simple approximation of $L_d=(4D\tau)^{0.5}$. Hence for diffusion time of 4 hours (τ) the diffusion length is estimated to be about 1800 nm. This diffusion depth thus, should be sufficient to produce an entirely doped ZnO nanowire with a diameter smaller than 1800 nm. During annealing at the applied temperatures here, a strong deformation and bending of the ZnO nanowires was observed. Therefore, to protect the nanowires from deformation, after SOD doping process, some nanowire samples were coated by a very thin SiN layer of about 10 nm.

Figure IV.2.d shows the last step of doping process involving the removal of coating layer from all the nanowires samples. CHF_3 reactive ion etching (RIE) was used in order to remove the doped coating layers of all samples and SiN layer (if it was applied). Hence in this work, doped nanowire samples refer to the ones after 3 steps of SOD doping process: Spin-on-coating, dopant diffusion upon annealing and RIE etching process. *Table IV.1* shows the list of the investigated phosphorous doped ZnO nanowire samples. All doped samples are annealed and etched.

Table IV.1: List of the investigated samples grown by MOCVD and doped by spin on doping process.

Sample Reference	Phosphorous doped	Annealed Temperature (°C)	SiN coating layer	Etched
P1	*No*	*No*	*No*	*No*
P750	*Yes*	*750*	*No*	*Yes*
PSiN750	*Yes*	*750*	*Yes*	*Yes*
P850	*Yes*	*850*	*No*	*Yes*
PSiN850	*Yes*	*850*	*Yes*	*Yes*

Since the application of this p-type doping process for ZnO nanowire is very new, different characterization techniques have been used to study the presence and distribution of the dopants.

IV.1.1 Morphology of nanowires

Prior to investigate the properties of doped nanowires, it is important to know the morphology of the undoped nanowires. The TEM and SAED images of undoped ZnO nanowires grown by MOCVD are shown in *Figure IV.*3. The TEM image of undoped ZnO nanowire shows the hexagonal facets typically observed for ZnO nanowires with wurtzite structure along c-axis grown.

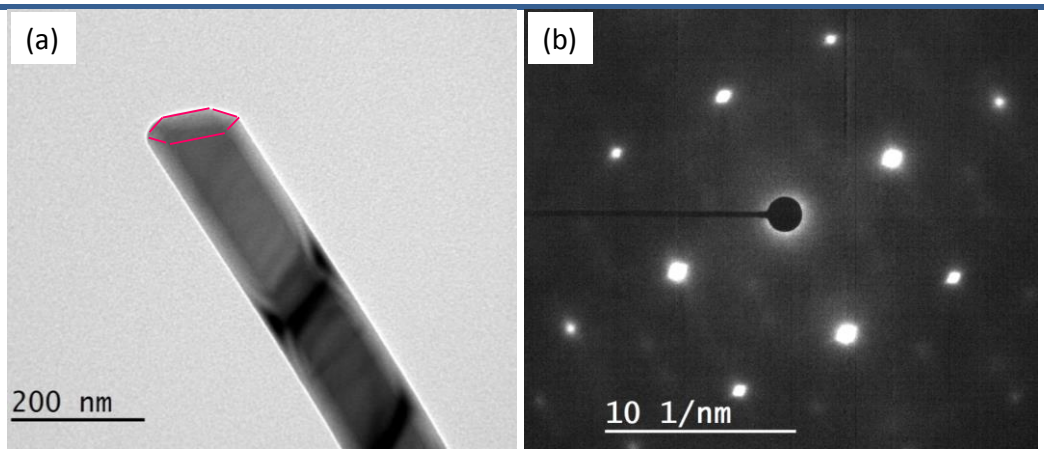

Figure IV.3: (a) TEM image of the undoped ZnO nanowire exhibiting a hexagonal facet, (b) SAED image of the nanowire.

Figure IV.3.b shows that nanowires are monocrystalline with a preferred growth direction along c-axis.

Figure IV.4 shows the SEM images of the nanowires after doping, annealing and etching process (PSiN750). The nanowires have about 4 µm length with sharp edges on the top which is generally due to the etching process. Some nanowires are slightly bent due to the annealing process.

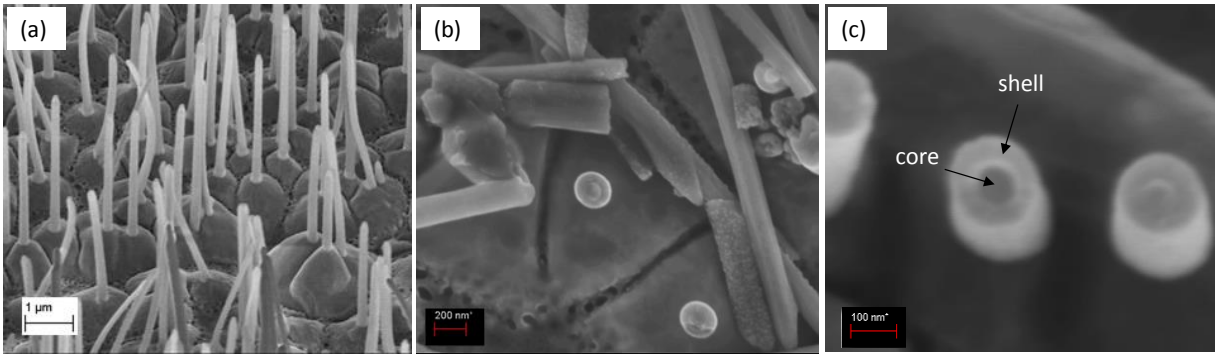

Figure IV.4: SEM image of ZnO nanowires after doping with phosphorous (a) overall view at 45°, (b) core-shell structure have been observed at the interior section of a nanowire, (c) shows a magnified view of this core-shell structure.

A better insight into the morphology of nanowires can be observed in *Figure IV.4.b*. presenting the cross-section of some nanowires. Details of the cross-section reveal a core-shell structure (*Figure IV.4.c*). The morphology and origin of this core shell structure is further studied by TEM and EDX measurements. *Figure IV.*5 shows the TEM and STEM images of the undoped and phosphorous doped nanowires.

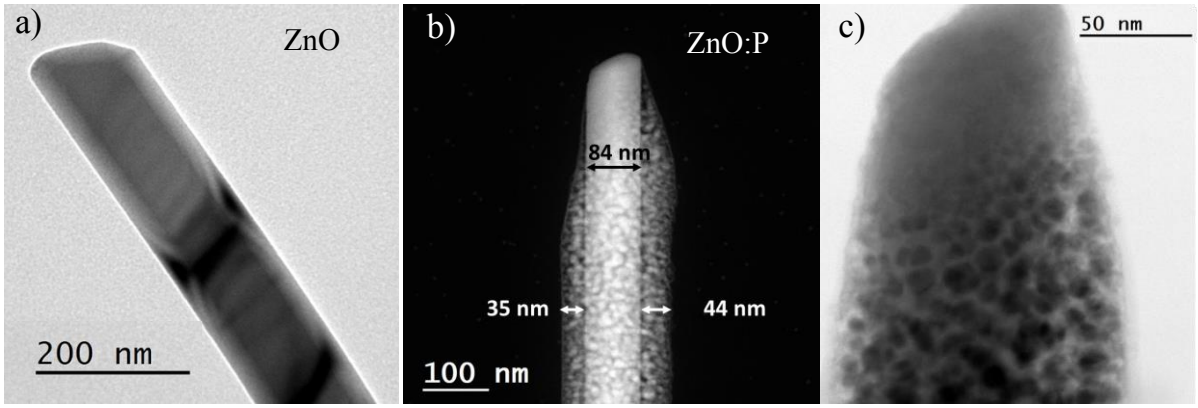

Figure IV.5: TEM and STEM images of ZnO nanowires, (a) before doping, (b) after doping, annealing and etching (c) a magnified image of the top section of the nanowire after doping process.

Figure IV.5.a, shows an undoped ZnO nanowire before doping process. The undoped ZnO nanowires throughout the sample exhibit a diameter varying between 120 to 200 nm. After SOD process, the diameter of the nanowires significantly decreased. TEM images of the doped ZnO nanowires (PSiN750) reveal a much smaller diameter for the doped nanowires. A core-shell structure with a very porous shell, a few tens of nanometer thick, was also revealed confirming the SEM observations. The core exhibited a smaller diameter than the undoped nanowire as it is indicated in *Figure IV.5.b*. The pores were found to have a diverse diameter size in the range of few nanometers to about 15 nm.

However, the main question is, "what is the origin of this porous layer?''. Since the doped nanowires after etching exhibit smaller diameter than the one of undoped nanowires, this reduction in diameter size can be referred to the strong etching process during which both SiN and SOD coating layers are removed entirely. One can extrapolate that further etching could cause additional removal of the ZnO nanowire surface forming a porous layer.

To support this hypothesis, EDX mapping has been carried out on both core and shell sections of the nanowires seen previously in *Figure IV.*5.*b*. The chemical maps are presented in *Figure IV.*6. The EDX mapping shows that the shell consists of only zinc and oxygen. No silicon or nitrogen was detected. This proves that the coating layers are removed entirely and a long etching process caused further removal from the ZnO nanowire surface forming a damaged porous layer.

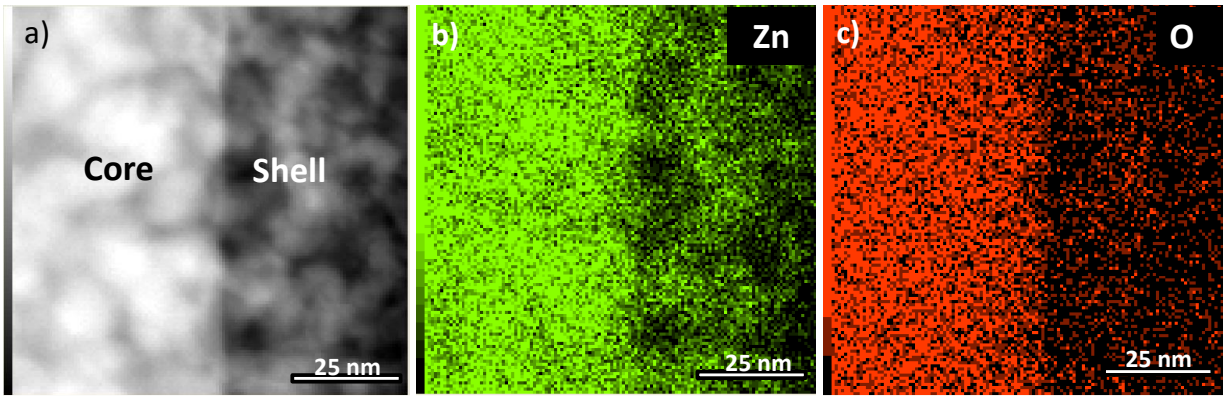

Figure IV.6: EDX mapping of elements in a single PSiN750 nanowire, (a) STEM image of the selected area, (b) and (c) zinc and oxygen distribution respectively.

IV.1.2 Raman spectroscopy

In order to investigate the presence of phosphorous dopants, Raman spectroscopy measurements were carried out at GEMaC laboratory. The results are shown in *Figure IV.7*.

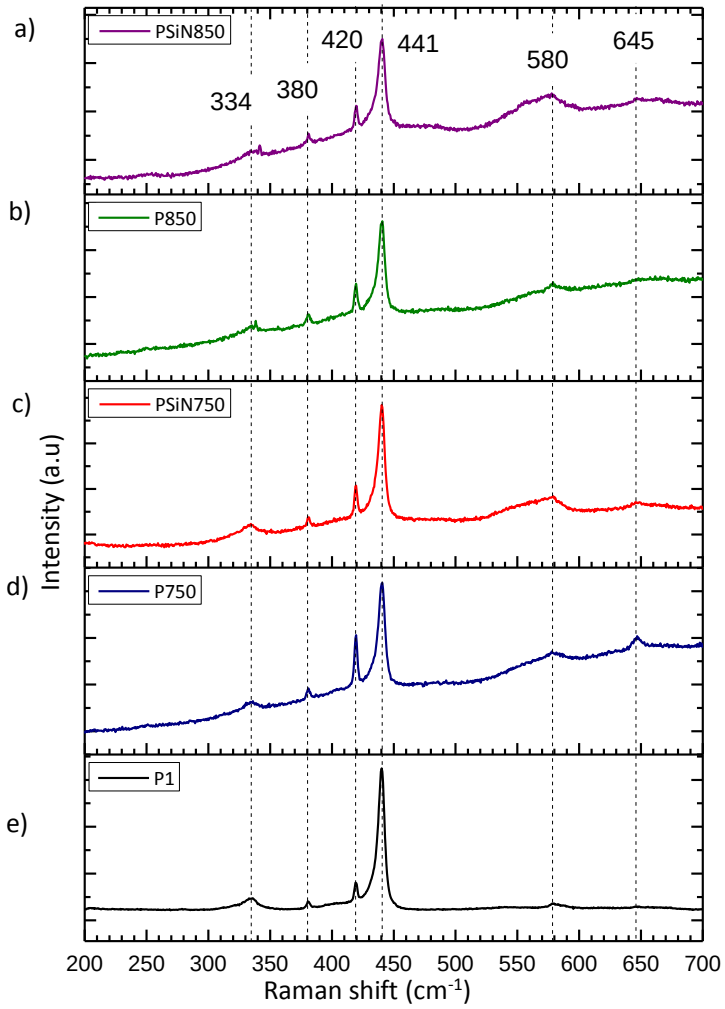

Figure IV.7: Raman spectra of the ZnO nanowires for pure and phosphorous doped ZnO nanowires.

Raman spectra of the samples exhibit the typical vibrational modes of ZnO. The peak at 441 cm^{-1} is assigned to the E_2 (high) mode which is the main vibrational mode in ZnO and its high intensity generally reflects the high crystallinity of the ZnO material. The peak at 382 and 420 cm^{-1} are placed near the frequency positions of A_1(TO) and E_1(TO) respectively (*Table II.3*).

The small peak observed at 333 cm^{-1} is assigned to the multiple-phonon-scattering process which usually occurs in ZnO thin films as well [Kaschner 2002 - Kerr 2007]. The origin of the vibrational mode at 580 and 645 cm^{-1} is controversial and it is ascribed to the

presence of nitrogen or to intrinsic host lattice defects. The peak at 645 cm^{-1} can be observed only for the samples P750 and PSiN750 which previously have been assigned to the presence of nitrogen [Kaschner 2002 - Kerr 2007]. However, Friedrich *et al.* have shown that the incorporation of nitrogen in ZnO exhibits a peak at about 275 cm^{-1} which is not the case in our samples [Friedrich 2007]. The origin of these two peaks will be discussed further in section IV.2.2.

In order to investigate the incorporation of phosphorous atoms in ZnO, Raman spectra of doped samples can be compared to the undoped one. In this case, we can clearly see that no significant change in the Raman spectra is observed after doping process. The classical ZnO vibrational modes observed for undoped ZnO are present for ZnO:P nanowires as well and no new vibrational modes is revealed which brings doubt to the effective presence of phosphorous atoms in ZnO nanowires.

IV.1.3 Photoluminescence

Photoluminescence for long has been known as a sensitive technique for investigation of impurities in ZnO matrix. Low temperature PL (2K) measurements were carried out on all doped and undoped samples and the results are shown in *Figure IV.*8.
For clarity, the spectrum is divided into two ranges: 2.90-3.30 eV (*a, b, c, d* and *e*) and 3.30-3.40 eV (*f, g, h, i* and *j*).

In a typical PL spectrum of ZnO, a broad band centered on 2.45 eV extending from blue to the green range is commonly seen. This peak was not observed in our samples. However, in the range of 2.90-3.30 eV (*Figure IV.8.e*), several peaks can be observed for undoped nanowires at 3.12, 3.29, 3.245 and 3.291 eV. For doped samples, these peaks disappeared entirely after doping process. Since doped samples are annealed at high temperatures, it is likely that these peaks are related to the presence of the defects which were healed by annealing. For pure ZnO, the longitudinal optical phonons replicas of the BE are expected in the range of 2.9 eV to 3.3 eV. In this range it is also possible to find shallow donor to shallow acceptor recombination (DAP) if sufficient amount of shallow acceptor is present which is not the case in our studied samples.

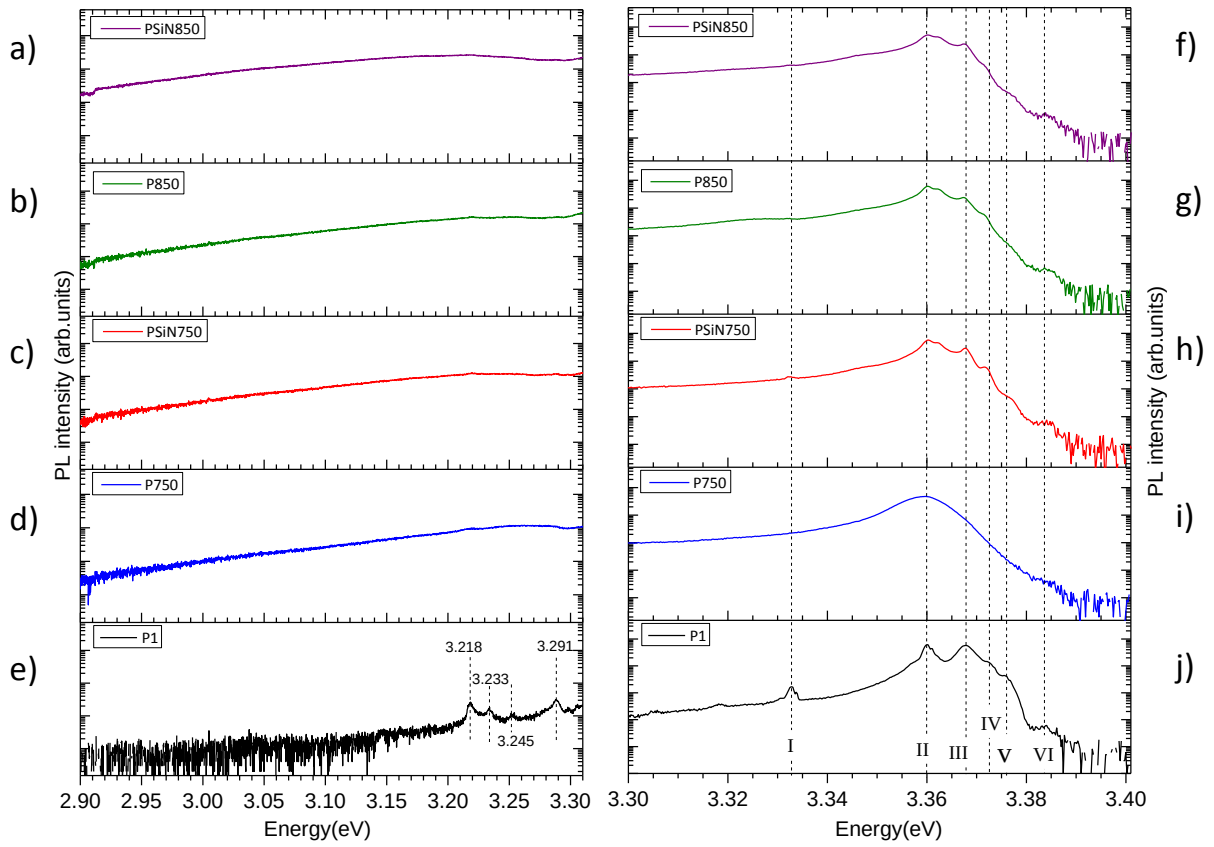

Figure IV.8: PL spectra of ZnO phosphorous doped samples (a,f) P1 pure ZnO nanowires, (b,g) P750 , (c,h) PSiN750, (d,i) P850 and (e,j) SOD PSiN850.

In the range of 3.30-3.40 eV (*Figure IV.8.j*), six peaks can be observed for pure ZnO nanowires. Recombination of excitons that are bound to structural defects can generate a prominent transition called Y_0 around 3.333 eV and also Y_1 seen at 3.336 eV [Meyer 2004 - Wagner 2010]. The Y_0 line was only observed for pure ZnO and it disappeared after SOD doping. The peaks appearing in the range of 3.355-3.375 eV are attributed to the transition of the excitons bound to the impurities. There is no definite assignment of all these bound excitons recombinations to a specific donor or acceptor; they are numbered I_0 to I_{10} in Reynolds *et al*. [Reynolds 1965]. Over the years, up to 20 different bound exciton transitions were reported and an extension of additional letters were introduced (I_{6a}) [Meyer 2004]. A list of common transitions in ZnO is provided by Meyer *et al*. [Meyer 2007 - Meyer 2004 - Meyer 2010]. In *Figure IV.8*, the main peaks observed for undoped ZnO are also present for doped ZnO nanowires except for the sample P750. In the PL spectrum of sample P750, we can see that a broad peak centered at about 3.360 eV replaces the peaks observed for other samples. The reason behind this event is not clear but it can be due to the change in crystal quality by annealing or incorporation of phosphorous atoms that will be further investigated in the

following. Since no significant change in PL spectra was observed after doping, the conclusion about the presence of the phosphorous atoms in ZnO nanowires cannot be confirmed by PL.

*Table IV.2: Exciton recombination energies and related properties for samples N1, N2, N3 and N4deduced from Figure IV.*19.

Energy (eV)					*Exciton*
P1	*P750*	*PSiN750*	*P850*	*PSiN850*	
3.218					*defects*
3.233					*defects*
3.245					*defects*
3.291					*defects*
I = 3.333					*Y_0-line [Meyer 2004]*
II= 3.360	*3.360*	*3.360*	*3.360*	*3.360*	*I_6 [Wang 2006]*
III= 3.368		*3.368*	*3.368*	*3.368*	*I_2 [Meyer 2004]*
IV= 3.372		*3.372*	*3.372*	*3.372*	*I_1 [Wang 2006]*
V= 3.371		*3.375*	*3.375*	*3.375*	*FX_A*
VI= 3.384	*3.384*	*3.384*	*3.384*	*3.384*	*FX_A*

The peaks that appear above the energies of the bound excitons, are related to the free exciton luminescence observable between 3.375 eV and 3.440 eV. The peaks observed in PL spectra and their origins according to the literature are summarized in *Table IV.2*.

Relying on the results obtained by Raman and PL, a thorough conclusion about the incorporation of the phosphorous cannot be obtained.

Hence, using APT can provide important information about the presence and the distribution of the dopants.

IV.1.4 Atom probe tomography

The first APT attempts, have shown unusual and ungoverned field evaporation during the experiments. The mass spectrum and the 3D reconstruction of the doped nanowire is shown in *Figure IV.9,* where both distribution of the atoms and mass spectra did not appear as it was expected.

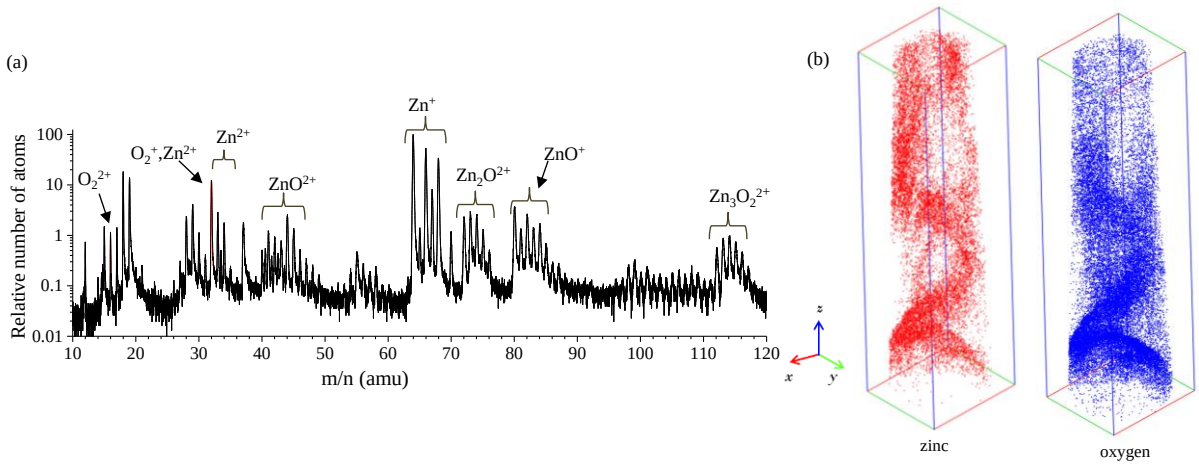

Figure IV.9: (a) APT mass spectrum of ZnO:P nanowire, only defined ZnO related peaks are indicated, (b) 3D distribution of zinc and oxygen atoms in an analyzed volume of 30x30x60 nm^3.

In the mass spectrum of the analyzed nanowire, the peaks related to the ZnO can be observed. Phosphorous is a monoisotopic element with an expected peak at 31 and 15.5 a.m.u. corresponding to P^+ and P^{2+} ions, respectively. A small peak at 31 a.m.u. is observed in the mass spectrum. However, since many extra peaks can also be observed (which we could not assign to a certain element), we assume their appearance as well as the one observed at 31 a.m.u. to be due to the unusual field evaporation. The volume reconstruction of the analyzed sample also shows an unusual distribution of the atoms. It should be noted that the analyzed nanowires originated from a small diameter (<150 nm) of nanowires, therefore the APT was directly performed on the nanowires without annular milling process.

Thus, the unusual field evaporation during APT experiment can be assigned to the presence of the highly porous surface observed by TEM. This porous structure can result in a non-uniform field distribution on the APT tip surface and consequently a non-uniform field evaporation of the elements. The 3D reconstruction of the analyzed volume (*Figure IV.9.b)* also confirms that we have analyzed the porous section of the nanowire probability due to declination of the tip. Hence, further APT analysis was carried out to provide the information from the core of the nanowires.

APT was performed on each of the four doped samples: P750, PSiN750, P850 and PSiN850. In order to avoid the uncontrollable field evaporation of the atoms due to the presence of the porous layer, annular milling of the nanowire before APT analysis can be used. In most cases a proper mounting of the nanowire during APT specimen preparation can help to analyze only the core of the tip. *Figure IV.10* shows the atom probe tomography analysis of PSiN750 nanowire. No annular milling was applied in this case (*Figure IV.10.a*).

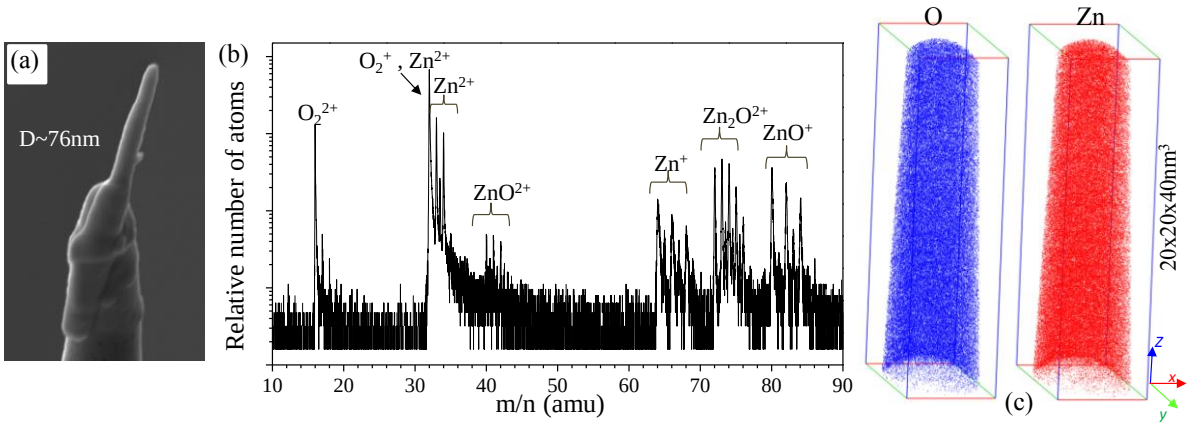

Figure IV.10: Atom probe tomography of (a) un-milled PSiN750 nanowire and the obtained (b) mass spectrum and (c) 3D distribution of O and Zn (shown in blue and red respectively).

A good resolution mass spectrum (*Figure IV.10.b*) was obtained and no porous layer has been observed in 3D reconstruction of the analyzed volume (*Figure IV.10.c*). Since the surface area of the APT analyzed volume is smaller than the nanowire diameter, the absence of the porous layer reflects that the 3D reconstruction of analyzed volume corresponds only to the core of the nanowire. Such APT results are important as they contain information directly from the core of the nanowires. The mass spectrum obtained by APT of the nanowire core (*Figure IV.10*) reveals no peak related to the presence of the phosphorous showing that the diffusion did not occur in the core of nanowires.

For a better comparison, APT was also carried out on a P750 nanowire that was previously annular milled in order to insure that porous layer is removed from the tip. *Figure IV.11.a* shows the corresponding mass spectrum of the nanowire.

No peak related to the presence of phosphorous can be observed. In the m/n range of 22-32 a.m.u. (*Figure IV.11.c*), some extra peaks are revealed. The peaks at 28, 29 and 30 a.m.u. are related to N_2^{2+}, N_2H^+ and NO^+. The use of N_2O as O precursor in the growth of undoped nanowire can be the result of this unintentional incorporation of the nitrogen atoms. The peak at 23.5 a.m.u. could be ascribed to the PO^{2+} molecular ion. However, this assignment is doubtful as no other P-related peaks appeared in the mass spectrum.

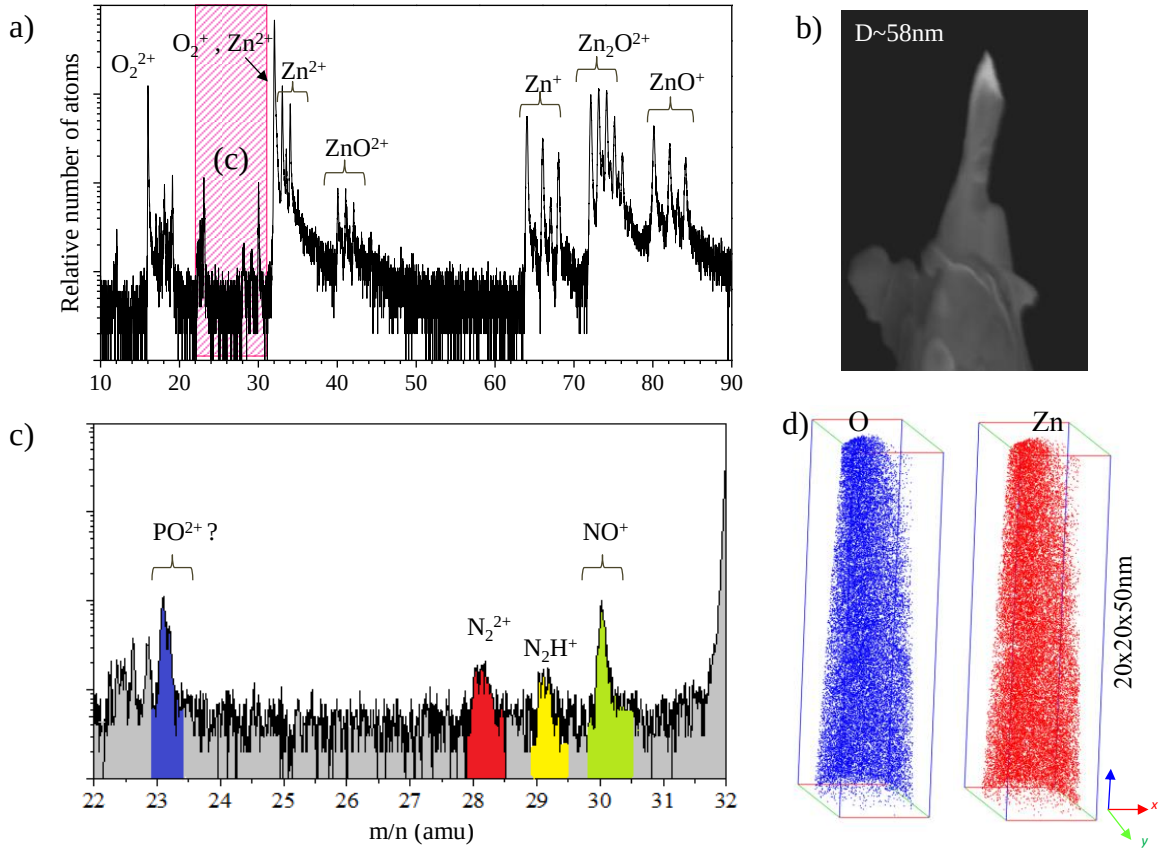

Figure IV.11: APT analysis of a milled P750 nanowire, (a) mass spectrum in the range of 10-90 a.m.u. of a milled nanowire shown in (b), (c) magnified view of the spectrum at the range of 22-32 a.m.u., (d) 3D distribution of Zn and O atoms in the analyzed volume.

APT experiments were carried out on all the samples repetitively to have a good statistics of the samples composition. Similarly as we have observed for the nanowires previously (*Figure IV.10* and *Figure IV.11*), no presence of phosphorous was observed indicating that even annealing at 850°C could not provide any significant change in doping process.

EDX spectra of these nanowires were carried out. The EDX was performed on three different zones of the nanowire: top, middle and bottom sections. Unfortunately, EDX spectra of none of the nanowires could reveal the presence of the phosphorous atoms. *Figure IV.*12 shows the EDX spectra obtained for the zones on top and the middle of one of analyzed P750 nanowires. No phosphorous was found in these regions.

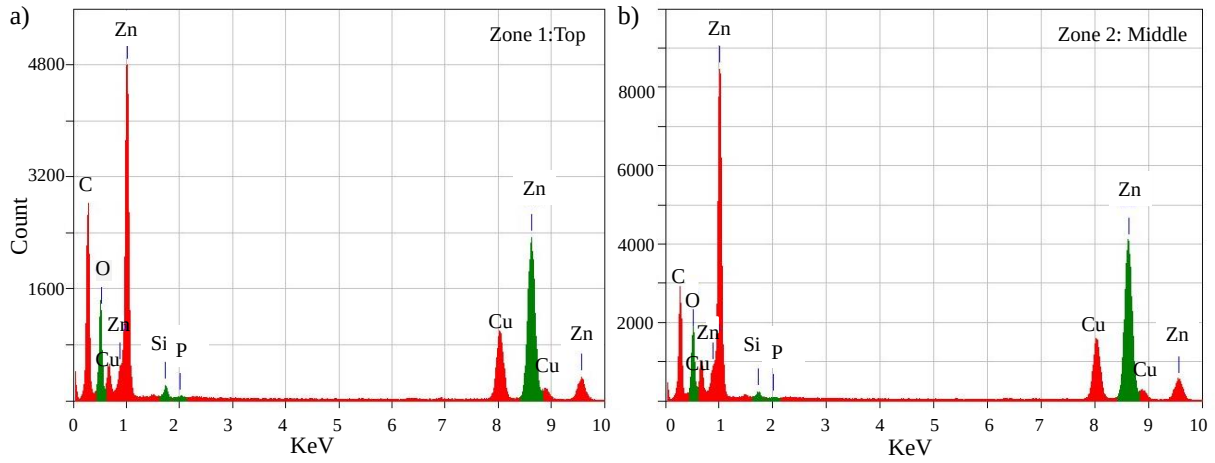

Figure IV.12: The EDX spectra of ZnO SOD 750 nanowire for different zones, (a) top, (b) bottom of the nanowire. The signals related to the Cu and C are caused by the sample holder.

Nevertheless, surprisingly, the EDX spectra on the bottom of the nanowire, has shown the presence of the phosphorous as it can be seen in *Figure IV.13.a*. The EDX mapping of the analyzed zone shows that the phosphorous can be found most probably on the very bottom of the nanowire, closer to the wetting layer. The reason why we could find phosphorous at the bottom of this nanowire is very interesting since it can help us to understand the dopant diffusion process. It is likely that the diffusion has not occurred entirely throughout the nanowire meaning that the real diffusion length was shorter than our estimated value probably caused by using not a precise diffusion coefficient value. As the etching was found to be stronger on top of the nanowire than its bottom, we can assume that the etching process removed the doped region of the nanowires mostly on the top of the nanowires. Hence, possibly, there is a higher chance that the phosphorous is present at interface of the nanowire and the wetting layer which were less affected by etching process. In order to support this idea, APT was performed on the wetting layer of the same series of nanowires (P750).

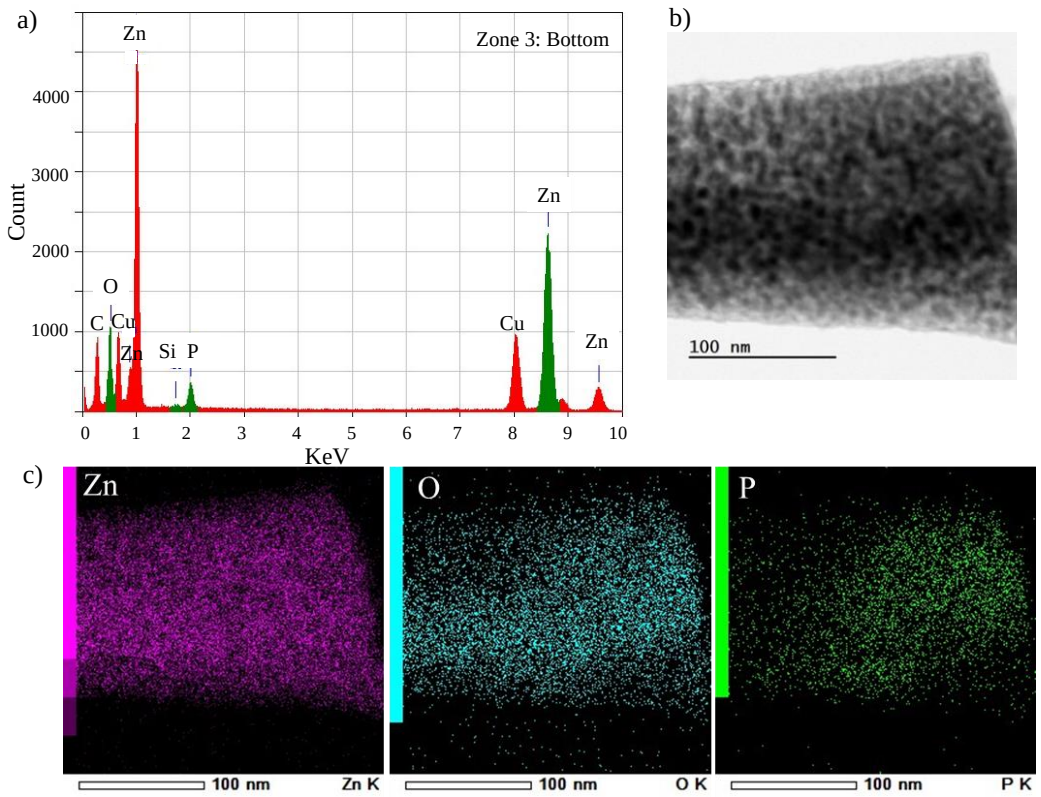

Figure IV.13: (a) EDX spectra of the bottom zone of the phosphorous doped nanowire, (b) TEM image of the selected area, (c) from right to left zinc, oxygen and phosphorous distribution respectively.

Figure IV.14 shows the APT results on the wetting layer of the nanowires. The mass spectrum presents the typical peaks of pure ZnO materials. In contrary to our assumption, no presence of phosphorous dopant was found.

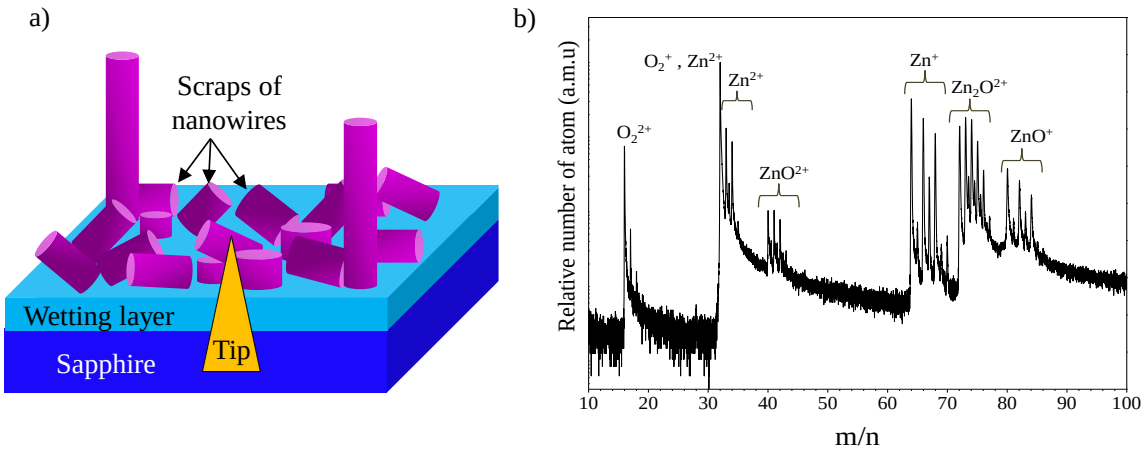

Figure IV.14: (a) a schematic view of the selected area for APT specimen preparation, (b)mass spectrum obtained by APT of the wetting layer.

From the results obtained for *ex-situ* phosphorous-doping of ZnO nanowires, we could not confirm the presence of dopants in ZnO nanowires. There is also a small chance that the doping process has taken place but in rare and random places of the sample. Another possibility is that the estimated annealing time was not sufficient for the thorough diffusion of the dopants to nanowire core under the applied condition. The doped area that could be closer to the edges of nanowire is then removed due to the strong etching process. Either case, for device application a homogenous distribution of dopants and a good control on doping process are crucial. In this case, considering the great potential of SOD doping process and its very new application for p-doping of ZnO nanowires, more investigation and modifications of parameters are necessary to exploit all the advantages SOD method can offer for p-type doping.

Another interesting feature in APT measurements of the nanowires with SiN coating was the considerable lack of oxygen in the nanowires. This lack of oxygen was found to be more important on the sides of the nanowires and in certain cases no oxygen was detected by EDX spectroscopy. The EDX mapping of the PSiN850 is shown in *Figure IV.15* which shows the negligible amount of O as compared to the other elements. The presence of a fluoride related peak can also be observed which is due to reactive ion etching (RIE) by CHF_3.

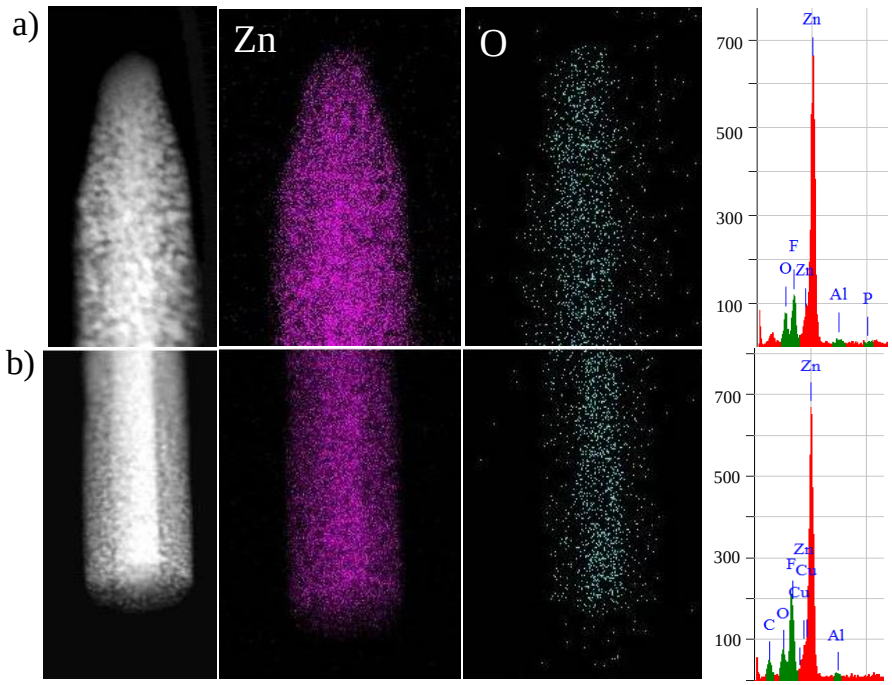

Figure IV.15 Energy dispersive spectra and map of elements in a single PSiN850 nanowire, (a) on top zone, (b) on bottom zone.

Since the loss of oxygen was only observed for the nanowires with SiN coating, we suspect that the lack of oxygen is due to the presence of SiN. Kalin *et al.* have shown that Si_3N_4 is not chemically stable in contact with oxidized steel at elevated temperatures. At 700 and 500°C, Si diffusion into the oxide layer resulted in the dissociation of the Si_3N_4 ceramic. At higher temperatures, Si_3N_4 reacts with the formation of N_2, SiO_2 and/or other complexes containing both Si and O [Kalin 2000].

Considering this condition, we can assume that during the annealing at 750 and 850°C, a part of oxygen was used to form SiO_2 which then was removed by etching. This could explain why we have the lack of oxygen on the samples with SiN coated layer particularly the one annealed at 850°C.

This loss of oxygen is very important since it should not be attributed to any of the artifacts during APT experiments discussed in chapter III. Therefore, prior to the APT measurements, a good knowledge of the growth condition and the sample morphology is necessary to make a reliable conclusion.

IV.2 Nitrogen doped ZnO nanowires

Nitrogen doped ZnO nanowires were grown directly using the MOCVD method at GEMaC laboratory (see II.1.2). Different concentrations of NH_3 were used for the doping of ZnO nanowires: 0, 10, 15 and 20 ml shown in *Table IV.3*. The influence of nitrogen concentration on the properties of these samples is examined in the following sections.

Table IV.3: List of nitrogen doped ZnO nanowire samples prepared at GEMaC Versailles.

Samples	*N1*	*N2*	*N3*	*N4*
NH_3 concentration (ml)	*0*	*10*	*15*	*20*

IV.2.1 Morphology of nitrogen doped ZnO nanowires

SEM images of the samples are shown in *Figure IV.16*. All doped and undoped nanowires exhibit a hexagonal morphology reflecting hexagonal wurtzite structure of ZnO.

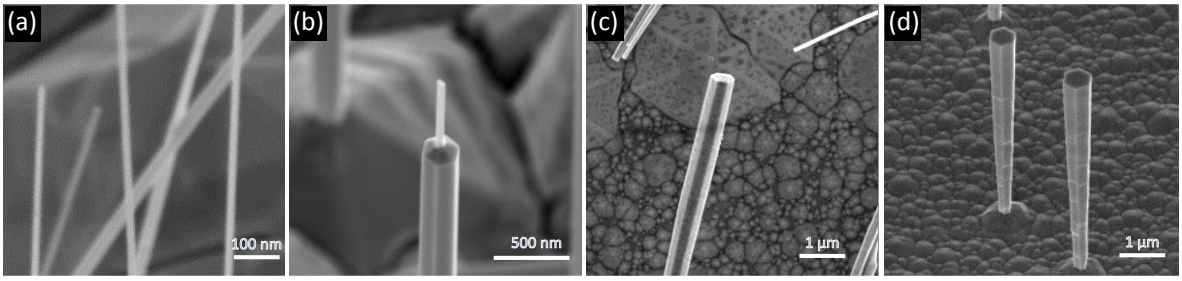

Figure IV.16: SEM image of (a) undoped and (b,c,d) nitrogen doped ZnO nanowires corresponding to the samples N2, N3 and N4 respectively. Undoped and doped ZnO nanowire exhibit hexagonal facets with strong tapered structure.

It can be seen that the hexagonal structure has been conserved after introducing the nitrogen atoms. However, introducing nitrogen impurities clearly influences the size (diameter) of the nanowires. It was observed that the increase in nitrogen concentration decreases the nanowire's length while it increases in diameter. This change in diameter varies from 30 nm for the pure one to about 250 nm for N2 doped. For N3 and N4 a wide range of different diameter size was observed where in some cases, this value reaches to about 1 µm. The tapering has also been observed for the nanowires with the diameter size increasing from bottom towards top of the nanowire. Strong tapering can be seen for N3 samples where the diameter of a single nanowire can vary from few tens to hundreds of nanometer moving from bottom to top of the nanowire. One reason resulting in the tapered morphology of nanowires can be due to disturbance in vapor pressure due to the introduction of nitrogen precursor. Other possible reasons could be the change in mobility of elements on the surface after introducing nitrogen and/or the adsorption of NH_3 in a way that it slows down the longitudinal growth and promotes the lateral growth instead. The latter can also explain why the doped nanowires are found shorter in length as compared to the undoped one for the same growth condition and duration.

SEM images of the nanowires exhibit two types of growth: The nanowires that originate directly from the surface of the ZnO wetting layer and the ones that are formed on top of hexagonal pyramids. The origin of formation of these pyramids was discussed by Perillat-Merceroz *et al.* and it was referred to the polarity of the nuclei that is formed. They have reported that ZnO nanowires grown by MOCVD exhibit Zn-polarity while pyramids are O-polar. Therefore, the growth of nanowires requires Zn-polarity nuclei. This type of growth has a high rate in the [0001] direction due to the low free energy of the {1-100} facets resulting in hexagonal morphology of ZnO nanowire [Perillat-M 2010 - Perillat-M 2012].

Figure IV.17.a shows the TEM image of the nitrogen doped ZnO nanowire (N3 sample).

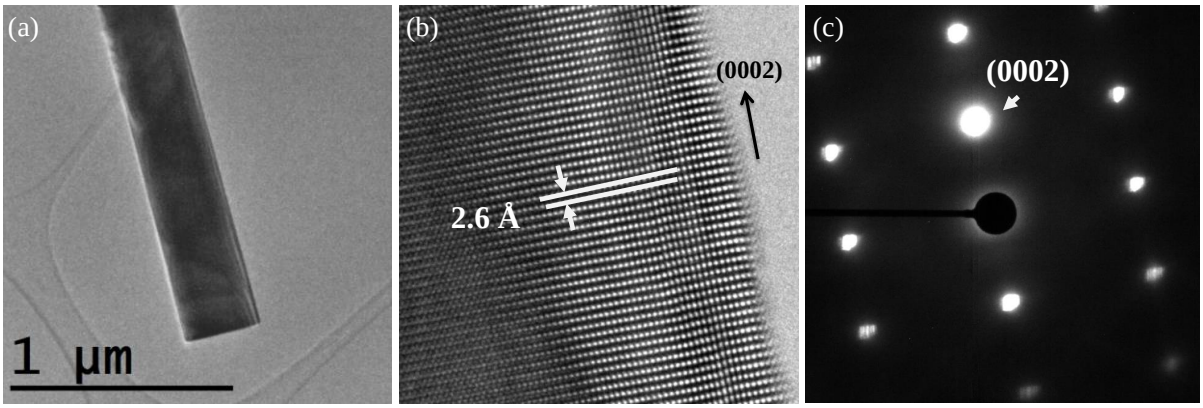

Figure IV.17: (a) TEM and (b) HRTEM image of N3 nanowire. SAED image of this nanowire shows the growth direction is along (0002).

The high resolution TEM image of the N3 nanowires (*Figure IV.17.b*) exhibit parallel crystal planes with the lattice spacing of 2.6 Å corresponding to the (002) plane characteristic of wurtzite ZnO. No dislocation or formation of new phases can be observed. However, there are some regions with non-parallel planes that are only due to the charge-effect caused by interaction of transmitted electrons and ZnO. The selected area electron diffraction pattern is shown in *Figure IV.17.c* reflecting a single crystal structure grown along c-axis observed.

Hence, we can conclude that nitrogen doping of ZnO still retains the hexagonal morphology and c-axis preferential growth direction that was observed for the undoped ZnO nanowires. This result indicates that introduction of nitrogen atoms in our process had no significant effect on the crystallographic structure and direction.

IV.2.2 Raman spectroscopy

In order to investigate the presence of nitrogen dopants in the ZnO nanowires Raman spectroscopy was carried out and compared to results obtained in case of undoped ZnO nanowires (*Figure IV.18.a*). The Raman measurements were carried out at GEMaC laboratory by of Mr.Emir Zehani under the supervision Dr.Alain Lusson.

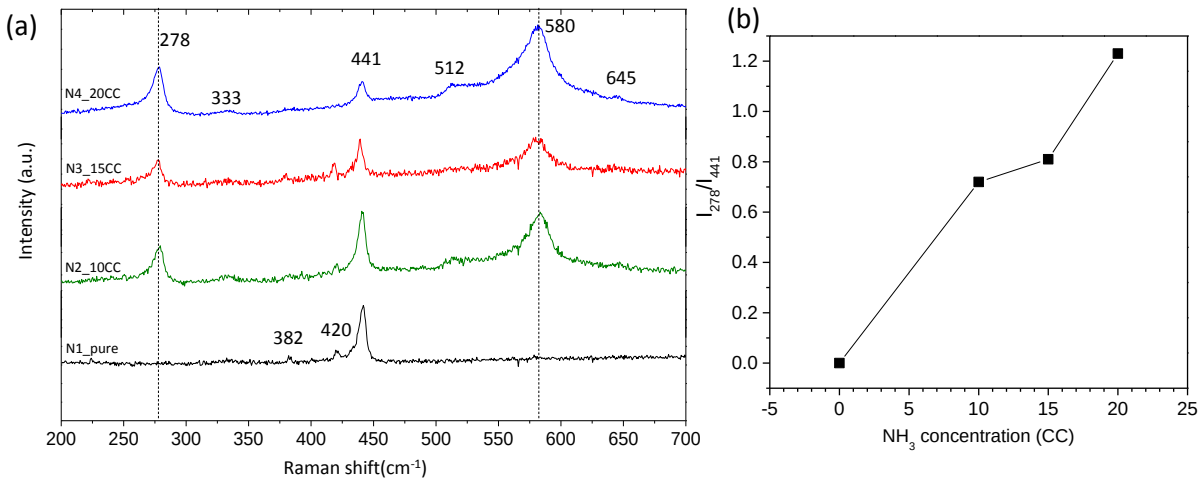

Figure IV.18: (a) macro Raman of undoped and nitrogen doped ZnO nanowires shown in blue and red respectively carried out at GEMaC (b) Raman intensity ratio of the peaks at 278 to 441 cm^{-1} as a function of NH_3 concentration.

For undoped ZnO (N1), three classical vibrational modes of ZnO can be found placed at 382, 420 and 441cm^{-1} ascribed to A_1(TO) and E_1(TO) and E_2(high) respectively. Deterioration of the E_2(high) mode at higher nitrogen concentration can be observed which can indicate that the crystal quality became worse by doping.

An important feature can be seen in Raman spectra of the doped nanowire as compared to the undoped one: the presence of the additional vibrational modes at 278, 512, 580, 645 cm^{-1}. The same modes at 275, 510, 582, 643, and 856 cm^{-1} have been reported previously for nitrogen doped ZnO thin films grown by CVD [Kaschner 2002 - Kerr 2007]. To confirm that these additional modes are nitrogen related, Kaschner *et al*. acquired Raman spectra of the nitrogen doped ZnO with different concentrations of nitrogen. It turned out that the intensity of these additional modes correlates linearly with the nitrogen concentration and can be used as a quantitative measure of nitrogen in ZnO. Kaschner *et al.* ascribed all these modes to the localized vibrations of nitrogen atoms on oxygen sites. However, Bundesmann *et al.* challenged this interpretation, as they detected similar peaks in ZnO thin films doped with Fe, Sb, and Al, intentionally grown without N incorporation. They ascribed the additional Raman peaks to intrinsic host lattice defects incorporation [Bundesmann 2003]. Friedrich *et al.* have also observed the same modes in nitrogen implanted single crystal. They ascribed all these peaks to the nitrogen related complexes [Friedrich 2007]. However, later it was shown that the vibrational mode at 275 cm^{-1} is due to an interstitial Zn atom bound to a substitutional nitrogen atom (N_O-Zn_i) whereas the mode at 582 cm^{-1} is related to the Zn_i-O_i complexes

[Friedrich 2009]. The controversy about the origin of these modes remains but generally it has been assigned either to local vibrational modes due to the nitrogen substitution or to intrinsic host lattice defects. Two more small peaks can be observed at 333 and 382 cm^{-1} which are assigned to multiple-phonon-scattering process and A_1(TO) respectively.

The influence of different nitrogen concentrations in N-doped samples is demonstrated by an intensity ratio of the nitrogen-related vibrational mode (278 cm^{-1}) to the one of ZnO at 441 cm^{-1} corresponding to E_2(high). This ratio is presented as I_{278}/I_{441} and shown in *Figure IV.18.b.* The figure shows a clear variation of I_{278}/I_{441} ratio towards higher values as NH_3 concentration increases. This demonstrates a stronger presence of nitrogen in ZnO nanowires as the NH_3 content increases in the MOCVD reactor. However, the distribution and homogeneity of nitrogen in the nanowires are yet unknown parameters while they are very important factors to evaluate the efficiency of doping process.

IV.2.3 Photoluminescence

PL spectra of the doped and undoped ZnO nanowires are shown in *Figure IV.19.* For a better discussion, the spectrum is shown in two separated regions: 3-3.3 eV and 3.3-3.4 eV.

In the range of 3-3.3 eV donor-acceptor pair transition can occur if a sufficient amount of shallow acceptor states is present. A peak at 3.239 eV can be observed in PL spectra of all doped samples (*Figure IV.19.a, b* and *c*) ascribed to the donor-acceptor pair (DAP). The presence of DAP peak indicates that the nitrogen acceptors are present in ZnO nanowires. Similar DAP energy was observed at 3.235 eV for nitrogen implanted bulk ZnO crystals by Meyer *et al.* [Meyer 2004]. It is interesting to mention that the presence of DAP peak appeared to be independent of the concentration of nitrogen.

In addition to DAP band, three broad energy bands at about 3.020, 3.091 and 3.164 eV are visible with an energy separation close to 72 meV ascribed to the longitudinal optical phonons replicas of DAP peak. As it was mentioned before, DAP peaks and its replica occurs only if there is enough of acceptor and donor. Since the ZnO crystals are intrinsically n-type, donor levels are expected. Therefore, the strong DAP peak and its replicas in this case reflects the presence of the acceptors.

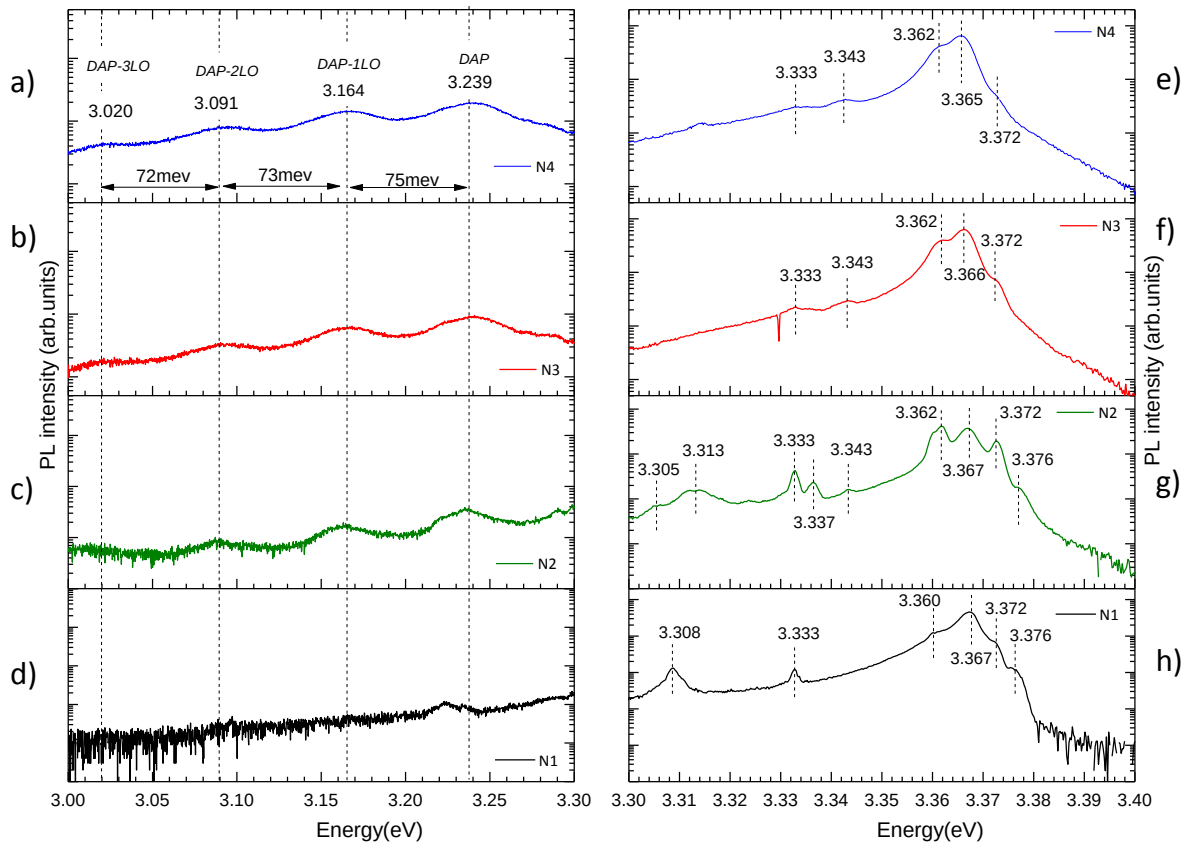

Figure IV.19: Photoluminescence spectra of the nanowires in 3-3.3 eV range and 3.3-3.4 range for the samples N4, N3, N2 and N1 shown respectively as (a,e), (b,f), (c,g) and (d,h).

The intensity of the replicas (1LO, 2LO, 3LO,...) with respect to the intensity of the DAP peak (zero phonon line located at 3.39 eV) can be theoretically described by Poisson distribution:

$$I_n = \frac{N^n}{n!} \quad , \tag{IV.1}$$

where I_n is the intensity of the n^{th} phonon replica (n=0,1,2,3,…) and n= 0 corresponds to the DAP line or so-called zero phonon line (ZPL). N, is the Huang-Rhys factor corresponding to the mean number of created phonons indicating the strength of electron-LO phonon interactions. For nitrogen doped ZnO, Huang-Rhys factor was observed to be N=0.85 [Zeuner 2002].

Table IV.5 presents the calculated N factor at each phonon replicas for the samples doped with different concentrations of nitrogen (N2, N3 and N4).

*Table IV.4: Huang-Rhys factor calculated for each phonon replica of the doped samples N2, N3 and deduced from Figure IV.*19.

	N2	*N3*	*N4*
n=1	*0.55*	*0.67*	*0.74*
n=2	*0.76*	*0.86*	*0.91*
n=3	*1.10*	*1.07*	*1.11*

The N values calculated for the samples are different that the expected value of 0.85 and it increases for higher replica numbers. Such behavior can be due to the additional excitation process caused by activation of the dopants.

The peaks appearing in the range of 3.3-3.4 eV of the PL spectra of the doped and undoped samples are related to the bound excitonic recombinations. For undoped ZnO nanowire N1 (*Figure IV.19.h*), the peak at 3.376 eV is ascribed to the free-exciton emission (FX_A). Strong lines observed in the 3.355-3.375 eV are associated with the transition of the excitons bound to the impurities. For undoped sample, three energy lines of I_1, I_2 and I_6 are visible at 3.372, 3.367 and 3.360 eV. The origin of the peak observed at 3.333 eV is still under debate but it is generally referred to the exciton bound to the structural defects (Y-line) or to the deep donor [Meyer 2004].

For doped samples (*Figure IV.19.e, f and g*), an interesting feature can be observed: the emergence of an energy line at 3.343 eV which was not observed for undoped nanowires. Park *et al.* attributed this peak to nitrogen related transition [Park 2008]. The transitions lines of I_1, I_2 are still present for doped samples.

An additional peak at 3.313 eV is observed for N2 sample. This peak was observed previously by Look *et al.* located near 3.315 eV and it was referred to A^0X line associated with N_O [Look 2002]. Later, it was shown that the samples with low hole concentration have D^0X transition at 3.364 eV and also an A^0X line at 3.315 eV, whereas in samples with higher hole concentration only A^0X line at 3.317 eV is present [Schirra 2008 - Ye 2007].
The peak at 3.31 eV was observed in variety of ZnO samples and has been ascribed to various recombination types most often as conduction band to acceptor transition.

In this work, we have tried to assign all the peaks observed in PL spectra of these samples. The result is summarized in *Table IV.5*. However, ascribing all observed peak is controversial due to the sensitivity of the PL measurements to the condition of the growth and the sample quality.

Table IV.5: Exciton recombination energies and related properties for samples N1, N2, N3 and N4 deduced from Figure IV.19.

Energy (eV)				Exciton
N1	N2	N3	N4	
3.308	3.305			?
	3.313			A^0X [Look 2002]
3.333	3.333	3.333	3.333	Y_0-line [Meyer 2004]
	3.337			?
	3.343	3.343	3.343	N related line [Park 2008]
3.360				D^0X (I_6) [Wang 2006]
	3.362	3.362	3.362	D^0X (I_{4a}) [Wagner 2010]
			3.365	I_4 [Wang 2006]
		3.366		I_2 [Meyer 2004]
3.367	3.367			I_2 [Meyer 2004]
3.372	3.372	3.372	3.372	I_1 [Wang 2006]
3.376	3.376			FX_A

Eventually, although photoluminescence is a well-known technique in investigating the presence of the dopants and defects, it cannot provide all necessary information about incorporation of nitrogen in ZnO nanowires.

IV.2.4 Electron energy loss spectroscopy

The presence of nitrogen was also examined by electron energy loss spectroscopy (EELS) as it is shown in *Figure IV.*20. EELS is an ideal supplementary technique that can give chemical information similar to that provided by X-ray absorption near-edge structures (XANES) and extended X-ray absorption fine structure (EXAFS). In comparison with the two previous techniques, the main advantage of EELS is its accessibility; it can be carried out in laboratories with access to the basic electron spectroscopic techniques. The obtained EEL spectra contain peaks that are used as fingerprints to define the corresponding elements. *Figure IV.*20, shows the EEL spectroscopy of a single nanowire (N3).

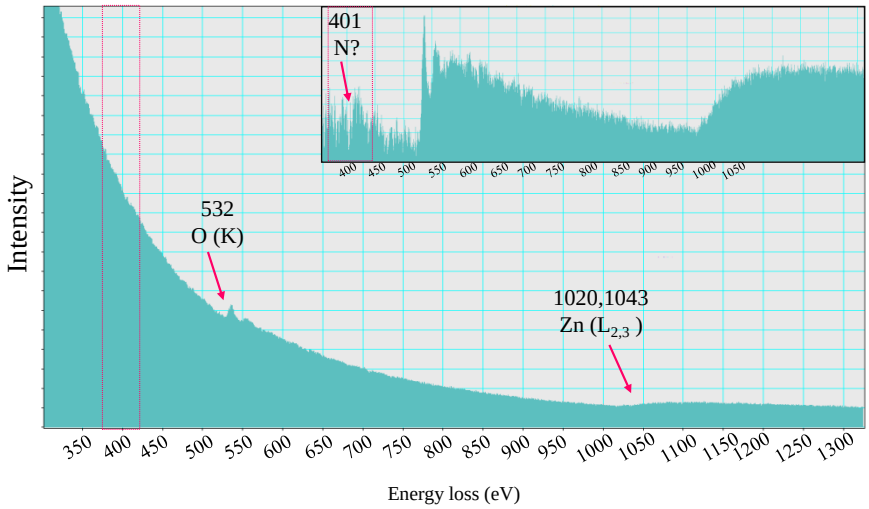

Figure IV.20: Electron energy loss spectrum of nitrogen doped ZnO nanowire, the inset shows the same spectrum after removing the background.

A peak at 532 eV was observed that is related to the K-level energy of oxygen. The broad peak at about 1020-1050 eV is assigned to the presence of the zinc. The presence of nitrogen should appear as a peak at 401 eV which in this case, was not observed. Even after the removal of the background (inset *Figure IV.*20), the presence of the nitrogen peak cannot be confirmed which shows the limit of this technique in investigation of such samples.

So far, considering PL and Raman studies there are evidence of nitrogen incorporation in ZnO nanowires grown by MOCVD. However for electronic and optical means, it is crucial to know the dopant concentration and to control the distribution of the dopants.

IV.2.5 Atom probe tomography

Figure IV.21 shows the mass spectra obtained by APT of a single N-doped ZnO nanowire (N3 sample). Some peaks corresponding to the presence of the nitrogen ions are clearly revealed. *Figure IV.21.b* and c present the magnified views of nitrogen related ranges of the obtained mass spectrum.

The peak at 28 a.m.u. corresponds to the N_2^+ ion. The peak at 14 a.m.u. can be assigned to either N^+ or N_2^{2+} or the mixture of both. As it was discussed previously for the case of oxygen peak at 16 a.m.u., the assignment of this peak to either ion or molecule can influence the value of the calculated concentrations. However in this case, due to the very small number of atoms at the peak 14 a.m.u., assigning this peak to either N^+ or N_2^{2+} does not affect the

overall nitrogen concentration. The peaks related to the nitrogen oxide complexes can be also observed at 30 and 46 a.m.u. assigned to NO^+ and NO_2^+ molecules.

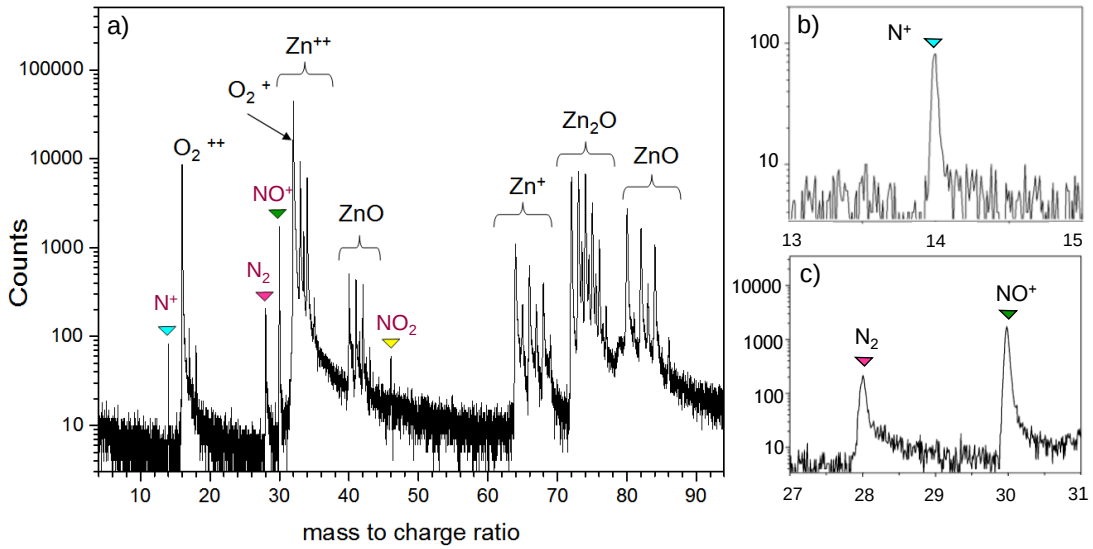

Figure IV.21: (a) Mass spectrum of the N3 nanowire, the nitrogen peaks are revealed on the spectrum, (b) and (c) magnified views of the mass spectrum.

.*Figure IV.22* shows the distribution of oxygen, zinc and nitrogen atoms in the analyzed volume where each dot represents one atom.

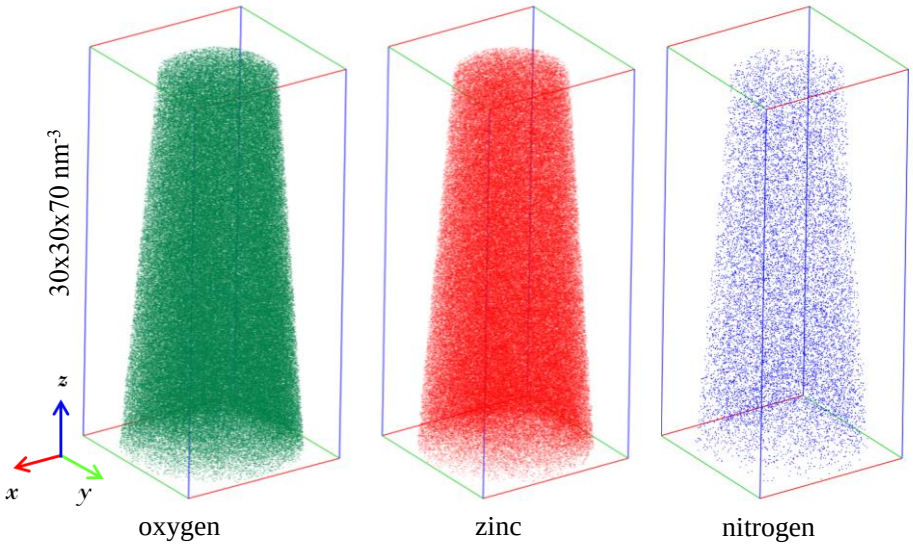

Figure IV.22: spatial distribution of O, Zn, and N shown in green, red and blue respectively obtained by reconstruction of the APT analysed volume.

As it can be seen in this figure, nitrogen atoms are distributed homogenously throughout the analyzed volume and no formation of clusters or new phases can be observed.

The average concentration of the nitrogen in the whole analyzed volume was found to be 3.4 x 10^{20} atom.cm^{-3} with an uncertainty of ± 0.1 x 10^{20}. In order to investigate the distribution of nitrogen component species, chi-square tests have been performed. The distribution of the N_2 and NO species that are retrieved from APT data are compared with the theoretical Poisson distribution and shown in *Figure IV.23.a* and *b*, respectively.

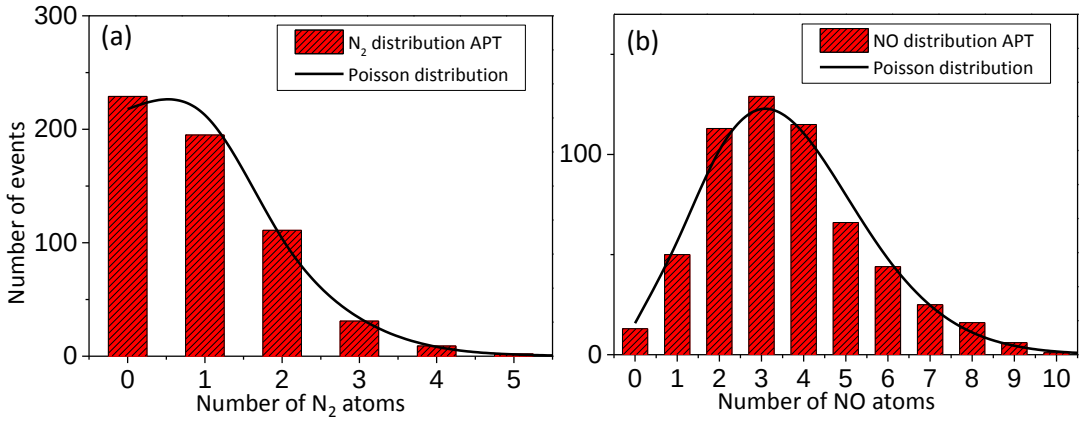

Figure IV.23: Frequency distributions of two main nitrogen species (N_2 and NO) compared to the Poisson distribution are shown as (a) and (b) respectively. The sampling distribution of 500 atoms was chosen for calculating the number of events.

Each bar in the figures indicates the number of corresponding species in a sampling volume of 500 atoms. For the corresponding degree of freedom, experimental chi-square values were compared to the theoretical one for 5% probability. In all cases, the measured chi-square value was smaller than the theoretical one, indicating that the distributions of nitrogen species in the analyzed volume are homogenous.

The same experiment has been repeated on different nanowires of the same sample (N3) and in all the studied nanowires no cluster or formation of new phases has been observed. Hence, we can certainly conclude that ZnO nanowires grown by MOCVD are successfully doped with nitrogen atoms homogenously distributed in the nanowire.

IV.2.6 Field-effect transistor characteristic

The results obtained by APT are very important for the development of an efficient growth technique and elaboration of high quality materials. However, the presence of the

doped acceptors in ZnO matrix cannot assure the p-type conductivity of ZnO. Hence, it is essential to verify the conductivity of doped materials. The field-effect transistor is the most common technique to estimate the carrier concentration and mobility in doped nanowires. Analysis was carried out at Institute NÉEL Grenoble in the framework of ANR project. *Figure IV.24.a* shows a device configuration of nitrogen doped ZnO nanowire (sample N3) electrically contacted to interdigitated electrodes on Si/SiO_2 substrates.

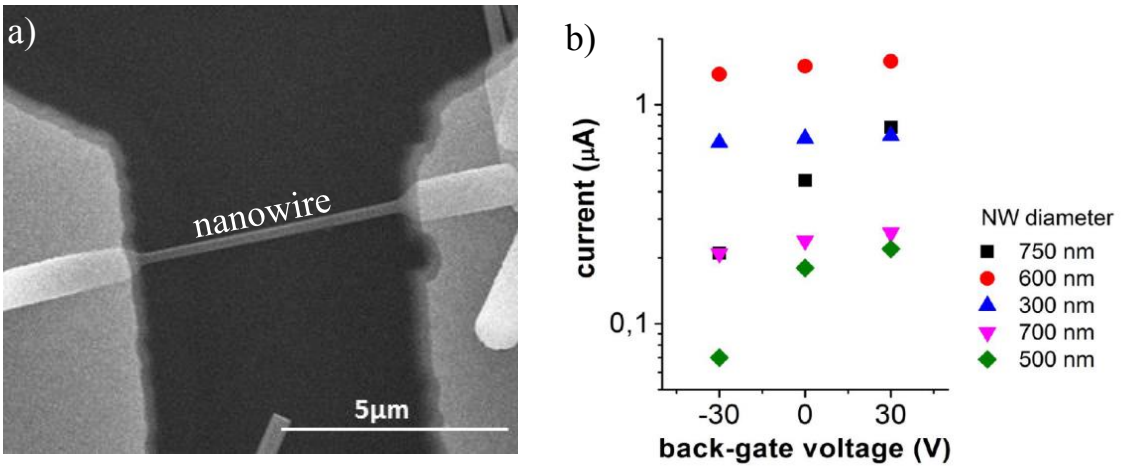

Figure IV.24: Field-effect transistor characteristic of nitrogen doped ZnO N3 sample (a) view of the measurements set-up showing a nanowire placed on Si/SiO2 substrates and provided with individual contacts, (b) a I_Vg data recorded for nanowires with different diameter size [performed at Institute NÉEL].

The effect of an applied gate voltage on the current is used to figure out the conductivity type of the nanowire. For nitrogen doped ZnO nanowire, we have observed for different sizes of nanowires, that the conductance is increasing as the voltage increases indicating that the nanowires exhibit n-type conductivity (*Figure IV.24.b*).

The origin of this n-type conductivity can be related to the high concentration of electrons. The total charge in the wire can be obtained by

$$Q = C.V_T\,, \tag{IV.2}$$

where V_T is the threshold voltage to deplete the wire and C is the capacitance commonly modeled as

$$C \approx \frac{2\pi\varepsilon.L}{\ln(\frac{2h}{r})}, \tag{IV.3}$$

where ε is the dielectric constant, h is the thickness of the SiO_2 substrate, L is the length and r is the radius of the nanowire.

The electron concentration can be then obtained by

$$n = \frac{Q}{2\pi r^2 L q} \tag{IV.4}$$

In our case, the electron concentration was found to be more than 10^{18} cm^{-3} which could likely be the reason of n-type conductivity.

The results on N-doped ZnO nanowires show that the nitrogen doping of ZnO nanowires are possible by MOCVD method. However, the p-type conductivity was not confirmed. The n-type conductivity of nitrogen doped ZnO is not surprising as it has been reported previously on the same system [Lyons 2009]. Based on the density functional calculations, Lyon *et al.* showed that nitrogen can create deep acceptor. Their results brought doubt to the fact that, doping with nitrogen can give rise to shallow acceptor level or p-type conductivity.

Despite many reports on a successful p-type conductivity of N doped ZnO [Look 2002 - Tsukazaki 2005], the lack of ZnO p-n junction based devices indicates that yet, there are problems associating the reliability, reproducibility and stability of p-type ZnO.

IV.3 Conclusion

The reliability of two different doping processes to achieve p-type ZnO nanowires were examined using conventional techniques. Some evidence of the presence or the absence of dopants was provided by conventional techniques. However, APT comes as an important technique providing direct information about the presence and distribution of dopants.

Ex-situ doping of undoped ZnO nanowires were carried out using spin-on doping process and phosphorous as the dopant. APT and different conventional techniques could not confirm the presence of phosphorous in the nanowires. The absence of the phosphorous can be due to the parameters used in the doping process such as annealing temperature and etching method.

Since this doping method is a new approach for p-type doping of ZnO nanowires, both MOCVD and *ex-situ* doping process used in this work need further experimental attempts and modification in order to obtain p-type ZnO nanowires. In this case, atom probe tomography plays an important role in examining the presence, distribution and concentration of the

dopants and their diffusion path through the nanowire and thus determining whether the doping method is successful.

Nitrogen doped ZnO nanowires grown by MOCVD were also examined by Raman, photoluminescence and electron energy loss spectroscopy. The techniques could reveal some evidence of the presence of nitrogen dopants in ZnO nanowires but yet leaving no clear answer to some important information such as concentration and distribution of dopants. 3D volume reconstruction of the analyzed nanowire by APT exhibits that the nitrogen atoms are uniformly distributed in the nanowire with an average concentration up to 3.4×10^{20} cm^{-3}. However, FET measurements revealed that the nanowires are n-type conductive.

CHAPTER V Taking advantage of luminescent lanthanide ions in ZnO matrix

In chapter I, we have discussed how the presence of lanthanide ions in ZnO matrix can provide luminescent centers and hence enhance the natural luminescent properties of ZnO. Depending on which rare earth element is used as optical dopant in ZnO, different colors of emission can be produced. For example, Tb doped ZnO provides green emission where Eu doped ZnO provides red emission. The choice in emission color is the main interest in studying ZnO doped with rare-earth elements not only for the fabrication of different basic color LEDs but also to generate white LED by mixing different basic color emissions.

As it was discussed in the first chapter, triad of red, green and blue colors (RGB system) can provide white color emission. However, RGB system involves more complex procedures and a strong control on color rendering, which makes this method more costly and less straight forward than phosphorous conversion method LED. Hence, using ZnO as host matrix can offer two main economic advantages: ZnO is cheap and abundant and also, it is possible to synthesize many different ZnO nanostructures using various low-cost techniques.

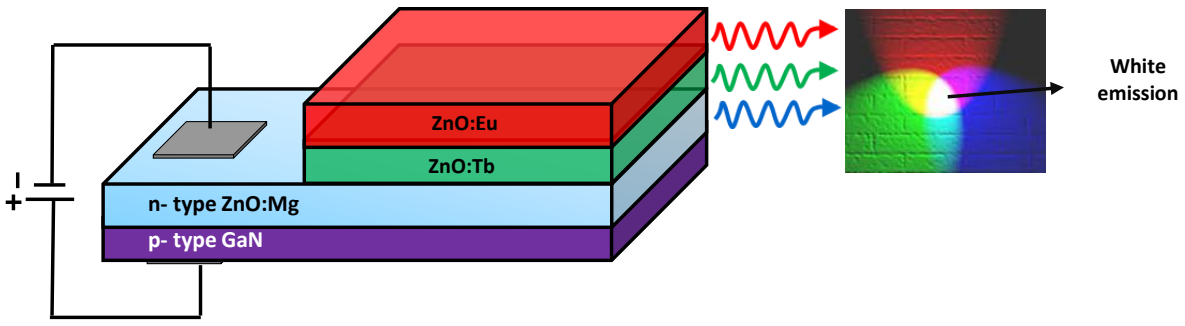

Figure V.1: ZnO heterojunction white LED, where the combination of red, green and blue color emitted from different doped layers results in white color emission.

Figure V.1 shows the protocol of LUZ project[1]. The main objective of this project is to synthesize ZnO based white LED using RGB system. In this work, in order to provide the red,

[1] Investissements d'avenir" program (ANR-10-LABEX-09-01), LABEX EMC3

green and blue emissions, ZnO thin films were doped with europium, terbium and magnesium respectively. Due to the difficulties in preparing p-type ZnO (discussed previously in chapter I and IV), commercial p-type GaN is used.

The application of ZnO:REE is not only limited to the LEDs, for applications such as laser diodes, optical fibers, displays and sensors utilizing UV to visible down-conversion, doping ZnO and other semiconductors with rare earth elements is an established strategy [Balestrieri 2013 - Bünzli 2005 - Rakov 2013]. Although one rare earth alone can lead to down conversion, the use of the combination of rare earth elements leads to a more efficient down conversion. So far, down-converting materials are based on Lanthanide^{3+}-Yb^{3+} couples and a transfer from ZnO to Yb has attracted many attentions [Chen.Y.D 2012].

In past years, many reports have been devoted to the synthesis of different ZnO materials doped with different rare earth elements and their optical properties [Balestrieri 2013 - Cetin 2009 - Fang 2005 - Kumar 2014 - Yang 2008]. In all cases, the optical properties of ZnO:REE are strongly dependent on the growth condition and post-deposition annealing process, as they rule the distribution of the active luminescent centers. Hence due to the great interest, this chapter is dedicated to the atomic investigation of ZnO materials doped with different rare-earth elements by atom probe tomography.

V.1 Terbium doped ZnO thin films

Undoped and Tb doped ZnO thin films were grown using magnetron sputtering with the conditions explained in II.1.1 (provided by CIMAP laboratory[1]). Post-deposition annealing of the doped samples was carried out for one hour under continuous nitrogen (N_2) flow at different temperatures: as grown, 400, 500, 600, 700, 800 and 900°C. The thickness of the films was measured to about 1.5µm and the Tb concentration is estimated to be 3%.

The effect of annealing temperature on Tb doped samples was examined by photoluminescence using excitation wavelength of 282 nm (*Figure V.2*).

[1] Centre de Recherche sur les Ions, les Matériaux et la Photonique, ENSICAEN

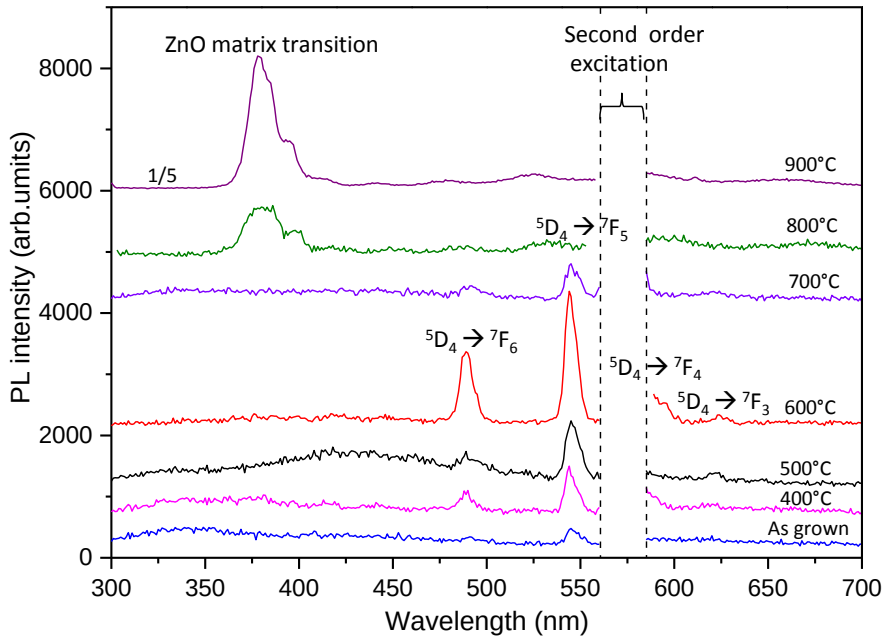

Figure V.2: Photoluminescence spectra of Tb doped ZnO thin films annealed at different temperatures using excitation wavelength of 282 nm at room temperature [Ziani 2014].

As it was previously shown in *Figure I.11*, Tb offers different energy levels and transitions. The peaks observed in the range of 450 to 650 nm in *Figure V.2* are ascribed to the different $^5D_4 \rightarrow {}^7F_j$ (j=6,5,4,3) transitions due to the presence of Tb^{3+} ions. For the sample annealed at 600°C, these transitions are at maximum values compared to other samples. The $^5D_4 \rightarrow {}^7F_5$ transition observed at 544 nm corresponds to the main green emission in Tb. This transition is more pronounced for the samples annealed at 600°C. For the samples annealed at temperatures above 600°C, the intensity of $^5D_4 \rightarrow {}^7F_j$ transitions decreases drastically until they disappear entirely at 800°C. Hence, the PL results suggest that the annealing up to 600°C enhances the Tb-related emissions whereas above this temperature, these emissions are strongly suppressed.

Several explanations can be suggested associated to this drastic change in Tb-related emissions. For example, annealing can result in the formation of new phases (such as terbium oxide) which can directly influence the crystal structure properties and lattice environment.

Another possibility of the change in the optical properties can be caused by the redistribution of dopants due to annealing. This redistribution can disturb the uniform distribution of dopants within the matrix and create aggregation or clusters which can result in a loss of optical properties. Balestrieri *et al*. have suggested that the diffusion of dopants

towards substrate can be also a possible reason for the loss in optical properties [Balestrieri 2013].

Besides, the insertion of Tb ions results in a change in ZnO lattice environment and it influences the defect concentration as well as generating some Tb-related defects. Since the defects play an important role in indirect excitation (explained in the following) of Tb atoms in ZnO matrix, the change in defect concentration affects the optical properties.

In general, rare-earth elements can be excited directly (using particular excitation wavelength) or by an indirect process through energy transfer from the matrix.

Several excitation mechanisms can be predicted for terbium atoms such as: direct Tb^{3+} excitation through the f–f transition, direct Tb^{3+} excitation through the f–d transition, excitation through the defect assisted energy transfer, and charge-transfer transition [Podhorodecki 2010]. In an indirect excitation of Tb ions (e.g. excitation via energy transfer), the Tb-related emission is yield by defects which participate in energy transfer. Hence the emissions from Tb should be dependent on the annealing as it changes the defect concentration in matrix. The indirect or direct excitation of the ions is dependent on the excitation energy that is used. In photoluminescent measurements of ZnO:Tb series presented in this work, the excitation wavelength of 282 nm is used which can result in a direct excitation of Tb ions. Nevertheless, in *Figure V.2* a strong influence of annealing on Tb-related luminescence can be observed which can indicate that the defects are involved in emissions from Tb. *Figure V.3* shows a possible transfer mechanism labeling the energy levels of Tb^{3+} ions in Tb doped ZnO thin films.

An electron at the ground state is first excited to the conduction band of ZnO, which relaxes to an energy level just below the conduction band through a non-radiative phonon emission. The defects (e.g. Tb_{Zn}, V_O and Zn_i) introduce energy levels in the band gap which can act as a deep level trap. The electron is then trapped by these defects and transferred to energy levels of Tb ($^5D_4$ or $^5D_3$) [Kumar 2014 - Singh 2014]. Hence, the Tb-related emission can occur only if a part of this energy is transferred to the D-levels in Tb. However, to assist in the Tb-related emissions, the defects should be close to the Tb lattice site. Besides, for Tb to provide luminescent centers in ZnO, it has to be present in Tb^{3+} state which depends on the lattice environment.

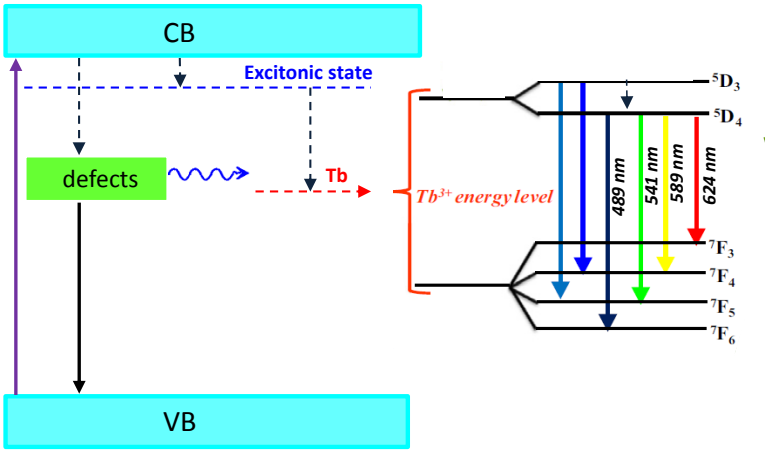

Figure V.3: A possible transfer mechanism leading to radiative transitions of Tb in ZnO matrix. Solid and dashed lines represent radiative and non-radiative emissions respectively.

Since annealing can heal the defects, the significant loss of Tb-related emission above 600°C (*Figure V.2*) can be due to the presence of a lower amount of defects. Considering that the low defect concentration is simultaneous with the loss in Tb-related emissions, it is likely that the Tb-emission is governed by an indirect excitation. Above 800°C, a near band edge peak at 387 nm appeared and its intensity becomes more pronounced at higher annealing temperatures. This peak is ascribed to the recombination of free excitons in ZnO [Yang 2011]. Below the annealing temperature of 600°C, the increase in the temperature involves more contribution of the Tb-related emissions.

Considering that most significant changes in PL results occur for annealing at 600 and 800°C (*Figure V.2*), these samples were chosen to further investigate the origin of this change in PL. Undoped and as grown Tb doped films are used as references. *Table V.1*, presents the list of the samples and growth information studied in this section.

Table V.1: List of studied Tb doped ZnO thin film samples prepared at CIMAP Caen.

samples	*T1*	*T2*	*T3*	*T4*
doped	*No*	*Yes*	*Yes*	*Yes*
annealing temperature (°C) for 1hr	*600*	*As grown*	*600*	*800*

V.1.1 XRD and structural properties

The presence of Tb and new phases in ZnO thin films were first studied by XRD. The main results are presented in *Figure V.4*. The XRD instrument used here is a D8 Bruker configured with a cobalt source providing the X-ray wavelength of 1.79Å. The XRD data were acquired using θ-2θ Bragg-Brentano configuration in the 2θ range of 20 to 90°. The preferred growth direction for all thin films was found to follow c-axis and along [002] direction with a peak position at about 40°.

However, other peaks such as (004) were also observed. The intensity of these peaks increases for annealed thin films. Some small peaks can also be observed particularly in the 2θ range of (45-75°), which can be associated with the presence of zinc silicates layer that is formed by the diffusion of Si from substrate towards the thin film during annealing. This layer has already been reported and evidenced by TEM [Balestrieri 2013 - Ziani 2014].

For Tb doped samples, some small peaks are also observed in the 2θ range of < 40˚ (shown by star sign in *Figure V.4*). The origin of this peak could be related to Tb or zinc silicates layers. Nevertheless, this peak is not present for pure ZnO film. Besides, for the as grown thin film, where no signal related to the substrate is detected, this peak is still present. Hence, it is more likely that this peak refers to some Tb related compositions.

More information can be obtained from XRD results by calculating the lattice parameter and grain size using angular position and width of the peaks. The comparison of the (002) peak position for different doped thin films were compared to the one of pure ZnO thin film showing a shift towards lower 2θ. This shift in peak position reflects the compressive or tensile stress created by the defects and/or impurities. The lattice stress can be estimated by calculating the c-parameter.

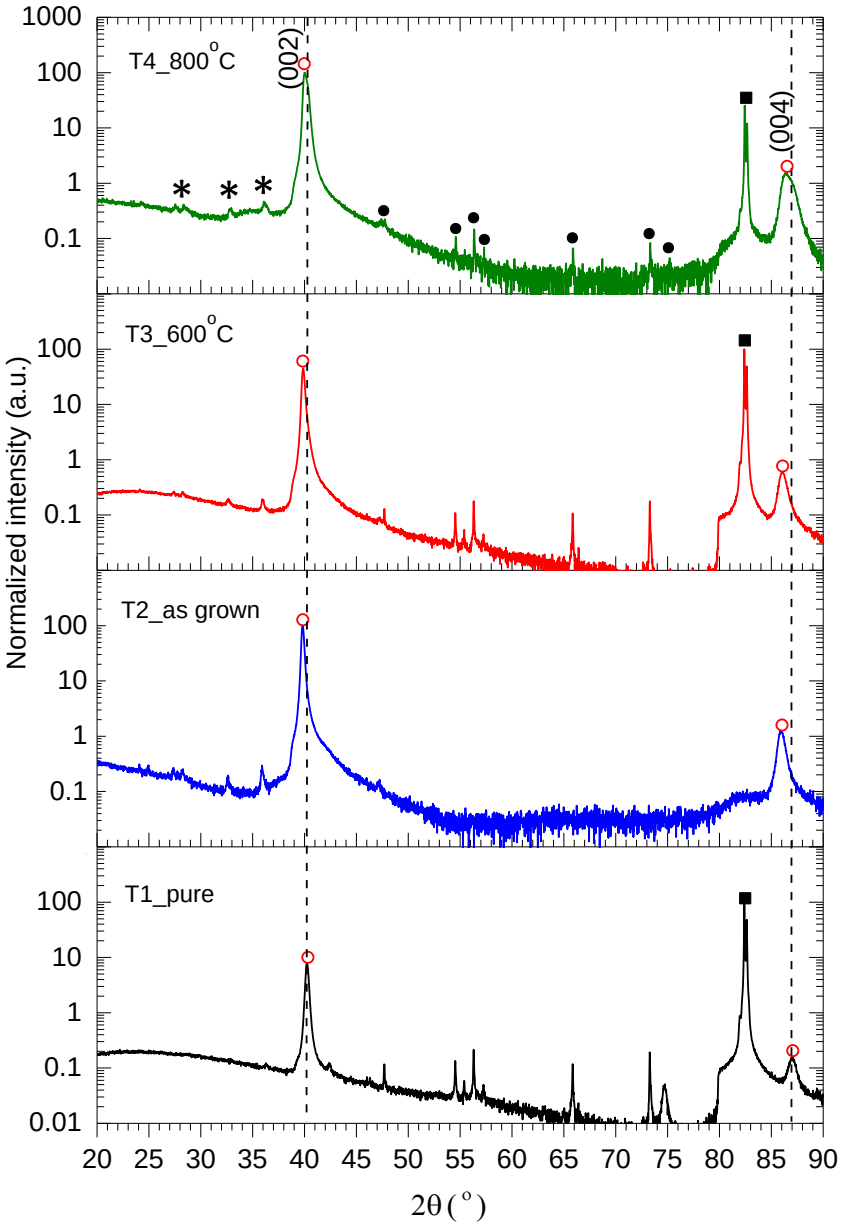

Figure V.4: XRD patterns corresponding to the undoped and Tb doped ZnO films. The intensity is normalized for better comparison. The symbol (■) and (●) indicate the peaks related to the Si substrate and zinc silicate, respectively. Some extra peaks are observed for ZnO:Tb films at lower angles (2θ<40°) shown by (*).

For hexagonal crystal structures, this parameter can be obtained via a relation between lattice parameters, and (*hkl*) indexes of lattice planes expressed as

$$\frac{1}{d^2} = \frac{4}{3}\left(\frac{h^2 + hk + k^2}{a^2}\right) + \frac{l^2}{c^2}, \qquad \text{(V.1)}$$

where *d* can be found via Braggs' law and *a*, *b* and *c* are lattice parameters

$$2d = \frac{n\lambda}{\sin(\theta)}, \tag{V.2}$$

n is an integer number and λ=λ(cobalt)=1.79 Å.

Thus, for hexagonal structured ZnO with crystal direction of (002), the equations (V.1) and (V.2) can be simplified to

$$c = \frac{\lambda}{\sin(\theta)}. \tag{V.3}$$

Figure V.5.a shows the corresponding c-parameter for each sample. In undoped ZnO, the values above the bulk value (5.207 Å) reflect the compressive stress caused by interstitial atoms. The values below the bulk value are referred to tensile stress produced by oxygen and zinc vacancies. In doped ZnO, the presence of the impurities can also induce the stress in the lattice. In this case, it can be seen that c-parameter of the doped thin films has increased as compared to the undoped one. Since the atomic radius of Tb is larger than that of Zn (1.603 and 0.88 Å respectively), the substitution of Zn by Tb in ZnO lattice is expected to result in an expansion of the lattice. This increase in lattice size is commonly used to evidence the presence of the dopant atoms occupying either Zn sites or interstitial sites or both. *Figure V.5.a* shows that for all doped samples, the c-parameter increases as compared to the undoped one, reflecting an expansion in the lattice. This expansion in lattice indicates that the Tb ions are successfully incorporated and likely replaced Zn^{2+} ions or interstitial sites.

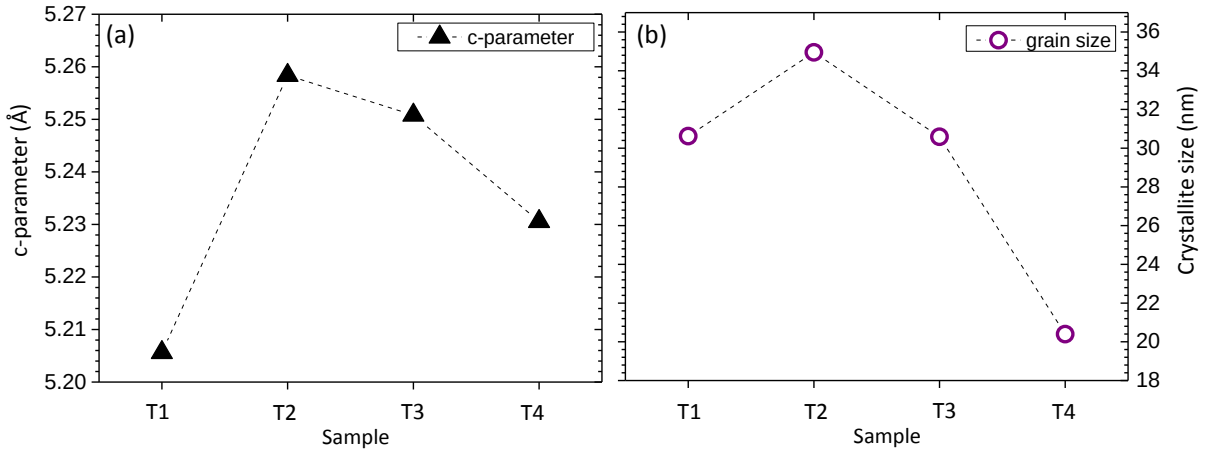

Figure V.5: The lattice c-parameter (a) and the crystallite size (b) of each sample deduced from XRD results.

It can also be observed that upon annealing and by increasing the annealing temperature, the c-parameter of doped thin films (T2, T3 and T4) becomes smaller. Lower c-parameter values indicate that the stress in the lattice (partially generated due to the insertion of dopants) is reduced.

The crystallite size can be estimated by Scherrer's formula using the peak width at full-width-half maximum

$$D_c = \frac{K\lambda}{\beta_{2\theta}\cos\theta_{\max}}, \qquad \text{(V.4)}$$

where $\lambda = \lambda_{Co} = 1.79$ Å and K is a dimensionless shape factor typically in the order of 0.9, $\beta_{2\theta}$ is the peak broadening at FWHM intensity in radian, and θ_{max} is Bragg's angle. The results (*Figure V.5.b*) show that by increasing the annealing temperature the crystallite size is decreasing more likely because the defects are healed and the stress induced by the presence of the dopants in the lattice is reduced.

For all the Tb doped thin film samples presented in this work, no clear evidence of formation of new phases was observed. Kumar *et al*. have observed, for a Tb content more than 5 mol%, Tb_2O_3 phase can be formed which acts as luminescence killer centers [Kumar 2014]. This was not the case in our work.

More information about the structure of the samples can be obtained by Raman spectroscopy.

V.1.2 Raman spectroscopy

Raman spectroscopy was performed at room temperature using green light (λ=532 nm). The results are shown in *Figure V.6*.

The several main peaks can be observed on Raman spectra at 440, 584 and 646 cm^{-1} for all thin films. The peak at 440 cm^{-1} is ascribed to E_2(high) and the peak at 584 cm^{-1} is close to the location of both A_1(LO) and E_1(LO). Yang *et al.* have observed a peak at 584 cm^{-1} for Tb doped ZnO nanowires and they ascribed this peak to E_1(LO) [Yang 2008]. However, as we have mentioned in chapter IV, the presence of nitrogen in ZnO can also create vibrational modes at 580 cm^{-1}.

For all doped and annealed thin films, the intensity of the peaks at 440 and 584 cm^{-1} decreased as compared to the pure one.

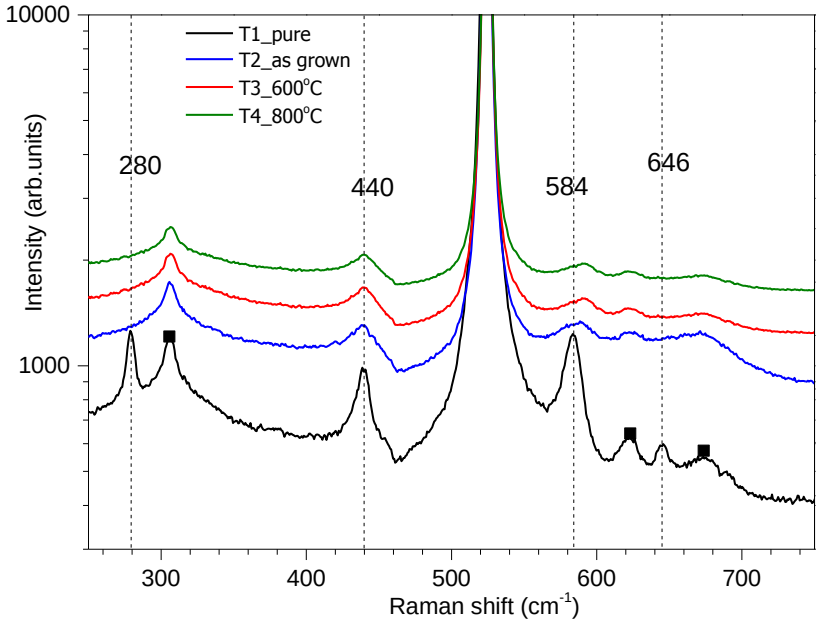

Figure V.6: Raman spectra of the ZnO:Tb thin films. The symbol (■) indicates the peaks related to the Si substrate.

A small shift and a broadening of the peaks after doping and annealing have been also observed. These changes in the peaks for doped thin films show that the crystal structure is degraded by introduction of dopants. This phenomena has been seen previously for Tb doped samples [Yang 2008].

Additional modes can be observed at 280 and 646 cm^{-1} for pure ZnO thin film which can be related to the presence of nitrogen due to the annealing. Nevertheless, the origin of these

modes is still controversial since they are not observed for the annealed Tb doped thin films. Atom probe tomography may bring additional inputs as reported in the following.

V.1.3 Atom probe tomography

As it was discussed before, the photoluminescence results suggest that difference in optical properties can be resulted from the different distribution and concentration of the luminescent centers due to the post deposition annealing process. The influence of annealing on concentration of the defects and distribution of the dopants is well-known. Annealing can heal the undesirable defects and lattice damages caused by introduction of dopants. Besides, annealing can also change the dopant distribution within the matrix and result in the formation of clusters or nanoparticles [Çetin 2007]. The concentration and distribution of the Tb dopants in ZnO thin films were thus carried out by atom probe tomography.

Figure V.7 shows the typical mass spectrum of ZnO:Tb obtained by APT using UV mode. Tb exists in only one stable isotopic mass of 159. Nevertheless in mass spectra, it mostly appears as Tb^{3+}, TbO^{2+}, TbO_2^{2+}, TbO^{+} and in some cases Tb^{2+} at the mass to charge ratio of 53, 87.5, 95.5, 175 and 79.5 a.m.u. respectively.

As a reminder, it is very important to keep in mind that, in APT analyses, Tb^{3+} only refers to the charge state of the evaporated ions and it should not be confused with the Tb in its trivalent charge state providing radiative centers.

Some extra nitrogen related peaks can also be observed in the mass spectrum shown with asterisk in *Figure V.7*.

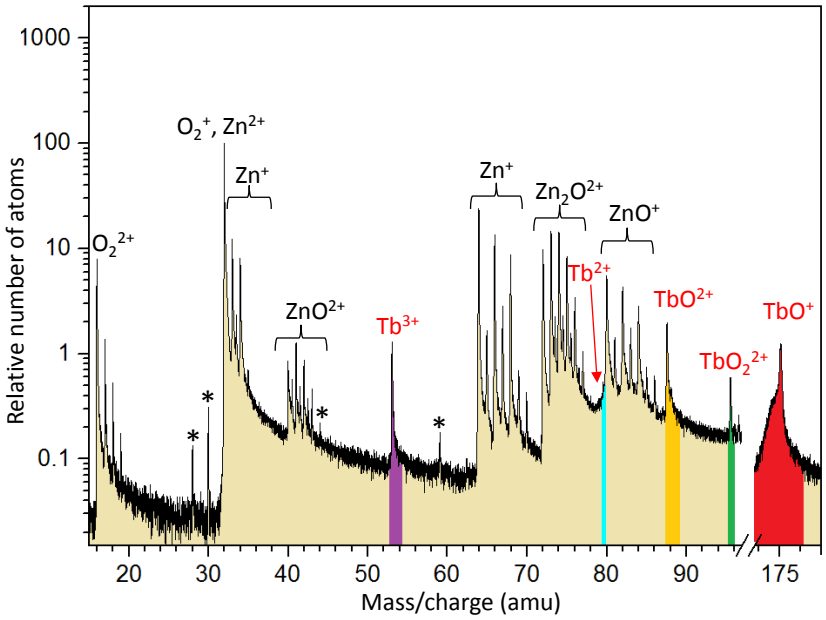

Figure V.7: Mass spectrum of ZnO:Tb thin film obtained by atom probe tomography. Tb-related peaks are shown in color.

The presence of nitrogen peaks was not highly pronounced in all the analyzed samples and hence its contribution as impurities can be due to the synthesis process or annealing under nitrogen atmosphere. Nevertheless, the presence of nitrogen peaks in mass spectra is consistent with the presence of nitrogen related Raman vibrational peaks at 280, 584 and 646 cm^{-1} discussed previously (*Figure V.6*)

The concentration of Tb for each sample is deduced from its APT mass spectrum obtained for the same volume size. The results are summarized in *Table V.2*.

Table V.2: Atomic concentration of Tb, Zn and O atoms in T2, T3 and T4 samples.

Atomic % (c ±Δc)	*T2*	*T3*	*T4*
Tb	*3.1 ± 0.1*	*1.7 ± 0.1*	*1.3 ± 0.1*
Zn	*52.2 ± 0.1*	*60.1 ± 0.1*	*47.0 ± 0.1*
O	*44.7 ± 0.1*	*38.3 ± 0.1*	*51.7 ± 0.1*

We have observed that less Tb concentration is detected for the annealed samples. For as grown ZnO:Tb thin film (T2), the atomic concentration is about 3.1 at.%, which is the expected value. However, for thin films annealed at 600 and 800°C, the Tb concentration is less than 2%. This change in concentration can be explained by either 1) diffusion of dopants

towards substrate or 2) APT artifacts. In both cases, a Tb detection loss can occur which is further studied in the following.

As we observed and reported in chapter III, the variation in concentration is ruled by APT conditions. We have discussed how to improve the quality of the APT of ZnO materials but the quantitative measurements yet needs further investigation. For a better comparison, Tb concentration of all samples is obtained with similar experimental conditions. For example, at the same laser pulse energy, the concentration of Tb for as grown and 800°C samples was measured to be 2.9 and 1.3 atomic percent, respectively. At the same charge state ratio, the concentration of Tb was found to be 3.1 and 1.3 atomic percent for as grown and annealed samples at 800 °C. These results show that, even if there is an influence of APT condition on the dopant concentration values, under the same condition, the Tb concentration of the as grown sample is always almost twice more than that of the annealed sample.

Nevertheless, yet, for a more reliable analysis, the influence of three APT variables (V_{DC}, flux and laser pulse energy) on the element composition of sample annealed at 600°C (T3) were studied (*Figure V.8*) [Mancini 2014].

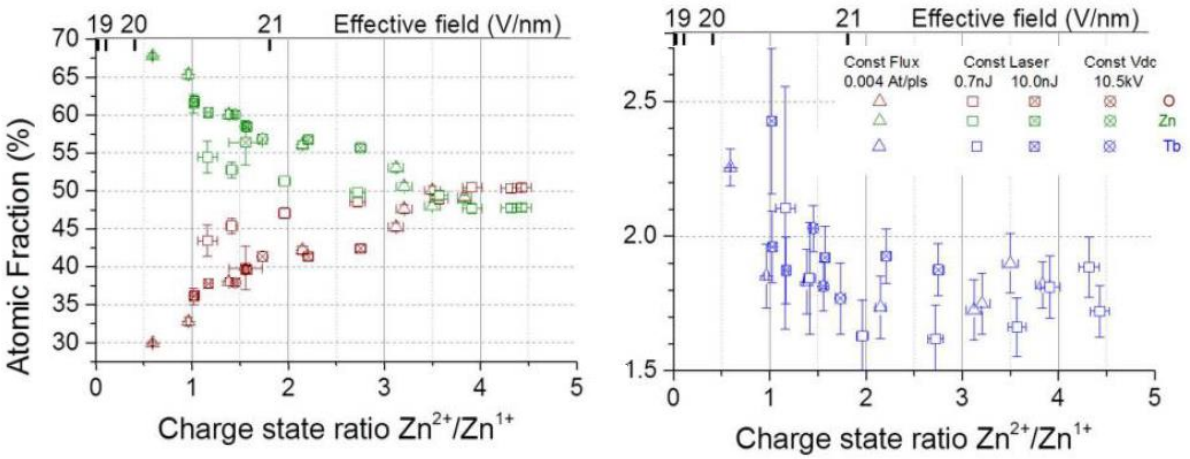

Figure V.8: Influence of surface electric field induced by different APT conditions on the measured composition of ZnO:Tb (sample annealed at 600°C). The variation in concentration of oxygen and zinc (left figure) and terbium (right figure) are shown in red, green and blue respectively [Mancini 2014].

Atomic concentration of zinc and oxygen exhibit the same behavior as it was seen previously in chapter III. Tb concentration exhibits a weak dependence on the surface electric field. Its value is stable around 1.7 atomic % at constant flux.

Thus, we can conclude that, the significant decrease in Tb content for annealed samples cannot be addressed to the loss of detection in atom probe tomography. This makes the hypothesis of migration of Tb atoms towards and into the substrate stronger. However, since the thickness of the films is more than 1.5 µm, the feasibility of Tb diffusion in such a large distance needs more investigation. Nevertheless, due to the thickness of the films, the APT analysis of such a large volume was not achieved in this work.

The 3D distribution of the Tb^{3+} ions in ZnO:Tb samples are shown in *Figure V.9*. At a first glance, the 3D distribution of the Tb atoms shows no formation of clusters in any of the analyzed samples.

For a more precise study, distribution of the Tb atoms is examined by frequency distribution and chi-square test. Sampling volume was chosen so that, each box of volume contains 500 atoms.

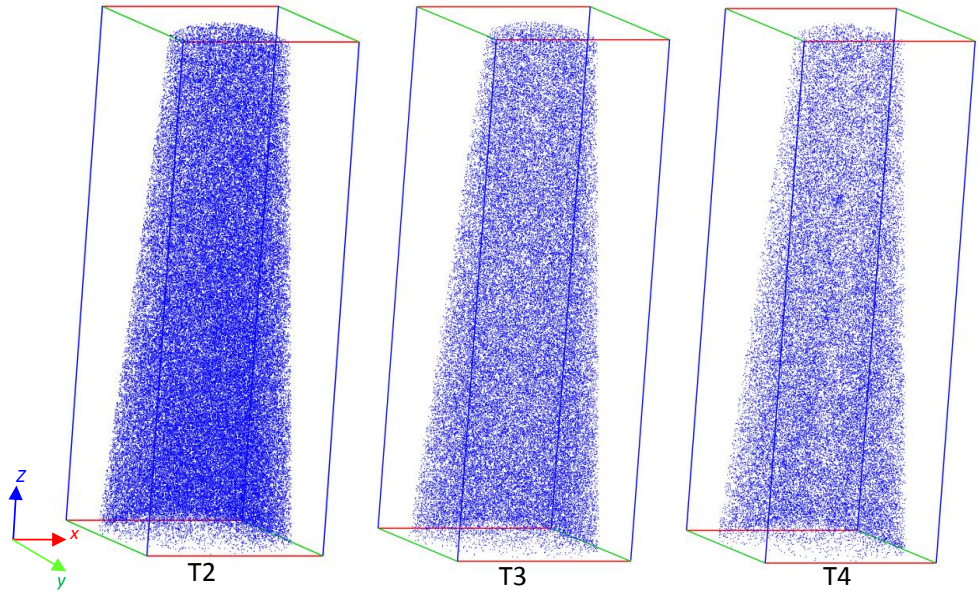

Figure V.9: Distribution of Tb atoms for three samples of T2, T3 and T4. For clarity reason only 50% of the atoms are shown and the analyzed volume is 38x38x107 nm^3.

The results are shown in *Figure V.10.a, b* and *c* corresponding to the distribution of Tb in T2, T3 and T4 samples. The number of Tb atoms found in each box is what is shown in the x-axis of frequency distribution plot. The experimental results retrieved from APT data are compared to the Poisson distribution. A deviation from homogenous distribution was observed for the samples annealed at 600 and 800°C. Chi-square test has confirmed the uniform distribution of Tb atoms in as grown sample (T2) and non-homogenous distribution for annealed samples (T3 and T4).

Although chi-square test is a common technique in investigation of the distribution, these sorts of tests are highly dependent on the size of the sampling box used for the determination of composition.

Philippe *et al*. have developed a new more sensitive approach to define the tiny clusters that requires no statistical sampling [Philippe 2009]. This approach is based on the first nearest neighbor (1NN) distances between solute atoms in a volume containing solvent and solute atoms. Using this approach can allow us to define even the very tiny cluster which is usually a tricky task in both atom probe tomography and atomic simulations.
Further information about this approach can be found in the annex.

Figure V.10.d, e and *f* present the 1NN approach for T2, T3 and T4 respectively. We can observe that for as grown sample (*Figure V.10.d*), only one atomic distance for Tb atoms can be observed centered at about 0.8 nm. The distribution is homogenous and no cluster can be observed. However, for annealed samples, such as T3, the 1NN approach (*Figure V.10.e*) reveals two peaks corresponding to two different distances. This means that in the sample annealed at 600°C, there are two characteristic distributions: some Tb atoms at the distance of about 0.7 nm (so called phase A) from each other and some others at the distance of 1.1 nm (called phase B).

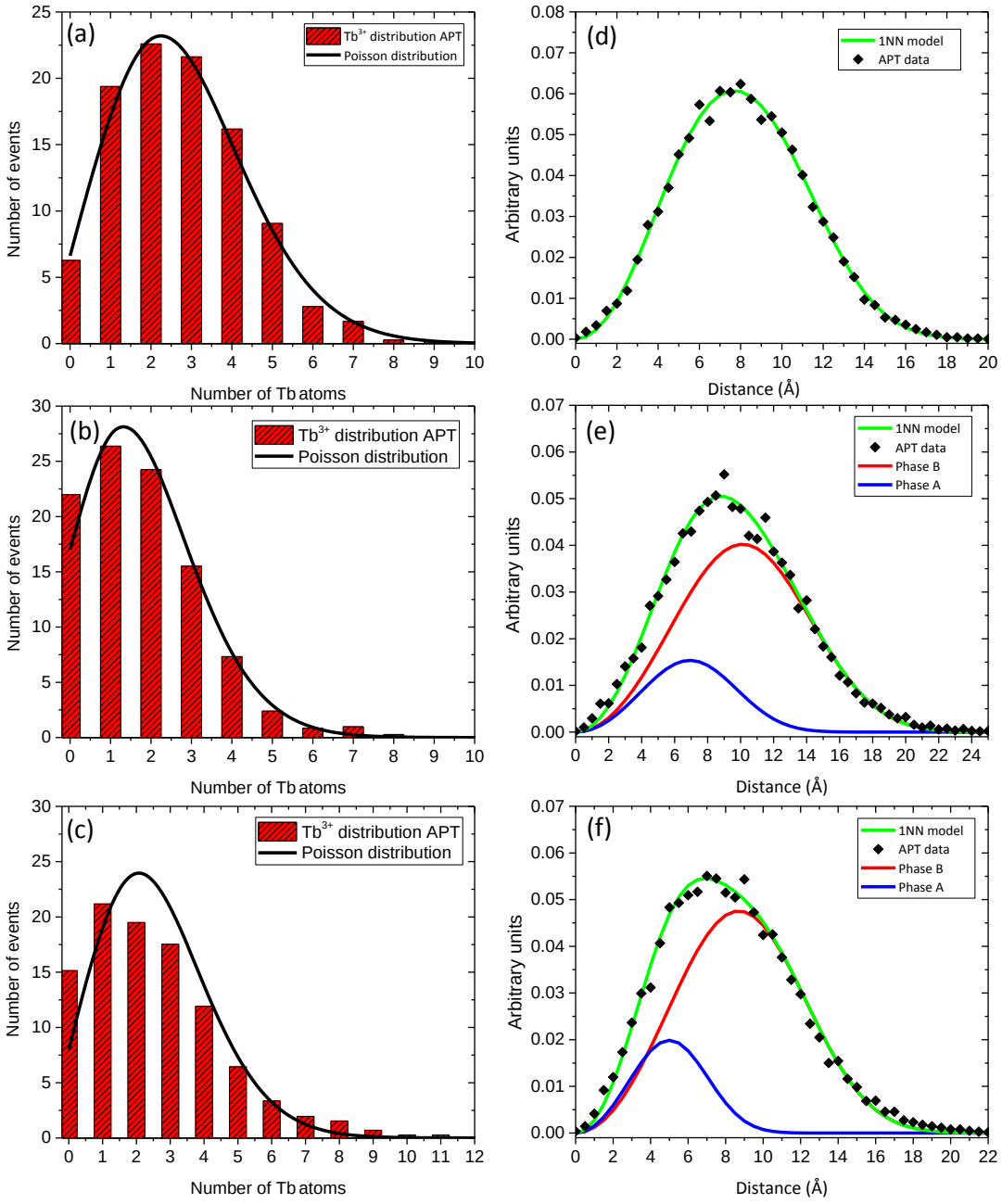

Figure V.10: Distribution of Tb atoms for three samples of T2, T3 and T4 using two approaches (a), (b), (c) frequency distribution (d), (e) and (f)1NN approach, respectively.

The 1NN approach for the sample annealed at 800°C reveals a non-uniform distribution of Tb atoms as well. The two observed "phases", show smaller atomic distances: 0.9 and 0.5 nm for phase B and phase A respectively. This means that by increasing the annealing temperature, the Tb atoms diffuse and tend to aggregate.

Hence, we can conclude that annealing favors Tb atoms aggregation, towards formation of stable clusters. Nevertheless, to support this idea, further analysis should be performed on

the samples annealed at much higher temperatures or/and during longer time in order to follow the influence of the annealing temperature on forming larger Tb clusters.

Non-uniform distribution of Tb atoms in both samples T3 and T4 (with maximum and minimum optical properties) casts doubt on whether the loss in optical properties is only due to non-uniform distribution of Tb. Nevertheless, Kumar *et al.* have observed for a small critical distance between the neighboring Tb^{3+} ions, non-radiative energy transfer between Tb^{3+} ions can occurs as a result of an exchange interaction or a multipole-multipole interaction [Kumar 2014].

However, in our work, it is not quite clear if such a small change in Tb distribution after annealing can actually cause such a severe loss in Tb-related emissions described previously (*Figure V.2*). This can lead to the possible conclusion that the loss of luminescence by annealing at 800°C is associated with the strong loss of ZnO defects that participate in energy transfer. This means the loss in Tb-related emissions. Besides, the presence of zinc silicate observed by XRD (*Figure V.4*), can act as the mediator for Tb-luminescence.

As annealing at 600°C shows the maximum optical properties in the visible range, we can conclude annealing at this temperature provides optimum crystal properties and Tb atom incorporation in ZnO film for excitation of Tb atoms.

Nevertheless, some other possibilities should also be taken into account influencing the optical properties of ZnO:Tb films such as migration of Tb atoms towards and into the substrate and/or the presence of Tb atoms that are not in their trivalent state. Each of these events can also result in the loss of Tb-related transitions which needs more investigations.

V.2 Ytterbium doped ZnO thin films

Yb doped ZnO thin films were grown using magnetron sputtering at Institut de Physique et de Chimie de Strasbourg laboratory (IPCMS) with the conditions explained in II.1.1. Previously, different techniques have been used in order to grow Yb doped ZnO thin films such as spray pyrolysis [Soumahoro 2011], thermal decomposition of Yb-doped zinc carbonate hydroxide [Shestakov 2012] and wet chemistry route [Otal 2015]. Among all techniques, magnetron sputtering is expected to offer a more homogenous distribution of Yb ions and therefore better optical properties. However, as it was mentioned in II.1.1, different growth parameters can directly affect the crystal quality and the distribution of the impurities.

The influence of annealing and growth temperature on ZnO:Yb thin films properties were studied. Yb doped thin films were prepared at two different growth temperatures of 15 and 400°C. ZnO:Yb thin film grown at 15°C was then annealed for 10 minutes at 700°C in Ar atmosphere. The films have a thickness of less than 100 nm. *Table V.3* presents a list of samples with their corresponding elaboration conditions.

Table V.3: List of studied Yb doped ZnO thin film samples prepared at IPCMS Strasbourg.

Sample	*Y1*	*Y2*	*Y3*
growth temperature(°C)	*15*	*400*	*15*
annealing temperature (°C)	*–*	*–*	*700 °C for 10 min*
thickness (nm)	*100*	*100*	*100*

V.2.1 XRD, structural and morphological properties

Figure V.11 presents the XRD results obtained on ZnO:Yb samples. Due to the small thickness of the thin films (<100 nm), strong signals from Si substrate can be observed.
The XRD pattern of all the samples, exhibit a peak at about 40° corresponding to the (002) orientation of the thin films. This peak shows a small shift towards higher 2θ values for the two samples Y2 and Y3. The XRD pattern of the sample Y2 (grown at 400°C) shows a peak related to the growth along (004).

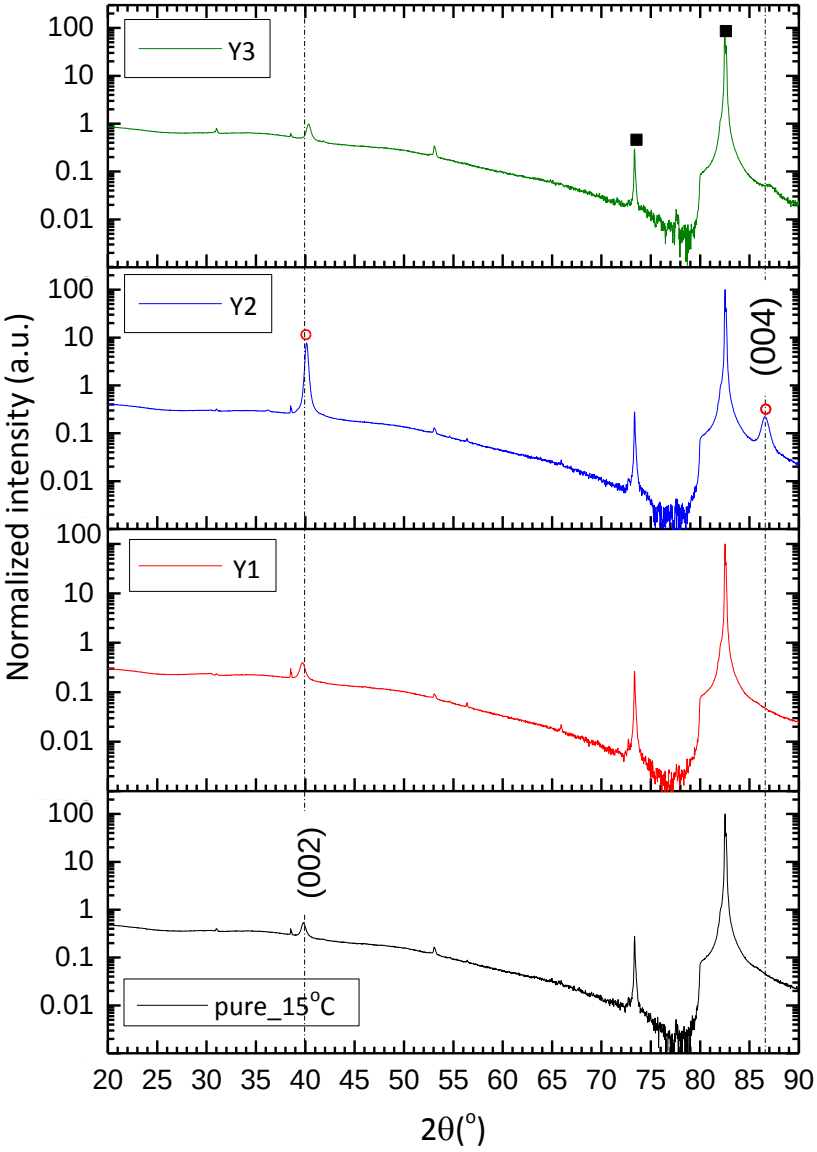

Figure V.11: XRD results obtained for ZnO:Yb samples. The intensity is normalized for better comparison. The symbol (■) indicates the peaks related to the Si substrate.

This peak appears when the crystallinity of the sample is good. For the sample annealed at 700°C, we observe broad (002) peak and small (004). Some low-intensity peaks can also be observed in XRD patterns related to a new phase which could be attributed to the $Zn_xSi_{1-x}O$ phase. This phase results from the Si diffusion across the film/substrate interface. Nevertheless, in all doped samples, no new phases associated with the presence of Yb could be found in the XRD patterns.

c-parameter and crystallite size of the thin films are deduced from the XRD results and shown in *Table V.4*. We can observe that introducing the Yb atoms in ZnO matrix has not

significantly modified the c-parameter value of the sample grown at 15°C (Y1) compared to the undoped sample. However, deposition at higher temperature (Y2) or after annealing (Y3) resulted in smaller c-parameter values, indicating a lower stress in the lattice. Annealing at 700°C could reduce the stress in the lattice caused by introduction of the Yb atoms and thus, exhibits a smaller lattice parameter (5.19 Å) compared to the one obtained before annealing (5.27 Å).

Comparing the crystallite size of the as grown ZnO:Yb sample (Y1) to the pure ZnO, we can observe a significant decrease. This decrease in crystallite size for sample Y1 is then partially recovered by annealing at 700°C (Y3). The smaller crystallite size of Y1 sample can reflect that introduction of Yb atoms creates lattice stress and Yb-related defects. These defects can prevent the grain growth and the increase in the crystallite size in sample Y3 shows that these defects are partially healed after annealing.

The highest crystallite size was obtained for the sample grown at 400°C (Y2). At this temperature, the diffusion of the Yb atoms in ZnO is stimulated which results in a lower concentration of defects and hence allows for a larger growth of the grain. Considering the significant difference in the crystallite size of the samples grown at 15°C and 400°C, we can conclude that the crystallite size is strongly dependent on the growth temperature rather than the annealing temperature. However, complementary information should be provided by annealing sample grown at 400°C under the same condition as the sample Y3.

Table V.4: List of studied Yb doped ZnO thin film samples prepared at IPCMS Strasbourg.

sample	*ZnO pure*	*Y1*	*Y2*	*Y3*
c-parameter (Å)	*5.26*	*5.27*	*5.22*	*5.19*
Crystallite size (nm)	*22.27*	*17.17*	*29.52*	*20.70*

The morphology of the samples were studied by atomic forced microscopy (AFM) as shown in *Figure V.12* [Balestrieri 2014].

The surface is mainly formed by small grains. The root-mean-square (RMS) of roughness measured for Y1, Y2 and Y3 samples are 1.61, 2.21 and 1.53 nm, respectively. The AFM results exhibit that higher growth temperature (400°C) results in larger grains and a higher surface roughness as compared to the thin film grown at 15°C. The annealing of the sample

grown at 15°C (Y3) could not result in a significant change in the morphology of the sample (*Figure V.12.c).*

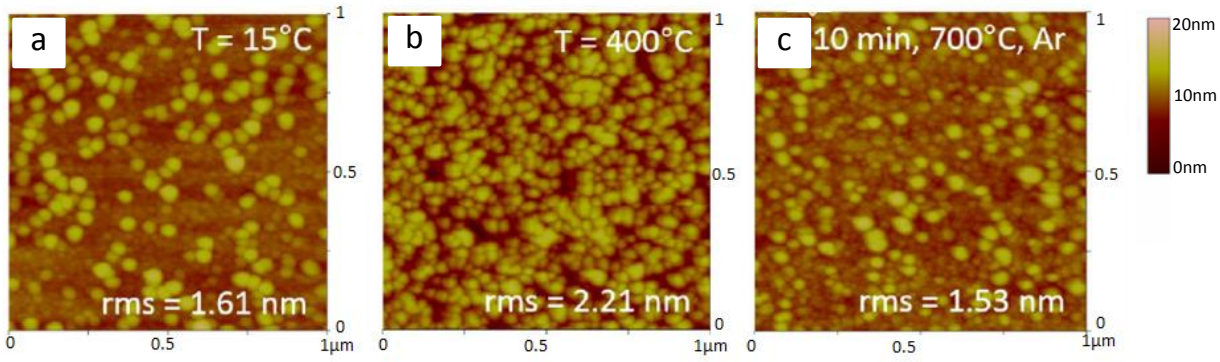

Figure V.12: AFM images of ZnO:Yb samples (a)Y1, (b)Y2, and (c)Y3 exhibiting the influence of deposition temperature and annealing on surface morphology [Balestrieri 2014]

The AFM results shown here are consistent with the results discussed for crystallite size in a way that the higher growth temperature leads to a major grain growth and also yields an increase in the surface roughness. However, annealing has shown a much smaller influence on the grain size.

Further information about the crystalline structure of the thin films was carried out by TEM analysis. *Figure V.13* shows the TEM and high resolution TEM images of ZnO:Yb thin film grown at 400°C (Y2).

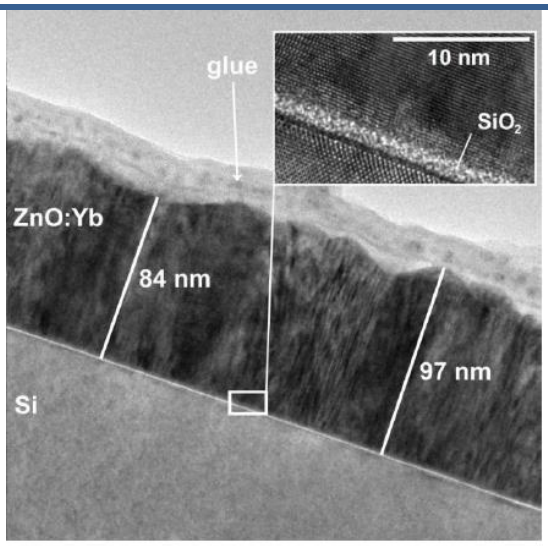

Figure V.13: TEM and HRTEM image of ZnO:Yb thin film deposited at 400°C grown on Si substrate [Balestrieri 2014].

The thin film shows a thickness of about 84 nm. At the interface of ZnO:Yb/Si, we can note the presence of a SiO_2 layer of about few nm thick. The formation of the SiO_2 layer is commonly observed for ZnO and other materials grown on Si substrate [Lardé 2011].

V.2.2 PL and luminescent properties

As it was discussed in *Figure I.11*, Yb creates only one luminescent line caused by $^2F_{5/2} \rightarrow {}^2F_{7/2}$ transition with a separation energy level of 1.3 eV (~950 nm). *Figure V.14* shows the schematic mechanism of the transitions in Yb doped ZnO.

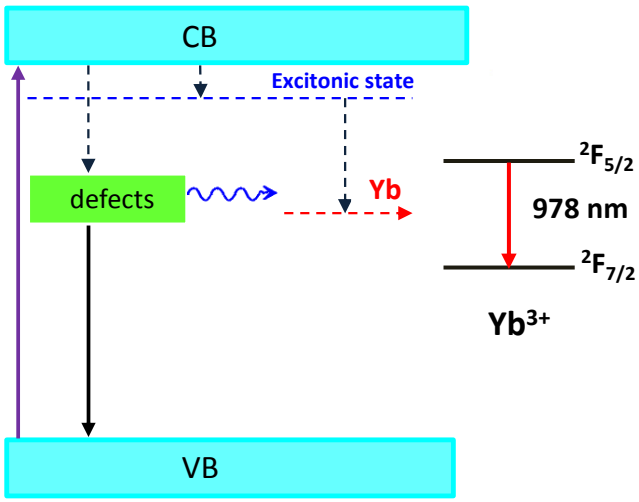

Figure V.14: The possible mechanisms leading to radiative recombination of Yb in ZnO matrix.

Figure V.15 shows the PL spectra of Yb doped samples using an excitation wavelength of 355 nm at room temperature. PL measurements were also carried out for the undoped thin film as a reference. The Yb-related transition at the excitation wavelength used in here provides indirect transition involving an energy transfer from the trap levels.

The Yb-related transition line at 978 nm can be observed in PL spectra of all ZnO:Yb thin films. This transition is minimum for the Y2 sample (grown at 400°C) and maximum for the sample annealed at 700°C (Y3).

Comparing the sample grown at 15°C after and before annealing (Y1 and Y3), we can observe that Yb-related transition is strongly enhanced after annealing at 700°C. Similar behavior has been previously seen for ZnO:Tb thin films annealed at 600°C. On the other hand, considering the two samples of Y1 and Y2 grown at 15 and 400°C respectively, we can

observe that the increase of the growth temperature from 15 to 400 °C, diminishes the Yb-related luminescent in ZnO.

Two important points can be extracted from PL results. First, annealing at 700°C can increase the Yb emission 43 times more than that of the same sample before annealing. Second, the increase in growth temperature from 15 to 400°C reduces the Yb emission (5 times smaller).

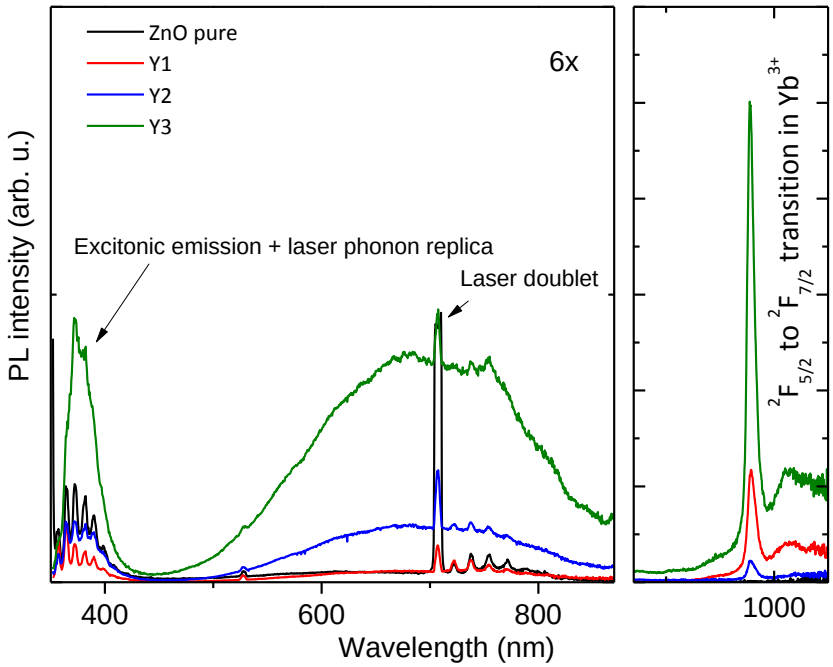

Figure V.15: Photoluminescent measurements of ZnO:Yb thin films using excitation wavelength of 355nm at room temperature [Balestrieri 2014].

As it was mentioned before, the emission from Yb is achieved through an indirect excitation mechanism with association of the matrix defects. Therefore, annealing at 700°C for 10 minutes is sufficient to reduce and to heal the stress created due to the presence of the Yb ions and provide a better distribution in ZnO leading to an improvement in luminescence of Yb ions. Nevertheless, the growth at 400°C can lead to the formation of much smaller amount of ZnO defects. As these defects participate in indirect excitation of the Yb ions, their lower concentration can be the reason of a lower Yb-related emission.

Other possibilities resulting in such changes in optical properties can be also attributed to the concentration of the incorporated Yb atoms, dopant distribution within the matrix or the diffusion of the dopants into the substrate. These issues are further studied by atom probe tomography.

V.2.3 Atom probe tomography

APT analysis has performed on all ZnO:Yb samples. *Figure V.16* shows a typical mass spectrum obtained by APT of Yb doped ZnO grown at 15°C.

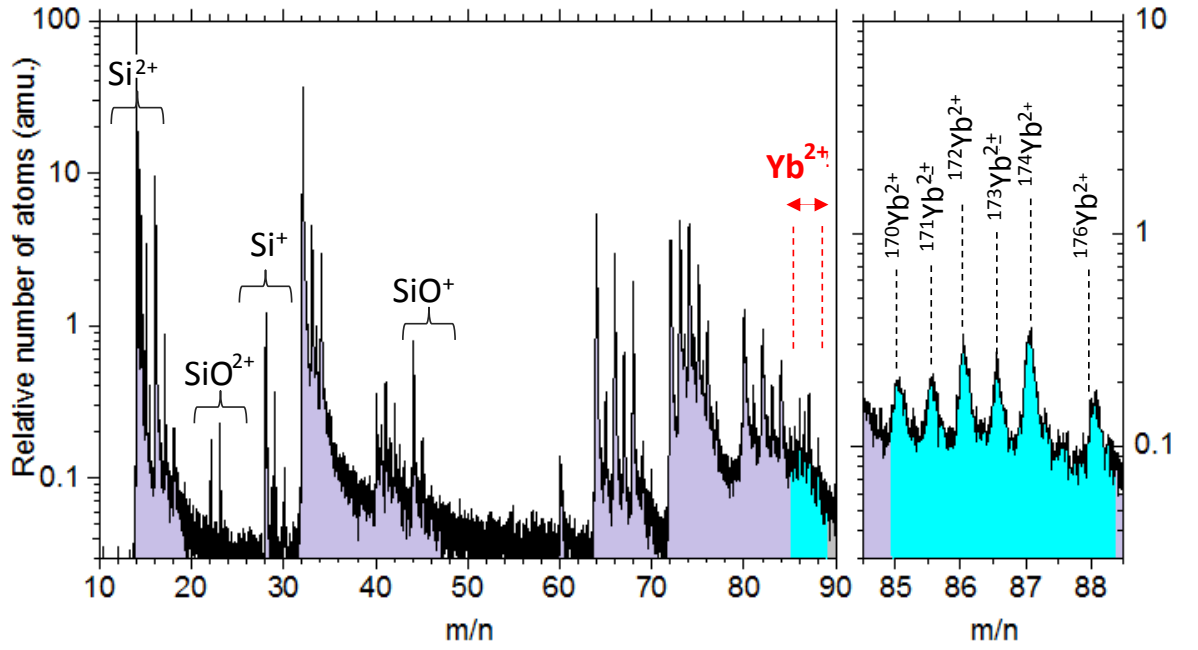

Figure V.16: Mass spectrum of Yb doped ZnO thin film grown at 15°C obtained by APT using UV laser mode. The peaks related to Yb elements are magnified and shown on left figure.

Ytterbium has seven isotopic mass. The different isotopic values of Yb and their abundancy are presented in *Table V.5*.

Table V.5: Yb isotopic abundancy and their relative mass to charge ratio

Isotope (Yb)	*168*	*170*	*171*	*172*	*173*	*174*	*176*
Natural abundance (atm%)	*0.13*	*3.04*	*14.28*	*21.83*	*16.13*	*31.83*	*12.76*
Charge state 2+ (Yb^{2+})	*84*	*85*	*85.5*	*86*	*86.5*	*87*	*88*

Yb concentration was deduced from the APT results shown in *Table V.6*. We can observe that the Yb concentration of 1.13 at.% was found for the ZnO:Yb sample grown at 400°C which is lower than the ones of two others grown at 15°C.

Table V.6: Atomic concentration of Yb atoms for Y1, Y2 and Y3 doped thin films.

Sample	*Y1*	*Y2*	*Y3*
Yb atomic concentration% (c)	*1.49*	*1.13*	*1.64*
± Δc	*0.03*	*0.03*	*0.03*

Energy-dispersive X-ray spectroscopy has been also performed in order to verify if this change in concentration is not caused by any APT artifacts.

EDX results also confirmed the presence of a lower Yb content for sample grown at 400°C (Y2) and higher Yb content for the sample grown at 15°C with annealing at 700°C (Y3).

Nevertheless, the difference in Yb content of the sample grown at 400°C as compared to the as grown one seems to be too small to be responsible for a 5 times lower Yb emission observed previously (*Figure V.15*).

3D maps of Yb atoms distribution for each ZnO:Yb sample are presented in *Figure V.17*. No formation of cluster or nanoparticles was observed in all samples.

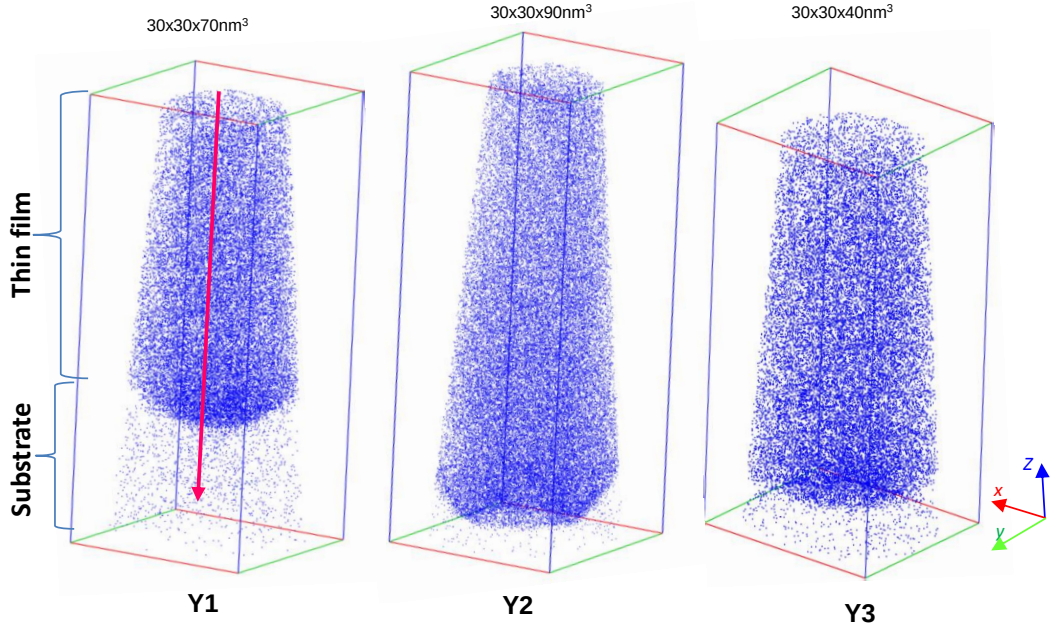

Figure V.17: 3D distribution of Yb atoms in different thin films Y1, Y2 and Y3 obtained by APT analysis exhibiting the Si/ZnO interface.

The homogeneity of the Yb atoms in ZnO thin films (far from substrate) was examined by Chi-square test. The frequency distributions of the Yb atoms for all three samples are shown in *Figure V.18.a, b* and *c* for a sampling box of 500 atoms and compared to a random

Poisson distribution. Each bar indicates the number of Yb atoms found in a volume of 500 atoms.

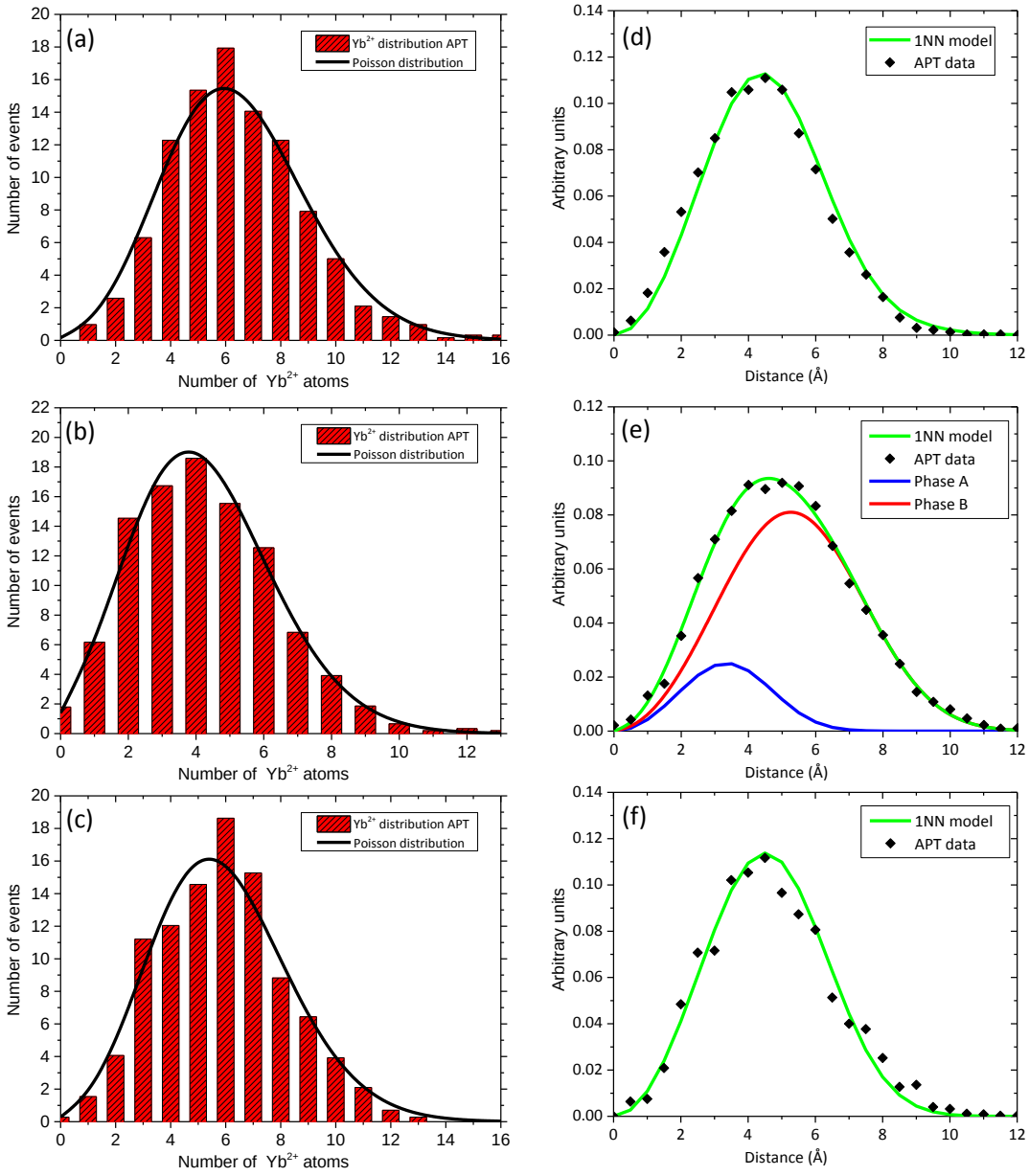

Figure V.18: Distribution of Yb atoms for three samples of Y1, Y2 and Y3 using two approaches (a), (b), (c) frequency distribution (d), (e) and (f)1NN respectively.

The results show a uniform distribution of Yb atoms for the sample grown at 15°C before and after annealing (Y1 and Y2 samples). In case of sample grown at 400°C, a non-uniform distribution was observed.

1NN approach has also been applied and is shown in *Figure V.18.d, e* and *f*. For the sample grown at 15°C, a uniform distribution of Yb atoms was confirmed both by chi-square

test and 1NN approach. This uniform distribution was conserved even after annealing at 700°C. Nevertheless, the distribution of Yb atoms in the sample grown at 400°C exhibited a slight deviation from uniform distribution. 1NN approach shows "two phases" where Yb ions are mostly at a distance of 0.35 and 0.55 nm from each other. From the results discussed above, we can conclude that the lowest Yb-related emission is observed where the distribution of Yb is non-uniform. Previously, for Tb doped ZnO films, we have observed that the distributions of Tb dopants were non-uniform for both samples with maximum and minimum Tb-related emissions. Hence, the distribution of dopants may not be the only reason affecting the loss in Yb-related emission. Nevertheless, there is still a chance that under a critical distance between the dopant atoms, the influence of non-uniform distribution of dopant becomes more important.

Figure V.19.a shows the concentration profile of the elements along z-axis and towards the substrate of the Y1 analyzed volume. At the interface of ZnO and Si substrate of the sample grown at 15°C (Y1), a thin layer of silicon oxide can be observed.

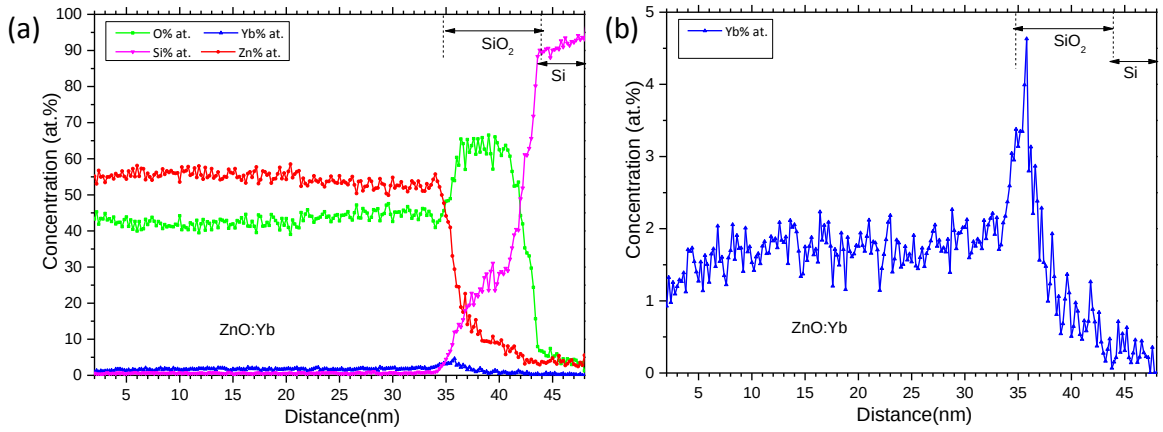

Figure V.19: (a) Concentration profile of different elements along z axis towards Si substrate of the analyzed samples obtained by APT of Y1 sample, (a) magnified view of Yb concentration profile

The presence of this layer has been previously seen by HRTEM (*Figure V.13*). No ytterbium atoms were found in Si substrate.

The concentration profile of Yb for each sample shows Yb segregation at the interface of ZnO/Si which appeared to be independent from the growth conditions used here. The same situation was previously observed for Co doped ZnO film where the Co dopants tend to occupy the sites closer to the interface [Lardé 2011].

Considering higher Yb-related emission of annealed sample (Y3) as compared to its emission before annealing (Y1), we can conclude that annealing at 700°C healed the defects and stress in the lattice caused by the presence of the Yb atoms (exhibiting a smaller c-parameter) resulting in better optical properties. On the other hand, the growth temperature of 400°C generates fewer defects (which also lead to a larger crystallite size). Considering the role of defects in Yb-emissions, lower quantity of defects can be the reason of a loss in Yb-related emission.

V.3 Conclusion

In this chapter, we have investigated ZnO thin films doped with two different rare earth elements, namely terbium and ytterbium. The influence of growth parameters such as growth and annealing temperature on optical and structural properties of the samples were discussed. It was observed that for ZnO:Tb films, the annealing up to 600°C can significantly enhance the Tb-related emissions. However, annealing above this temperature, revealed a drastic loss of these emissions. For ZnO:Yb thin films, it was observed that increasing the growth temperature from 15 to 400°C could diminish the Yb-related transition. Nevertheless, annealing the sample grown at 15°C at the annealing temperature of 700°C could significantly enhance the Yb-related transition. This behavior was observed previously and was mainly addressed to optical activation, cluster-like distribution and migration of the REE within the matrix. In this work, thanks to atom probe tomography technique, we have observed that the distribution of the Tb and Yb atoms within the ZnO matrix has no or small contribution in optical properties of the samples. Hence, the variation in optical properties can be attributed to the presence of the defects and the concentration of the optically activated rare earth elements within ZnO matrix. However, in order to support this idea, further investigation on a wider range of samples is necessary. ZnO:Yb thin films annealed at 700°C and ZnO:Tb films annealed at higher temperatures (higher than 1000°C) are good examples for a complementary investigation of the annealing effects on optical properties and a possible cluster formations respectively.

Conclusions and perspectives

The context of this work concerns the large interests in application ZnO nanomaterials in optoelectronic and electronic device as it was discussed in the introduction. Due to its unique properties, ZnO is an unrivaled semiconductor as compared to the commonly used large band gap semiconductors. Nevertheless, finding an efficient and reliable synthesis and doping process has been the subject of many research efforts over decades. In recent years, due to the advances in both understanding the physical properties of ZnO and development of techniques, the number of reports and associated literature has been intensified. However, despite these efforts, a reliable method of synthesis and doping was not well-established. Particularly, in case of p-type doping of ZnO nanomaterials the reproducibility of the method is still a challenge. Although many new and advanced methods have been developed for synthesis of doped ZnO materials, the same conventional characterization techniques are yet used to identify the observed phenomena or properties. As these techniques are subjected to many technical limits or resolution, they are not always able to provide a clear answer. In this work, we have introduced the application of laser assisted atom probe tomography as a main characterization technique to study the incorporation of dopant in ZnO matrix. The results obtained by this technique could pave the way to have a better understanding of the results observed by conventional techniques.

In chapter II, first, the samples studied in this work, with their synthesis processes were described. In the second part of the chapter, the conventional characterization methods used in this work namely TEM, photoluminescence and Raman spectroscopy are introduced.

The samples were then analyzed at atomic scale by laser assisted atom probe tomography in order to obtain the chemical information and spatial distribution of the elements and dopants. The application of this technique for ZnO materials has barely been discussed previously. Hence in chapter III, after a detailed description of atom probe tomography technique, we give a close insight into the interaction of laser-ZnO materials (femtosecond pulses on nanosamples). Two different ZnO nanostructures, thin film and nanowire, were studied. It has been shown that the measured concentrations of oxygen and zinc are strongly dependent on the analysis parameters (laser wavelength, laser pulse energy and continuous voltage value). We have also shown that lower surface electric field on the specimen is obtained for high laser energies resulting in biased zinc-rich measurements. Inversely, decreasing the laser energy creates higher electric field under which the oxygen deficiency is recovered. Further

decrease of the laser energy has shown to result in biased oxygen-rich measurements observed in both UV and green laser modes. The reason behind this behaviour is yet ambiguous. Nevertheless, we have proposed several explanations: 1) the formation of neutral oxygen at lower field which remain un-detected and result in oxygen deficiency, 2) evaporation of the zinc atoms between or after pulses causing lower detection of zinc atoms at higher field, 3) crystallographic poles which creates non-uniform surface electric field at higher laser energy. We have shown that stoichiometric APT measurement is possible for a precise range of surface electric field (Zn^{2+}/Zn^{+} ratio around 3.5) in both UV and green mode regardless of the morphology of the specimen. Since in green mode, the field evaporation of ZnO materials requires a stronger increase in V_{dc}, hence we consider UV laser mode as a more appropriate analysis condition. Same variation in concentration with laser energy has been also observed for the doped ZnO materials. Hence, in order to avoid non-uniform surface electric field and non-stoichiometric measurement, we suggest performing analysis at lower laser pulse energy. Further investigations using this technique along with other conventional techniques are the subject of the chapters IV and V.

The main objective of this project was to produce p-type ZnO nanowires for application in 1-dimensional ZnO homo-junctions. Phosphorous and nitrogen doped ZnO nanowires were grown using *ex-situ* and *in-situ* processes respectively. The results presented in chapter IV deal with the reliability of each doping process. Hence, each series of samples were examined by different techniques. In case of spin on doped *ex-situ* phosphorous doping of ZnO nanowire, Raman, photoluminescence and EDX could not confirm the presence of the dopants. The atom probe tomography analyses of the nanowires confirmed the absence of the phosphorous dopants both in the nanowires and the wetting layer. The spin-on doping process involves the diffusion of phosphorous atoms from a coating layer into the core of the nanowires at high temperature, followed by the removal of the coating layer via an etching process. Hence, the reason behind the absence of the P atoms can be due to the annealing conditions. For example, low annealing temperature and short annealing time can only allow for diffusion close to the surface of the nanowire which eventually, was removed by the strong etching. TEM and SEM images have also shown the presence of a porous layer around ZnO nanowire which is formed due to the strong etching. In case of nitrogen doped ZnO grown by MOCVD, the presence of nitrogen was confirmed by Raman and photoluminescence. Atom probe tomography has shown a uniform distribution of nitrogen dopants in ZnO nanowires, with a concentration of about 3.4 $x10^{20}$ $atom.cm^{-3}$. Nevertheless,

the field effect transistor test has shown an n-type conductivity of the nitrogen doped ZnO nanowires.

In chapter V, we have described ZnO thin films grown by magnetron sputtering doped with terbium and ytterbium in order to obtain the light emission near or in the visible. The influence of annealing and growth temperature on optical properties of the samples, were studied. It was observed that for Tb doped samples, post-deposition annealing up to 600°C, strongly increases the Tb-related emissions whereas above this temperature, an optical quenching was observed. Generally accepted reasons of this optical quenching reported in the literature were addressed to the formation of new phases such as terbium oxide and/or formation of nano-particles and clusters at high annealing temperatures. These phases can act as luminescent killers. In our work, XRD and Raman results confirmed the absence of the new phases. Atom probe tomography results have also shown that there is no formation of clusters that could be related to the loss of optical properties at 800°C. Nevertheless, using 1NN approach, we have observed that a new phase of Tb atoms is formed where Tb atoms are at a smaller distance to each other or in other words begin to aggregates.

In case of Yb doped ZnO thin films, an increase in growth temperature to 400°C resulted in the loss of Yb-emission. Annealing the as grown sample at 700°C could strongly enhance the Yb emission. We have observed that the growth at 400°C disturbs the distribution of Yb atoms and results in non-uniform distribution of the ions.

Nevertheless, in both cases of Tb and Yb doped ZnO thin films, it is hard to conclude that such a loss in optical properties is related only to the non-uniform distribution of dopant. Hence, it seems that strong change in optical properties is more likely related to the concentration of defects in ZnO matrix that participate in excitation of rare earth dopant.

However, for a better understanding of the effect of the annealing process, the study of new samples should be considered.

Many perspectives are suggested for improving both atom probe tomography measurements and incorporation of dopants.

To improve the atom probe tomography measurements, we suggest a delicate choice of samples. Analysis on a thin film containing multi-layers of doped ZnO with different dopant concentrations from highly doped to pure ZnO can help us to calibrate the APT measurements. The dopants should be chosen so that it will allow us to measure its precise concentration using techniques such as SIMS for a comparison with atom probe tomography results. The choice of substrate is also important, as for the aluminum doped multi-layer ZnO

deposited on sapphire; the diffusion of Al from substrate to the doped ZnO layers is possible which can influence the final conclusion.

In case of p-type doping of ZnO nanowires, some modifications in synthesis process are needed. For *ex-situ* doped ZnO, these modifications can be a better control on etching process, longer diffusion time, or using higher temperatures for diffusion of dopants.

In case of nitrogen doped nanowires, we have observed that the MOCVD results in a uniform distribution of dopants. Hence to track the conductivity of the nanowires, we suggest a series of nitrogen doped ZnO nanowires with different concentration of nitrogen in order to determine if the p-type conductivity can be obtained at any of these concentrations. Besides, for a better understanding of the influence of the growth condition on dopant incorporation, the diffusion of the dopants into the matrix can be predicted by simulations and be compared to the experimental results of APT.

In case of rare earth elements, we have observed that the increase of annealing temperature decreases the distance between Tb atoms. Hence, it is interesting to analyze the ZnO:Tb samples annealed at much higher temperatures in order to track the distribution of the dopants and their influence on the optical properties. In case of Yb doped ZnO, the annealing of as grown samples could strongly increase the Yb-related emissions without changing the uniform distribution. Hence, it is interesting to perform the same annealing condition for the sample grown at 400°C and to follow the influence of annealing on its optical properties and distribution of the Yb dopants.

Prior to this work, the fundamental studies of atom probe tomography of ZnO materials were unexplored. Hence the discussion we provided here and the suggested prospective can pave the way for much vaster application of atom probe tomography not only for ZnO materials but also for all II-VI and III-V semiconductors as well.

Annex

- **First nearest neighbor approach (1NN)**

1NN approach is used in order to identify the tiny clusters observed in APT volume reconstruction and to derive their compositions. The approach is based on the statistics of distribution for the first nearest neighbor distances (r) between solute atoms in the volume.
The theoretical distributions of the 1NN distances $P(r)$ can be described as,

$$P(r) = 4\pi r^2 Q C_0 \exp\left(-\frac{4}{3}\pi Q C_0 r^3\right) \quad , \tag{1}$$

where $P(r)$ gives the density probability to find two first nearest neighbor atoms at the distance r within dr. Q is the APT detection efficiency and C_0 is the observed concentration. The most probable 1NN distance (r_0) for random system can be obtained where the distribution $P(r)$ is maximum ($dP/dr=0$) and it is expressed as

$$r_0 = \left(\frac{1}{2\pi Q C_0}\right)^{1/3} \quad , \tag{2}$$

For a system with a uniform distribution of the atoms (*figure.1.a*), the 1NN model (using equations 1 and 2) can be calculated and compared to experimental data obtained by APT (*figure.1.b*). In both cases, only one maximum distance between atoms can be observed.

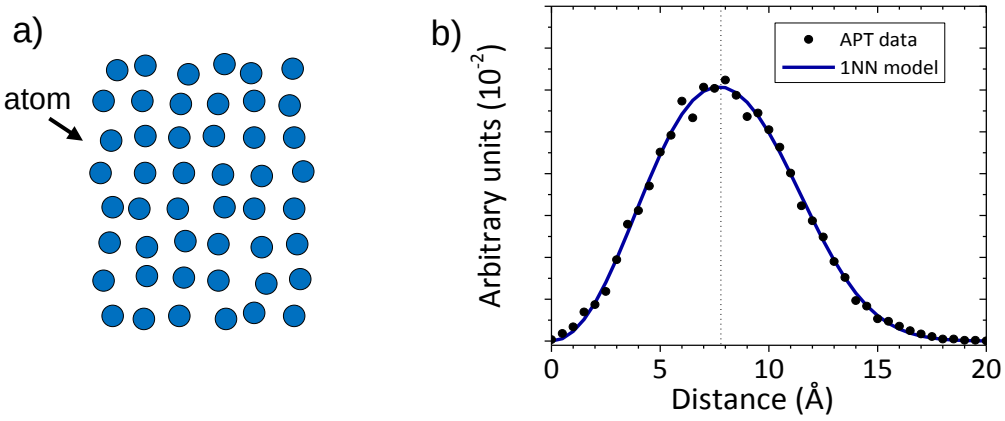

Figure.1.a) System with a uniform distribution of the atoms, b) distribution of the first nearest neighbour atoms obtained by APT as compared to the 1NN model. Only one most probable distance can be found at r~0.8 nm indicating a uniform distribution of atoms.

For a non-uniform distribution of the atoms (*figure.2.a*), more than one maximum distance is expected. Hence, in 1NN approach, the probability density *P(r)* for two distribution phases, (A) and (B), can be described as the sum of intrinsic distribution of each phase

$$P(r) = (1-f)[4\pi r_A^{\,2} Q C_A \exp(-\frac{4}{3}\pi Q C_A r_A^{\,3})] + f[4\pi r_B^{\,2} Q C_B \exp(-\frac{4}{3}\pi_B Q C_B r_B^{\,3})] \quad , \qquad (3)$$

where *f* is the atomic fraction and is described as

$$f = \frac{C_B}{C_A}(\frac{C_0 - C_A}{C_B - C_A}) \quad , \qquad (4)$$

The 1NN approach for a non-uniform distribution of atoms within a matrix is compared to the APT data (*figure.2.b).* 1NN approach shows two most probable maximum distances between atoms, indicating a small clustering of some atoms [Philippe 2009].

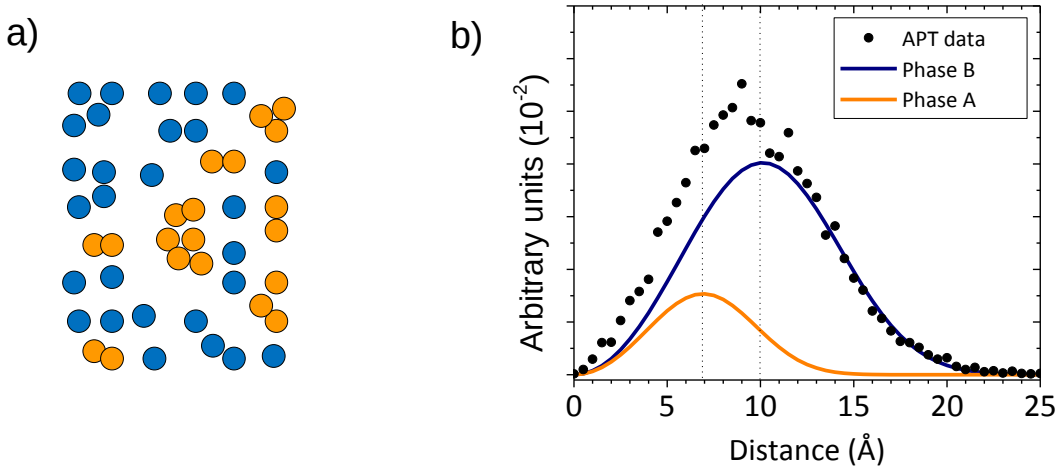

Figure.2.a) System with a non-uniform distribution of the atoms, b) distribution of the first nearest neighbour between atoms obtained by APT as compared to the 1NN model. The 1NN model shows the presence of two different distances between the atoms with the most probable distances of r~0.7 nm and r~10 nm indicating a non-uniform distribution of the atoms.

References

[Allred 1961] A.L. Allred, J. Inorg. Nucl. Chem., 17, 1961, 215.

[Alves 2009] E. Alves, N. Franco, N.P. Barradas, F. Munnik, T. Monteiro, M. Peres, J. Wang, R. Martins, E. Fortunato, Vacuum, 83, 2009, 1274.

[Amano 1989] H. Amano, M. Kito, K. Hiramatsu, I. Akasaki, Jpn. J. Appl. Phys., 28, 1989, l2112.

[Bachhav 2011] M. Bachhav, R. Danoix, F. Danoix, B. Hannoyer, S. Ogale, F. Vurpillot, Ultramicroscopy, 111, 2011, 584.

[Balestrieri 2013] M. Balestrieri, G. Ferblantier, S. Colis, G. Schmerber, C. Ulhaq-Bouillet, D. Muller, A. Slaoui, A. Dinia, Sol. Energy Mater. Sol. Cells, 117, 2013, 363.

[Balestrieri 2014] M. Balestrieri, Transparent conductive oxides with photon converting properties in view of photovoltaic applications : the cases of rare earth-doped zinc oxide and cerium oxide; Strasbourg, 2014.

[Bas 1995] P. Bas, A. Bostel, B. Deconihout, D. Blavette, Appl. Surf. Sci., 87–88, 1995, 298.

[Behrends 2009] A. Behrends, A. Bakin, A. Waag, Microelectron. J., 40, 2009, 280.

[Behrends 2012] A. Behrends, A. Wagner, M.A.M. Al-Suleiman, H.-J. Lugauer, M. Strassburg, R. Walter, A. Weimar, A. Waag, A. Bakin, Phys. Status Solidi A, 209, 2012, 708.

[Bhavanasi 2013] V. Bhavanasi, C.B. Singh, D. Datta, V. Singh, K. Shahi, S. Kumar, Opt. Mater., 35, 2013, 1352.

[Blumtritt 2014] H. Blumtritt, D. Isheim, S. Senz, D.N. Seidman, O. Moutanabbir, Nanotechnology, 25, 2014, 435704.

[Bundesmann 2003] C. Bundesmann, N. Ashkenov, M. Schubert, D. Spemann, T. Butz, E.M. Kaidashev, M. Lorenz, M. Grundmann, Appl. Phys. Lett., 83, 2003, 1974.

[Bünzli 2005] J.-C.G. Bünzli, C. Piguet, Chem. Soc. Rev., 34, 2005, 1048.

[Cadel 2009] E. Cadel, F. Vurpillot, R. Lardé, S. Duguay, B. Deconihout, J. Appl. Phys., 106, 2009, 044908.

[Cao 2011] L. Cao, L. Zhu, J. Jiang, R. Zhao, Z. Ye, B. Zhao, Sol. Energy Mater. Sol. Cells, 95, 2011, 894.

[Cerezo 1985] A. Cerezo, C.R.M. Grovenor, G.D.W. Smith, Appl. Phys. Lett., 46, 1985, 567.

[Çetin 2007] A. Çetin, R. Kibar, M. Ayvacıklı, Y. Tuncer, C. Buchal, P.D. Townsend, T. Karali, S. Selvi, N. Can, Surf. Coat. Technol., 201, 2007, 8534.

[Cetin 2009] A. Cetin, R. Kibar, S. Selvi, P.D. Townsend, N. Can, Phys. B Condens. Matter, 404, 2009, 3379.

[Chao 2013] L.-C. Chao, J.-W. Chen, H.-C. Peng, C.-H. Ho, Surf. Coat. Technol., 231, 2013, 492.

[Chen.W 2011] W. Chen, Modélisation de la croissance des nanofils de Si et métrologie à l'échelle atomique de la composition des nanofils. phdthesis, Université de Rouen, 2011.

[Chen.J 2004] J. Chen, Z. Feng, P. Ying, M. Li, B. Han, C. Li, Phys. Chem. Chem. Phys., 6, 2004, 4473.

[Chen.Y.J 2009] Y.J. Chen, C.H. Ho, H.Y. Lai, J.H. Du, JOM, 61, 2009, 23.

[Chen.Y.M 2011] Y.M. Chen, T. Ohkubo, K. Hono, Ultramicroscopy, 111, 2011, 562.

[Chen.D 2012] D. Chen, Y. Wang, M. Hong, Nano Energy, 1, 2012, 73.

[Chen.M.T 2010] M.-T. Chen, M.-P. Lu, Y.-J. Wu, J. Song, C.-Y. Lee, M.-Y. Lu, Y.-C. Chang, L.-J. Chou, Z.L. Wang, L.-J. Chen, Nano Lett., 10, 2010, 4387.

[Chikoidze 2008] E. Chikoidze, M. Modreanu, V. Sallet, O. Gorochov, P. Galtier, Phys. Status Solidi A, 205, 2008, 1575.

[Choi 2011] Y.-S. Choi, D.-K. Hwang, B.-J. Kwon, J.-W. Kang, Y.-H. Cho, S.-J. Park, Jpn. J. Appl. Phys., 50, 2011, 105502.

[Chu 2008] S. Chu, J.H. Lim, L.J. Mandalapu, Z. Yang, L. Li, J.L. Liu, Appl. Phys. Lett., 92, 2008, 152103.

[Cuscó 2007] R. Cuscó, E. Alarcón-Lladó, J. Ibáñez, L. Artús, J. Jiménez, B. Wang, M.J. Callahan, Phys. Rev. B, 75, 2007, 165202.

[Da Costa 2005] G.D. Costa, F. Vurpillot, A. Bostel, M. Bouet, B. Deconihout, Rev. Sci. Instrum., 76, 2005, 013304.

[Dawahre 2012] N. Dawahre, G. Shen, S. Balci, W. Baughman, D.S. Wilbert, N. Harris, L. Butler, R. Martens, S.M. Kim, P. Kung, J. Electron. Mater., 41, 2012, 801.

[Desnica 1998] U.V. Desnica, Prog. Cryst. Growth Charact. Mater., 36, 1998, 291.

[Devaraj 2013] A. Devaraj, R. Colby, W.P. Hess, D.E. Perea, S. Thevuthasan, J. Phys. Chem. Lett., 4, 2013, 993.

[Dhara 2012] S. Dhara, P.K. Giri, Thin Solid Films, 520, 2012, 5000.

[Diercks 2013] D.R. Diercks, B.P. Gorman, R. Kirchhofer, N. Sanford, K. Bertness, M. Brubaker, J. Appl. Phys., 114, 2013, 184903.

[Dingle 1969] R. Dingle, Phys. Rev. Lett., 23, 1969, 579.

[Duguay 2010] S. Duguay, M. Ngamo, P.F. Fazzini, F. Cristiano, K. Daoud, P. Pareige, Thin Solid Films, 518, 2010, 2398.

[Fan 2007] J.C. Fan, Z. Xie, Q. Wan, Y.G. Wang, J. Cryst. Growth, 307, 2007, 66.

[Fang 2005] Z.B. Fang, Y.S. Tan, H.X. Gong, C.M. Zhen, Z.W. He, Y.Y. Wang, Mater. Lett., 59, 2005, 2611.

[Fang 2008] F. Fang, D.X. Zhao, J.Y. Zhang, D.Z. Shen, Y.M. Lu, X.W. Fan, B.H. Li, X.H. Wang, Mater. Lett., 62, 2008, 1092.

[Fang 2009] X. Fang, J. Li, D. Zhao, D. Shen, B. Li, X. Wang, J. Phys. Chem. C, 113, 2009, 21208.

[Friedrich 2007] F. Friedrich, N.H. Nickel, Appl. Phys. Lett., 91, 2007, 111903.

[Friedrich 2009] F. Friedrich, M.A. Gluba, N.H. Nickel, Appl. Phys. Lett., 95, 2009, 141903.

[Gault 2006] B. Gault, F. Vurpillot, A. Vella, M. Gilbert, A. Menand, D. Blavette, B. Deconihout, Rev. Sci. Instrum., 77, 2006, 043705.

[Gault 2012] B. Gault, M.P. Moody, J.M. Cairney, S.P. Ringer, Atom Probe Microscopy; 2012 edition.; Springer: New York, 2012.

[Gilbert 2007] M. Gilbert, F. Vurpillot, A. Vella, H. Bernas, B. Deconihout, Ultramicroscopy, 107, 2007, 767.

[Gomer 1959] R. Gomer, J. Chem. Phys., 31, 1959, 341.

[Grovenor 1982] C.R.M. Grovenor, G.D.W. Smith, Surf. Sci., 123, 1982, l686.

[Hafdallah 2011] A. Hafdallah, F. Yanineb, M.S. Aida, N. Attaf, J. Alloys Compd., 509, 2011, 7267.

[Hanfa 2009] L. Hanfa, Z. Huafu, L. Chengxin, Y. Changkun, J. Semicond., 30, 2009, 023001.

[Hofmann 2002] D.M. Hofmann, A. Hofstaetter, F. Leiter, H. Zhou, F. Henecker, B.K. Meyer, S.B. Orlinskii, J. Schmidt, P.G. Baranov, Phys. Rev. Lett., 88, 2002, 045504.

[Hosono 2002] H. Hosono, H. Ohta, K. Hayashi, M. Orita, M. Hirano, J. Cryst. Growth, 237–239, Part 1, 2002, 496.

[Huang.D 2013] D. Huang, X. Zeng, Y. Zheng, X. Wang, Y. Yang, Front. Optoelectron., 6, 2013, 114.

[Huang.S 2014] S. Huang, Y. Chen, X. Wei, M. Yin, J. Nanosci. Nanotechnol., 14, 2014, 4574.

[Huang.Y 2014] Y. Huang, W. Zhou, P. Wu, Solid State Commun., 183, 2014, 31.

[Inoue 2009] K. Inoue, F. Yano, A. Nishida, H. Takamizawa, T. Tsunomura, Y. Nagai, M. Hasegawa, Ultramicroscopy, 109, 2009, 1479.

[Jang 2005] S. Jang, J.-J. Chen, B.S. Kang, F. Ren, D.P. Norton, S.J. Pearton, J. Lopata, W.S. Hobson, Appl. Phys. Lett., 87, 2005, 222113.

[Janotti 2009] A. Janotti, C.G.V. de Walle, Rep. Prog. Phys., 72, 2009, 126501.

[Jeong 2004] S.H. Jeong, J.H. Boo, Thin Solid Films, 447–448, 2004, 105.

[Kalin 2000] M. Kalin, J. Vižintin, J. Vleugels, O. Van Der Biest, Mater. Sci. Eng. A, 281, 2000, 28.

[Kang 2003] J.S. Kang, H.S. Kang, S.S. Pang, E.S. Shim, S.Y. Lee, Thin Solid Films, 443, 2003, 5.

[Kanjolia 2011] R. Kanjolia, A.C. Jones, S. Ashraf, J. Bacsa, K. Black, P.R. Chalker, P. Beahan, S. Hindley, R. Odedra, P.A. Williams, P.N. Heys, J. Cryst. Growth, 315, 2011, 292.

[Kao 2014] T.-H. Kao, J.-Y. Chen, C.-H. Chiu, C.-W. Huang, W.-W. Wu, Appl. Phys. Lett., 104, 2014, 111909.

[Kar 2010] J.P. Kar, S.N. Das, J.H. Choi, T.I. Lee, J.M. Myoung, Appl. Surf. Sci., 256, 2010, 4995.

[Kaschner 2002] A. Kaschner, U. Haboeck, M. Strassburg, M. Strassburg, G. Kaczmarczyk, A. Hoffmann, C. Thomsen, A. Zeuner, H.R. Alves, D.M. Hofmann, B.K. Meyer, Appl. Phys. Lett., 80, 2002, 1909.

[Kellogg 1982] G.L. Kellogg, Appl. Surf. Sci., 11–12, 1982, 186.

[Kellogg 1980] G.L. Kellogg, T.T. Tsong, J. Appl. Phys., 51, 1980, 1184.

[Kerr 2007] L.L. Kerr, X. Li, M. Canepa, A.J. Sommer, Thin Solid Films, 515, 2007, 5282.

[Kim 2006] D. Kim, T. Shimomura, S. Wakaiki, T. Terashita, M. Nakayama, Phys. B Condens. Matter, 376–377, 2006, 741.

[Kim 2007] D.C. Kim, W.S. Han, B.H. Kong, H.K. Cho, C.H. Hong, Phys. B Condens. Matter, 401–402, 2007, 386.

[Kim 2010] Y. Kim, W. Lee, D.-R. Jung, J. Kim, S. Nam, H. Kim, B. Park, Appl. Phys. Lett., 96, 2010, 171902.

[Kingham 1982] D.R. Kingham, Surf. Sci., 116, 1982, 273.

[Kinno 2014] T. Kinno, M. Tomita, T. Ohkubo, S. Takeno, K. Hono, Appl. Surf. Sci., 290, 2014, 194.

[Kirchhofer 2013] R. Kirchhofer, M.C. Teague, B.P. Gorman, J. Nucl. Mater., 436, 2013, 23.

[Kittel 2004] C. Kittel, Introduction to Solid State Physics; 8 edition.; Wiley: Hoboken, NJ, 2004.

[Klingshirn 2010] C.F. Klingshirn, Zinc Oxide: From Fundamental Properties Towards Novel Applications; Springer, 2010; Vol. 120.

[Kohan 2000] A.F. Kohan, G. Ceder, D. Morgan, C.G. Van de Walle, Phys. Rev. B, 61, 2000, 15019.

[Kong 2008] J. Kong, S. Chu, M. Olmedo, L. Li, Z. Yang, J. Liu, Appl. Phys. Lett., 93, 2008, 132113.

[Kumar 2014] V. Kumar, S. Som, V. Kumar, V. Kumar, O.M. Ntwaeaborwa, E. Coetsee, H.C. Swart, Chem. Eng. J., 255, 2014, 541.

[Kumar 2014] V. Kumar, V. Kumar, S. Som, M.M. Duvenhage, O.M. Ntwaeaborwa, H.C. Swart, Appl. Surf. Sci., 308, 2014, 419.

[Lardé 2009] R. Lardé, L. Lechevallier, A. Zarefy, A. Bostel, J. Juraszek, J.M.L. Breton, B. Rodmacq, B. Dieny, J. Appl. Phys., 105, 2009, 084307.

[Lardé 2011] R. Lardé, E. Talbot, P. Pareige, H. Bieber, G. Schmerber, S. Colis, V. Pierron-Bohnes, A. Dinia, J. Am. Chem. Soc., 133, 2011, 1451.

[Lee 2009] J.Y. Lee, J.H. Lee, H. Seung Kim, C.-H. Lee, H.-S. Ahn, H.K. Cho, Y.Y. Kim, B.H. Kong, H.S. Lee, Thin Solid Films, 517, 2009, 5157.

[Limpijumnong 2004] S. Limpijumnong, S.B. Zhang, S.-H. Wei, C.H. Park, Phys. Rev. Lett., 92, 2004, 155504.

[Lin 2001] B. Lin, Z. Fu, Y. Jia, Appl. Phys. Lett., 79, 2001, 943.

[Liu 1992] M. Liu, A.H. Kitai, P. Mascher, J. Lumin., 54, 1992, 35.

[Look 2001] D.C. Look, Mater. Sci. Eng. B, 80, 2001, 383.

[Look 2002] D.C. Look, D.C. Reynolds, C.W. Litton, R.L. Jones, D.B. Eason, G. Cantwell, Appl. Phys. Lett., 81, 2002, 1830.

[Look 2004] D.C. Look, B. Claflin, Phys. Status Solidi B, 241, 2004, 624.

[Look 2005] D.C. Look, G.C. Farlow, P. Reunchan, S. Limpijumnong, S.B. Zhang, K. Nordlund, Phys. Rev. Lett., 95, 2005, 225502.

[Look 2006] D.C. Look, In Zinc Oxide Bulk, Thin Films and Nanostructures; Jagadish, C.; Pearton, S., Eds.; Elsevier Science Ltd: Oxford, 2006; pp. 21–42.

[Lü 2010] J. Lü, K. Huang, J. Zhu, X. Chen, X. Song, Z. Sun, Phys. B Condens. Matter, 405, 2010, 3167.

[Lyons 2009] J.L. Lyons, A. Janotti, C.G.V. de Walle, Appl. Phys. Lett., 95, 2009, 252105.

[Makino 2001] T. Makino, Y. Segawa, M. Kawasaki, A. Ohtomo, R. Shiroki, K. Tamura, T. Yasuda, H. Koinuma, Appl. Phys. Lett., 78, 2001, 1237.

[Mancini 2014] L. Mancini, N. Amirifar, D. Shinde, I. Blum, M. Gilbert, A. Vella, F. Vurpillot, W. Lefebvre, R. Lardé, E. Talbot, P. Pareige, X. Portier, A. Ziani, C. Davesnne, C. Durand, J. Eymery, R. Butte, J.-F. Carlin, N. Grandjean, L. Rigutti, J. Phys. Chem. C, 2014.

[Mao-Shui 2007] L. Mao-Shui, P. Zhi-Yong, X. Xian-Wu, D. Ying, H. Sheng-Hao, Chin. Phys., 16, 2007, 548.

[Marquis 2010] E.A. Marquis, J.M. Hyde, Mater. Sci. Eng. R Rep., 69, 2010, 37.

[Marzouki 2010] A. Marzouki, F. Falyouni, N. Haneche, A. Lusson, P. Galtier, L. Rigutti, G. Jacopin, M. Tchernycheva, M. Oueslati, V. Sallet, Mater. Lett., 64, 2010, 2112.

[Meyer 2004] B.K. Meyer, H. Alves, D.M. Hofmann, W. Kriegseis, D. Forster, F. Bertram, J. Christen, A. Hoffmann, M. Straßburg, M. Dworzak, U. Haboeck, A.V. Rodina, Phys. Status Solidi B, 241, 2004, 231.

[Meyer 2007] B. Meyer, J. Sann, S. Lautenschläger, M. Wagner, A. Hoffmann, Phys. Rev. B, 76, 2007.

[Meyer 2010] B.K. Meyer, J. Sann, S. Eisermann, S. Lautenschlaeger, M.R. Wagner, M. Kaiser, G. Callsen, J.S. Reparaz, A. Hoffmann, Phys. Rev. B, 82, 2010.

[Miller 1996] M.K. Miller, A. Cerezo, M.G. Hetherington, G.D.W.S. FRS, Atom Probe Field Ion Microscopy; Clarendon Press | Monographs on the Physics and Chemistry of Materials 52, 1996.

[Minegishi 1997] K. Minegishi, Y. Koiwai, Y. Kikuchi, K. Yano, M. Kasuga, A. Shimizu, Jpn. J. Appl. Phys., 36, 1997, l1453.

[Monakhov 2009] E.V. Monakhov, A.Y. Kuznetsov, B.G. Svensson, J. Phys. Appl. Phys., 42, 2009, 153001.

[Montenegro 2012] D.N. Montenegro, A. Souissi, C. Martínez-Tomás, V. Muñoz-Sanjosé, V. Sallet, J. Cryst. Growth, 359, 2012, 122.

[Morkoç 2009] H. Morkoç, Ü. Özgür, In Zinc Oxide; Wiley-VCH Verlag GmbH & Co. KGaA, 2009; pp. 131–244.

[Mouton 2012] I. Mouton, R. Lardé, E. Talbot, E. Cadel, C. Genevois, D. Blavette, V. Baltz, E. Prestat, P. Bayle-Guillemaud, A. Barski, M. Jamet, J. Appl. Phys., 112, 2012, 113918.

[Müller 1956] E.W. Müller, K. Bahadur, Phys. Rev., 102, 1956, 624.

[Müller 1968] E.W. Müller, J.A. Panitz, S.B. McLane, Rev. Sci. Instrum., 39, 1968, 83.

[Myers 2012] M.A. Myers, M.T. Myers, M.J. General, J.H. Lee, L. Shao, H. Wang, Appl. Phys. Lett., 101, 2012, 112101.

[Nakamura 1991] S. Nakamura, Jpn. J. Appl. Phys., 30, 1991, l1705.

[Nakamura 1991] S. Nakamura, T. Mukai, M. Senoh, Jpn. J. Appl. Phys., 30, 1991, l1998.

[Nath 2012] S. Nath, J. Prakash, J. Xiong, J.-M. Myoung, In Nanowires - Recent Advances; Peng, X., Ed.; InTech, 2012.

[Ngamo 2010] M. Ngamo, S. Duguay, P. Pichler, K. Daoud, P. Pareige, Thin Solid Films, 518, 2010, 2402.

[Nickel 2003] N.H. Nickel, K. Fleischer, Phys. Rev. Lett., 90, 2003, 197402.

[Oppenheimer 1928] J.R. Oppenheimer, Phys. Rev., 31, 1928, 66.

[Orloff 2003] J. Orloff, L. Swanson, M. Utlaut, High Resolution Focused Ion Beams: FIB and its Applications: Fib and Its Applications : The Physics of Liquid Metal Ion Sources and Ion Optics and Their Application to Focused Ion Beam Technology; Springer Science & Business Media, 2003.

[Otal 2015] E.H. Otal, E. Sileo, M.H. Aguirre, I.O. Fabregas, M. Kim, J. Alloys Compd., 622, 2015, 115.

[Özgür 2005] Ü. Özgür, Y.I. Alivov, C. Liu, A. Teke, M.A. Reshchikov, S. Doğan, V. Avrutin, S.-J. Cho, H. Morkoç, J. Appl. Phys., 98, 2005, 041301.

[Pan 2001] Z.W. Pan, Z.R. Dai, Z.L. Wang, Science, 291, 2001, 1947.

[Park 2002] C.H. Park, S.B. Zhang, S.-H. Wei, Phys. Rev. B, 66, 2002, 073202.

[Park 2008] S.H. Park, J.H. Chang, H.J. Ko, T. Minegishi, J.S. Park, I.H. Im, M. Ito, D.C. Oh, M.W. Cho, T. Yao, Appl. Surf. Sci., 254, 2008, 7972.

[Park 2014] J.Y. Park, J.H. Lee, G.S.R. Raju, B.K. Moon, J.H. Jeong, B.C. Choi, J.H. Kim, Ceram. Int., 40, 2014, 5693.

[Perillat-Merceroz 2010] G. Perillat-Merceroz, P.H. Jouneau, G. Feuillet, R. Thierry, M. Rosina, P. Ferret, J. Phys. Conf. Ser., 209, 2010, 012034.

[Perillat-Merceroz 2012] G. Perillat-Merceroz, R. Thierry, P.-H. Jouneau, P. Ferret, G. Feuillet, Nanotechnology, 23, 2012, 125702.

[Philippe 2009] T. Philippe, F. De Geuser, S. Duguay, W. Lefebvre, O. Cojocaru-Mirédin, G. Da Costa, D. Blavette, Ultramicroscopy, 109, 2009, 1304.

[Podhorodecki 2010] A. Podhorodecki, M. Banski, J. Misiewicz, J. Serafinczuk, N.V. Gaponenko, J. Electrochem. Soc., 157, 2010.

[Rakhesh 2007] V. Rakhesh, M. Junaid Bushiri, V.K. Vaidyan, J. Optoelectron. Adv. Mater., 9, 2007, 3740.

[Rakov 2013] N. Rakov, W. Lozano B., E.L. Falcão-filho, R.B. Guimarães, G.S. Maciel, C.B. de Araújo, Opt. Mater. Express, 3, 2013, 1803.

[Reynolds 1965] D.C. Reynolds, C.W. Litton, T.C. Collins, Phys. Rev., 140, 1965, a1726.

[Riley 2012] J.R. Riley, R.A. Bernal, Q. Li, H.D. Espinosa, G.T. Wang, L.J. Lauhon, ACS Nano, 6, 2012, 3898.

[Roussel 2011] M. Roussel, W. Chen, E. Talbot, R. Lardé, E. Cadel, F. Gourbilleau, B. Grandidier, D. Stiévenard, P. Pareige, Nanoscale Res. Lett., 6, 2011, 271.

[Roussel 2013] M. Roussel, E. Talbot, C. Pareige, R.P. Nalini, F. Gourbilleau, P. Pareige, Appl. Phys. Lett., 103, 2013, 203109.

[Sakurai 1978] T. Sakurai, R.J. Culbertson, A.J. Melmed, Surf. Sci., 78, 1978, l221.

[Santhanagopalan 2015] D. Santhanagopalan, D.K. Schreiber, D.E. Perea, R.L. Martens, Y. Janssen, P. Khalifah, Y.S. Meng, Ultramicroscopy, 148, 2015, 57.

[Schirra 2008] M. Schirra, R. Schneider, A. Reiser, G.M. Prinz, M. Feneberg, J. Biskupek, U. Kaiser, C.E. Krill, K. Thonke, R. Sauer, Phys. Rev. B, 77, 2008, 125215.

[Shen 2014] Y. Shen, X. Chen, X. Yan, F. Yi, Z. Bai, X. Zheng, P. Lin, Y. Zhang, Curr. Appl. Phys., 14, 2014, 345.

[Shestakov 2012] M.V. Shestakov, A.N. Baranov, V.K. Tikhomirov, Y.V. Zubavichus, A.S. Kuznetsov, A.A. Veligzhanin, A.Y. Kharin, R. Rösslhuber, V.Y. Timoshenko, V.V. Moshchalkov, RSC Adv., 2, 2012, 8783.

[Silaeva 2014] E.P. Silaeva, L. Arnoldi, M.L. Karahka, B. Deconihout, A. Menand, H.J. Kreuzer, A. Vella, Nano Lett., 14, 2014, 6066.

[Singh 2014] N.S. Singh, S.D. Singh, S.D. Meetei, Chin. Phys. B, 23, 2014, 058104.

[Sohn 2014] J.I. Sohn, Y.-I. Jung, S.-H. Baek, S. Cha, J.E. Jang, C.-H. Cho, J.H. Kim, J.M. Kim, I.-K. Park, Nanoscale, 6, 2014, 2046.

[Souissi 2013] A. Souissi, N. Haneche, A. Meftah, C. Sartel, C. Vilar, A. Lusson, P. Galtier, V. Sallet, M. Oueslati, J. Lumin., 136, 2013, 265.

[Soumahoro 2011] I. Soumahoro, G. Schmerber, A. Douayar, S. Colis, M. Abd-Lefdil, N. Hassanain, A. Berrada, D. Muller, A. Slaoui, H. Rinnert, A. Dinia, J. Appl. Phys., 109, 2011, 033708.

[Stavola 1998] M. Stavola, Identification of Defects in Semiconductors; Édition : 1.; Academic Press, 1998.

[Su 2012] J. Su, C. Tang, Q. Niu, C. Zang, Y. Zhang, Z. Fu, Appl. Surf. Sci., 258, 2012, 8595.

[Sun 2006] J.W. Sun, Y.M. Lu, Y.C. Liu, D.Z. Shen, Z.Z. Zhang, B.H. Li, J.Y. Zhang, B. Yao, D.X. Zhao, X.W. Fan, Solid State Commun., 140, 2006, 345.

[Sun 2008] J.C. Sun, H.W. Liang, J.Z. Zhao, J.M. Bian, Q.J. Feng, L.Z. Hu, H.Q. Zhang, X.P. Liang, Y.M. Luo, G.T. Du, Chem. Phys. Lett., 460, 2008, 548.

[Sun 2009] X.W. Sun, B. Ling, J.L. Zhao, S.T. Tan, Y. Yang, Y.Q. Shen, Z.L. Dong, X.C. Li, Appl. Phys. Lett., 95, 2009, 133124.

[Talbot 2009] E. Talbot, R. Lardé, F. Gourbilleau, C. Dufour, P. Pareige, EPL Europhys. Lett., 87, 2009, 26004.

[Talbot 2013] E. Talbot, R. Lardé, P. Pareige, L. Khomenkova, K. Hijazi, F. Gourbilleau, Nanoscale Res. Lett., 8, 2013, 39.

[Tao 2012] P. Tao, Q. Feng, J. Jiang, H. Zhao, R. Xu, S. Liu, M. Li, J. Sun, Z. Song, Chem. Phys. Lett., 522, 2012, 92.

[Theys 2002] B. Theys, V. Sallet, F. Jomard, A. Lusson, J.-F. Rommeluère, Z. Teukam, J. Appl. Phys., 91, 2002, 3922.

[Tsong 1984] T.T. Tsong, Phys. Rev. B, 30, 1984, 4946.

[Tsong 1976] T.T. Tsong, J.H. Block, M. Nagasaka, B. Viswanathan, J. Chem. Phys., 65, 1976, 2469.

[Tsong 1978] T.T. Tsong, Y.S. Ng, A.J. Melmed, Surf. Sci., 77, 1978, l187.

[Tsong 1982] T.T. Tsong, S.B. McLane, T.J. Kinkus, Rev. Sci. Instrum., 53, 1982, 1442.

[Tsukazaki 2005] A. Tsukazaki, A. Ohtomo, T. Onuma, M. Ohtani, T. Makino, M. Sumiya, K. Ohtani, S.F. Chichibu, S. Fuke, Y. Segawa, H. Ohno, H. Koinuma, M. Kawasaki, Nat. Mater., 4, 2005, 42.

[Tuomisto 2005] F. Tuomisto, K. Saarinen, D.C. Look, G.C. Farlow, Phys. Rev. B, 72, 2005, 085206.

[U.S. Department of energy] energy.gov/science-innovation/science-technology

[Vaithianathan 2005] V. Vaithianathan, B.-T. Lee, S.-S. Kim, Appl. Phys. Lett., 86, 2005, 062101.

[Vaithianathan 2005] V. Vaithianathan, B.-T. Lee, S.S. Kim, J. Appl. Phys., 98, 2005, 043519.

[Van de Walle 2000] C.G. Van de Walle, Phys. Rev. Lett., 85, 2000, 1012.

[Van de Walle 2001] C.G. Van de Walle, Phys. B Condens. Matter, 308–310, 2001, 899.

[Vidya 2012] R. Vidya, P. Ravindran, H. Fjellvåg, J. Appl. Phys., 111, 2012, 123713.

[Wagner 2010] M.R. Wagner, Fundamental properties of excitons and phonons in ZnO: A spectroscopic study of the dynamics, polarity, and effects of external fields, Universitätsbibliothek, 2010.

[Wang 2004] Z.L. Wang, J. Phys. Condens. Matter, 16, 2004, r829.

[Wang 2003] Z.L. Wang, X.Y. Kong, J.M. Zuo, Phys. Rev. Lett., 91, 2003, 185502.

[Wang 2006] B. Wang, M.J. Callahan, L.O. Bouthillette, C. Xu, M.J. Suscavage, J. Cryst. Growth, 287, 2006, 381.

[Wei 2007] Z.P. Wei, Y.M. Lu, D.Z. Shen, Z.Z. Zhang, B. Yao, B.H. Li, J.Y. Zhang, D.X. Zhao, X.W. Fan, Z.K. Tang, Appl. Phys. Lett., 90, 2007, 042113.

[Williams 2009] D.. Williams, C.B. Carter, Transmission Electron Microscopy; 2nd ed.; Springer, 2009.

[Xiao 2008] Z.Y. Xiao, Y.C. Liu, R. Mu, D.X. Zhao, J.Y. Zhang, Appl. Phys. Lett., 92, 2008, 052106.

[Yang 2008] L. Yang, Y. Tang, A. Hu, X. Chen, K. Liang, L. Zhang, Phys. B Condens. Matter, 403, 2008, 2230.

[Yang 2008] Y. Yang, X.W. Sun, B.K. Tay, G.F. You, S.T. Tan, K.L. Teo, Appl. Phys. Lett., 93, 2008, 253107.

[Yang 2011] J. Yang, X. Li, J. Lang, L. Yang, M. Wei, M. Gao, X. Liu, H. Zhai, R. Wang, Y. Liu, J. Cao, Mater. Sci. Semicond. Process., 14, 2011, 247.

[Ye 2007] J.D. Ye, S.L. Gu, F. Li, S.M. Zhu, R. Zhang, Y. Shi, Y.D. Zheng, X.W. Sun, G.Q. Lo, D.L. Kwong, Appl. Phys. Lett., 90, 2007, 152108.

[Yi 2010] J.B. Yi, C.C. Lim, G.Z. Xing, H.M. Fan, L.H. Van, S.L. Huang, K.S. Yang, X.L. Huang, X.B. Qin, B.Y. Wang, T. Wu, L. Wang, H.T. Zhang, X.Y. Gao, T. Liu, A.T.S. Wee, Y.P. Feng, J. Ding, Phys. Rev. Lett., 104, 2010.

[Zeng 2007] Y.J. Zeng, Z.Z. Ye, W.Z. Xu, B. Liu, Y. Che, L.P. Zhu, B.H. Zhao, Mater. Lett., 61, 2007, 41.

[Zeuner 2002] A. Zeuner, H. Alves, D. m. Hofmann, B. k. Meyer, A. Hoffmann, U. Haboeck, M. Strassburg, M. Dworzak, Phys. Status Solidi B, 234, 2002, r7.

[Zhang 1999] S.B. Zhang, S.-H. Wei, A. Zunger, Phys. B Condens. Matter, 273–274, 1999, 976.

[Zhang 2001] S.B. Zhang, S.-H. Wei, A. Zunger, Phys. Rev. B, 63, 2001, 075205.

[Zhang 2008] J.-Y. Zhang, P.-J. Li, H. Sun, X. Shen, T.-S. Deng, K.-T. Zhu, Q.-F. Zhang, J.-L. Wu, Appl. Phys. Lett., 93, 2008, 021116.

[Zheng 2009] M. Zheng, J. Wu, Appl. Surf. Sci., 255, 2009, 5656.

[Zheng 2011] Y.-Z. Zheng, X. Tao, Q. Hou, D.-T. Wang, W.-L. Zhou, J.-F. Chen, Chem. Mater., 23, 2011, 3.

[Ziani 2014] A. Ziani, C. Davesnne, C. Labbé, J. Cardin, P. Marie, C. Frilay, S. Boudin, X. Portier, Thin Solid Films, 553, 2014, 52.